Si-based epitaxy processes for 14 and 10 nm CMOS technologies : Morphology and structure

Victorien Paredes-Saez

N°d'ordre NNT : 2017LYSEI032

THESE de DOCTORAT DE L'UNIVERSITE DE LYON

opérée au sein de

L'institut national des sciences appliquées de Lyon

Ecole Doctorale N° 34

Ecole Doctorale « Matériaux de Lyon »

Spécialité Matériaux

Soutenue publiquement le 12/05/2017, par :

Victorien Paredes-Saez

Procédés d'épitaxie spécifiques au CMOS 14 et 10 nm: morphologie et structure

---

Devant le jury composé de :

Berbezier Isabelle, Directrice de Recherche CNRS, IM2NP, Rapporteur
Fontaine Chantal, Directrice de Recherche CNRS, LAAS-CNRS, Rapporteur
Renard Charles, Chargé de Recherche CNRS, C2N, Examinateur
Bischoff Jean-Luc, Professeur des Universités, UHA, Examinateur

Dutartre Didier, Docteur, STMicroelectronics, Co-directeur de thèse
Bremond Georges, Professeur des Universités, INL, Directeur de thèse

Contents

Abreviations

a_{Ge}	Ge lattice constant
a_{Si}	Si lattice constant
a_{SiGe}	SiGe lattice constant
$a^{//}_{SiGe}$	In-plane lattice constant of SiGe
$a^{\perp}_{SiGe}$	Out-of-plane lattice constant of SiGe
AZ	Active zone
AFM	Atomic force microscopy
ALE	Anisotropic loading effect
AMAT	Applied Material
BA	Backside angle
CMOS	Complementary Metal Oxide Semiconductor
CVD	Chemical vapor deposition
d_{hkl}	Spacing distance
D	Dose
DCS	Dichlorosilane
DIBL	Drain-induced Barrier Lowering
ELO	Epitaxial lateral overgrowth
ER	Etch rate
FA	Front-side angle
FD-SOI	Fully-depleted Silicon-on-insulator
FM	Frank-van-der Merwe
FOUP	Front opening unified pod
f_x	Misfit
GR	Growth rate
lowGR	Low growth rate (2.2 nm/min)
medGR	Intermediate growth rate (3.4 nm/min)
highGR	High growth rate (4.0 nm/min)
HBT	Heterojunction bipolar transistor
h_c	Critical thickness
HKMG	High-K Metal Gate
HRXRD	High resolution X-ray diffraction
ITRS	International Technology Roadmap for Semiconductor
LL	Load lock
MBE	Molecular beam epitaxy
MBIR	Model-based infrared reflectometry
MOS	Metal Oxide Semiconductor
MOSFET	Metal Oxide Semiconductor Field Effect Transistor
NSEG	Non-selective epitaxial growth
PID	Proportional-Integrative-Derivative
PSD	Power spectral density
R_{MAX}	Maximal topography
R_{RMS}	Root-mean square roughness
RSD	Raised source and drain
RT-CVD	Rapid thermal chemical vapor deposition

SCE	Short-channel effect
S/D	Source and drain
SE	Spectroscopic ellipsometry
SEG	Selective epitaxial growth
SEM	Scanning electron microscopy
SIA	Semiconductor Industry Association
SiGe	Silicon-gemanium
SiGe:B	Boron-doped silicon-germanium
SIMS	Secondary ion mass spectroscopy
SK	Stranski-Krastanov
SPM	Scanning probe microscopy
T_{eq}	Temperature at the “equilibrium” state
TEM	Transmission electron microscopy
th	Thickness
UHV-CVD	Ultra-high vacuum chemical vapor deposition
UTB SOI	Ultrathin Body Silicon-on-insulator
VT	Threshold voltage
VW	Volmer-Weber
XGe	Germanium content (between 0 and 1)
XPS	X-ray photo-electron spectroscopy
XRD	X-ray diffraction
XRF	X-ray fluorescence
γ	Surface energy
λ	Wavelength

General context and introduction

Once upon a time, the transistor.

It all began in 1947 when William Shockley, John Bardeen, and Walter Brattain had the brilliant and ingenious idea to produce the first transistor in the world (shown in ***Fig. 0-1***). This marvelous discovery, which resulted in the procurement of a Novel Price for these scientists in 1956, has led to the advent of the microelectronics.

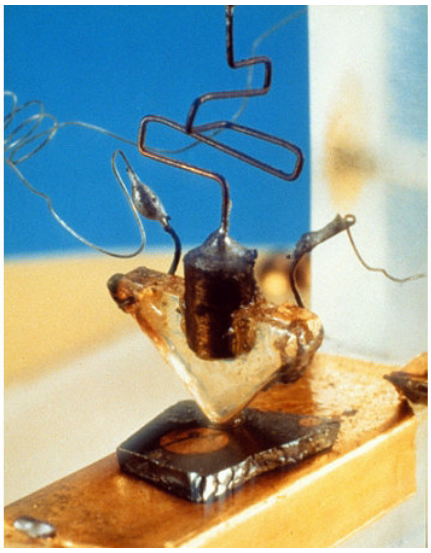

Fig. 0-1*: The first semiconductor amplifier: the point-contact transistor, with two metal points in contact with a sliver of germanium.*

Since when, an unremitting race against time began to continuously enhance the performances leading to a continuous decrease of the transistors' size. It was only 40 years ago, the channel length of transistors was of several micrometers whereas nowadays, thanks to the improvement of fabrication techniques such as lithography, the dimensions have been reduced to only about 10 nanometers and less.

When talking about scaling, it is very important to introduce the famous empirical Moore's law. This law is issue from an observation made by the Intel co-founder Gordon E. Moore in 1965 in which he made the postulate of a doubling every year in the number of components per integrated circuits. In 1975, he revisited the forecast rate, stating that the device count per unit area must double and the area for the same device count must drop by half every two years [Moore 75]. At that point, the reduction of dimensions in MOS (Metal Oxide Semiconductor) technologies followed with such an astonishing accuracy this empirical extrapolation. As a result, a large number of industries (like IBM, Intel or STMicroelectronics) have made of this law their main roadmap in order to increase the productivity, to reduce the cost and to enhance devices' performances (***Fig. 0-2***). Furthermore, the Semiconductor Industry Association (SIA) has charted its membership to develop in 1998 the International Technology Roadmap for Semiconductors (ITRS). As a consequence, the channel length, the

gate oxide thickness and source/drain junction depth have been reduced in a way the channel length which was several micrometers in 1970 is today only few nanometers. In other words, the fabrication of integrated circuits of few cm² in which are patterned several millions of transistors is now possible.

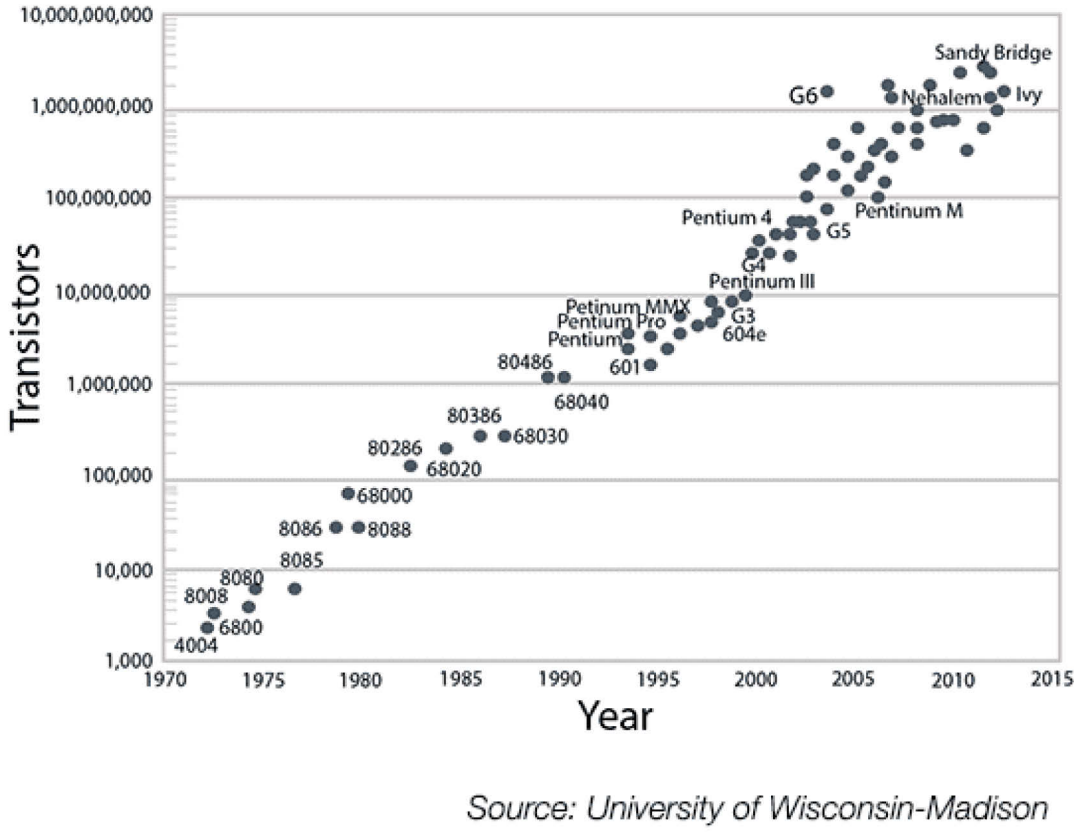

***Fig. 0-2**: Moore's law and evolution of silicon technology.*

However, there is a real problem with exponential increase in a sense it rapidly approaches the infinity, while physical systems cannot run into infinity. Moore himself has said "no exponential is forever" [Moore 03] Therefore, the recent technological progresses on advanced devices for Complementary Metal Oxide Semiconductors (CMOS) technologies are approaching some physical limitations such as optical lithography, gate dielectric thickness, short channel, etc, which will be described later on in this chapter. Also, as process technologies continued to shrink towards 20-nanometers, it became impossible to achieve a similar scaling of certain device parameters, particularly the power supply voltage, which is the dominant factor in determining dynamic power. Consequently, new challenges and efforts have to be defined in order to improve the transistor's performances. One of the most promising modifications addressing many problems encountered in the chip was the introduction and the adjustment of new materials. These materials include low-resistivity conductors, low-K dielectrics, and strained Si adding, for instance, a layer with a larger lattice parameter than Si [Maiti 98] [Currie 04]. This is the case of $Si_{1-x}Ge_x$ (SiGe) alloys. SiGe presents a real interest due to its attractive crystalline, mechanical and electronics properties [Ribot 02]. This way, SiGe alloys are integrated in more and more complex structures, and their applications are numerous. Historically, the SiGe was introduced for the fabrication of the

bipolar transistor's base. Lately, it was integrated as a booster for the holes mobility in the source and drain p-type Metal Oxide-Semiconductor Field-Effect Transistor (pMOSFET). The increase of the holes mobility is due to the strain that is exerted in the channel.

The Metal Oxide-Semiconductor Field-Effect Transistor

In the Metal Oxide-Semiconductor Field-Effect Transistor (MOSFET), the current is controlled by applying an electric field perpendicular to both the semiconductor surface and to the direction of current. The phenomenon allowing this control is called field effect, whence the term field-effect transistor. ***Fig. 0-3*** shows the structure of an n- (or p-) channel MOS Field Effect Transistor. In the case of a NMOS transistor, on the p substrate there are two highly n-doped regions called source and drain. For a PMOS transistor, the substrate is n-doped while the source and the drain are p-doped. A thin layer of oxide (SiO_2 and HfO_2 in recent MOSFET) allowing the electrical insulation is deposited at the surface of the substrate between the source and drain. On this insulating layer, the gate is formed. Even though the current structure of MOSFET is really complex (e.g. the gate is formed of TiN and Polycrystalline Si), the schematic representation bellow may be used to describe the basic principle of a transistor.

In a MOSFET, the electrical junction n/p or p/n are essential. They represent the main reservoir of the carrier charges (electrons or holes) and are separated by the channel. The channel is therefore a potential barrier controlled by the gate. When a zero-bias is applied to the gate, the transistor is equivalent to two back-to-back diodes and the current is zero. However, when the voltage is large enough (threshold voltage), an electron inversion layer is created in the channel allowing the carrier charges to flow and a current is then generated between the source and the drain. In a general way, the drain is polarized whereas the source and the substrate are connected to ground. In the case of an NMOS transistor, the carriers in the inversion layer are electrons whereas in PMOS transistor, the carriers are holes.

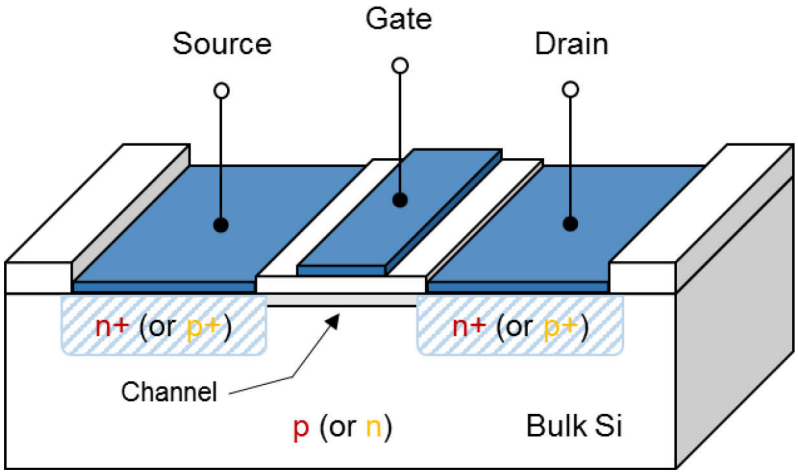

Fig. 0-3*: Schematic diagram of n- (or p-) channel MOSFET.*

To form a Complementary MOS (CMOS) inverter, the basic building block of CMOS logic, both NMOS and PMOS transistors connected together in the same circuit are required.

Why is scaling coming to an end?

Although the scaling of transistors has always succeeded to overcome all the predicted barriers which have been defined in 1970 just shortly after Moore proposed the law [Hoeneisen 72], many experts are claiming the end of the process of shrinking CMOS transistors that no amount of research can push past. In this section, some limitations are briefly described.

Physical limitations

The first limitations when dealing with scaling are obviously the physical limitations. Indeed, the hard limit is clearly the size of the atom or molecule, since devices cannot be smaller than the dimension of a single atom or molecule. Also, some detrimental issues can be added when decreasing devices dimension including the reduction in gate dielectric thickness and channel length. First, a thin enough gate dielectric may lead to quantum mechanical tunneling increasing exponentially the gate leakage current, reducing reliability and degrading channel mobility [Tyagi 07]. Second, channel engineering intended to control threshold voltage (e.g. a short channel allows a faster switching operation since carriers travel a shorter distance from source to drain) and prevent punch-through. However, detrimental issues can be found for too short channels. As example, short channels enable the majority carriers to flow from source to drain even if the transistor is turned off, resulting in punch-through, drain-induced barrier lowering (DIBL) and as a result leakage currents. Since CMOS technology is bounded, an optimal device miniaturization with maximal processing performance should exist. [Frank 06]. In other words, beneath a certain dimension and at a fixed power, the overall performances of the device deteriorate. This is attributed to the trade-off between the benefits of the scaling (reducing capacitance and enabling increasing performance at fixed power) and the increase of leakage current, due to quantum mechanical tunneling, as soon as the dimensions are sufficiently reduced.

Material limitations

The change in materials for CMOS technology has known a slow advancement but increasingly it has become obvious that the adjustment of materials influencing directly the properties of the devices can overcome many problems encountered in the chips. Indeed, from 1980 to 1995, substantially new materials were introduced at the rate of about one every two or three generations [Nowak 02]. Still now, substantial efforts are required to introduce new materials and many researchers are studying the possibility, as example, to introduce III-V semiconductor materials in CMOS devices. Many other materials are studied, but major new changes in materials are very difficult and costly.

It was shown by Lo *et al.* that a reduction of oxide thickness from 2 nm to 1.5 nm produces leakage current of two order of magnitude [Lo 97], which is unacceptable for devices. An alternative to overcome these problems was the introduction of new dielectric materials which could create a good interface with Si, comparable to Si/SiO_2. This is the case of high dielectric constants materials (High-K) (e.g. hafnium dioxide HfO_2) allowing the thickness of the gate dielectric to be increased while still maintaining the same gate capacitance characteristics. Since the 28 nm node, another material was introduced in the gate in order to be able to modulate the threshold voltage. Indeed, for a gate made of SiO_2/HfO_2/Polycrystalline Si stack, Fermi level is blocked in the middle of Si gate avoiding to drop the threshold voltage of the transistor. A metal was then introduced between the High-K material and the polycrystalline Si. Typically, this metal can be titanium nitride (TiN). This high-k/metal gate (HKMG) technology was a fundamental shift in Si CMOS since it was the relatively pure SiO_2 gate oxide

interface that initially made Si CMOS more attractive than other transistor technologies [Chau 04] [Mistry 07].

Another major issue that was subjected to long discussions concerns hole and electron mobility. The most promising and efficient method is to introduce physical strain inside the silicon lattice. To do so, a layer with a lattice constant different from Si is added to the silicon. The lattice mismatch between both materials introduce a strain that will expand or stretch the silicon. This allows the holes and electrons to flow more freely thus reducing device resistance and other properties effected by electron/hole mobility. SiGe is the perfect material which brings all the requirements needed together to enhance most of the device's performances. This material is the real concern of the present thesis, and is extensively studied in the following chapters.

Technology and economic limitations

CMOS technology is based on the fabrication of patterns on the substrate by means of masks and lithography. As a consequence, lithography is the key technology to pursue the race to transistor scaling, and may in the same way impede future scaling of devices. Indeed, it was assumed that spatial resolution smaller than the wavelength used for the lithographic process requires trade-off between complex, costly masks and possible design constraint [Hoeneisen 72]. Moreover, the cost of lithography tool, including that required for making masks and the research to reduce the minimum wavelength (nowadays into the extreme ultraviolet spectrum: 13 nm wavelengths), attains so extreme elevated amount that this is beginning to limit the profitability of increased scaling. To be noted, the purchase of lithography tools represent one of the bigger investments in microelectronics industry. In summary, Manufacturing tolerance, and therefore economics, may dictate an end to the scaling of silicon devices before the fundamental limits are reached.

The transistor of today

Even though all the mentioned developments of HKMG and strain techniques to improve the device performances, the continued transistor scaling leads to many other degradations since the minimum dimension of planar transistors has fallen below 90 nm. Indeed, the distance between the source and drain junctions is now so close that the gate has difficulty in maintaining electrostatic control over the channel, resulting in degradation of short-channel effects, including *threshold voltage roll-off*, *drain-induced barrier lowering* (DIBL), *charge mobility degradation* and *threshold voltage variation*. The *threshold voltage roll-off* is when the threshold voltage of the device is reduced due to the fact that the depletion regions of the source and drain intrude into the channel allowing the current to flow from source to drain easier. This results in an increased difficulty to turn the transistor fully off, increasing its leakage current and therefore power consumption. *DIBL* is produced when the source and the drain are close enough so that they become electrostatically coupled, increasing the leakage current. To summarize in other words, unacceptably high leakage currents appears when the device is in the off-state. Conversely, to maintain a low off-state current specification, the device cannot achieve high drive current when biased in the on-state. To maintain a continuous improvement of performances, the conventional planar (2-D) structure of the MOSFET built on Si bulk substrate is no more suited and new architectures providing better electrostatic integrity and suppressing short-channel effects, have to be considered. Two different design approaches have been studied and are displayed in ***Fig. 0-4***.

A first one replaces the bulk silicon of a normal transistor by a thin layer of Si (< 10 nm thick) built on an insulating layer (SiO_2), creating a device that is often called an ultrathin body silicon-on-insulator (UTB SOI), also known as a fully depleted SOI (FD-SOI). By limiting the amount of Si in the device, the capacitive coupling between the gate and channel increases while the coupling between drain and channel commensurately decreases. The main advantage of the FD-SOI MOSFET over other advanced transistor structures is the relative ease of processing due to the planarity of the structure; most conventional bulk MOSFET fabrication processes can be used for UTB SOI MOSFETs with little modification. Moreover, it provides a significant reduction in power consumption, a faster switching speed, an availability to back-biasing to control the threshold voltage (VT) and a layout library compatible with existing Si bulk technologies.

A second approach is to create a non-planar, double-gate (or Tri-gate, as Intel has named its three-sided device) transistor built either on Si bulk substrate or on SOI substrate. FinFET designs use a conducting channel that rises above the level of the insulator, creating a thin silicon structure, shaped like a “fin”. The transistor gate is then draped over the top of the channel like an upside-down U, bracketing it on three sides and giving the gate almost complete control of the channel. All the main components of the transistor (source, drain, channel, and gate) sit on top of the device’s substrate. FinFETs are already implemented in high-volume production [Auth 12]. The strong electrostatic control afforded by ensuring that the gate is close to all areas of the channel makes it easier to control the device’s threshold voltage, reducing leakage between source and drain, as well as making it possible to switch it more quickly. The other main strengths of FinFET are a significant reduction in power consumption (about 50% over 32 nm), a faster switching speed and an effective speed/power trade-off possible with multi-VT. Contrarily to FD-SOI MOSFET, this structure is difficult to build since a high aspect ratio stripes is needed (narrow stripe width to control SCE and tall stripe height to achieve high current per unit layout area). However, FinFET technology provides better electrostatic control and thus relaxes the TSi thinness requirement compared to the FD-SOI MOSFET by a factor of two [Fossum 07].

Both schemes offer the same basic advantage: by thinning the channel, they bring the gate closer to the drain. When a transistor is off, the drain’s electric field can take one of two paths inside the channel to zero-voltage destinations. It can propagate all the way across the channel to the source, or it can terminate at the transistor’s gate. If the field gets to the source, it can lower the energy barrier that keeps charge carriers in the source from entering the channel. But if the gate is close enough to the drain, it can act as a lightning rod, diverting field lines away from the source. This cuts down on leakage, and it also means that field lines don’t penetrate very far into the channel, dissipating even more energy by tugging on any stray carriers.

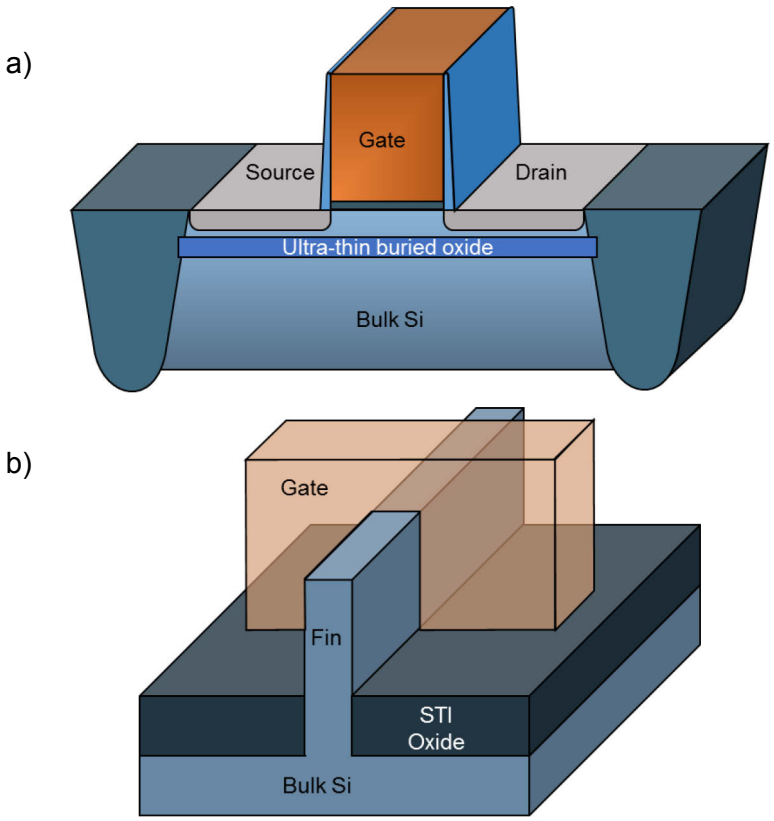

***Fig. 0-4**: Schematic representation of a) FD-SOI MOSFET and b) FinFET.*

Motivations

Today, the performance improvements of CMOS transistors lays mainly on the replacement of materials by new ones with better characteristics, and more recently on the development of new structures and architectures. In particular, the use of “fully-depleted” channels allows a good electrostatic control of the transistors and minimizes the short-channel effects. Thus, the carrier charges pass through a very thin layer, in the range of few nm. This was obtained by two different technologies: the Tri-gate transistor from Intel or the FD-SOI transistor proposed by STMicroelectronics. These new structures are possible with the addition of several steps of epitaxies, mainly the SiGe channel for threshold voltage and strain control (increasing the mobility in the channel), and the doped-SiGe in the source and drain (S/D): boron-doped SiGe and phosphorous-doped $Si_{1-y}C_y$, for the resistance and strain control. For these applications, these epitaxies must be selective in order to be grown in specific areas only. The selectivity in SiGe and Si epitaxies is a well-known process that has been studied for several years. In addition to that, all these epitaxial layers are grown in their unstable domains whether it be chemical (solubility limit), or mechanical (presence of extreme strains from 1 to 3 GPa), or morphological (very small patterns having dimensions of few nm and very thin films of few nm). Moreover, the thickness/width ratio is very important resulting in new considerations such as the 3D aspects of epitaxial objects. The faceting effects and anisotropies must also be taken into account rendering the industrial processes very complicated. Finally, the epitaxial layers are even more affected and sensitive to any process changes such as the temperature or the pressure. As a result, cautious cares must be done in order to keep an acceptable morphology. The recent trends can be summarized by three primordial properties: size, strain and chemical

composition, which are interdependent, all of this knowing that the chemical compositions and mechanical strains are more and more high, and that the dimensions are smaller and smaller.

Axes of research

The discussion so far can be summarized as follows. The requirements on future CMOS technologies pose the need for epitaxies with smaller and smaller dimensions and high doping levels. In these ranges of dimensions (few nanometers are reached), the control of the morphological aspects is now very important and crucial for the device performances. In this thesis, the morphological behavior of SiGe and boron-doped SiGe layers grown on patterned wafers is pointed out. The manuscript is divided into five chapters.

The Chapter 1 exposes the basics of epitaxy and hetero-epitaxy, introducing the notions of critical thickness, relaxation and compressive biaxial strain in addition with the Si and SiGe properties. The different growth modes are also described. Then, the chemical vapor deposition's principles of silicon, silicon-germanium and boron-doped silicon-germanium followed by the chemical reactions occurring during the growth are given. Different growth techniques are exposed showing the main advantages and drawbacks of each technique. Finally, some literature on selective epitaxial growth and loading effects are presented.

All the experimental details are described in the Chapter 2. After a brief introduction of the SiCoNi process used for the substrate cleaning before any growth, the epitaxy chamber is exposed followed by some results on the influence of the PID values and the lamp ratios on the process temperature. This part is very important for the following due to the fact that the temperature's effects on the epitaxies' morphology are in-depth studied. In a third part, the different characterization techniques are briefly presented. The atomic force microscopy technique is presented more in details since it is the main tool used for the morphological characterizations in this thesis.

The Chapter 3 is devoted to the as-deposited epitaxial layers' morphology. Different patterns are shown and described in terms of roughness (very large patterns, or equivalently blanket wafer) and faceting. Concerning this last one, "infinite" lines, square and rectangle shaped patterns are used. The notions of Si passivation and active ramps during the process and their importance to study the "real" as-deposited morphology are addressed. It is worth to note as of now that all the needed precautions are taken during this study in order to be the most accurate as possible.

In the Chapter 4, the post-annealed morphology of silicon-germanium is studied in details introducing the notions of Stranski-Kastanov-like relaxation and thermal rounding. The influence of temperature and duration during annealing as well as the pressure and the carrier gas on the morphology is given. The thermal rounding's kinetics is quantified. Then, the morphological behavior of silicon and silicon-germanium caps grown by epitaxy on an undulated surface is studied. Different parameters like germanium content or growth kinetics are changed in order to see their influence on the caps' morphology.

The industrial applications of boron-doped silicon-germanium are given in the Chapter 5. First, the growth kinetics of boron-doped layers and the dopant incorporation are preliminary studied. The morphology of these layers is then characterized. The influence in terms of faceting, epitaxy quality and lateral overgrowth of doping concentration is presented. Third, the influence of the thermal treatment is exposed. Finally, the main results obtained in the previous chapters are applied in the devices and more precisely in source and drain regions. The aim

was to find a process that allows a controlled (faceted or not) morphology to be reached in between two gates with an acceptable boron concentration.

The final part is devoted to the general conclusion that will summarize and conclude the whole five chapters.

Chapter 1

Si, SiGe and boron doped SiGe properties

Silicon and its related compounds (like silicon-germanium) are the main materials used in microelectronics. Their excellent mechanical, thermal, electronic and optical properties as well as their low cost have bring them to the best materials suited for almost all the microelectronics' applications. As a result, they were subjected to many researches and are nowadays well-known materials. They are in the majority of cases, grown by means of epitaxy, whose the main technique used in the industry is the Rapid Thermal Chemical Vapor Deposition.

This first chapter exposes the basics of epitaxial growth of silicon-germanium alloy. After a brief reminder of the beginning of silicon and germanium in microelectronics, both materials will be described in terms of crystalline properties and solubility. The fundamental notions in hetero-epitaxy, as example relaxation, compressive strain and growth modes will be defined. The general principle of the growth technique by Chemical Vapor Deposition as well as the chemical reactions occurring during the growth are given. Finally, the selective epitaxial growth and the loading effects will be introduced.

I/ Si and SiGe

I.1) Introduction: Silicon as the main material for microelectronics

The beginning of silicon and germanium in microelectronics.

Historically, germanium was firstly used due to its lower melting point than silicon (930°C against 1410°C) allowing the fabrication and the purification of a germanium crystal easier. This is how was born in 1947 the first transistor (germanium point-contact mode). It was only few years after that silicon was preferred due to its ability to withstand high temperatures, the high stability and insulator properties of SiO_2 and the fact that it is easier to process than any other competitors. Moreover, its huge abundance allowing the acquisition of substrate at much lower cost made silicon the most popular semiconductor for the production of integrated circuits, dooming germanium to an end, at least for a while.

The emergence of a new alloy: silicon-germanium in microelectronics.

In the past, germanium was abandoned at the cost of silicon and its fate seemed to be sealed. However, at the end of the 1980s, the desire of enhancing the bipolar transistor's performances led to the trend of changing the initial silicon base by a silicon-germanium base. This would allow a better sizing and control of base's dimensions. Moreover, since germanium was a well-known material with the same crystal structure and similar chemical bonding than silicon, it was the best candidate to make a substitutional binary alloy with silicon, i.e. silicon and germanium atoms will take the same lattice sites in the composite system $Si_{1-x}Ge_x$. Most of all, in the same time, the development of new epitaxy techniques capable of depositing high quality silicon thin films at relatively low temperature (550-750°C) such as Molecular Beam Epitaxy (MBE) or Ultra High Vacuum Chemical Vapor Deposition (UHV-CVD) made possible the integration of crystalline alloys like SiGe in the next technologies.

I.2) SiGe crystalline properties

I.2.a) Structure

Silicon (Si) and germanium (Ge) have the same crystalline structure which is diamond type, with lattice constants of 5.431 Å and 5.658 Å, respectively. The diamond unit cell is similar to the face-centered cubic (fcc) cell with atoms at each corner and at each face of the cube. Unlike the fcc unitcell, the diamond cell hosts four additional interior atoms represented by the red-filled circles in ***Fig. I-1***. These atoms are located in tetrahedral sites at (¼, ¼, ¼) coordinates.

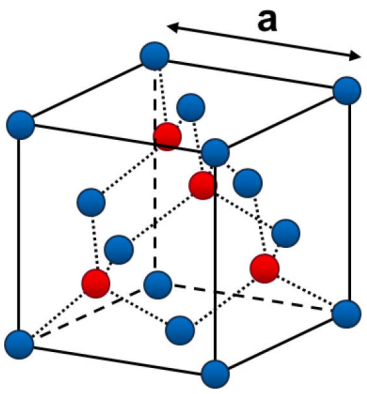

Fig. I-1*: The sketch of the diamond structure. The blue atoms are located at the center of the faces and at the vertex of the cube whereas the red atoms are located inside the cube in the tetrahedral sites at (¼, ¼, ¼) coordinates.*

The similarities in terms of structure and chemical properties of both materials allow the formation of a substitutional binary alloy $Si_{1-x}Ge_x$. This means that they have complete solubility in each other both in solid and liquid states over the entire composition range as can be seen from the equilibrium phase diagram (see ***Fig. I-2***). Indeed, as seen in ***Fig.I-2***, whatever the Ge concentration x of the alloy and the temperature, the alloy exists either as a homogeneous liquid (*l* for liquidus), as a homogeneous solid (*s* for solidus) or as a two-phase system with liquid and solid part (*l*+*s*) [Ibach 09].

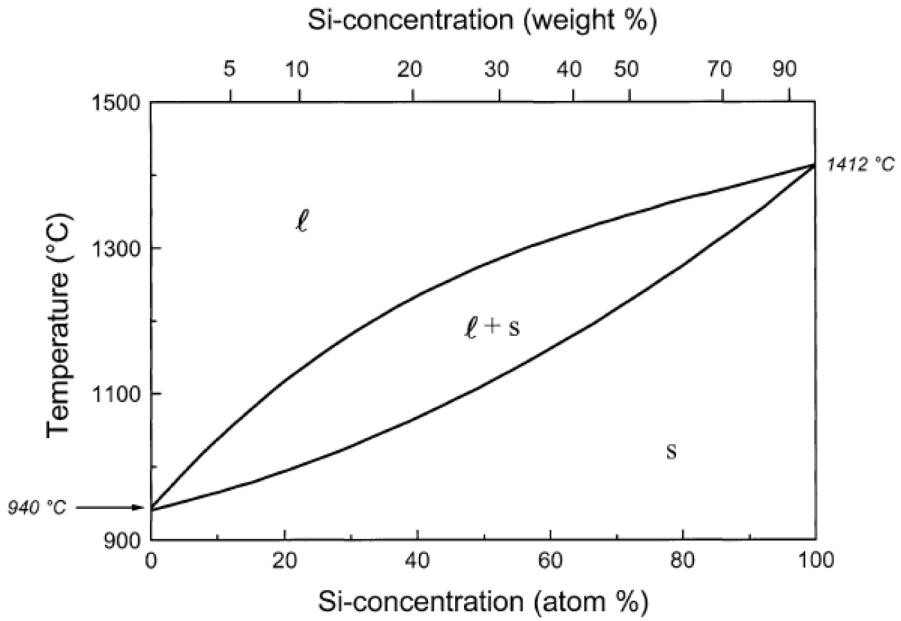

Fig. I-2*: Equilibrium phase diagram of SiGe system. This shows the complete miscibility of silicon and germanium. [Ibach 09]*

In order to understand the properties of an alloy, it is very important to determine its atomic structure, in which bond-length relaxation and lattice constant are the key parameters. Since the lattice constant of Ge is 4.18% larger than that of Si, a first estimation of bulk SiGe alloy's lattice constant has been described by Vegard's law [Vegard 21] which is approximately equal to the composition-weighted average of the lattice constants of the pure materials. In other

words, this law is a linear interpolation of intermediate values by limiting values of Si and Ge constants (a_{Si} and a_{Ge}, respectively) and is defined as

$$a_{Si_{1-x}Ge_x} = a_{Si}(1-x) + a_{Ge}x \qquad \text{Eq. I-1}$$

This law gives a good description of SiGe lattice parameter. However, Dismukes et *al.* [Dismukes 64] have discovered a variation from this linearity between predicted values and measured values. With their experimental data, a finer description was performed stipulating that the SiGe lattice constant's evolution as a function of germanium concentration follows the parabolic law (Eq. I-2, a_{SiGe} is given in Å)

$$a_{Si_{1-x}Ge_x} = 5.431 + 0.200x + 0.027x^2 \qquad \text{Eq. I-2}$$

In the ***Fig. I-3*** bellow, showing the evolution of the SiGe lattice parameter as a function of germanium concentration, it appears that the difference between both laws is relatively low and is largest for germanium concentration of about 50%. The cubic law of Herzog et *al.* [Herzog 95] is also plotted in ***Fig. I-3*** and it is clearly observed that the difference with the Dismukes' law is negligible.

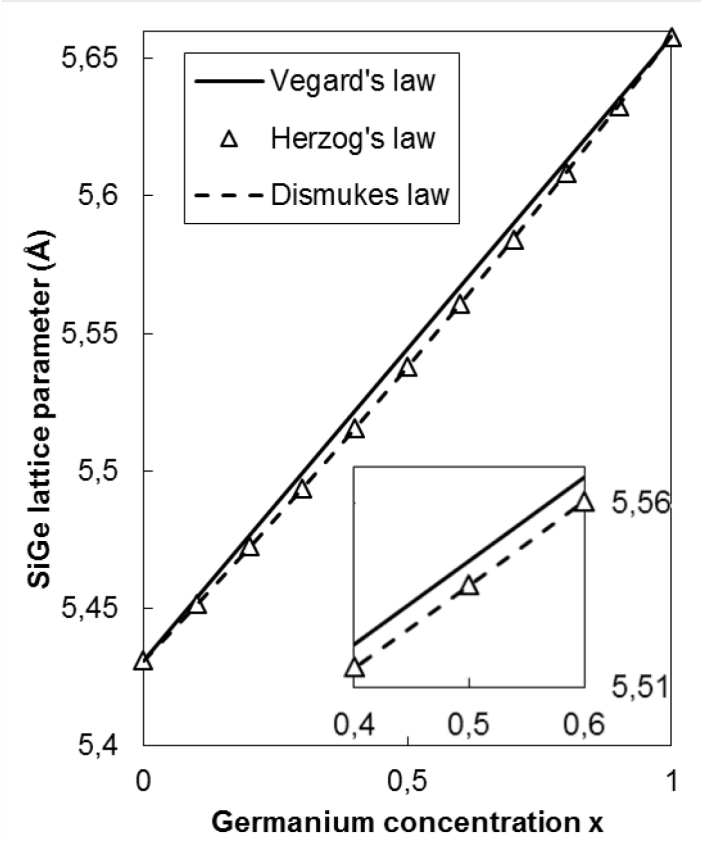

Fig. I-3*: Evolution of SiGe lattice parameter as a function of germanium concentration x, for the three different laws.*

Since SiGe layer has a larger lattice constant compared to Si, a mismatch system is established with compressive strain. The compressive strain increases with germanium concentration. This mismatch between both lattice constants is define as misfit

$$f_x = \frac{a_{Si_{1-x}Ge_x} - a_{Si}}{a_{Si}} \qquad \text{Eq. I-3}$$

Using Eq. I-1, the misfit reduces to:

$$f_x = 0.042x \qquad \text{Eq. I-4}$$

As a result of the induced strain, the SiGe film may have a defect-free growth and adapts in-plane the lattice constant of Si, or the SiGe film may be fully-relaxed creating dislocations near the interface Si/SiGe (see ***Fig. I-4***). In a general way, the dislocations propagate preferentially along the {111} planes from the hetero-structure's interface to the surface: in this case, they are called threading dislocations. The material may also be found in a partially relaxed state.

In the defect-free case, $a^{//}_{SiGe}$ (in-plane) is equal to the lattice constant of Si. As a result, an elongation of the lattice parameter along the growth direction (out-of-plane) occurred; the SiGe layer is consequently biaxially compressed (or pseudomorphic).

When the elastic energy hidden in the lattice of a strain material is too large, it can be released totally or partially. This can be achieved when the germanium content of the film is too high or more commonly when the layer thickness exceeds a certain value called critical thickness. The elastic energy increases linearly as a function thickness until the critical value is reached. Above this thickness, the material releases the energy resulting in the creation of misfit dislocations interacting with the electrical, optical and thermal properties of the material, typically degrading the performance of devices. Indeed, these dislocations can become recombination centers or pathways for electrical transport increasing the leakage current and/or creating locally short-circuits. They can also have parasitic effects on the species' diffusion.

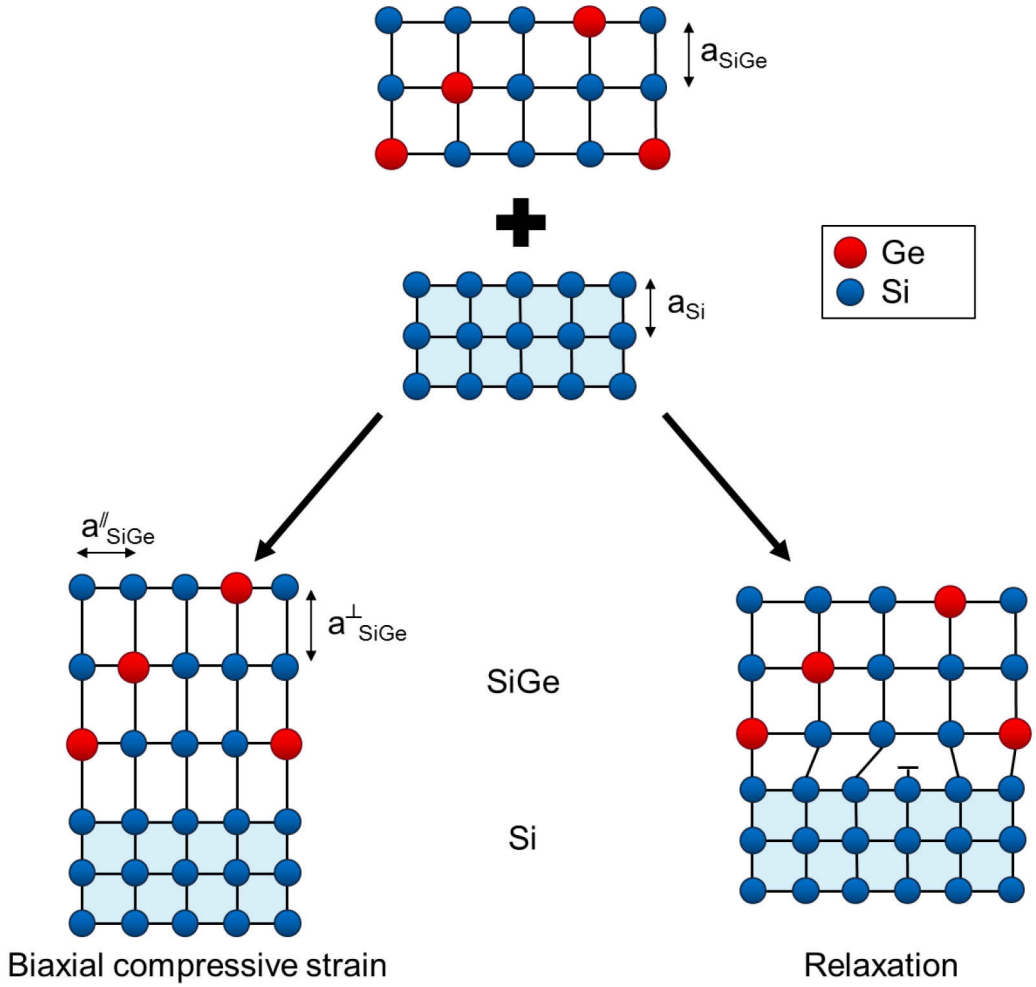

***Fig. I-4**: Schematic illustration of pseudomorphic (bottom left side) and fully-relaxed (bottom right side) grown SiGe layer on Si substrate. $a^{//}_{SiGe}$ and $a^{\perp}_{SiGe}$ are the in-plane and out-of-plane lattice constant of SiGe, respectively.*

I.2.b) Critical thickness

Several models have been developed to predict the critical thickness of a strained layer, and the notion was first initiated by Van der Merwe [Merwe 63]. Later Matthew and Blakeslee [Matthews 74] introduced the mechanical equilibrium theory. According to their theory, the critical thickness can be obtained at the equilibrium balance between two energies: the energy that is due to the lattice mismatch and the tension energy that is needed to create at least one dislocation. Solving the equilibrium state, it produces a critical thickness (h_c) of

$$h_c \approx \frac{b}{2\pi f_x} \frac{(1-\nu\cos^2\theta)}{(1+\nu)\cos\lambda}\left[\ln\left(\frac{h_c}{b}\right)+1\right] \qquad \text{Eq. I-5}$$

Where b is the slip distance which for misfit dislocations is the Burgers vector, f_x is the misfit define in Eq. I-3, ν is the Poisson ratio, θ is the angle between the dislocation line and its Burgers vector and λ is the angle between Burgers vector and the direction in the interface normal to the dislocation line.

By taking the misfit between pure Si and Ge, then Eq. I-6 reduces to

$$h_c \approx \frac{5.5\text{Å}}{x}\ln(10h_c) \qquad \text{Eq. I-6}$$

x being the germanium concentration.

It is clear from reduced Eq. I-6 that h_c for a pseudomorphic growth strongly depends on germanium concentration x, and decreases with increasing Ge content. In theory, as long as the critical thickness is not exceeded, no dislocations will be observed. However, it has been shown by a number of experiments in the early 1980s that the critical thickness can be exceeded without apparition of dislocations. SiGe layers with thickness greater than h_c are defined as metastable (the metastable phase describes a state of the material for which the strain is well present, but the elastic energy is weak enough not to lead to dislocations). Experimental critical thickness for plastic relaxation at 550°C as a function of Ge content were obtained by Bean *et al*. [Bean 84]. These experimental values were used by the same group to establish the following People and Bean formula showing the dependence of h_c on the misfit [People 86]

$$h_c \approx \frac{1.9 * 10^{-2}\ \text{Å}}{f_x^2}\ln\left(\frac{h_c}{4\ \text{Å}}\right) \qquad \text{Eq. I-7}$$

Fig. I-5 shows experimental and predicted values of critical thickness as a function of Ge concentration. The region between the curve defined by the mechanical equilibrium theory of Mattews and Blakeslee and the curve defined by People and Bean formula (Eq.I-7) represents the metastable region. Above this limit, the material is relaxed. This graph also shows the experimental values of Kasper *et al.* [Kasper 75] made at growth temperature of 750°C. It is observed that for higher temperatures the critical thickness is closer from the mechanical equilibrium theory than for low temperatures. Similar observations were made by Houghton *et al.* [Houghton 90] for a growth temperature of 950°C. They showed that their data and the theoretical data are matched. As a result, the critical thickness also depends on the process conditions since the lower the growth temperature the higher the experimental critical thickness for plastic relaxation of SiGe on Si (see ***Fig. I-5***). These experimental data were attributed in part to the difficulty in detecting low densities of dislocations but predominantly related to the existence of a kinetic barrier to dislocation formation and/or migration in metastable layers [People 86]. More recently, Hartmann et al. [Hartmann 11] have demonstrated critical thickness for plastic relaxation for Ge content 22%, approximately two times higher than predicted by the People and Bean theory. In their experiments, the method of deposition was different since they used an industrial 200 mm rapid thermal chemical vapor deposition (RT-CVD) tool instead of molecular beam epitaxy (MBE) tool.

All the previous mentioned experiments were performed on blanket wafer but one can interrogate on the influence of pattern size on the critical thickness. This influence was extensively studied by Luryi *et al.* [Luryi 86] and Fitzgerald *et al.* (for InGaAs material grown on circular or square mesa structures) [Fitzgerald 89] who discovered that the misfit dislocation density formed during film growth is reduced when the growth area is reduced. As a consequence, films can be grown fully strained to much greater thicknesses on small areas than on large areas due to the blocking effect of dislocation propagation at the edge.

Considering now SiGe selectively grown on Si substrate (since oxide patterning is used to define the growth area), Noble *et al.* [Noble 90] showed a reduction in misfit dislocation density when growth takes place in small areas. In a same way, a selective process will give higher values of h_c than a non-selective process.

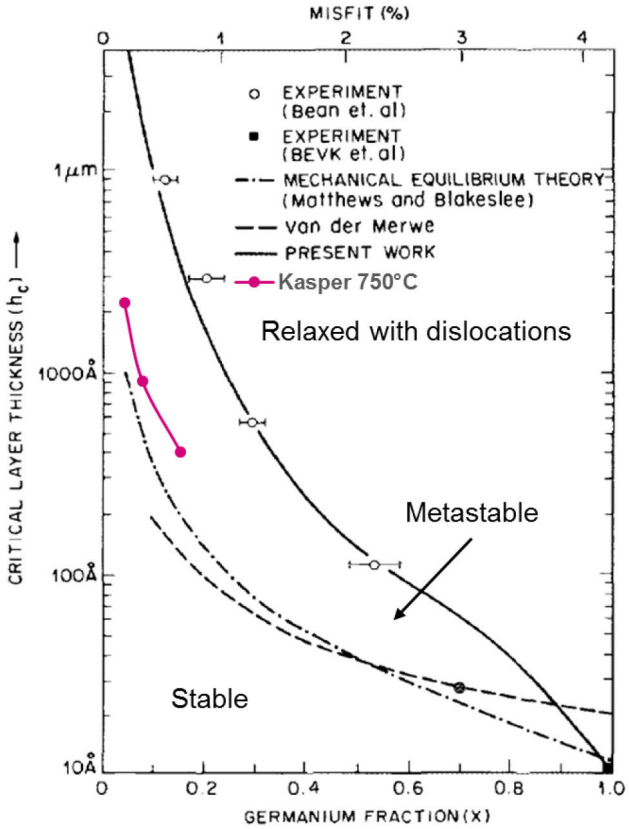

***Fig. I-5**: Plot of the theoretical and experimental critical layer thicknesses as a function of germanium fraction x for $Si_{1-x}Ge_x$ materials. Three main regions are indicated on the graph. The stable region is given by the mechanical equilibrium theory of Mattews and Blakeslee (dashed-dotted line). The material is relaxed for values above the critical thickness obtained by People and Bean (white circles) for temperature of 550°C. Picture taken from [People 86]. A growth temperature of 750°C is also displayed through the pink line. This experiment was performed by Kasper et al. [Kasper 75].*

Fig. I-6 shows XRD diagram and 1 x 1 µm² AFM image of a 400 nm thick SiGe (35%) layer presenting dislocations (white dash lines). The XRD diagram has a triangular shape, in the semi-log plot and cannot be fitted with the theoretical curve.

a)

b)

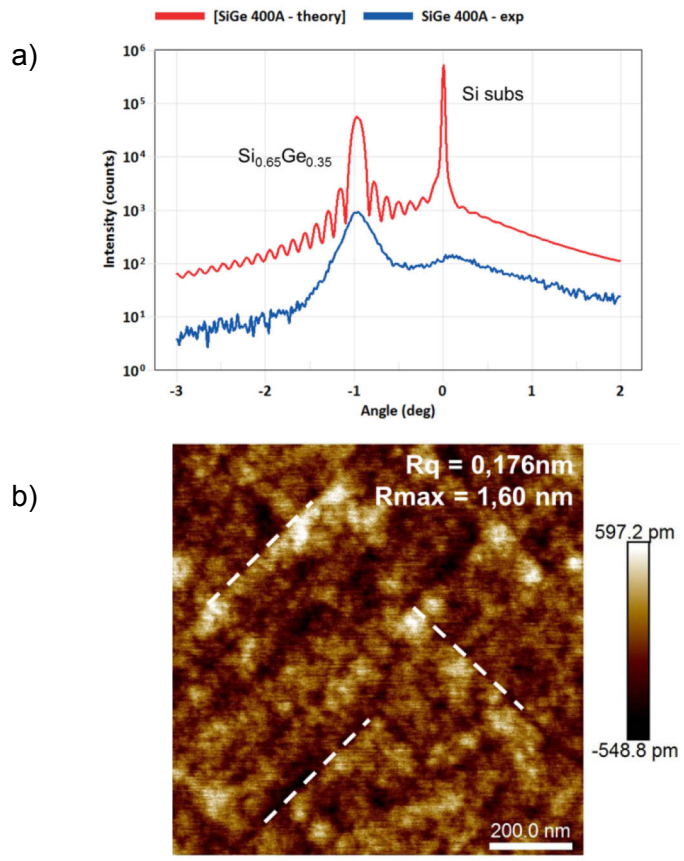

***Fig. I-6**: a) XRD diagram of thick $Si_{0.65}Ge_{0.35}$ (400 Å) in theory (red curve) and experimental (blue curve). Curves are shifted vertically (Intensity x 1 for the blue curve, Intensity x 10 for the red curve) for clarity. The fit reveals defaults on the epitaxial layer. b) 1 x 1 µm² AFM image of the thick SiGe presenting misfit dislocations (in white dash line).*

I.2.c) Hetero-epitaxy growth modes

Hetero-epitaxy has different growth modes depending on the growth conditions and the strain in the hetero-epitaxial film (misfit between the film and the substrate and the free energy of the interface). Like any other physical system, the substrate/film system will minimize its energy, favoring the configuration with the lowest free surface energy. The growth mode is directly linked to the film morphology, giving the structural properties such as perfection, flatness and interface abruptness of the layers.

During hetero-epitaxy, there is a competition between both substrate and film surface energies ($\gamma_{substrate}$ and γ_{film}, respectively) and the interface energy ($\gamma_{interface}$). Experimentally, three classical growth modes are well known, as shown in ***Fig. I-7***.

$$\gamma_{substrate} \geq \gamma_{film} + \gamma_{interface}$$

Frank-van der Merwe mode (FM): Layer-by-layer growth or 2D growth. The growing layer reduces the surface energy, leading to a complete wetting of the surface. Thus, a new layer is nucleated only after completion of the layer below.

$\gamma_{substrate} < \gamma_{film} + \gamma_{interface}$

Volmer-Weber mode (VW): island growth or 3D growth. The growing layer increases the interface energy, leading to a non-wetting of the surface. The consequence is the formation of three-dimensional ad-atom clusters or islands on the substrate causing rough multi-layer films to grow.

Initially,
$\gamma_{substrate} \geq \gamma_{film} + \gamma_{interface}$
Then,
elastic energy to be added

Stranski-Krastanov mode (SK): layer-by-layer followed by island growth. SK mode is considered as intermediate between the FV and VW growth modes. Typically, the first layer wets the surface but the subsequent layers do not. This change in balance of force is often due to significant lattice misfit between the deposited film and the substrate. The lattice mismatch between the substrate and the film creates a build-in strain as a consequence of the increasing elastic energy with increasing layer thickness. In contrast to plastic strain relaxation, there are no dislocations.

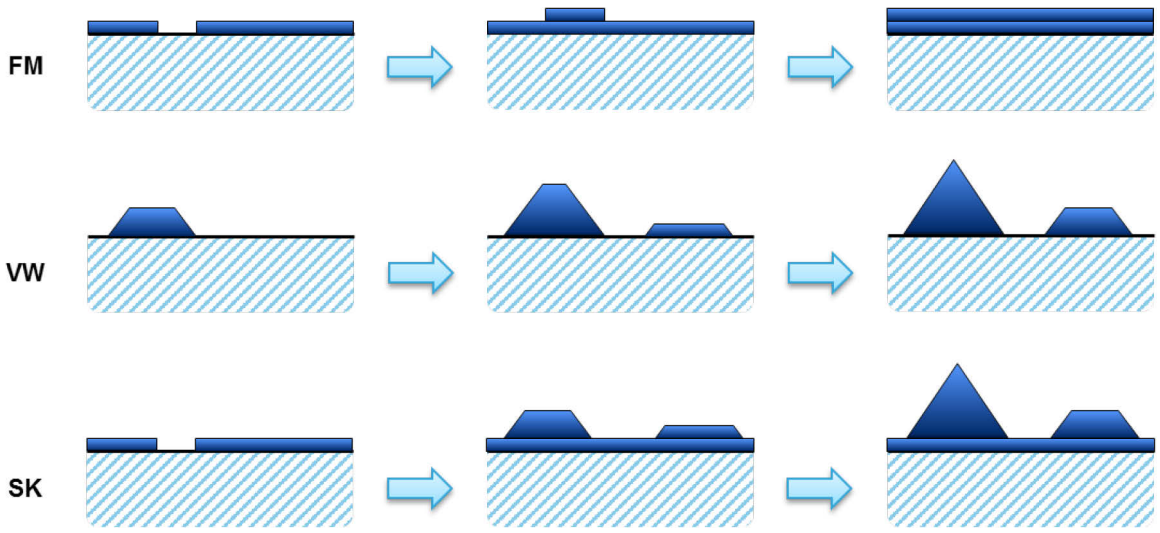

***Fig. I-7**: Schematic representation of the hetero-epitaxial growth modes. Three main growths are represented (from top to bottom): Frank-van der Merwe mode (FM), Volmer-Weber mode (VW) and Stranski-Krastanov mode (SK). From left to right, the pictures show the evolution on the growth when increasing the growth time.*

III/ Epitaxy process for layer deposition

There are in practice two main techniques for the growth of epitaxial layers. The first one is the molecular beam epitaxy (MBE), the second is chemical vapor deposition (CVD). Concerning CVD technique, there are lots of groups, like e.g. plasma enhanced CVD, ultra-high vacuum CVD, low-pressure CVD, or rapid thermal CVD (RT-CVD). Among all the possible choices, the preferred technique for industrial applications is undeniably RT-CVD. First of all, a non-exhaustive list of differences between both CVD and MBE techniques is given. The main force of CVD compared to MBE is the use of gases as precursors. Indeed, they offer several

advantages contrary to solid sources used in MBE. First, they avoid having to work under extremely high vacuum conditions. Also, there is no need that the source is located inside the chamber when using gaseous precursors and in the same way it is easier to change the source only by changing the gas bottle without having to open the entire chamber. Third, it is easier to obtain and manipulate very pure gases than very pure solid sources. Finally, it is easy to carry gases and to control their flow. The precursors are not the only advantages of CVD. The growth rate is generally higher for CVD than MBE. Moreover, it is possible to make selective growths by CVD in the case of patterned substrates (partially covered with SiO_2 or silicon nitride). Other advantages have made RT-CVD the most appreciated technique in the industrial world among all CVD techniques. Processes have a very high flexibility in terms of pressure (from low pressure to atmospheric pressure), temperatures (from 350°C to 1200°C) or even chemistry (both hydrogen-based and chlorine-based precursors can be used). Furthermore, it is possible to grow epitaxial films in both deposition regimes, i.e. surface reaction and mass transport-limited kinetics. Then, as its name indicates, very fast temperature ramps can be done. Finally, another very important point is the fact that an in-situ chamber cleaning is possible before any epitaxies. This is usually realized at high temperature using HCl gas. All these advantages have led the RT-CVD technique to the very top and have made of this technique is most famous and mature technique for any industrial applications. However, few drawbacks can be found like, the complex temperature uniformity on the substrate and temperature control. Second, the growth kinetics are usually more difficult to model than for any other techniques.

III.1) Epitaxy by Chemical Vapor Deposition

III.1.a) Definition

The word epitaxy was firstly used by Royer in 1928 and is derived from the Greek “epi” which means “upon”, and “taxis” meaning “to arrange”. Thus, Si epitaxy refers to the ability to add and arrange Si atoms upon a single crystal surface. It is the regularly oriented growth of one crystal upon another. As a result, a substrate is needed used as a model for atomic arrangement and as mechanical support for the grown layer. Two different kind of epitaxies are recognized. First, it could be either a homo-epitaxy growth in which the epitaxial layer is of the same material as the substrate or a hetero-epitaxy in which the epitaxial layer is a different material than the substrate (e.g. SiGe on Si).

III.1.b) Growth steps and mechanisms

All the epitaxial films made during this study were realized in a RT-CVD reactor (*see Chapter 2 - II/ Epitaxy chambers*). RT-CVD consists in the reaction of volatile silicon precursors with the substrate so that Si is given to grow a solid film. The substrate temperature provides the activation energy needed to activate the chemical reaction. The success of silicon epitaxy is driven by a high surface mobility for the arriving atoms (surface cleaning before epitaxy in required, see *Chapter 2 – I/ SiCoNi chamber for surface preparation*), numerous equivalent growth sites and acceptable growth rates. The CVD growth results in several mutually dependent steps:

1- Bulk transport of gaseous precursors into the process volume by forced conversion, usually thanks to a carrier gas (H_2 in most cases).
2- Gaseous diffusion of the precursors to the substrate surface
3- Adsorption of precursors onto the surface

4- Chemical reaction by precursor decomposition
5- Surface diffusion of the atoms until a nucleation site, nucleation and growth of the film
6- Reaction by-product desorption
7- Gaseous transport of by-products
8- Bulk transport of by-products out of process volume

Fig. I-8 shows a simplified representation of the different steps occurring du epitaxial growth.

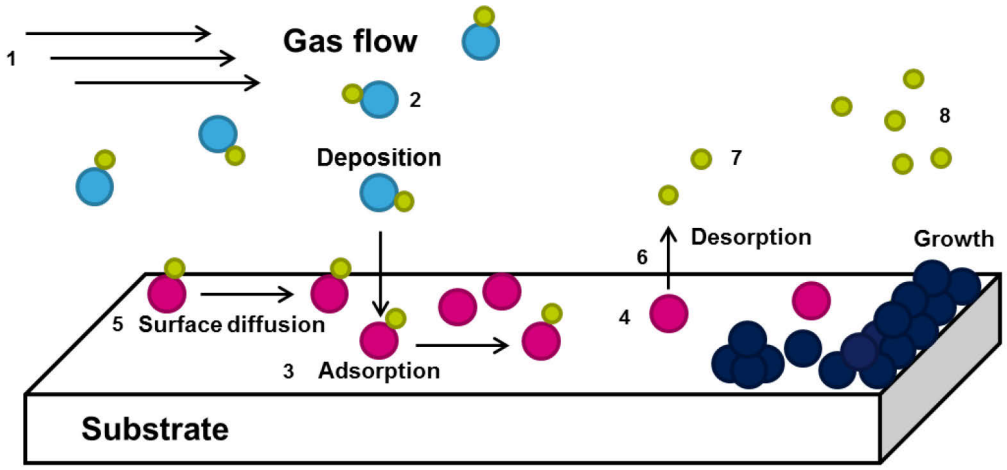

***Fig. I-8**: Schematic representation of elemental steps of a growth by CVD.*

The precursors used for silicon epitaxy by CVD in H_2 atmosphere are usually hydrogen- and chlorine-based precursors such as SiH_4 (silane), Si_2H_6 (disilane), and SiH_2Cl_2 (dichlorosilane or DCS). The use of Cl as precursor was introduced to allow the epitaxy to be selective (*see Chapter 1 - III.2) Selective epitaxial growth*). As a counterpart, the growth rate for an epitaxy using this kind of precursors (for same experimental conditions – temperature, flow…) is reduced compared to an epitaxy with hydrogen-based precursors. During this work, DCS and disilane were used as silicon precursors. For SiGe growth, GeH_4 (germane) was used as precursor in addition to DCS.

During an epitaxial growth, the film growth mechanism in mainly driven by three steps: the adsorption of gaseous precursors on the substrate surface, the diffusion and chemical reaction onto the surface, and the desorption of the gaseous by-products. When the temperature of the gas-phase is high enough, reactions may occur in the gas-phase leading to a decomposition of precursors located in the gas-phase. However, the growth temperatures used in every experiment were relatively low (<750°C) avoiding the decomposition. All the growths of this thesis were performed using a DCS chemistry as Si precursor, and H_2 as carrier gas. The equations related to a SiH_4 chemistry are given as references since SiH_4 is a well-known precursor and one of the pioneers. Number of authors have reported in literature the Si growth mechanism using SiH_4 as precursor and H_2 as carrier gas [Greve 93] [Liehr 90] [Dutartre 92]. It was modeled that the hydrogen desorption allows the Si atoms' adsorption and thus limits the growth's kinetics. SiH_4 and H_2 adsorb independently on two free sites. Taking into account the simultaneous contribution of both H_2 and active hydrides, the entire model can be described by the following general equation:

$$SiH_4(g) + 2\_ \longrightarrow 2\underline{H} + 2H_2 + Si \qquad \text{Eq. I-8}$$

The symbol "_" represents a fee site on the Si surface, (g) indicates that the element is in gas phase. Underlined species (e.g. $\underline{Si}$) indicates that these species are adsorbed on the substrate surface.

The following equations described for relatively low temperatures, the chemical reactions occurring during silicon epitaxy using DCS precursors. For an epitaxy using DCS as precursor, the reaction pathway is the following. According to the work of Coon *et al.* and Hierlemann *et al.* [Coon 93] [Coon 92] [Hierlemann 95] SiH_2Cl_2 molecules adsorb directly on free sites on the silicon substrate surface.

DCS adsorption

$$SiH_2Cl_2(g) + 1\_ \longrightarrow \underline{Si}H_2Cl_2 \qquad \text{Eq. I-9}$$

SiH_2Cl_2 dissociation into Si, H and Cl

$$\underline{Si}H_2Cl_2 + 4\_ \longrightarrow \underline{Si} + 2\underline{H} + 2\underline{Cl} \qquad \text{Eq. I-10}$$

Hydrogen desorption

$$H_2(g) + 2\_ \longrightarrow 2\underline{H} \qquad \text{Eq. I-11}$$

HCl and Cl_2 desorption

$$\underline{H} + \underline{Cl} \longrightarrow HCl(g) + 2\_ \qquad \text{Eq. I-12}$$

$$2\underline{Cl} \longrightarrow Cl_2(g) + 2\_ \qquad \text{Eq. I-13}$$

$SiCl_2$ desorption

$$Si + 2\underline{Cl} \longrightarrow SiCl_2(g) + 2\_ \qquad \text{Eq. I-14}$$

For temperatures above 800°C, it was shown [Hierlemann 95] the pyrolysis reactions in the gas phase have to be considered since the decomposition of DCS into $SiCl_2$ and H_2 is energetically the most favorable pathway. Then, $SiCl_2$ can adsorb on the silicon surface and decompose leading to a second pathway to the deposition mechanism valid at high temperatures:

$$SiCl_2 \longrightarrow 2\underline{Cl}(s) + \underline{Si} \qquad \text{Eq. I-15}$$

In the case of SiGe epitaxy, a germanium precursor must be added in the chemistry in addition to silicon precursor (DCS in our case); this precursor was the germane (GeH_4) which is the most established one for RT-CVD applications. Germane is considered to have similar decomposition than silane. However, the Ge-H bond energy is weaker than the Si-H bond energy, so its decomposition occurs at lower temperatures [Greve 93]. In other words, adding germane into the chamber it is possible to make SiGe epitaxies at much lower temperatures than silicon without decreasing the growth rate. The chemical reactions for the adsorption and decomposition of germane are the following [Cunningham 91]:

Surface process of adsorption

$$GeH_4(g) + 2\_ \longrightarrow \underline{Ge}H_3 + \underline{H} \qquad \text{Eq. I-16}$$

Surface decomposition and diffusion

$$\underline{Ge}H_3 \longrightarrow \underline{Ge}H + H_2(g) \qquad \text{Eq. I-17}$$

Lattice incorporation

$$\underline{Ge}H + \underline{H} \longrightarrow Ge + H_2(g) + 2\_ \qquad \text{Eq. I-18}$$

III.1.c) Growth kinetics and dependence of growth rate on the process parameters

In general, different process parameters affect the growth rate in epitaxy by CVD. A non-exhaustive list can be given: the temperature, the flow rate of precursors, the deposition pressure and the choice of active and carrier gases. These parameters will influence first, the arrival of precursors' molecules on the surface, and second the desorption of species present on the surface. Indeed, the number of free sites on the surface is limited by the coverage which is the result of some chemical reactions between the surface sites and the gas molecules, e.g. dichlorosilane, germane. ***Fig. I-9*** shows the Arrhenius diagram of the (001) silicon surface's growth rate for two different chemistries: SiH_4/H_2 and SiH_2Cl_2/H_2. The growths were performed at 15 Torr with a partial pressure of 44 mTorr for both silicon precursors. Two distinctive regimes are clearly defined: one at low temperature (T_{SiH4} < 750°C and T_{DCS} < 800°C) and the other at high temperature (T_{SiH4} > 800°C and T_{DCS} > 800°C). In the temperature ranges used for this study (550°C – 750°C), the coverage is mainly constituted by hydrogen atoms creating Si-H bonds [Oura 99] and/or by chlorine atoms (see ***Fig. I-10***). The sites with hydrogen and chlorine coverage are inactive to further chemisorptions. The release of free sites is then limited by the species desorption, which is more or less effective whether the temperature is high or low; thus, at high temperatures, the desorption occurs rapidly [Greenlief 95] whereas the desorption is the main growth limiting factor at low temperature [Kim 93]. As example, it is observed in ***Fig. I-10*** that at about 700°C, almost 45% of all the sites on the surface are occupied by Cl and H atoms – majority by Cl – implying that only half of the surface is free for the DCS adsorption. It is worth noting that, in a low temperature regime, the activation energy of hydrogen desorption from a (001) surface is 47 kcal/mol or equivalently about 2 eV [Sinniah 89] and the activation energy for Cl desorption is 73 kcal/mol or equivalently about 3.1 eV [Hierlemann 95]. As a result, two existing regimes in CVD are clearly defined:

- **High temperature regime**, where the growth rate is limited by the transport of gaseous precursors to the substrate. It tends to saturate thus depends very weakly on the temperature. In this regime, the hydrogen desorption is very effective and the amount of precursor's molecules and their adsorption is the limiting factor. The growth rate depends only on the flow rate of the active gas. This regime is also called the *diffusion regime*.
- **Low temperature regime**, where the growth rate strongly depends on the temperature. It is limited by the availability of free sites and by the desorption of species present on the surface, which is thermally activated. This regime is called *reaction limited*. The deposition rate varies exponentially with the reverse temperature according to Arrhenius equation:

$$GR = A * \exp\left(-\frac{E_A}{k_B T}\right) \quad \text{Eq. I-19}$$

Where A is the pre-exponential factor, k_B is the Boltzmann constant, T is the growth temperature and E_A is the activation energy.

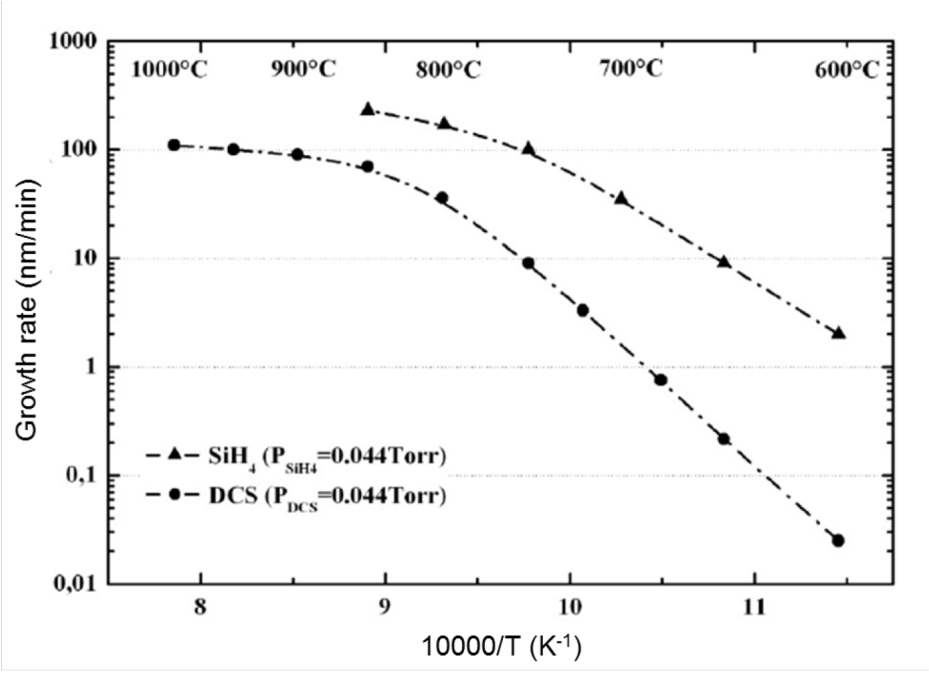

Fig. I-9: *Arrhenius plot of the (001) silicon surface's growth rate for two chemistries: SiH_4/H_2 and SiH_2Cl_2/H_2. These epitaxies were performed at 15 Torr with a silicon precursor's partial pressure of 44 mTorr. Taken from [Pribat 10].*

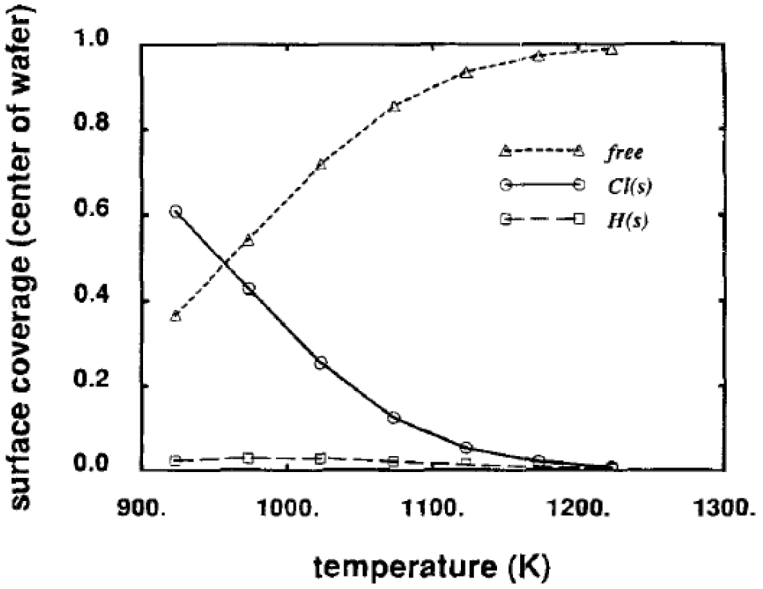

Fig. I-10: *Surface coverage for DCS as a function of temperature. Data from [Hierlemann 95]. At temperatures above 900°C, the surface is completely free, while at low temperature the surface sites are blocked by Cl(s).*

As already mentioned, in the case of SiGe epitaxy, the germane is added in the chemistry. ***Fig. I-11*** represents the Arrhenius plot of $Si_{0.8}Ge_{0.2}$ growth rate as a function of the temperature. The Si growth rate is also given as a reference. The partial pressure of GeH_4 is adjusted as a function of the temperature so that the germanium concentration is 20%. The partial pressure of SiH_4 and the total pressure are maintained at 44 mTorr and 15 Torr, respectively. The SiGe growth rate's behavior is similar to the Si one with the presence of two distinctive regimes; a first one at high temperature for which the growth rate is limited by the transport of gaseous precursors, and a second one for which the growth rate is thermally activated. The main difference can be found in the low temperature regime. Indeed, it is observed that the SiGe growth rate is higher than the Si growth rate. This can be explained by the hydrogen desorption occurs faster starting from a germanium atom than starting from a silicon atom. Thus, the germanium acts as a catalyzer activating the hydrogen desorption.

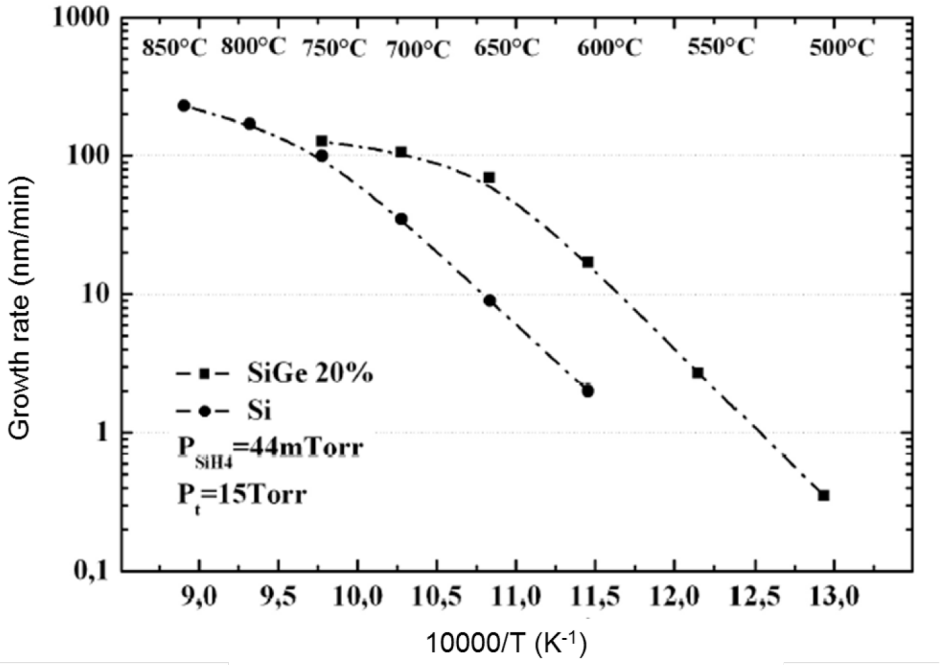

Fig. I-11*: Arrhenius plot of Si and $Si_{0.8}Ge_{0.2}$ growth rate with a 44 mTorr SiH_4 chemistry. The total pressure is 15 Torr.*

III.1.d) In-situ boron-doped SiGe

Boron is one of the most widely used p-type dopant in the fabrication of silicon microelectronics. For a long time, ion implantation was used for impurity doping. However, high energetic ions may lead to different problems like channeling effect or damage in the lattice consisting of a distribution of vacancies and a similar distribution of interstitials. These point defects are extremely mobile and may form stable extended defects such as clusters or dislocations. An alternative to implantation is the *in-situ* doping during Si or SiGe epitaxy. This technique is widely used in many industrial applications like for instance in raised source and drain CMOS regions or intrinsic bases of HBT devices. The problems of defects creations due to implantations are completely suppressed since boron atoms are well incorporated inside the

lattice and no lattice defects are observable. Moreover, *in-situ* boron doping in Si or SiGe layers is well controlled and exhibits a quasi-complete incorporation and electrical activation far superior to any other p dopant commonly used such as indium, gallium or aluminum. Furthermore, the doping being obtained directly inside the chamber during the epitaxy process, this leads to a cost reduction, high throughput, compatibility with standard semiconductor processing, and capability of well-controlled epitaxial growth even at low temperatures, which are very important in an industrial environment. In practice, the precursor for boron doping in a RT-CVD reactor is the diborane (B_2H_6).

It is well-known that the introduction of dopants into Si will induce a mechanical stress in the substrate changing the lattice structure. When boron is incorporated in the lattice as dopant, a local lattice contraction occurs because the bond length for Si-B is shorter than for Si-Si. It was shown by Horn et al. [Horn 55] that one single boron atom exerts a 0.26% lattice contraction per atomic percentage of boron in silicon at room temperature. In the case of boron incorporation into SiGe, the lattice mismatch between the Si and the SiGe layer is reduced. As a result, the strain is also reduced since boron atoms are much smaller than both Si and Ge atoms. This phenomenon is called strain compensation leading to higher dopant activation and a larger bandgap.

III.2) Selective epitaxial growth

Selective Epitaxial Growth (SEG) is used for a long time in various technologies which require Si-based epitaxy, such as MOSFETs, heterojunction bipolar transistors (HBT) or optoelectronics. SEG is needed since a growth must be done on a particular area but not all around. Moreover, since the dimensions of transistors reached few nanometers, a very accurate control of SEG becomes essential for device's performances. Next-generation devices, such as 14 nm FD-SOI or FinFET, need a SEG process not only for improvement of the performance but also for the operation with expected characteristics. This is a technique offering many advantages ranging from the application of strained SiGe epitaxial films used to increase hole's mobility and performance of pMOSFET devices to intrinsic Si epitaxial layers used to reduce short channel effects (SCE) [Kuppurao 08]. Cyclic epitaxy and etch technique is attractive as it gives access to lower deposition temperatures with an acceptable growth rate as no HCl is added during the deposition steps. Other types of advantages have been reported, especially for device fabrication. Indeed, SEG leads to fully self-aligned device architectures that are simpler, or even to novel device structures. Nowadays, SEG is the key step to maintain CMOS device performance with continued scaling. This is why it is one of the most effective and widely used techniques to grow RSD made of SiGe layers [Holt 08].

The basic aim of SEG is to grow layers on Si and not on dielectric material. An example of SEG is given in ***Fig. I-12*** which shows SEM micrographs of a selective SiGe epitaxial layer (in-situ Boron-doped) grown at T < 650°C. The concentrations of Germanium and Boron in the film are ~32% and ~3.1020 at/cc, respectively. On the images, no polycrystalline growth occurs on the top of the gate, and on the contrary only growth of single crystalline SiGe is present on the active area.

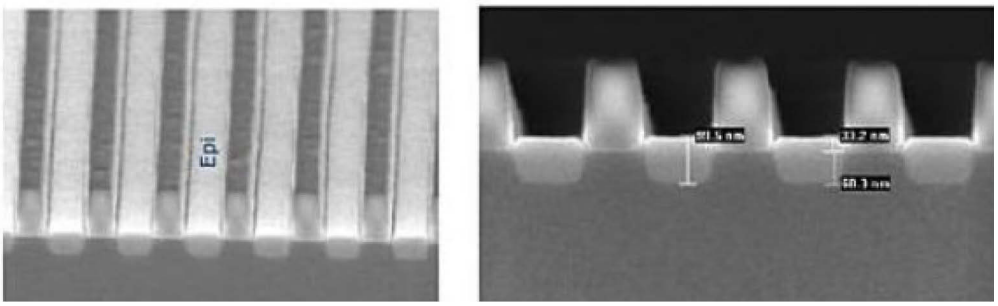

Fig. I-12*: SEM images of in-situ Boron doped selective SiGe epitaxy grown on recessed structures. [Kuppurao 08]*

During a non-selective epitaxial growth (NSEG), this phenomenon will not be possible. ***Fig. I-13*** demonstrates the difference between SEG and NSEG on the same type of substrate (Si area surrounded by SiO_2). In ***Fig. I-13*** a), the process is selective whereas in ***Fig. I-13*** b), it is not selective. It is well visible for the second case that a formation of polycrystalline grains on SiO_2 occurred. On the contrary, in the first case, the growth only occurred on Si area and not on SiO_2, i.e. it is selective.

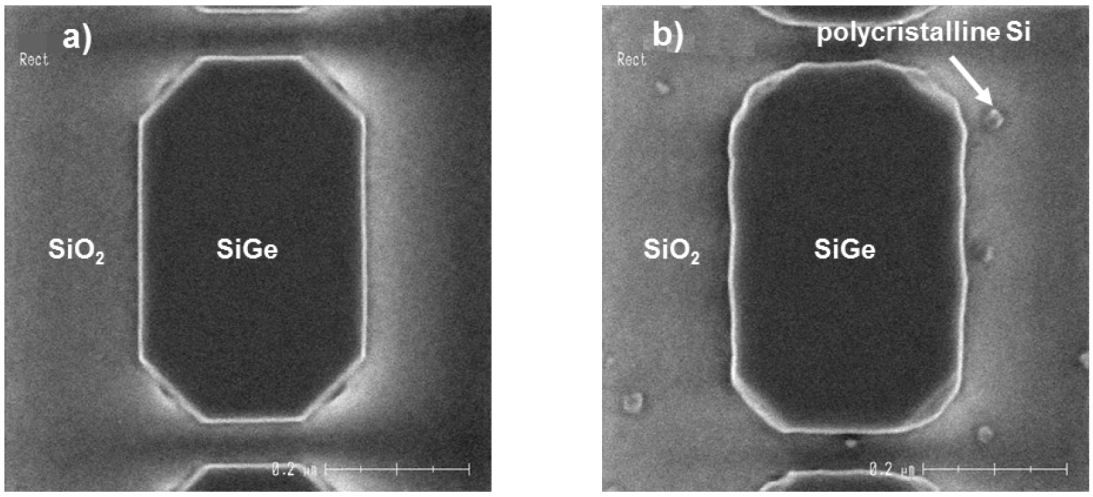

Fig. I-13*: Top-view SEM micrographs of SiGe layers grown on Si area surrounded by SiO_2. On a) the deposition was selective contrary to b). The presence of polycrystalline Si growth is the result of a selectivity loss.*

The concept of SEG is based on the presence of a nucleation step of silicon before deposition over a dielectric and not over silicon. If the process is well chosen, the amount of energy (corresponding to the nucleation step) is large enough to produce growth selectivity. The selectivity of the process depends on several parameters such as the precursor used. The most common precursor is the SiH_2Cl_2 (DCS). Also, the addition of the appropriate amount of HCl to the gas phase can make the growth selective. One explanation among others can be the following: the adsorption of H and Cl atoms on free sites on the dielectric limits the adsorption of Si or Ge precursor molecules and by the way prevents the nucleation on the dielectric material.

Another process which allows such results is the so-called cyclic epitaxy. This technique is based on the fact that polycrystalline Si (or SiGe) etches much faster than single crystalline Si (or SiGe). Therefore, by alternating deposition and etch steps, no growth on the dielectric

occurs, if the process is well controlled (time etch versus time deposition) and if the HCl partial pressure is high enough. This technique is needed when the top of the gates is either not protected or imperfectly protected by a hard mask (for instance SiO_2). This is the case for some device integration schemes as reported by Hartmann *et al*. [Hartmann 13]. The standard process they used first was a classical SEG. However, this process (even though totally selective versus SiO_2 or Si_3N_4) leads to formation of parasitic growths called poly-Si mushrooms on top of unprotected or imperfectly protected gates. This unwanted growth may lead to poly-gate depletion effect that is detrimental to the device. Also, shielding effects may occur. This phenomenon is depicted in ***Fig. I-14***. The solution of this problem was to introduce the cyclic epitaxy. To do so, they developed two ‘‘mushroom-free’’ processes. The first one consists in the SEG of Si, followed by the selective etch with a high HCl mass-flow of the poly-Si mushroom sitting on top of the gate. The second process consists in five SiH_2Cl_2 + HCl growth steps separated from one another by four smaller HCl mass-flows etch steps. Thanks to these techniques, they managed to make the “mushrooms” seen in ***Fig. I-14*** disappear and to preserve the wanted morphology of the gate.

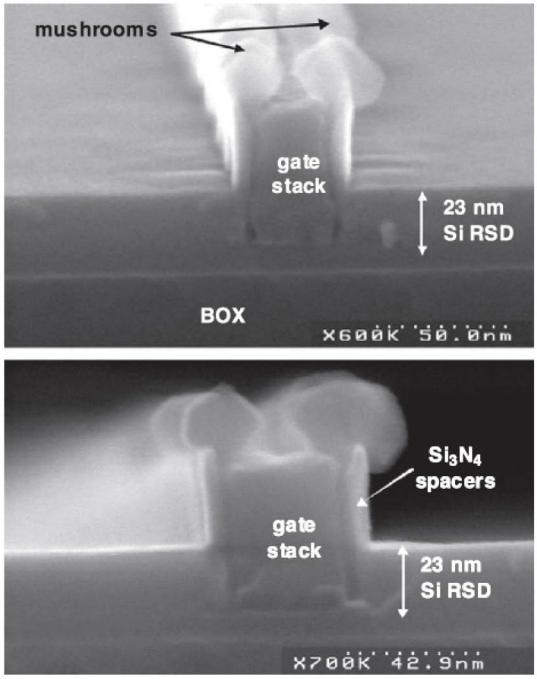

Fig. I-14*: 3D and cross-sectional SEM pictures of a short gate length MOSFET after the 750°C, 20 Torr selective epitaxial growth of 23 nm thick Si raised sources and drains. [Hartmann 13]*

III.3) Loading effects

The loading effect can be defined as the modification of the characteristics (in term of thickness, composition) of an epitaxial layer depending on the mask of the substrate. The micro loading effect is mainly defined as a change in thickness when the feature size decreases. It has been seen in different reports [Reichel 12] that the deposition’s thickness increases for narrow width transistors compared to nominal (large) width transistors, as depicted in ***Fig. I-15***.

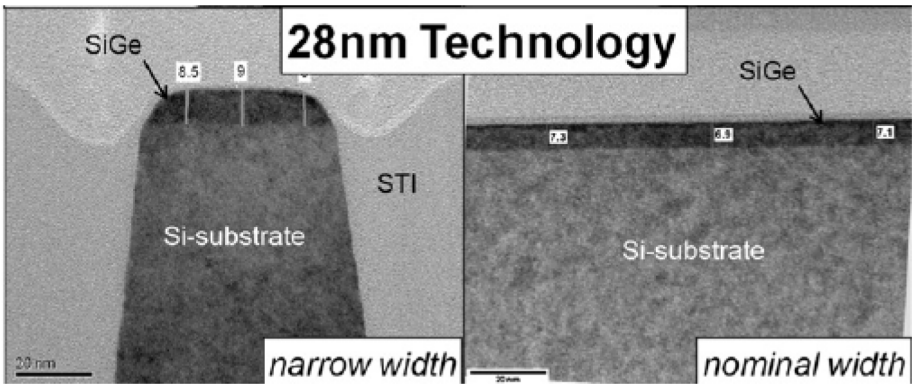

***Fig. I-15**: SiGe channel's thickness on narrow width and nominal width transistors for 28 nm technology. [Reichel 12]*

On the contrary, macro (or global) loading effect refers to differences obtained for a same process. These differences correspond to different layers on substrates which have a different Si to mask area ratio. Different researches were done to demonstrate this loading effect. A comparison between three different substrate's types was investigated by Dutartre *et al*. [Dutartre 08]: a bare Si wafer and two SiO_2 patterned wafers with 23% and 1% of Si area. The results are given in ***Fig. I-16***. It is clear that in the whole temperature range from 600°C to 750°C, the growth rate increases when decreasing the Si surface area. The explanation is the number of available active molecules which is higher for a smaller active Si area (precursor consumption decreases with total Si area). These available active molecules enhancement results in an increase of the growth rate.

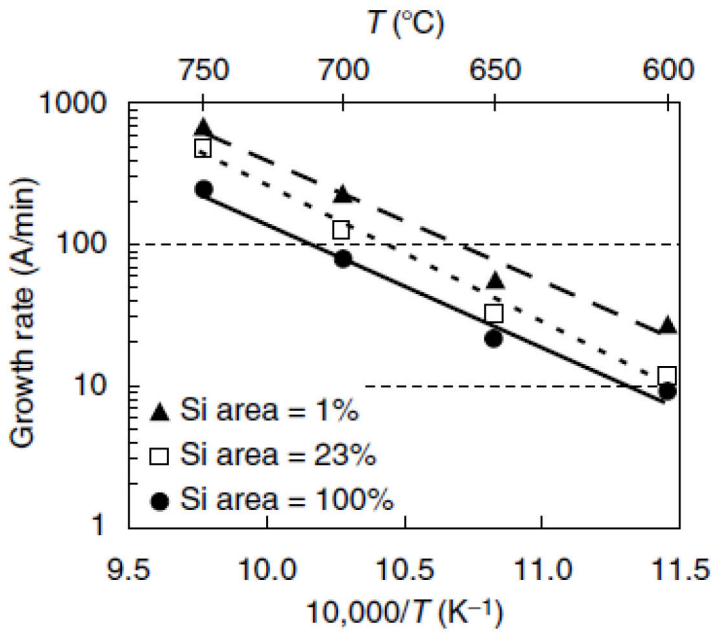

***Fig. I-16**: Global loading effect in DCS–GeH_4–HCl–H_2-based SiGe SEG. A decrease of the Si area from 100% to 1% leads to an increase of the growth rate. [Dutartre 08]*

The same authors showed the global loading effect of the Ge content. They demonstrated for the same substrate types as described above, the increase of Ge incorporation when increasing the SiO_2 area (equivalently decreasing Si surface area). It also can be explained by a reduced depletion of the gas phase which allows a better Ge incorporation.

Growth kinetics anisotropy was also studied by Pribat *et al*. [Pribat 11]. For these studies, the ratio r_{hkl} was defined as the growth rate of corresponding (hkl) plane (GR_{hkl}) divided by the growth rate of (001) surface (GR_{001}). Then it is defined by:

$$r_{hkl} = \frac{GR_{hkl}}{GR_{001}}$$

It was shown that the kinetics of the different planes is defined as $GR_{111} < GR_{113} < GR_{001}$ and seems to equalize at low temperatures. In the case of SiGe material and at high temperature (750°C), the GR_{001} is 5 and 3 time higher than GR_{111} and GR_{113}, respectively. On the contrary, at lower temperature (500°C), GR_{001} is the lowest with r_{hkl} values of 1.4, 1.2 and 1.1 for (110), (113) and (111) planes, respectively. Above 650°C, the kinetics anisotropy is quasi-independent of the temperature whereas below 650°C it depends on temperature.

The loading effect and pitch dependence on facetted epitaxies were studied by Loubet *et al*. [Loubet 10] The pitch is defined as shown in ***Fig. I-17***, i.e. the distance between the same sides of two adjacent gates. Thus, going towards next-generation technologies and smaller structures, the pitch (or space between two spacers) is being reduced. As a consequence, the morphology of the grown material between two gates will change. A cyclic epitaxy with DCS/HCl/H_2 was used to deposit RSD. In ***Fig. I-18*** due to the physical proximity of facets, we can see that both loading and geometry effects affects the epitaxial growth. Indeed, the deposited matter thickness decreases when the pitch decreases as well. Also, it was observed two different regimes during the process depending on the number of cycles: a linear regime and saturation in thickness when the {111} facets are merging together. This is well visible in the ***Fig. I-19***. This growth self-limitation in the case of saturation can be explained by the no longer nucleation along both the SiN spacers and [100] direction. They also demonstrated that sharp (111)-facetted RSD using cyclic epitaxy is extendable beyond 20 nm node. However, obtaining pure {111} facet is a real challenge since multi-faceting at the {111} facet boundaries appear leading to self-limitation of the growth before the geometrically expected saturation thickness.

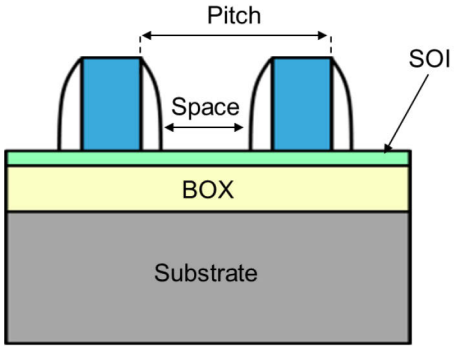

Fig. I-17*: Schematic of FD-SOI structure. The RSD are grown in between the two gates. The concept of pitch and space are introduced.*

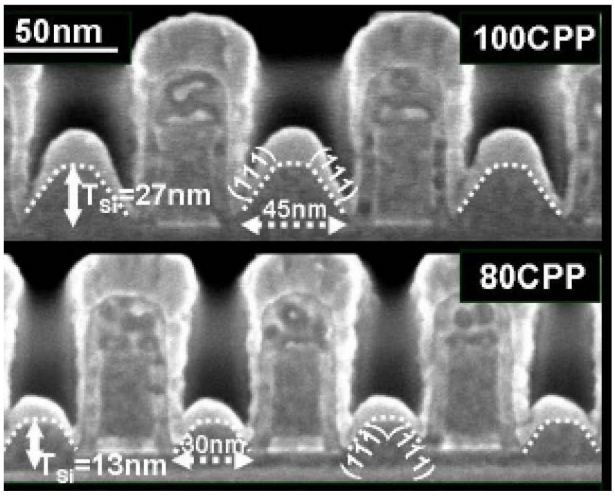

Fig. I-18: *TEM cross-section showing the gate's pitch dependence of RSD epitaxy using cyclic deposition/etch at 750°C in the case of a faceted (111) RSD epitaxy. [Loubet 10]*

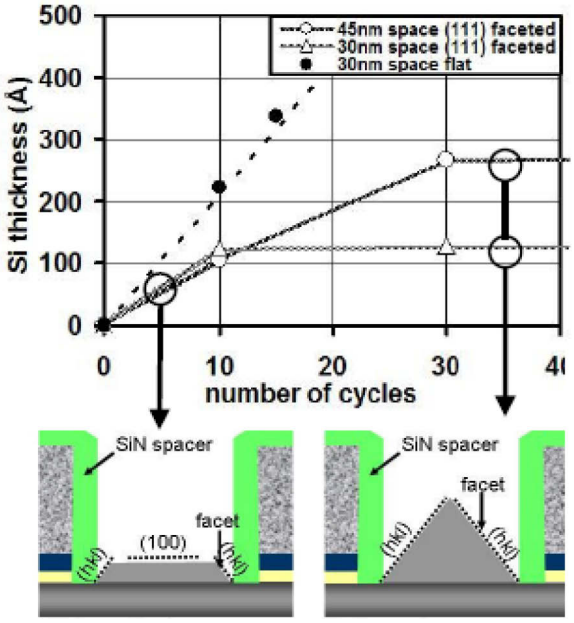

Fig. I-19: *RSD thickness obtained for flat and (111)-faceted shapes as a function of the number of cycles. 30nm and 45nm spaces are showing a common linear growth regime (left) followed by a saturation mode when facets are merged (right). [Loubet 10]*

IV/ Conclusion

In this chapter the Si-based materials' properties were exposed. The notions of pseudomorphic and fully-relaxed SiGe layer grown on Si substrate, as well as the critical thickness were introduced. The different main growth modes in epitaxy as *Frank-van der Merwe* mode, *Volmer-Weber* mode and *Stranski-Krastanov* mode are presented. The last one

is the most important in this study since some similarities with this mode will be further discussed.

All the epitaxial layers are performed in an industrial RT-CVD tool. This is, nowadays, the most used technique in the semiconductor industry due to its numerous advantages compared to any other competitors. The different mechanisms occurring during the growth are explained and described. They can be enumerated as follow: the adsorption of gaseous precursors on the substrate surface, the diffusion and chemical reaction onto the surface, and the desorption of the gaseous by-products.

The Si growth kinetics and the influence, e.g. of the temperature on the growth rate are given in the case of SiH_4 and DCS precursors. Two regimes are usually described in CVD: the high temperature and the low temperature regimes. For the first one, the growth rate is limited by the transport of gaseous precursors to the substrate. For the second one, the growth rate is limited by the availability of free sites and by the species' desorption present on the surface. The influence of the Ge and the B on the kinetics is also given. The germanium acts as a catalyzer activating the hydrogen desorption and thus increases the GR in the low temperature regime. Concerning the B, the GR increases also due to an enhancement of the H desorption. In addition, the strain is also reduced since boron atoms are much smaller than both Si and Ge atoms.

Finally, the notion of selective epitaxial growth was introduced since all the layers studied during this work are selectively grown on the Si active zones. This means that the growth occurs only on the desired zones and not around (in the majority of cases, the dielectric materials).

Chapter 2

Experimental details

The experimental details will be given in the chapter 2. First, the surface cleaning used prior any growth, followed by the presentation of the epitaxy chamber are discussed. In order to study with accuracy, the annealing's influence on the epitaxies' morphology, the temperature must be well controlled and precautions must be taken. Consequently, some preliminary experiments were performed to study the influence of the temperature PID controller values and the lamp ratios on the process temperature. Then, the main characterization techniques used in this thesis will be briefly presented.

I/ SiCoNi chamber for surface preparation

The acquisition of atomically clean surface prior to epitaxial growth is an essential condition. Indeed, an epitaxial layer grown on a contaminated surface will lead to the formation of defects inside the material which the presence must be avoided. In the case of an epitaxy-regrowth, it is even more critical since intermediate technological treatments may pollute the semiconductor's surface, and even more damage the surface or the material itself. Furthermore, it is essential not to introduce in the epitaxy chamber contaminants that could pollute the enclosure. In our case, the Si surface always presents a thin layer of native oxide which must be removed before epitaxy in order to ensure a defect-less grown layer. There are numerous possibilities to clean a Si surface prior to epitaxy but only one was used during this work. This process patented by Applied Materials [Kao 05] and called SiCoNi is an *in-situ* cleaning which could replace the conventional wet surface cleaning. Since the SiCoNi chamber is directly integrated to the RT-CVD tool, no contact with the ambient air is done between the surface cleaning and the epitaxy. However, the real interest of this process is that it allows a much faster wafer processing due to the fact that the wafer, right after the cleaning process, can directly be moved from the SiCoNi chamber to the epitaxy chamber. Moreover, it is a low temperature process (< 200°C) avoiding degradation of the pattern morphology. Finally, this technique is very selective over silicon and other materials already present before epitaxy (e.g. silicon nitride).

The principle of the process is described in ***Fig. II-1***. It uses a mixture of ammonia NH_4 and nitrogen trifluoride NF_3 gases flowing through a plasma. Reactive plasma by-products (NH_4F and/or NH_4F-HF) are formed and react with the SiO_2 surface layer creating a $(NH_4F)_2SiF_6$ thin solid film, NH_3 and H_2O products. The NH_3 and H_2O may be removed by vacuum pump. The $(NH_4F)_2SiF_6$ solid by-products are then removed by heating up the substrate close to 200°C which sublimate the $(NH_4F)_2SiF_6$ film into volatile products NH_3, HF, and SiF_4. These products are then evacuated from the chamber leaving an oxide-free Si surface.

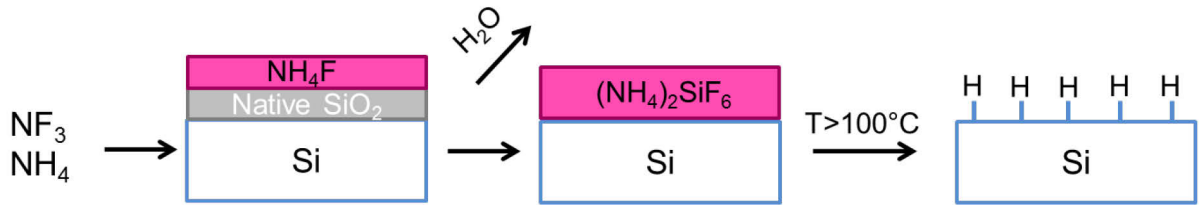

Fig. II-1*: Principle of the Siconi process. NH_4F are formed and react with the SiO_2 surface layer creating a $(NH_4F)_2SiF_6$ thin solid film. The film is then removed to leave an oxide-free Si surface.*

II/ Epitaxy chambers

In this work, the epitaxy tool used for the experiments was a RTCVD reactor EPI Centura 300 from Applied Materials (AMAT). It can handle 300mm wafers. The EPI Centura 300 is a multi-chamber tool, i.e. it is composed of several modules interconnected to each other thanks to a transfer chamber (see ***Fig. II-2***). All around this last one, there are two load locks (LLA and LLB) for wafer loading and unloading, two process chambers where the epitaxy is

performed, the SiCoNi chamber (not in the figure) for *in-situ* cleaning, and a chamber (not shown in the figure) allowing the cool down of the wafer after being processed. Both LLA and LLB are the interface between the clean room and the process chambers. They allow the loading of a Front Opening Unified Pod (FOUP) of 25 wafers. In order to minimize the contaminations, right after the wafer loading, the air is pumped and replaced by nitrogen, the pressure is then reduced. The transfer chamber aims, as its name suggests, at transferring the substrates from one chamber to another through a robot. It is preferably at reduced pressure (<50 Torr) allowing also a very good isolation of the process chambers avoiding any atmospheric contamination from each wafer loading and unloading. The cooling chamber consist in a metallic plate inside which cooled water flows. The substrate is placed on this plate and the good conductivity of metals allows the cool down of the wafer. The SiCoNi chamber is used for in-situ cleaning which the process is briefly described in Chapter 2-I.

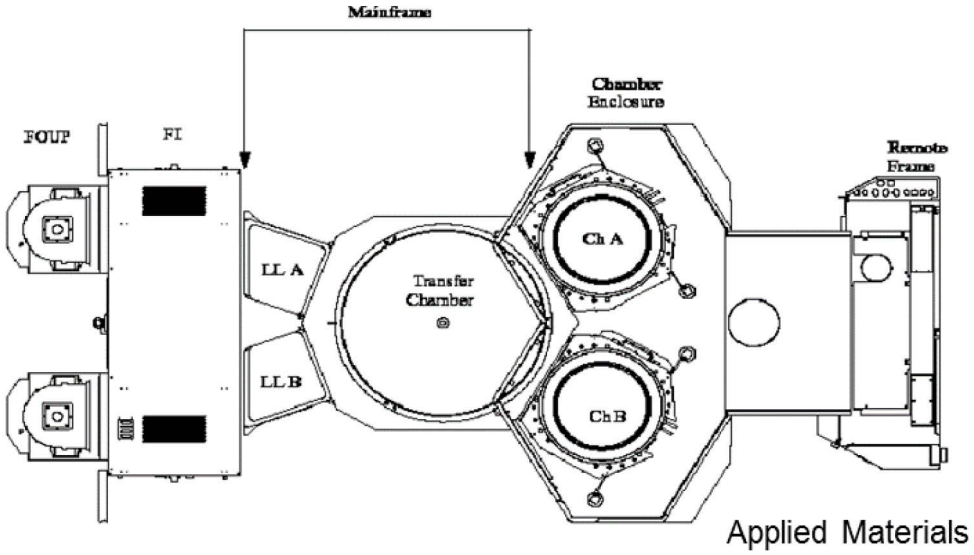

Fig. II-2*: Schematic drawing of the EPI Centura from AMAT. The SiCoNi chamber is not shown here but is attached to the transfer chamber. Both chamber A and B are used for different in-situ doping. [AMAT 04]*

Each chamber is used for specific processes to avoid any cross contamination: the chamber B is used for *in-situ* p-type doping (SiGe:B in this case) while the chamber A is devoted for *in-situ* n-type doping. Intrinsic layers can be grown in both chambers. The system allows only a single wafer processing in the chamber, as depicted in ***Fig. II-3***. The walls of the chamber are made of fuse quartz and dome-shaped which strengthen the chamber and prevent its implosion at low pressure. The substrate is placed on a graphite susceptor coated by SiC, which rotates during the process to enhance the film uniformity in terms of concentration and grown thickness. The gases are injected inside the chamber from one side and evacuated from the other side. Metallic contaminations are avoided by coating by quartz both the gas entrance and exit. Both the susceptor and the wafer are heated from the top and the bottom thanks to different lamp module. The top is heated by an upper lamp module composed of 20 halogen lamps in the inner and of 12 lamps in the outer zone, while the bottom heating is ensured by a lower lamp module constituted of 12 (inner) and 32 (outer) lamps. The power of lamps can be adjusted by the power lamp ratio which can be used to improve the uniformity. Temperatures ranging from 350°C and 1200°C can be attained with this system. The use of lamps for heating allows fast ramps in temperature. This way, temperature ramps of 15°C per second can easily

be done. The whole process module is cooled by an air and water cooling. The substrate temperature is measured by two pyrometers, one located next to the upper lamp module, measuring the emission from the wafer center, another located next to lower lamp module, measuring the emission from the bottom of the susceptor. The top pyrometer is calibrated by the silicon emissivity and cannot be used if no substrate is present on the susceptor. The temperature is controlled by the bottom pyrometer and by a proportional-integral-derivative (PID) control loop. The PID constants can easily be adjusted directly in the recipe and adapted to any situations whether it be fast high temperature ramps or cool down ramps to minimize the possible temperature overshoots. An overshoot (inversely undershoot) is the difference between the max peak and the setpoint temperature value when the temperature exceeds (inversely below) this value before stabilizes. If a system has a quick response, it will typically have a larger overshoot value. If a system has a slow response, typically the overshoot is very small.

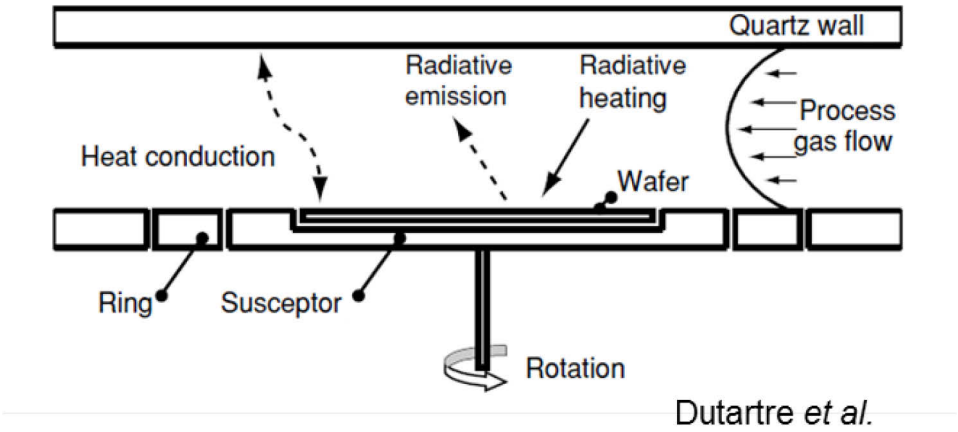

***Fig. II-3**: Schematic cross-section representation of the RT-CVD reactor. The rotating wafer is lamp-heated from top and bottom. The temperature is measured by top and bottom pyrometers.*

Influence of PID constants on the top and bottom pyrometer's reading

Before starting this part, it is important to note that there are two successive control loops with different PID constants: the temperature PID and the power PID. The temperature PID is related to the susceptor, while the power PID is directly related to the lamps. The PID values that are discussed in the following are the power PID. It makes sense that the temperature PID can be adjusted to improve the temperature's control but its influence is not studied here. A scheme is given in ***Fig. II-4*** to briefly describe the lamps' system. A PID control loop consists in three parameters: the Proportional Gain (P), the Integral Time Constant (I), and the Derivative Time Constant (D). These constants are used to obtain stable powers as required by the temperature PID as quickly as possible. The power PID values default defined by the supplier were too slow for the needed applications and should have to be modified. Thus, the aim is to find faster PID constants that address the needs, i.e. fast temperature ramps with fast stabilization and overshoots as low as possible.

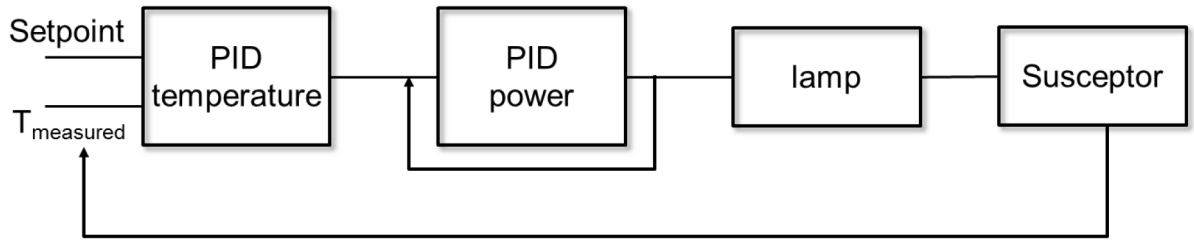

Fig. II-4*: Scheme describing the lamps' system. The temperature of each process chamber in the Epi Centura 300 system is controlled by the use of a Proportional Integral Derivative (PID) control system. It is a closed loop system.*

The influence of the power PID values in terms of temperature ramp and overshoot (or undershoot) is given is this part. Two PID constants were used, a fast one 0.2/0.1 and a slow one 0.1/2. The experiment consists in 7 temperature steps which are successions of downward and upward ramps in temperature followed by a stabilization step. The set-point temperatures (controlled by the bottom pyrometer) were 630°C (reference temperature), 650°C, 675°C and 700°C. The stabilization steps were chosen long enough (120 sec or 60 sec) so that the system can stabilize correctly. ***Fig. II-5*** shows the top pyrometer measurements for both PID values. To note that the temperatures measured by the top pyrometer are not the same as the set-point temperature (user define). The difference in temperature between the two pyrometers measurements is explained in the following section. The different steps are enumerated bellow:

- Ramp to 630°C + 60 sec of stabilization
- Ramp to 650°C + 120 sec of stabilization
- Ramp to 630°C + 60 sec of stabilization
- Ramp to 675°C + 120 sec of stabilization
- Ramp to 630°C + 60 sec of stabilization
- Ramp to 700°C + 120 sec of stabilization
- Ramp to 630°C + 60 sec of stabilization

First, comparing both PID constants it is observed that for the fastest one the temperature stabilizes faster. **Table II-1** gives the durations needed to reach the stabilization at the wanted temperatures both PID values. In average for the slow PID, the system needs more than 57 sec to stabilize compared to 36 sec for the fast PID. A gain of 38% is reached by changing the PID constants.

TABLE II-1: Durations in seconds needed to reach the stabilization at the wanted temperatures for slow and fast PIDs.

Set-point temperature	Slow PID 0.1/2	Fast PID 0.2/0.1
650°C	58	39
675°C	57	34
700°C	58	35

Second, when studying the influence of the thermal treatments on a grown material it is important to be comparable between each annealing temperature and the overshoot after the

temperature must as low as possible. Indeed, most of the time this overshoot is not repeatable and during this overshoot the layer can undergo a significant morphology evolution that can induce errors in the results. **Table II-2** gives the overshoot values measured by the top pyrometer for each set-point temperature and both slow and fast PID. The overshoots are much higher for the slow PID and moreover increase with increasing the temperature. The overshoot increases of almost a factor of 2 for the slow PID. In average, the overshoot is equal to 5.4°C for 0.1/2 PID while it is only equal to 2.7°C for the 0.2/0.1 PID. Once again, a gain of 50% can be reached. Same observations can be done concerning undershoots (after a temperature decrease) and it is even more pronounced. Indeed, the values are much more spaced comparing both PIDs. Furthermore, the system cannot stabilize during the 60 sec of stabilization regarding the slow PID.

TABLE II-2: Overshoot values in °C obtained by the top pyrometer for the slow and fast PID. To note the overshoot is defined as the difference between the higher temperature value and the stabilized temperature.

Set-point temperature	Slow PID 0.1/2	Fast PID 0.2/0.1
650°C	3.7	2.2
675°C	5.6	2.5
700°C	6.8	3.4

The PID is an important parameter that must be optimized in any situations to obtain the best process. The overshoots can be removed completely by adjusting the values of the PID but is was not the subject of this thesis. The fast PID was good enough to be comparable between each successive study.

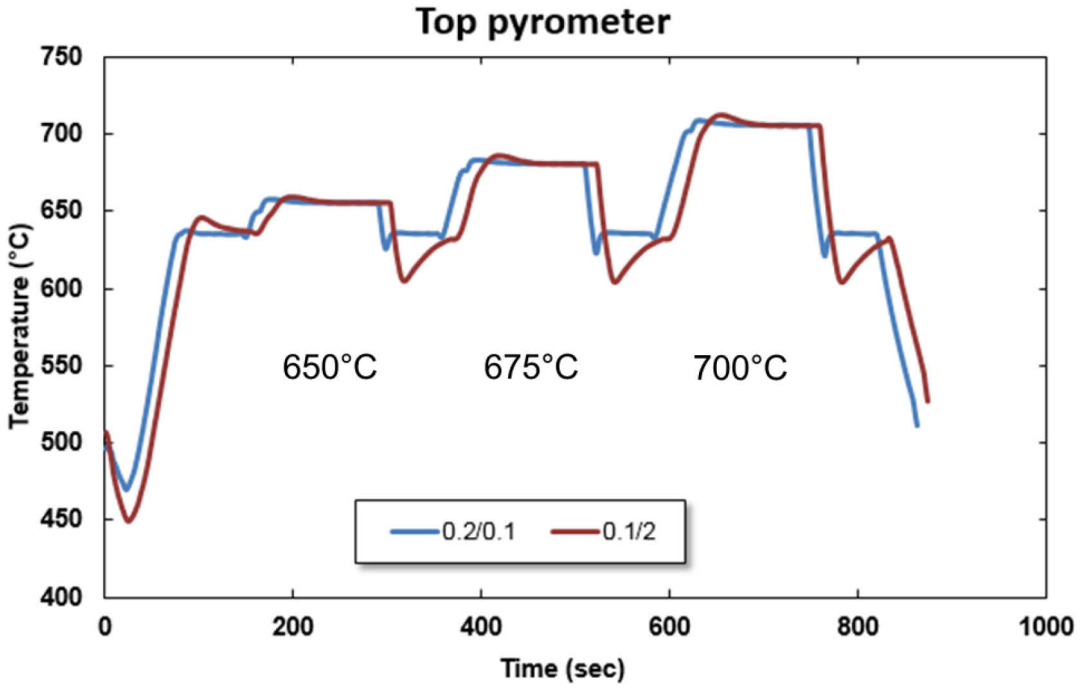

***Fig.II-5**: Top pyrometer's measurement for PID values of 0.1/2 and 0.2/0.1. The temperatures given on the graph are the set-point temperatures and do not correspond to the top pyrometer's measurement since there is an offset between both pyrometers.*

Influence of lamp power ratio and pressure on the top and bottom pyrometer's reading

As already mentioned, the temperature in this system is controlled by the bottom pyrometer. In other words, the set-point temperature (defined by the user) is driven by the pyrometer measuring the emission of the bottom of the susceptor. However, the real process temperature is the one located at the surface of the wafer, which depends on the optical properties of this wafer. As a result, there is a temperature variation between the real and the set-point temperature. It was shown that this variation varies with the wafer emissivity (global loading effect), the top/bottom lamp ratio, and gas conductivity [Dutartre 01]. Moreover, the pressure also impacts the thermal susceptor/wafer coupling and thus the temperature variation. Indeed, as soon as the pressure is decreased the thermal conduction decreases as well, leading to a bad thermal coupling [Dutartre 16]. The effects of pressure and lamp ratio on the offset between both actual (wafer) and set-point (susceptor) temperatures is depicted in ***Fig. II-6***. In the figure, both the top (in red) and the bottom (in blue) pyrometer measurements are shown. For this experiment, a patterned wafer similar to the ones used during this thesis, was processed. The lamp ratios are defined by three constant values which are power ratios as followed:

$$\frac{P_{bottom}}{P_{total}} / \frac{P_{top,inner}}{P_{top}} / \frac{P_{bottom,inner}}{P_{bottom}}$$

Where, P_{total} is the total power, P_{bottom} is the power distributed to the whole bottom lamps, P_{top} is the total power distributed to the whole top lamps, $P_{top,inner}$ is the power distributed to the top inner lamps, and $P_{bottom,inner}$ is the power distributed to the bottom inner lamps. To remind that the top and bottom lamps' systems are divided in two specific zones: inner and outer zones. For example, a lamp ratio of 73/60/20 means that 73% of the total power are distributed to the bottoms lamps and 27% to the top lamps. Then, 60% of the 27% are distributed to the *inner* top lamps and 40% of the 27% to the *outer* top lamps. Equivalently, the value 20 means that 20% of the 73% are distributed to the *inner* bottom lamps and that 80% of the 73% are distributed to the *outer* top lamps.

Different lamp ratios (73/60/20, 63/60/20 and 53/60/20) and H_2 pressures (5 Torr, 10 Torr, 20 Torr, 40 Torr and 200 Torr) were used. The set-point temperature was 650°C (as given by the bottom pyrometer in blue). Each step in the figure, regarding one lamp ratio, corresponds to a change in pressure and was chosen long enough so that the temperature can stabilize. For sake of simplicity, the lamp ratios will be named as 73%, 63% or 53% since it is the only parameter that changes in this study. First, it is clear that the lamp ratio modulates the top pyrometer's measurements. Indeed, for a given pressure, e.g. 20 Torr, the temperature offset between the top pyrometer and the bottom pyrometer varies: 43°C for 73%, 59.5°C for 63% and 76.4°C for 53%. Second, the pressure also impacts significantly the top pyrometer's measurement. ***Fig. II-7*** shows more in details the influence of the pressure on the top reading temperature for each lamp ratio. For both 73% and 63% ratios, the top temperature increases with increasing pressure but the contrary is observed for 53%, i.e. the top temperature decreases when the pressure increases. At 73%, it varies from 678.5°C to 703°C; at 63%, it increases from 704.4°C to 713.8°C; and at 53% it varies from 732°C to 723.2°C for pressures from 5 Torr to 200 Torr. Consequently, the pressures have a significant impact on the temperature and these variations must be taken into account when comparing e.g. thermal treatments at different pressures. This is the case when studying the thermal rounding in small patterns at several H_2 pressures (*see Chapter 4 - II.2.c) Influence of carrier gas during anneal:*

N2). Finally, ***Fig. II-8*** summarizes what it was observed previously. It shows the top temperature as a function of pressure for the three investigated lamp ratios. As already mentioned, the top temperature increases with increasing the pressure for 73% and 63% but decreases for 53% lamp ratio. A clear last observation is that there is a particular lamp ratio for which there is no more influence of the pressure, as shown by the dashed line in the figure. This can be obtained for a lamp ratio just in between 53% and 63%, i.e. 58% corresponding to a temperature of about 718°C. This temperature's value thus, corresponds to the real setpoint temperature of 650°C. Indeed, at this "equilibrium" state, the vertical heat flux can be considered as null and the real temperature of the wafer is equal to the temperature of the susceptor. The 68°C difference between both temperatures corresponds to the presence of patterns on the wafer that makes its emissivity change, leading to an additional offset in the pyrometer's reading. Out of this "equilibrium", the top temperature tends to approach to 718°C when the pressure increases. This due to the fact that the gas conduction increases when the pressure increases resulting in a lower offset. However, even at higher pressures the top reading temperature will not reach the value due to the fact that the conductivity cannot run to infinity when increasing the pressure. In addition, when heating more in one side than in the other (introducing a heating disequilibrium), the heat flux increases leading to a higher offset. This is especially the case for a lamp ratio at 73% meaning that 73% of the total power are distributed to the bottom lamps. That is why the offset is higher for this ratio than the others: e.g. at 200 Torr, the offset between the "equilibrium" temperature and the top pyrometer's reading is 15°C for 73% compared to 4.2°C for 63% and -5.2°C for 53%.

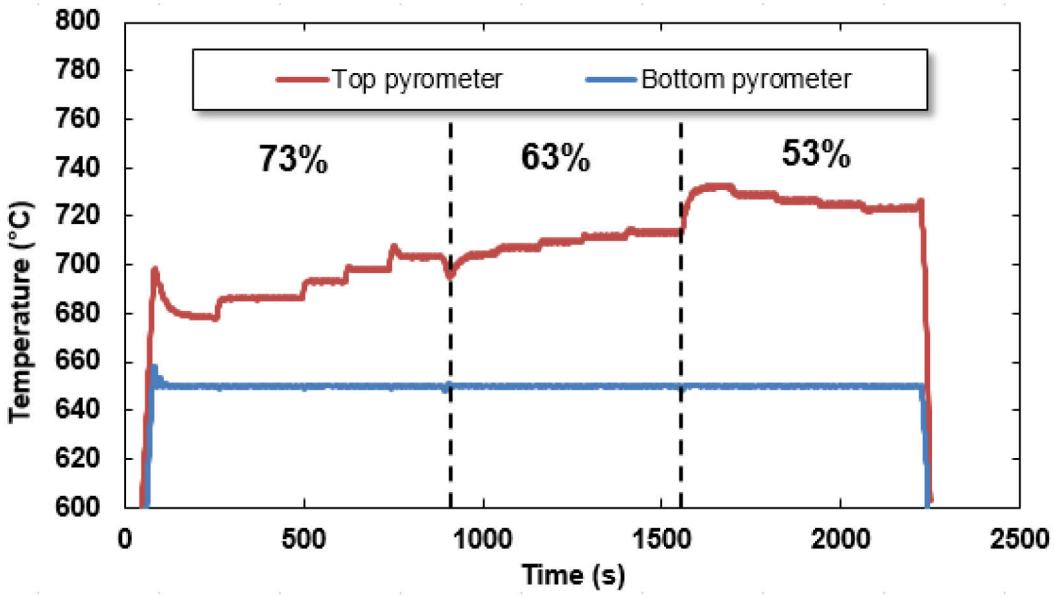

Fig. II-6*: Lamp ratio and pressure dependence of the top pyrometer's measurement. Lamp ratios of 73%, 63% and 53% and pressures of 5, 10, 20, 40 and 200 Torr are shown. The set-point temperature is 650°C (blue line) controlled by the bottom pyrometer. The variation of the temperature is measurement thanks to the top pyrometer.*

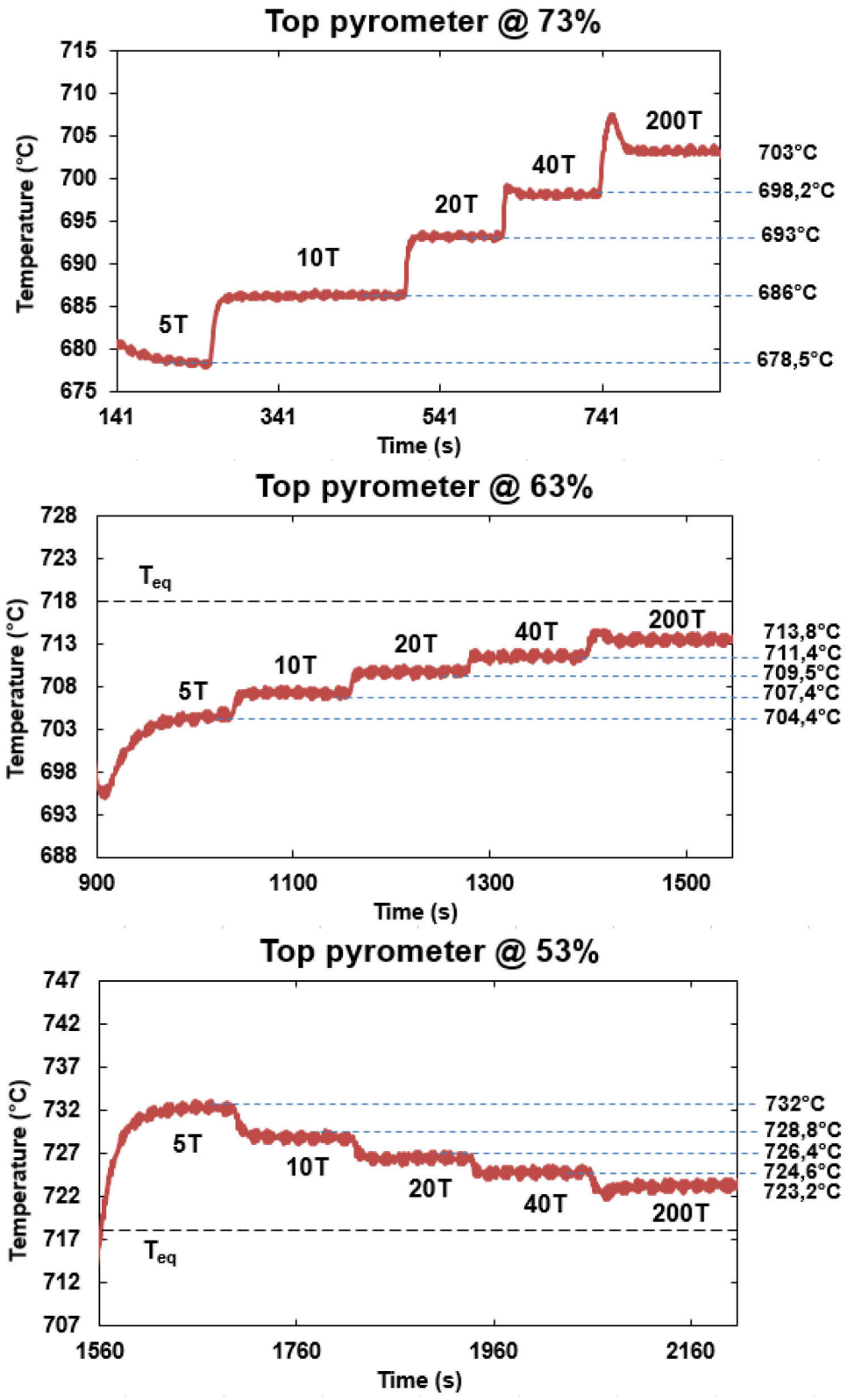

Fig. II-7: *Top pyrometer's measurement for different H_2 pressures: 5, 10, 20, 40 and 200 Torr. Lamp ratio of (top) 73%, (middle) 63% and (bottom) 53% are used. The pressure has a significant influence on the top temperature leading to an important offset between the actual (wafer) and the set-point (susceptor) temperature. The temperature at the "equilibrium" state (T_{eq}) is shown for indicative purposes.*

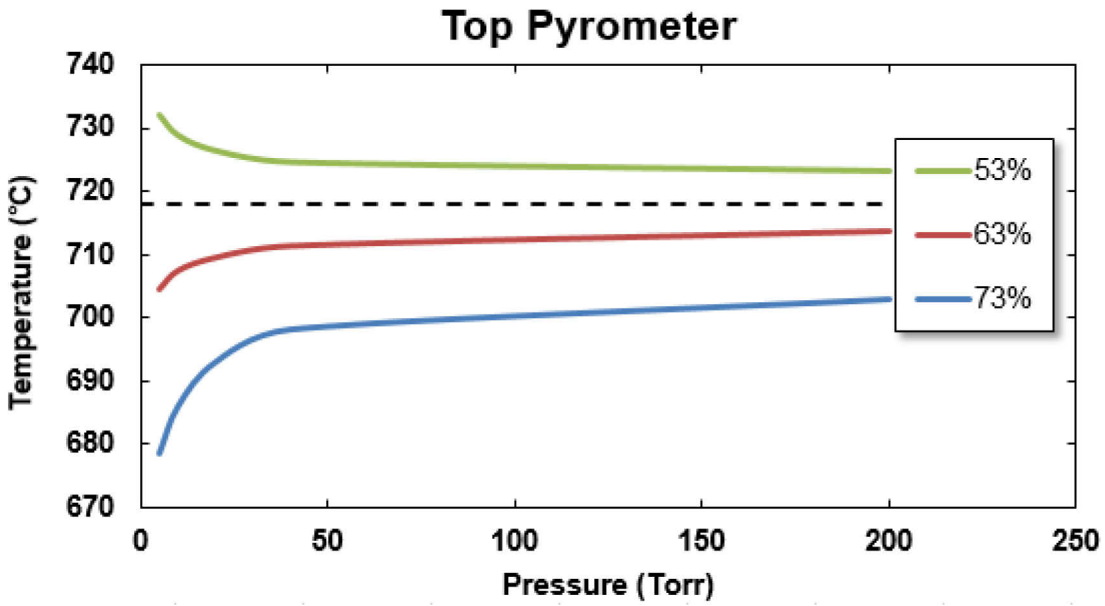

***Fig. II-8**: Top pyrometer's measurement as a function of H_2 pressure for the three investigated lamp ratios: 73% (blue), 63% (red) and 53% (green). It is clearly observed that there is a particular lamp ratio (shown with the black dashed line) for which there is no more pressure dependence of the temperature offset. This is obtained for a ratio of 58%.*

III/ Characterization techniques

The epitaxial layers were characterized by several techniques in order to obtained chemical, physical or morphological information. This section is divided into two parts: one for the morphological aspects of epitaxial layers, the other one gathers information about the material itself such as chemical composition, deposited thickness… Most of the tools presented here are located in clean room (in-line tools) simplifying some characterizations. However, few of them are outside the clean room (mainly for the morphology's characterization like atomic force microscopy or transmission electron microscopy) meaning a careful displacement of the wafers in sealed boxes.

III.1) Morphology characterization

III.1.a) Atomic Force Microscopy

In a speech at the Nobel Price banquet, a wise person, a pioneer of electron microscopy known as Ernst Ruska has said: "*Das Lichtmikroskop öffnete das erste Tor zum Mikrokosmos. Das Elektronenmikroskop öffnete das zweite Tor zum Mikrokosmos. Was werden wir finden wenn wir das dritte Tor öffnen?*" or more easily in English "*The light microscope opened the first gate to microcosm. The electron microscope opened the second gate to microcosm. What will we find opening the third gate?*" This third gate, the path to the infinitesimally small was in fact the invention of the Scanning Probe Microscopy (SPM). The first microscope born of SPM was first introduced by G. Binnig and H. Rohrer in 1986. They were half awarded (the other half to Ernst Ruska for his fundamental work in electron optics, and for the design of the first electron microscope) the same year for their design of the scanning tunneling microscope

allowing the study of insulator's topography in the nanoscale range. Shortly afterwards, G. Binnig *et al*. [Binnig 86] have demonstrated the efficiency of another powerful tool, the Atomic Force Microscopy (AFM). Combining both principles of STM and surface scanning with a cantilever, the authors showed that up to atomic resolutions can be obtained when imaging under ambient atmosphere, conductive or non-conductive materials. The principle was to obtain an image of the surface's sample thanks to the interaction forces between the surface and the cantilever (tip). Since then, AFM technique was extensively studied and is now suited for different environments such as high vacuum, liquids, low temperatures, and also for many applications from biology to microelectronics.

In atomic force microscopy, a sharp probe is brought into close proximity to a sample. Probe and sample are subsequently moved relative to each other in a raster pattern, and a quantity is measured in a serial fashion at discrete locations (pixels). The working principle is based on the measurement of any interaction between the tip and sample surface by monitoring the displacement of the free end of the attached cantilever. The forces on the cantilever are more or less important depending on the distance with the surface, leading to a change in the cantilever deflection. The forces are either attractive when the tip is far (1-10nm) from the surface (Van Der Waals, capillarity…), or repulsive when the tip is located at less than 1nm from the surface (Coulomb potential). The small (angular) movement of the lever is commonly measured by a laser beam that is reflected off the cantilever and directed onto a split photodetector (***Fig. II-9***). For a small displacement, the restoring force exerted by the cantilever is described by the Hooke's law.

.

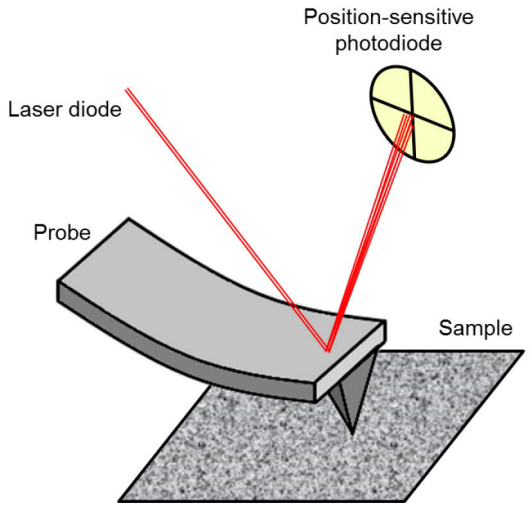

Fig. II-9*: Schematic representation of the probe scanning a sample. The variation of the tip's deflection is measured by a laser diode reflected off the cantilever and directed onto a split photodetector.*

Fig. II-10 below shows the plot of force as a function of the distance between the probe and the sample described by the Lennard-Jones potential. This potential is well suited for the AFM since it describes the interaction between two atoms, in this case, one coming from the probe, and the other one from the sample. The dominant interactions at short-probe distances are Van der Waals interactions. During contact with the sample, the predominantly experiences repulsive Van der Waals forces (contact mode) leading to tip deflection. When the tip is further from the surface, attractive Van der Waals forces are dominant (non-contact mode).

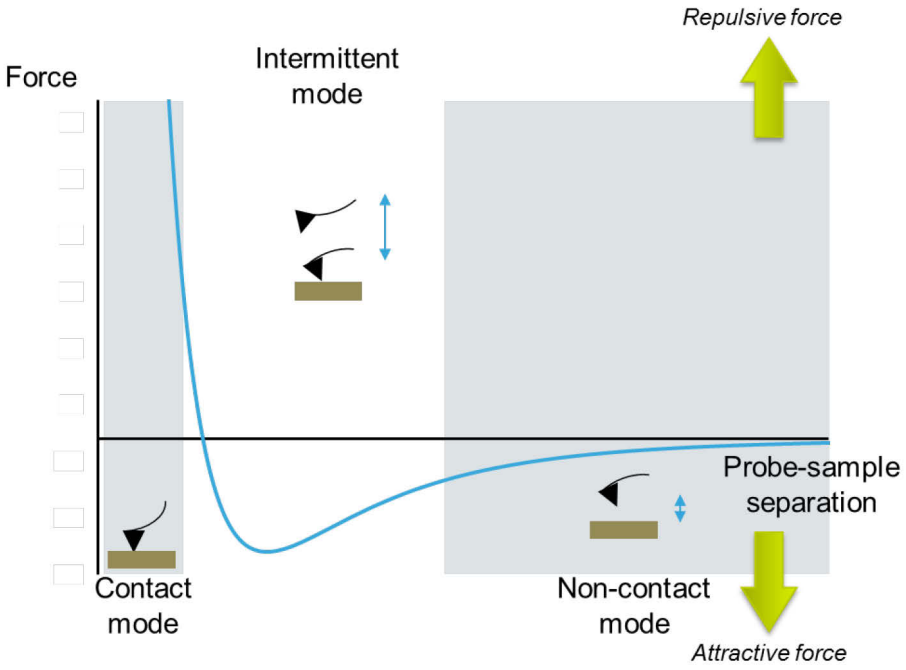

***Fig. II-10**: Plot of force as a function of probe-sample separation*

Three different operating modes are available in AFM.

In contact mode, the tip is brought in contact with the surface (less than 0.5nm). In this case, the tip bends due to repulsive forces (Coulomb interactions). By maintaining a constant cantilever deflection (using the feedback loops) the force between the probe and the sample remains constant and an image of the surface is obtained by recording the voltage applied to the piezoelectric actuator. High resolution can be obtained with this mode. However, since the probe is very close (in contact) to the surface and endures large interactions with the sample, common damages may be produced to the probe and to soft samples.

In intermittent mode (or tapping), the cantilever is excited by piezoelectric and oscillates at or near its resonant frequency. Here, a large amplitude of oscillation (20 - 200 nm) is used and the distance with the surface is comprised between 0.5 and 2nm. In this mode, the amplitude and the frequency of the driving signal are kept constant, leading to a constant amplitude of the cantilever oscillation. The interaction of forces acting on the cantilever when the tip comes close to the surface cause the amplitude of the cantilever's oscillation to change (usually decrease) as the tip gets closer to the sample. The height is adjusted to maintain a set cantilever oscillation amplitude while the sample is scanned. An image is produced by imaging the force of the intermittent contacts of the tip with the sample surface. The advantage of this mode is that soft samples can be scanned without damages. Also, the tip is protected because it is not in contact with the sample and subjected to less strong forces.

The last operating mode is called **non-contact mode**. It is quite similar to the previous mode in a sense that the cantilever oscillates near its resonant frequency but the amplitude of the oscillations are much smaller (few nanometers) and the cantilever remains in the attractive region. The forces in this region acts to decrease the resonance frequency of the cantilever, which combined with the feedback loop system maintains a constant oscillation amplitude or frequency by adjusting the average tip-to-sample distance. Measuring the tip-to-sample distance at each (x,y) data point allows the scanning software to construct a topographic image of the sample surface.

AFM was widely used to obtain the morphology of Si-based films since it is a technique giving good three-dimensional information and easy to use. The first use of AFM was to characterize easily the epitaxial layers' morphology, especially the facets and their corresponding angle without using TEM images. Indeed, TEM images are quite long and difficult to obtain.

Despite the ability to reach high spatial resolution, the acquired surface topography image can sometimes not correspond to the real surface features due to the effect of the instrument on the object resulting in the artifacts appearance. That is why, prior to any measurements, some questions must be addressed such as the probe's type to be used and which operating mode and parameters. Concerning the probes, it was required probes with the lowest front-side (FA) and backside angles (BA) and nominal tip radius in order to properly characterize the facets, e.g. the {111} facets with an angle of 54.7°. Different cases are shown in ***Fig. II-11***. In the figure, the dash lines represent the image profile of the studied object. If the FA and BA are too high the facets will not be resolved and it will be impossible to characterize the pattern's morphology. Second, the tip radius must be as low as possible. Indeed, in a case of a pattern as shown in ***Fig. II-11***, a non-appropriate tip radius will lead to an increase of the pattern's size (especially the top surface). In this case, it will not be possible to characterize, for example, the epitaxial lateral overgrowth. Moreover, a too high tip radius will not allow the facets located in between two walls (as depicted in ***Fig. II-12***) to be resolved. Finally, the choice of the appropriate probe was very important for the thesis since the morphology's study is the main axe of research. A good probe will allow to obtain AFM profiles the closest to reality.

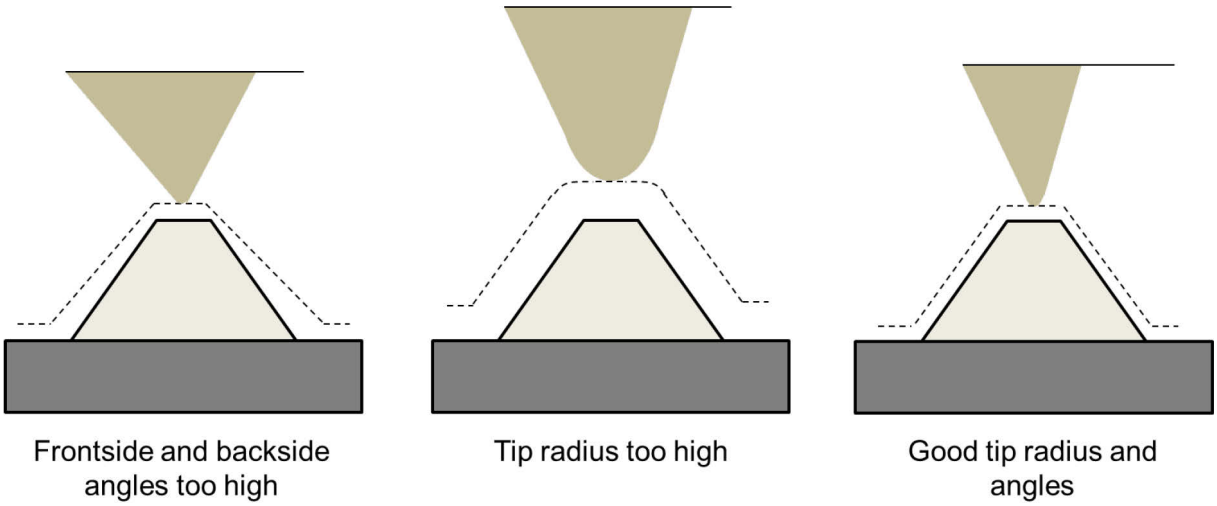

Fig. II-11*: Schematics of the studied object (here a pattern presenting {111} facets) for different probe's geometries. From left to right: the probe has FA and BA too high to resolve the facets, the probe has a too high curvature radius growing the pattern's size and an appropriate probe leading to a good morphological characterization. The dash lines represent the image profile of the object.*

Fig. II-12 shows the same object as previously but located in between two gates. The characterization of the structure is very critical even with a sharp tip. Indeed, for a layer much thinner than the gates, the tip cannot see the facets and make a profile of the top surface only. As a result, a solution is to grow thicker layers in a way that the thickness reaches (or goes over) the gates. In this case, the probe will be able to take a profile in between. Once again,

the curvature of the tip must be small to be capable of characterize this structure. It is obviously evident that a wall perpendicular to the surface (which is the case of {001} facets) cannot be resolved by AFM due the presence of FA and BA.

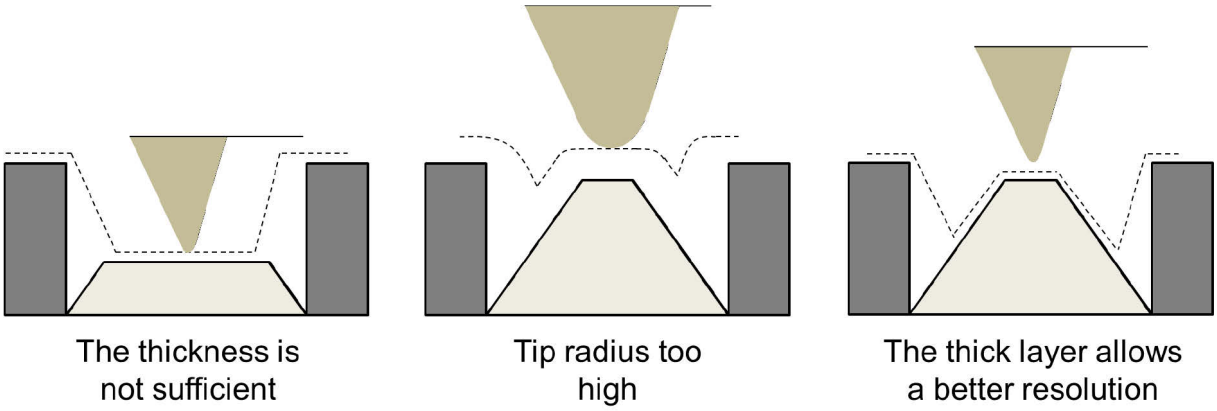

***Fig. II-12**: Schematics of the studied pattern presenting {111} facets located in between two gates for different probe's geometries and layer's thicknesses. In order to resolve the facets in this structure, a solution is to grow thicker layers.*

Two probes were then used depending on the sample to be characterized: TESPA and ScanAsyst from Bruker. These probes have a front angle of 25 ± 2.5° and a back angle of 15 ± 2.5° with a nominal tip radius of 8 nm. The TESPA were more suited to characterize the morphology and thus the facets, while the ScanAsyst were more suited to measure low roughness since it provides better repeatability. ***Fig. II-13*** below shows a SEM image of a TESPA AFM probe.

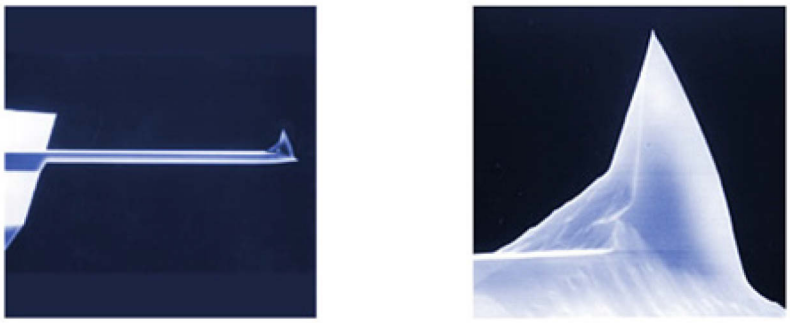

***Fig. II-13**: SEM image of a standard AFM probe. In this case, the probe is a TESPA probe from Bruker.*

Obviously, the main operating mode used was tapping mode since it is the most common operating mode and the less destructive. Also, it was possible to choose different scan's directions also called trace or retrace. These directions correspond to the back and forth movement of the probe during the scan, and as already mentioned both the front-side and backside angles are different, meaning that depending on the data used (trace or retrace) the measured angle will be different as well (only the case for angles higher to 75° with respect to the surface). For all the measurements, the retrace data were chosen since it provided better angle's measurements in between two walls. To obtain the largest number of points per area of interest with the least noise, the main used scan's size was 1 µm (or less) and the tip's

frequency used in the majority of case was 1 Hz. In addition, the scan's pattern was 512 x 512 (line x points per line). Moreover, it has the advantage to obtain images relatively rapidly (less than 9 min for one image). Finally, all the samples to be characterized were placed in a way that the pattern was (almost) perpendicular to the scan direction in order to obtain better measurements (e.g. of facets).

The microscope used for the studies on which this thesis is based is the Bruker Dimension FastScan. The Z sensitivity of this tool is less than 0.1 nm, thus all the raw data extracted from the tool (e.g. the roughness) are considered as very accurate and correct. However, the main disadvantages of AFM are that the tool is not located in the clean room (meaning that no return in clean room is possible after being outside) and the fact that an AFM image takes a certain to be acquired. As a consequence, the films were firstly observed and compared (if needed) in a Scanning Electron Microscope.

III.1.b) Scanning Electron Microscopy

An electron microscope uses a highly-energized electron beam as a source of illumination, allowing a much higher resolving power than a light microscope. As a result, the structure of smaller objects (from 1 to 100 nm) can be revealed. However, the use of electron obligates the inside of the electron optical system and the sample chamber to be kept at a high vacuum of 10^{-3} to 10^{-4} Pa. The Scanning Electron Microscope (SEM) is not only a morphology observation instrument but also a versatile instrument capable of performing elemental analysis. The working principle of SEM is based on the interactions of electrons with sample. When incident electrons penetrate the sample, they are scattered within the sample and gradually lose their energy until they are absorbed by the specimen. This behavior is given in ***Fig. II-14***. The scattering range of the electrons depends on the electron energy and on the specimen itself (atomic number of the elements inside the sample, the density of the constituent atoms…). The higher the energy, the larger the scattering range. On the contrary, the larger the density or atomic number, the smaller the scattering range.

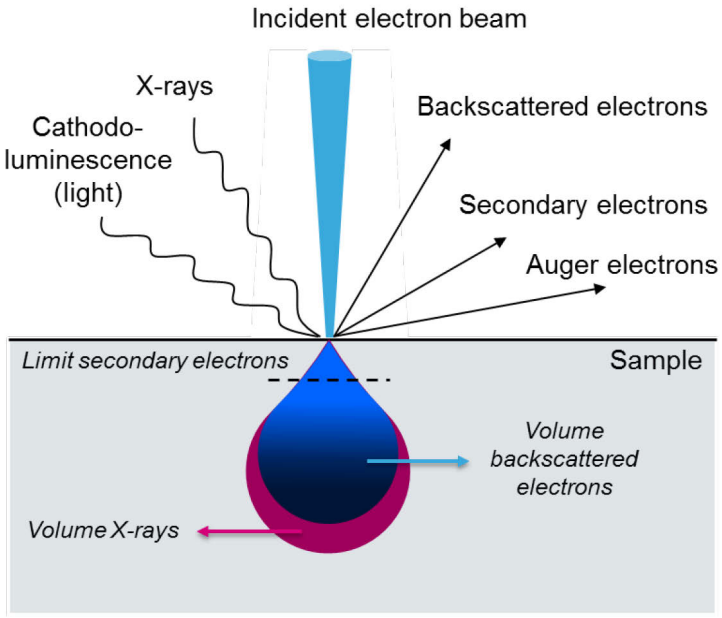

Fig. II-14*: Emission of several electrons and electromagnetic waves from the sample.*

Complex interactions of the beam electrons with the atoms of the specimen produce wide variety of radiation. There are two types of interactions: elastic scattering for which the kinetic energy of the particle is conserved; and inelastic scattering for which the particle loses energy. Various signals are emitted from the specimen when the incident electrons enter the sample. The SEM utilizes these signals to observe and analyze the sample surface, and to produce images. The main signals are the **secondary electrons**, the **backscattered electrons** and the **X-rays**.

SEM is often used in semiconductor industry in top view mode in a clean room environment. The main application is the measurement of “critical dimensions” (or CD) of lines after photolithography. 300mm wafers can directly be observed inside the SEM without any cleavage. In this work, most of the films after being deposited were firstly observed by top view SEM before being observed by AFM. This allowed to have a first information on the structure, the morphology and the quality of the deposited film. However, since AFM gives better images with more information on the topography, very few SEM images are presented in this work. The SEM-CD tool used is the Hitachi CG5000.

III.1.c) Transmission Electron Microscopy

TEM is a very powerful technique to get images with high resolution and information about chemical composition of materials down to the atomic scale. In this work, TEM analysis was used for the determination of the sample structure. Like SEM, TEM is also an electron microscope associated with a beam of electrons, which passes through a sample to be analyzed. The difference here is that the accelerating voltage is much higher in TEM (several hundreds of kV) as compared to SEM. As they pass through the sample, electrons interact in different ways with atoms, resulting in elastic and inelastic scattering of electrons.

The main drawback of TEM is the sample preparation which is quite long and difficult. Also, since working in an industrial environment, the access to TEM analysis was limited. Moreover, all the analyses were subcontracted and thus were not priority. As a consequence, for this work, TEM was used only to obtain the morphology of specific patterns, when AFM was not sufficient, and few TEM images were possible. The TEM was the FEI Tecnai.

III.2) Material characterization

III.2.a) Spectroscopic Ellipsometry

Spectroscopic ellipsometry (SE) is a non-perturbing optical technique for investigating surfaces and thin films based on the measurement of the change of light’s polarization after reflection on a given sample. It is non-destructive, easy to use, fast and cost effective, and allows the characterization of composition, roughness, thickness, optical indices (n and k) and other material properties. These are the main reasons why SE is widely used as a line measurement tool in semiconductor manufacturing.

The specimen to be analyzed is exposed to an incident monochromatic and polarized beam, and the state of polarization of the reflected light is analyzed. The polarization state of the light incident upon the sample may be decomposed into two components, one perpendicular to the plane of incidence, the second parallel to the plane of incidence. The complex reflection

coefficient of both components, *rs* and *rp* respectively, depends on the interaction with the material being investigated. The reflected radiation passes then through an analyzer before falling into the detector. The analyzer allows the measurement of these reflection coefficients. In practice, ellipsometry measures the complex reflectance ratio ρ, defined as the ratio of *rp* over *rs*, which expresses therefore the change in polarization between the incident beam and the reflected beam. The angle of incidence, θ, is chosen close to the Brewster angle of the sample to ensure a maximal difference in *rp* and *rs*.

$$\rho = \frac{r_p}{r_s} = \tan\psi\, e^{i\Delta} \qquad \text{Eq. II-1}$$

Where ψ is the amplitude component and Δ is the phase difference of the p and s linearly polarized components upon reflection. Because SE measures the ratio of two values, it can be highly accurate and reproducible. Moreover, since the ratio is a complex number, it also contains “phase” information, rendering the measurement very sensitive.

During an ellipsometry measurement, the normalized Fourier coefficient α and β are measured. They can be written as:

$$\alpha = \frac{\tan^2\psi - \tan^2 A}{\tan^2\psi + \tan^2 A}\ , \qquad \beta = \frac{2\tan\psi\cos\Delta\tan A}{\tan^2\psi + \tan^2 A} \qquad \text{Eq. II-3}$$

Where A is the orientation of the polarizer with respect to the plane of incidence.

The SpectraFx 100 manufactured by KLA Tencor was used for this work to determine the alloy composition and layer thickness of SiGe. These measurements were most of the time compared to XRD since XRD provides more accurate measurements of Ge content while (for thin layer < 10nm) SE is more accurate with respect to the thickness. The technique was also used to determine the Si growth rate and thickness. However, since most all the layers are grown on Si substrate a thin layer of SiGe, for which the thickness is known, must be grown before the Si layer. This SiGe layer acts as a marker allowing the determination of the Si layer’s thickness.

III.2.b) X-Ray diffraction

Based upon the scattering of x-rays, XRD has become the first technique for investigating the structure of crystalline materials, aiding in the new frontiers of nanotechnology. It is a well-known and established technique, which is essential in the field of thin films grown by means of epitaxy. Indeed, it allows very quickly to determine the quality of the epitaxial layer, since it is very sensitive to any defects located inside the material.

X-rays have wavelength is the same order of magnitude as the spacing between planes in the crystal, they produce a diffraction pattern when hitting the sample. Diffraction occurs when each object in a periodic array scatters radiation coherently, producing concerted constructive interference at specific angles. To produce significant diffraction, the wavelength of the wave and the spacing between the scatterers should be similar in size. In a crystal, the atoms are arranged in an ordered and periodic manner, lying on mathematical planes, designated by their Miller indices hkl. They scatter the X-ray waves, primarily through the atoms' electrons.

The strong peak of intensity that is produced by the coherent scattering of the atomic arrangement in a crystal is called the Bragg diffraction peak ad is obtained when the Bragg's law is satisfied (Eq. II-4):

$$2d_{hkl}\sin\theta_B = n\lambda \qquad \text{Eq. II-4}$$

Where n is the order of diffraction, λ is the wavelength of the incident X-ray beam, d_{hkl} is the atomic spacing and θ_B is the Bragg's angle for which a constructive interference can occur. ***Fig. II-15*** shows an incident x-ray beam interacting with the atoms arranged in a periodic manner. The atoms, can be viewed as forming different sets of planes in the crystal.

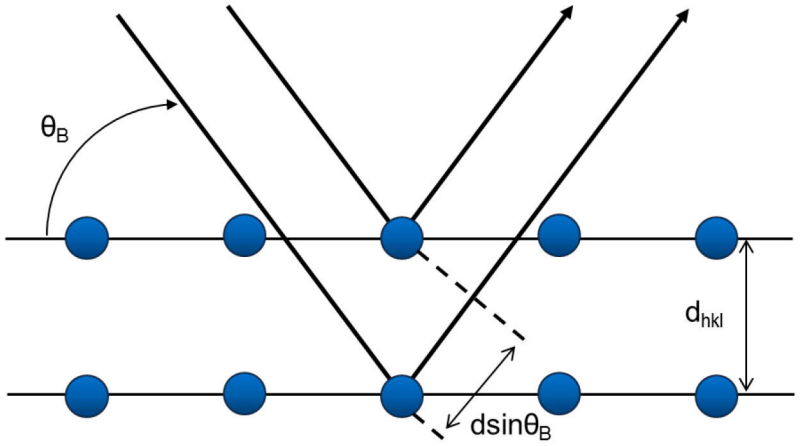

Fig. II-15*: Bragg's law. Two beams with identical wavelength and phase approach a crystalline solid and are scattered off two different atoms within it. The lower beam traverses an extra length of* $2d_{hkl}\sin\theta_B$*. Constructive interference occurs when this length is equal to an integer multiple of the wavelength of the radiation.*

The diffractometer used during this study for the characterization of SiGe and boron-doped SiGe layers is a high-resolution XRD (HRXRD) from Jordan Valley (JVX 7200). The advantage of this tool is that it was specially designed and optimized for small-spot and fast in-line measurements on product wafers provided by both a convergent beam and a linear 1D detector [Wormington 11]. An X-ray tube with a copper anode is used together with a doubly curved crystal (DCC) optic to generate the incident $Cu_{K\alpha}$ -X-ray beam (with wavelength of 1.54 Å). The beam is then focused before hitting the surface of the specimen. The background noise can be reduced by adding a shaper and slit collimators into the beam. In this configuration, the wafer is not rotated: in this case, the source and detector are moved to satisfy the nominal Bragg condition for the reflection of interest. The diffracted intensity is measured as a function of the incidence angle of the beam. A schematic diagram of HRXDR is displayed in ***Fig. II-16***.

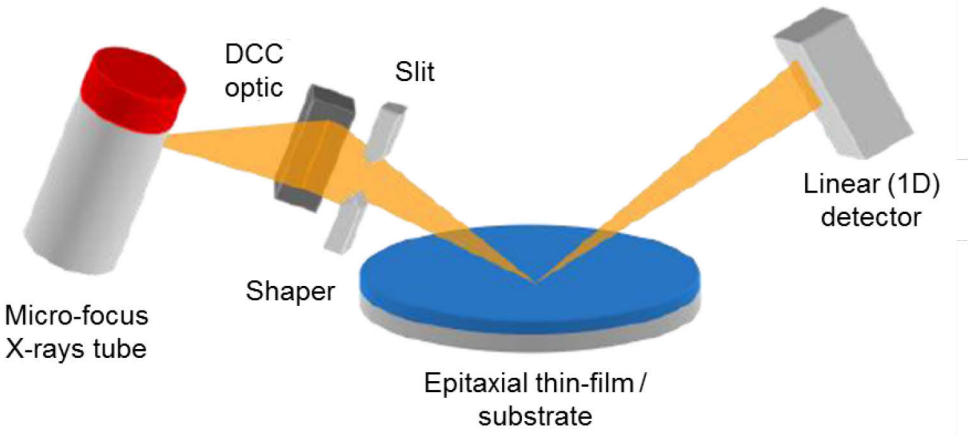

***Fig. II-16**: Schematic diagram of HRXRD from Jordan Valley. Image taken from [Wormington 11].*

For XRD on silicon and/or germanium, the Bragg peaks from symmetric (004) and asymmetric (224) Miller planes are the most commonly used. Both peaks are useful since they allow the size of both in plane and out of plane lattice parameters to be determined. In our case, only the (004) Miller plane is used. For an orthorhombic lattice, the spacing distance d_{hkl} is calculated via Eq. II-5:

$$d_{hkl} = \frac{1}{\sqrt{\frac{h^2}{a^2} + \frac{k^2}{b^2} + \frac{l^2}{c^2}}} \qquad \text{Eq. II-5}$$

Where *hkl* are the Miller indices, and a, b and c the lattice constants of the material. In the particular case of a fully-relaxed SiGe(:B) epitaxy, Eq. II-6 is reduced to eq. II-7, since a=b=c:

$$d_{hkl} = \frac{a}{\sqrt{h^2 + k^2 + l^2}} \qquad \text{Eq. II-7}$$

However, for a fully strained SiGe(:B) epitaxy, c has to be considered since it is larger than $a_{Si} = a^{//}_{SiGe}$ (defined as the out-of-plane lattice constant $a^{\perp}_{SiGe}$, *see Chapter 1 I.2) SiGe crystalline properties*), and a = b = a_{Si}. In an XRD rocking curve (see ***Fig. II-17***), the germanium content makes the SiGe peak's position move to lower scan angle (to the left on the (004) Si peak); in other words the Ge concentration is determined by the position of the SiGe peak with respect to the Si peak. On the contrary, when incorporating boron in the SiGe lattice, the SiGe peak shifts to higher angles. This effect is due to strain compensation and will be discussed more in details in *Chapter 5 I/* . From the lattice constants, the Ge content can be deduced from the Dismukes' law, as mentioned in the *Chapter 1-I*.

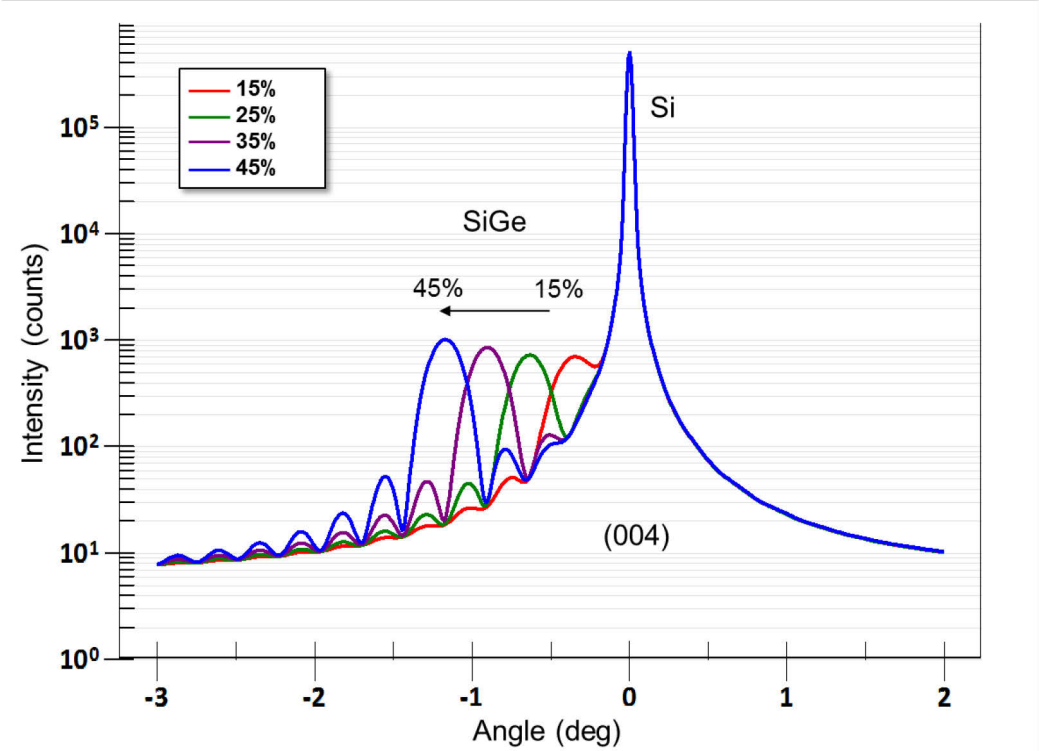

***Fig. II-17**: Theoretical rocking curves for 20nm SiGe grown on Si (001) substrate. The germanium content varies from 0.15 to 0.45. This makes the SiGe peak moves towards lower angles.*

III.2.c) Model Based Infrared Reflectometry

Model Based Infrared Reflectometry (MBIR) from Semilab was used in this study to obtain the carriers' dose and concentration in boron-doped SiGe layer grown on patterned wafers: the system allows the measurement in small boxes area with dimensions of 100 x 52 µm². The technique uses an infrared light with a wavelength comprises between 0.9 and 20 µm. For this range of wavelength, the silicon is transparent. Noise reflection from the backside on the wafer is not taken into since it is blocked thanks to the optical configuration of the instrument, providing a real accurate measurement of the top layer. Thus, the technique is based upon the measurement of the light reflection on the sample to be investigated and the reflectance R of the sample is measured thanks to an IR detector. Also, a silicon wafer is used as a reference to remove the perturbing elements detecting by IR spectroscopy (such as H_2O or CO_2). In the IR range, the dielectric constant, ε, of the doped material can be approximated by a mixture of the silicon background material and a Drude dispersion term (Eq. II-8 below).

$$\varepsilon(\nu) = \varepsilon_{Si}(\nu) - \frac{4\pi N q^2}{\nu^2 + i\nu\gamma}/(2\pi c m^*) \qquad \text{Eq. II-8}$$

Where v is the wavenumber (cm^{-1}), N is the concentration of the activated carriers (cm^{-3}), q the elementary charge ($1.6x10^{-19}$ C), m* the effective mass of the carrier (kg), and γ the carrier scattering rate (cm^{-1}). The reflectance is very sensitive to the active dopant concentration. Indeed, the more the active dopants, the more the reflectance, as shown in ***Fig. II-18***.

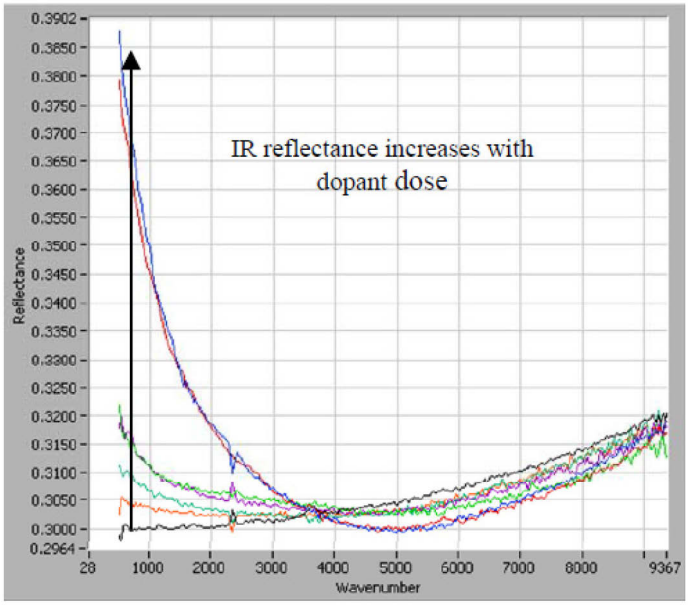

***Fig. II-18**: MBIR measurements giving the reflectance as a function of wavenumber of boron-doped SiGe layers for various concentration of boron. Image taken from [Duru 13]*

The output parameter of the model used was the boron active dose (in at/cm²). The carrier concentration was obtained by measuring the thickness of the layer (by means of XRD or ellipsometry) and calculating the division of the dose by the thickness.

III.2.d) X-Ray Fluorescence

X-ray fluorescence (XRF) is a non-destructive technique used for qualitative and quantitative chemical analysis of materials. A specimen is irradiated by an X-ray source to cause the elements in the specimen to emit their characteristic X-rays fluorescence. A detection system is then used to measure the position and the intensity of XRF peaks. The principle of the fluorescence in a material is the following. When a material is excited by short wavelength X-rays, one or more electrons may be ejected from the atom leaving one or more holes in the inner orbital rendering the electronic structure of the atom unstable. This phenomenon is called ionization. As a result of this ionization, electrons from higher orbitals drops into the holes left behind. This replacement of electrons manifests by the emission of a photon whose energy is equal to the energy difference of the two orbitals involved. Thus, radiations emitted from the material, have an energy characteristic of the atoms present.

In this study, XRF was used to determine the germanium concentration of boron-doped SiGe layers, since the conventional spectroscopic ellipsometry and XRD techniques were not sufficient to obtain the “real” concentration. Indeed, in the case of XRD measurement, the boron shifts the SiGe peak to higher angle (see *Chapter 5 II)* resulting in a decrease of the “apparent” Ge concentration. XRF measures a number of atoms in the layer which allows an exact Ge concentration to be obtained. To do so, a calibration curve of the signal’s intensity as a function of germanium dose was first needed. An advantage with this technique is that the Ge intensity and the Ge dose are proportional, which means that only two points are needed for this calibration curve, e.g. a known SiGe layer (thickness and XGe measured by SE or XRD) and a Si substrate without grown SiGe. Knowing the Ge content of the first layer, the

lattice parameter can be calculated with the Dismukes' equation (given in Eq. I-2 in Chapter 1-I). The total number of atoms (in cm^3), N_{tot}, in SiGe can then be estimated by:

$$N_{tot} = \frac{8}{a_{SiGe}^3} \quad \text{Eq. II-9}$$

The volume's contraction due to the strain is not taken into account in this formula. Finally, the dose (in at/cm^2) can be extracted with the following formula:

$$D = XGe * th * N_{tot} \quad \text{Eq. II-10}$$

Where *XGe* is the Ge content comprises between 0 and 1, and *th* is the thickness of the reference SiGe layer.
The calibration curve is obtained by plotting the Ge intensity (XRF) as a function of the Ge dose calculated via Eq. II-10. Secondly, the total number of atoms (in at/cm^3) was plotted as a function of the Ge concentration *[Ge]* in SiGe lattices. The total number of atoms is obtained thanks to the Dismukes' equation for Ge contents XGe arbitrarily chosen (e.g. between 0 and 1) and Eq. II-9. The Ge concentration *[Ge]* is then obtained by:

$$[Ge] = XGe * N_{tot} \quad \text{Eq. II-11}$$

With these two curves it is now possible to measure the XGe_{SiGeB} of the investigated SiGe:B layer. Indeed, with the Ge intensity measured by XRF and the calibration curve, the Ge dose (D_{SiGeB}) can be extracted. This allows the Ge concentration $[Ge]_{SiGeB}$ to be obtained, knowing the sample's thickness (th_{SiGeB}) by:

$$[Ge]_{SiGeB} = {}^{D_{SiGeB}}/_{th_{SiGeB}} \quad \text{Eq. II-12}$$

Finally, the XGe_{SiGeB} can be calculated knowing the total number of atoms (corresponding to the measured $[Ge]_{SiGeB}$) by:

$$XGe_{SiGeB} = {}^{[Ge]_{SiGeB}}\Big/_{N_{tot,SiGeB}} \quad \text{Eq. II-13}$$

III.2.e) Secondary Ion Mass Spectroscopy

Secondary Ion Mass Spectroscopy (SIMS) is a technique used to characterize the chemical composition of thin films by sputtering the surface of the layer by a focused ion beam, and collecting and analyzing the ejected secondary ions. The ratio of the mass over the charge of these secondary ions is then measured to determine the element, or isotopic composition of the surface. A depth between 1 and 2 nm can be scanned. However, the depth is not an accurate measurement; that is why the sputtering time is more commonly used. SIMS was used for determining the total concentration of boron in SiGe layers to be then compared with MBIR measurements. The boron measurement at very high concentration is an extrapolation of low doping measurements.

III.2.f) X-Ray Photo-Electron Spectroscopy

The X-Ray Photo-Electron Spectroscopy is non-destructive surface (from 1 to 10 nm) characterization technique based on the study of the kinetic energy's distribution of the photoelectrons ejected from a sample after irradiation by X-rays having a known energy hv. The photons' energy is focused with a monochromator around the $K_{\alpha 1}$ peak of Al, at 1487eV ±0.115eV. The XPS principle is defined by the conservation of the incident photon's energy given in Eq. II-14.

$$h\nu = E_K + BE + \phi \qquad \text{Eq. II-14}$$

With hv being the incident photon's energy, E_K the kinetic energy of the photoelectron, BE the binding energy of the state previously occupied by the electron and ϕ is the Fermi level mismatch between substrate and detector.

During this work, XPS was used first to characterize the SiGe surface passivation by Si atoms and especially the passivation layer's growth kinetics. Second, it was used to characterize the SiGe wetting layer after annealing at relatively high temperature. To do so, the intensities of two Ge's peaks of different energies were used: the $Ge2p_{3/2}$ and Ge3d photoelectrons located at theoretical binding energies of 1217 eV and 29 eV, respectively. The $Ge2p_{3/2}$ is more surface sensitive since it is located to lower kinetic energies (higher binding energies). It was then more suited to characterize the very thin layers. On the contrary, the Ge3d photoelectron being located to higher kinetic energies (or lower binding energy) is more depth sensitive and thus more appropriate to study thicker films. The mean free path of the $Ge2p_{3/2}$ and Ge3d photoelectrons in Si (obtained by [Tanuma 94] are 9.19 Å and 32.3 Å, respectively. The films' characterization is based on the peak's area measurement and especially on the variation of the area after different process' steps.

IV/ Conclusion

To conclude this chapter, it was seen that prior any growths, the surface must be cleaned and decontaminated. During this thesis, it was done through a plasma cleaning in a SiCoNi chamber.

In a second part, the epitaxy equipment from AMAT was described. This was followed by the tuning of very important parameters for the temperature's control. These parameters are the PID constants and the lamp ratios. It was shown that with adapted and optimized PID constants, the temperature overshoot can be completely suppressed, and the temperature can stabilize much faster than for non-appropriate PID constants. In the other hand, it was demonstrated that the lamp ratios have a real impact on the top pyrometer's reading. For a given pressure in the chamber, variations of more than 40°C can be reached by changing e.g. the lamp ration from 73% to 53%. Moreover, it was shown that the chamber's pressure can also change a lot the top pyrometer's reading. This variation must be taken into account when the pressure must be changed during a process but the temperature must remain the same. This will the case in the Chapter 4, when dealing with different annealing pressures. Finally, it was observed that there is a particular lamp ratio for which the pressure's dependence on the top temperature does not exist. In this particular case, this was obtained for a lamp ratio of about 58%.

The third part was devoted to the characterization techniques. For the morphology's characterization, the AFM was the main tool used during this thesis. Many different questions were addressed concerning the best method to measure with a good accuracy the facets in the epitaxial layers. The scan's direction and frequency, the probe's nature, etc., were consequently chosen with that perspective. The SEM and TEM techniques were also used. Concerning the material's characterization, SE and XRD were used to measure the thickness, XRF, MBIR and SIMS for the Ge and B concentration, and XPS for the Si passivation kinetics.

Chapter 3

As-deposited epitaxy

The continuous transistor scaling has led to the apparition of new effects concerning the epitaxy's morphology due to the objects' small size. As a result, the control of the epitaxy's morphology is of great importance in microelectronics since it become one of the main crucial factor to improve the devices' performances.

The third chapter is devoted to the as-deposited epitaxies' morphology and the main effective methods to maintain the morphology. First, some backgrounds on the faceting phenomenon and the anisotropies that are involved will be given. Then, the morphology of as-grown epitaxies in different size patterns are shown. The dimensions vary from several tens of micrometers to tens of nanometers. Third, the notion of surface passivation by silicon atoms is defined and studied using a dichlorosilane chemistry. This will lead to the quantification of the passivation's kinetics using XPS for two different temperatures. Finally, the use of passivating the surface in two different applications will be discusses and it will be proven that in some cases, the passivation is mandatory to preserve the morphology.

I/ Faceting phenomenon

In this part, the morphology of the as-deposited epitaxies is presented. Different patterns of different sizes will be shown. It is important to keep these morphologies in mind since they will be further discussed. Some background is also given in terms of faceting and anisotropic loading effect, especially in SiGe epitaxy.

Faceting background.

Faceting has been reported in epitaxy processes and especially in selective epitaxy growth (SEG), where the appearance of {111}, {113} and {110} is widespread. It is then of great concern in crystal growth because the growth rate of facets varies with their crystallographic orientation. Facet formation makes possible the fabrication of new nanoscale structures for metal-oxide-semiconductor (MOS). However, the faceting mechanism is very complex and is not totally understood. Usually, the formation of facet is described by the Wulff construction and corresponds to the thermodynamic equilibrium shape of crystals. Nevertheless, in selective epitaxial growth the observed facets are not necessarily an equilibrium state of crystal since they depend on the process conditions. Indeed, the lowest kinetics facets limit the growth along this direction and thus are the ones that can be observed. As a result, the crystalline planes' anisotropic growth is the origin of the observed faceting.

The most important facets already seen in literature are the {311} and {111} facets. These two facets may co-exist in a same growth but depending on different parameters such as temperature or the selectivity of deposition, one of them will be preferred. For instance, it has been seen by Dutartre *et al*. [Dutartre 06] that at 700°C (30% Ge) {311} facets start to propagate. However, at lower deposition temperature (of about 600°C), the {311} facets fade away until they completely disappear and give way to {111} facets. The authors explain this phenomenon by the change of growth rate anisotropy at elevated lower temperatures.

Other results have been done by Talbot *et al*. [Talbot 04]. Indeed, the authors highlighted the SiGe faceting and focused on the comparison between Si and SiGe SEG, as illustrated in ***Fig. III-1*** (Scanning electron microscopy (SEM) images). In particular, they showed the morphology of Si and SiGe SEG deposited in similar conditions at 750°C. We can clearly observe that the morphology is completely different. In the case of SiGe SEG, {111} and {311} facets rapidly propagate whereas no facets can be seen in Si SEG. They also estimated the kinetics of the different planes. To do so, they defined r_{111} and r_{311} as ratios of the growth rate (GR) between {111} and {311} planes, and (001) ones, respectively. Their results are the following: 0.48 for r_{311} and 0.23 for r_{111}. It means that the GR is higher for {311} than for {111}.

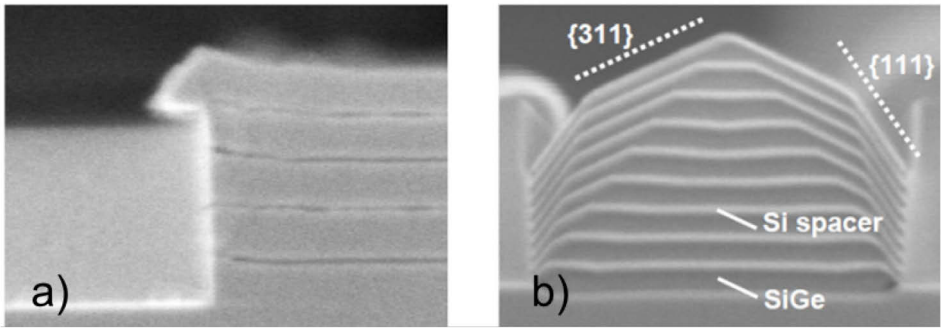

Fig. III-1: *SEM cross-section of SEG on Si/SiO2 patterned wafers at 750°C a) Si and b) SiGe. [Talbot 04].*

Faceting's phenomenon was studied by Pribat *et al.* [Pribat 11]. For their studies, epitaxial layers of SiGe made of 20% of Ge were grown by RT-CVD technique in a non-selective epitaxy growth (NSEG) way. Two types of substrate (P1 and P2) with <110> oriented patterns were used as given in ***Fig. III-2***. P1 presents a surface morphology made of (001)-(110)-(001) planes. P2 substrate is made of (001)-(111)-(113)-(001) planes.

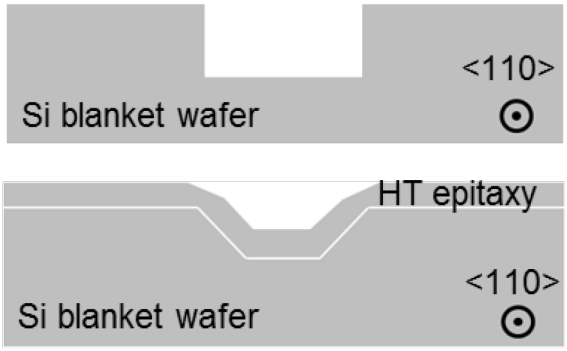

Fig. III-2*: Above: P1 substrate made of (001)-(110)-(001) planes. Below: P2 substrate made of (001)-(111)-(113)-(001) planes, from bottom to top.*

The morphology of SiGe growth at various temperatures is presented in the SEM views (***Fig. III-3***). They observed in the low temperature range (500°C) a good and flat epitaxy on (001) surface. On the contrary, on the other surfaces, there is an isotropic formation of a quasi poly-crystalline material which disappears when temperature increases. On P2 substrate and in the same temperature range, steps appear on {113} plane which may be attributed to Stransky-Krastanov (SK) effect.

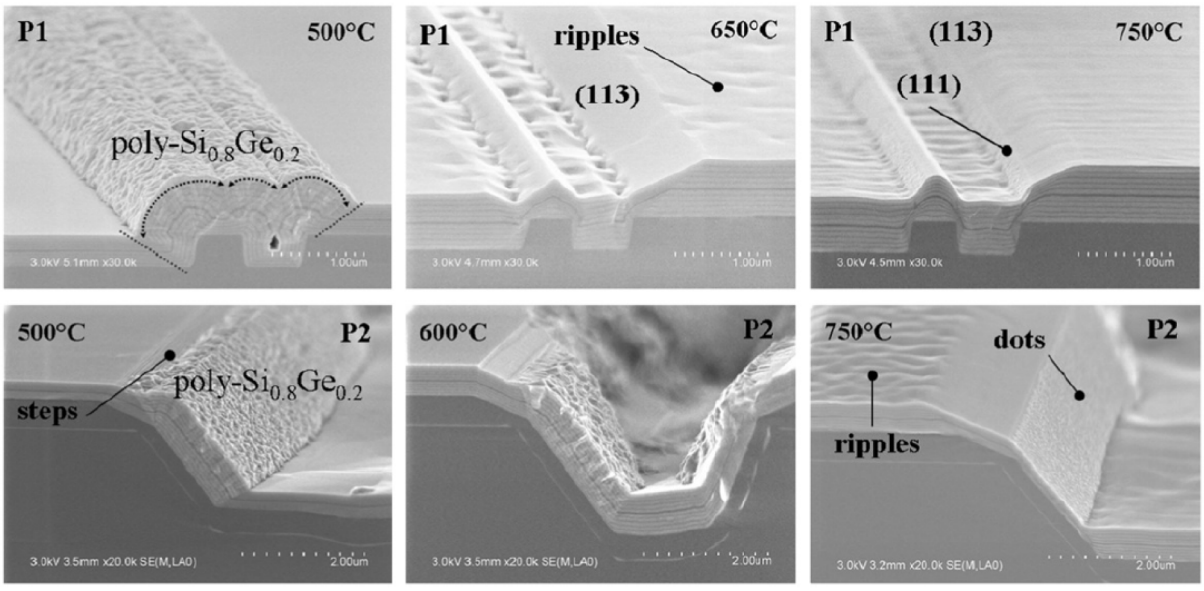

Fig. III-3*: SEM views of SiGe alloy n-SEG grown on P1 and P2 substrates at different temperatures. The morphology and the crystal quality depend on the crystal orientation but also on the temperature. Defects (ripples on (001) surface and dots on (111) plane) are still present at 750°C. Furthermore, at high temperature the {111} and {113} facets are dominant, whatever the substrate considered [Pribat 11].*

On P1 structure, when increasing the temperature (650°C), {111} and larger {113} facets are created from the initial (001)-(110) surface, making the initial (110) plane disappear. As a consequence, the surface morphology after the epitaxial growth completely changed and is made of (001)-(111)-(113)-(001) surfaces from bottom to top, with dominating {113} facets. Another point is the (001) surface which seems to be undulated. These kinds of undulations can once again be attributed to SK growth mode. At 750°C, the {111} facets are more pronounced at the cost of {113} facets.

Several other studies were performed by Loubet *et al*. [Loubet 10]. For instance, they studied the impact of HCl partial pressure on the RSD epitaxy shape. To do so, they used a standard chlorinated chemistry using direct injection of SiH_2Cl_2 (DCS)/HCl. The temperature range of 750°C - 800°C was studied at constant DCS mass flow but with various HCl concentrations. ***Fig. III.4*** a) and b) shows the influence of HCl partial pressure. Epitaxy shape is modified from flat to faceted while the DCS/HCl ratio decreases from 1.2 to 1.0. Therefore, HCl gas is the main parameter which controls the facet extension. Then, faceted epitaxies may be obtained for a wide range of temperature playing on this parameter as we can see in ***Fig. III-4*** b) and c). Here again, it was proved that only {311} facets are present for high temperatures but starts to fade away when the temperature decreases until their disappearance. At this point (750°C) only a flat epitaxy delimited by (100) planes is observed.

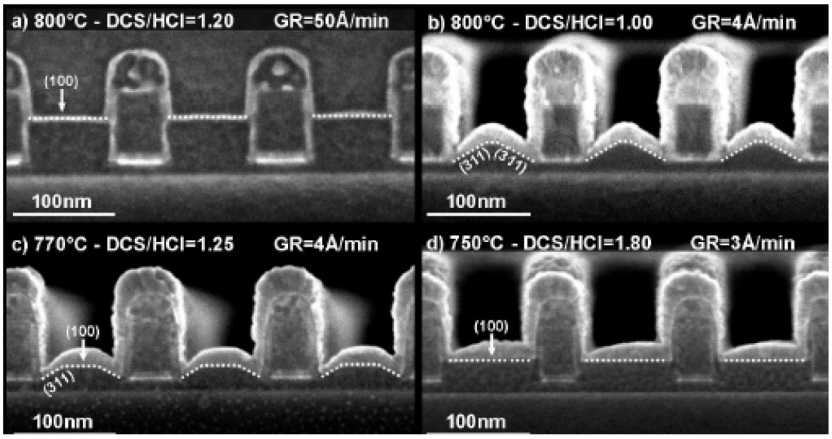

Fig. III-4*: SEM cross section after RSD using standard DCS/HCl/H2 gas mixture. a) DCS/HCl ratio=1.20, b) DCS/HCl ratio=1.00 at 800°C, c) DCS/HCl ratio=1.25 at 770°C and d) DCS/HCl ratio=1.80 at 750°C. The temperature and HCl partial pressure change the morphology. [Loubet 10]*

Anisotropic loading effect (ALE) background

ALE in selective SiGe epitaxy was extensively studied by Dutartre and Seiss [Dutartre 12] [Seiss 13-4]. For this study, both <100> and <110> orientations were investigated. ***Fig. III-5*** shows high resolution Transmission electron microscopy (TEM) images of SiGe epitaxy. The growth was performed with a mixture of DCS, GeH_4 and HCl gases with H_2 as carrier gas. The deposition was carried out at 620°C. Film thicknesses of 19nm with 27% Ge were obtained. The observed morphologies are totally different: there is formation of {100} facets for <100>-oriented patterns whereas in the case of <110>-oriented patterns the {111} facets are present. Another result is the lateral overgrowth in both cases. For <100> oriented patterns, this overgrowth is equal to the growth thickness. Actually, it is clear in ***Fig. III-5*** a). However, the

lateral overgrowth is less pronounced for the <110> orientation and it was shown that it is equal to 0.4 time the thickness and the growth kinetics as compared to the {001} plane is 0.32.

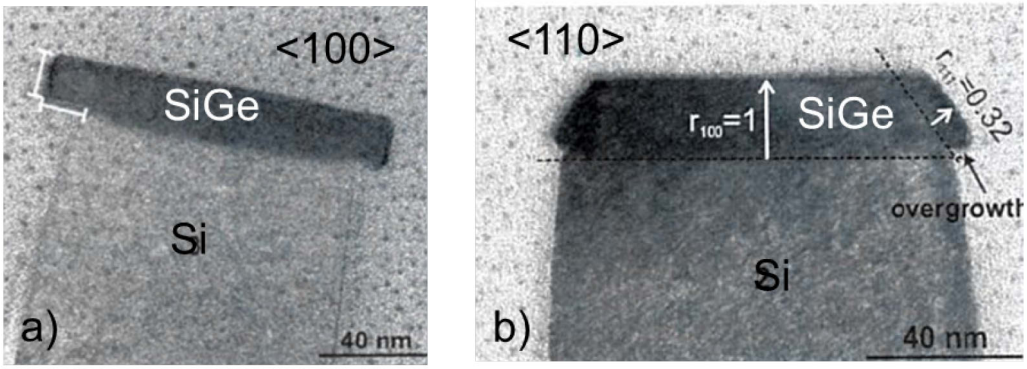

Fig. III-5*: Magnified TEM bright field image of a) <100>-oriented patterns and b) <110>-oriented patterns. The lateral overgrowth is larger for concave edges. [Dutartre 12]*

Due to this anisotropy in faceting, ALE was introduced and corresponds to an orientation-dependence of effective thickness. Indeed, it is described that the effective thickness, defined as the ratio between SiGe grown volume and initial Si active area, is much higher for <100> orientation compared to <110>. The comparison between both orientations in term of effective thickness is given in ***Fig. III-6***. The study was made in lines of different widths for a nominal SiGe thickness of 20 nm. It is well visible that the effective thickness increases faster with decreasing line width in the case of <100> oriented lines.

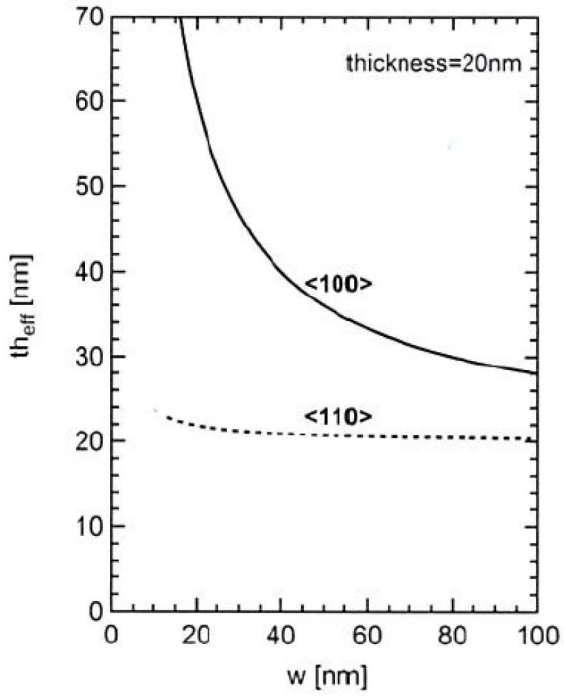

Fig. III-6*: Comparison of effective thickness (th_{eff}) between both orientations <100> and <110> as a function of line width w. The thickness of the film is 20nm. th_{eff} increases much faster for <100> than for <110>. [Seiss 13-4]*

Another study by the same author deals with the time non-linear loading effect and refers to the fact that the effective thickness of a certain object increases non-linearly as a function of time. This effect is present for both orientation but is more important for <100>-oriented lines. It means that during a process, more matters are deposited at the end than at the beginning. The obtained results are given in ***Fig. III-7***. The linear growth rate of a blanket wafer, similar as in large pattern (in dashed line) is also given as a reference.

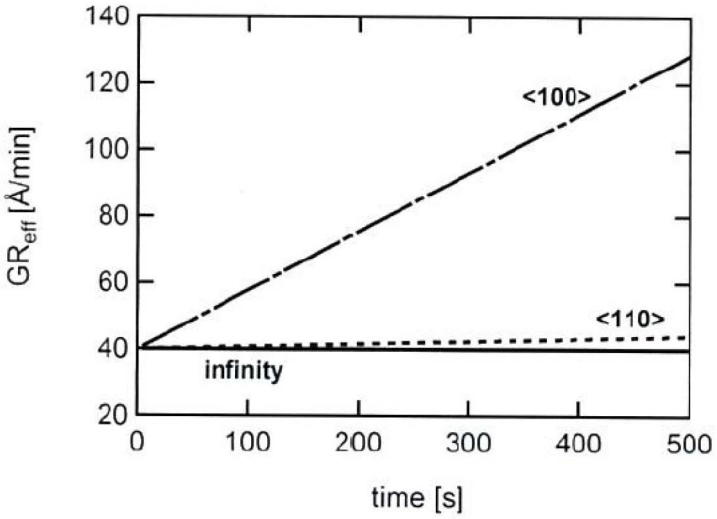

Fig. III-7*: Comparison of effective growth rate as a function of time for a 30nm wide line oriented along <100> or <110>. The growth rate increases linearly with time for both orientations. However, it is more pronounced for <110>. The "infinity" continuous line represents the constant growth rate for a blanket wafer. [Seiss 13-4]*

Finally, the fact that the Ge concentration into the epitaxial SiGe layer depends on the crystal orientation of the line is called anisotropy chemical loading effect. It was shown that the Ge content is homogeneously distributed for <100>-oriented lines. In contrast, a higher Ge content is found next to the {111} facets for <110>-oriented lines. It results in a higher average Ge concentration on <110> orientation. This study is very important for Si-based technologies. It is well-known the Ge content is an important parameter in term of device performance. Indeed, by modulating the Ge content and therefore the band gap, the threshold voltage tuning can be performed. The introduction of SiGe channel was used for this reason.

II/ Kinetics of Si and SiGe's growth's kinetics

All the Si or SiGe growths studied during this thesis were performed in the industrial EPI Centura 300 of AMAT. The DCS was used as Si precursor. The GeH_4 and HCl are added in the chamber for SiGe growth, respectively as Ge precursor and to maintain the selectivity. The carrier gas was H_2. The Si layers were grown at a total pressure of 20 Torr at 715°C. The SiGe layers were grown at a pressure of 20 Torr at 610°C or 630°C. Both temperatures were used to further study the influence on the Si passivation kinetics (*see Chapter 2 – IV*). This preliminary part gives the growth's kinetics for both Si and SiGe on patterned wafers as a function of DCS partial pressure (for Si growth, see ***Fig. III-8***) or GeH_4 partial pressure (for SiGe growth, see ***Fig. III-9*** and ***Fig. III-10***). The XGe as a function of the GeH_4 pressure is also plotted.

For Si growth at 715°C, the GR increases from 23 Å/min to 40 Å/min while increasing the DCS partial pressure from 3.84 mT to 14.6 mT. The DCS partial pressure used in this manuscript was 68 mT corresponding to a GR of 34 Å/min.

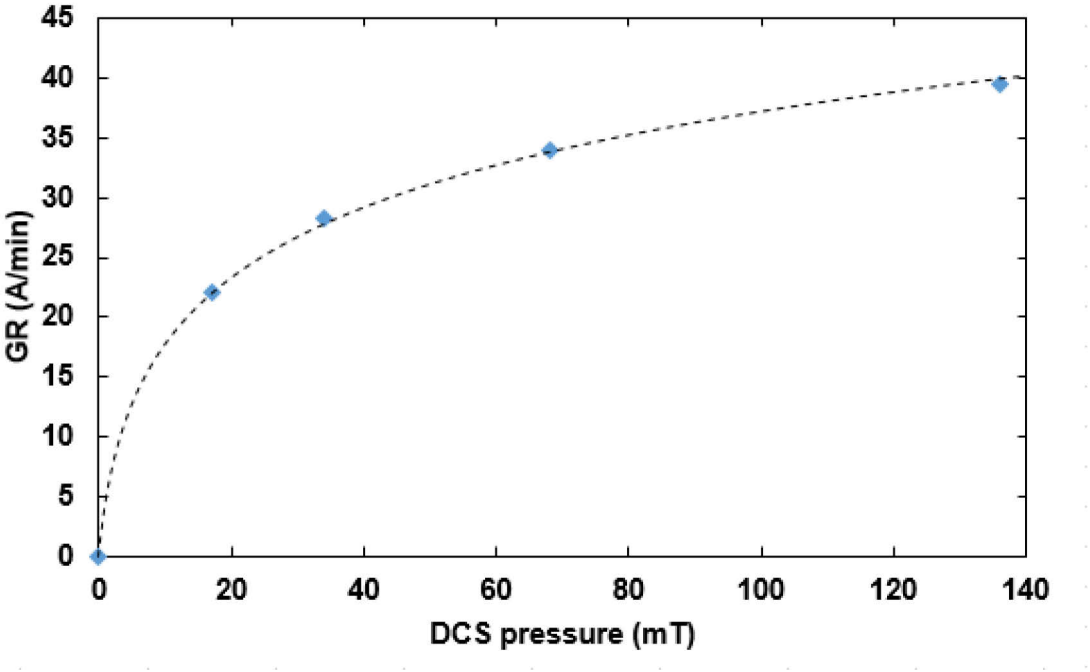

***Fig. III-8**: Si growth rate as a function of DCS partial pressure. The growth temperature is 715°C.*

The GeH_4 pressure's influence on the SiGe GR and the XGe is given in the figures below. ***Fig. III-9*** corresponds to SiGe layers grown at 630°C and ***Fig. III-10*** corresponds to SiGe layers grown at 610°C. At 610°C, the DCS and HCl partial pressures were adjusted so that the selectivity was maintained and the GR was relatively high enough. Indeed, growths at 610°C were performed with the same HCl and DCS mass flows (DCS = 50 sccm and HCl = 25 sccm) for GeH_4 partial pressures of 7.79 mT and 14.6 mT. For a partial pressure of 14.6 mT, the GR dropped to 32.4 Å/min (compared to 70.9 Å/min at 630°C) and the Ge content was 35%. For a partial pressure of 7.79 mT, the GR fell down to 1 Å/min (compared to 33.7 Å/min at 630°C) and the Ge was about 30%. Since a Ge content of 25% was needed, a continuous decrease of the GeH_4 pressure will lead to a too low GR which is not acceptable. In order to continuously decrease the XGe while keeping a GR high enough, the DCS and HCl partial pressures were adjusted: the DCS flow was increased to 200 sccm and the HCl flow to 50 sccm.

Regarding both temperatures, the GR increases with increasing the GeH_4 partial pressure. At 630°C, it increases from 2 Å/min to 70.9 Å/min, and at 610°C, it increases from 5.6 Å/min up to 9.4 Å/min. This is due to the catalysis of H desorption from the surface by Ge atoms, freeing sites for growth. Concerning the XGe, at 630°C it increases from 23% to 33% and at 610°C it increases from 23% to 28%. During this work, the SiGe 25% layers were grown either at 630°C or at 610°C using a GeH_4 partial pressure of 3.84 mT (GR = 13.3 Å/min) or 10.18 mT (GR = 7.5 Å/min), respectively. The SiGe 31% layers were grown at 630°C using a GeH_4 partial pressure of 7.79 mT (GR = 33.7 Å/min).

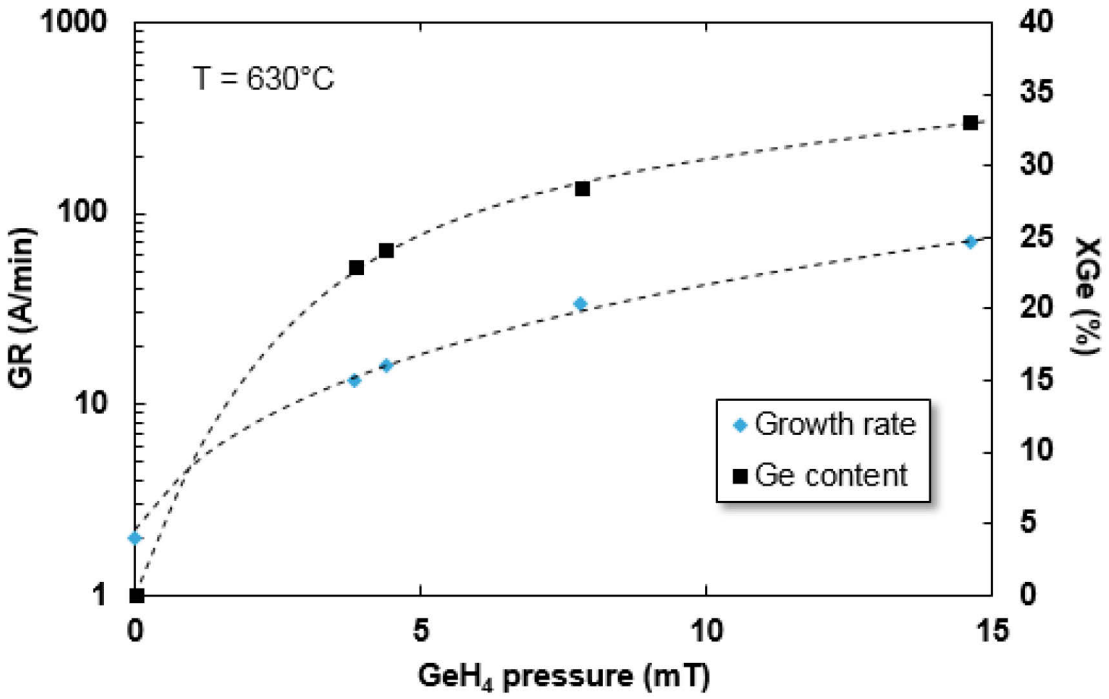

***Fig. III-9**: SiGe growth rate and Ge concentration as a function of GeH_4 partial pressure. Growth at 630°C. DCS = 50sccm, HCl = 25sccm.*

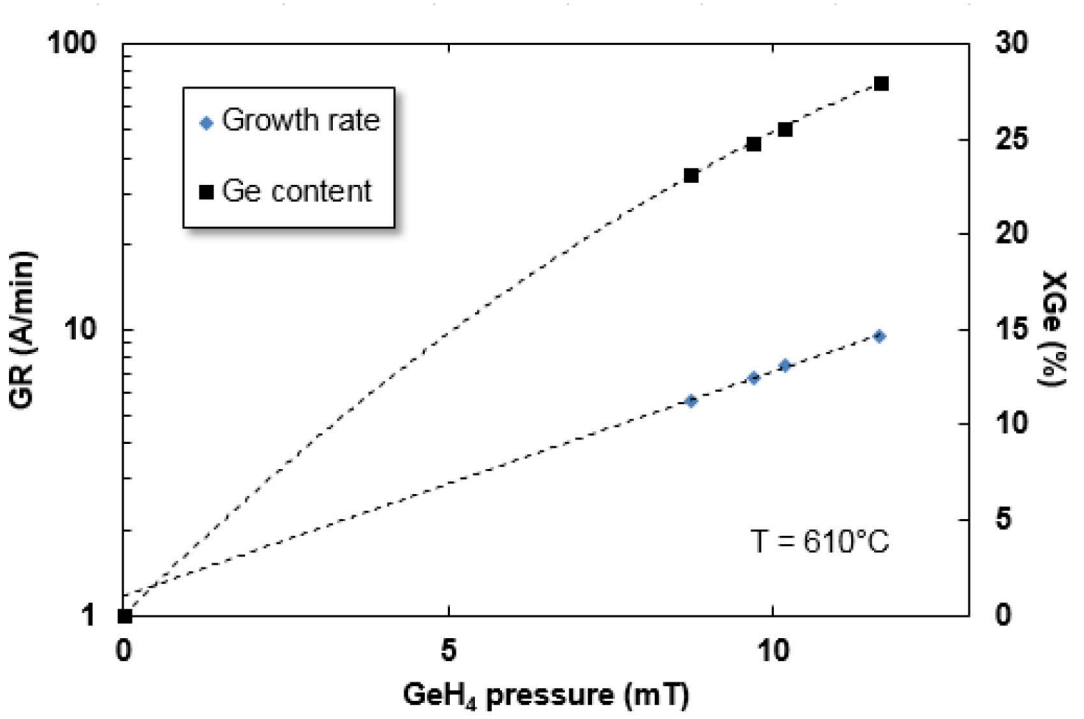

***Fig. III-10**: SiGe growth rate and Ge concentration as a function of GeH_4 partial pressure. Growth at 610°C. DCS=200sccm, HCl=50sccm.*

III/ Morphology of as-deposited Si-based epitaxy

The as-deposited morphology was also observed in details in this thesis to get some references for the following studies. Selective growth of the as-deposited samples was realized in the EPI Centura 300 of AMAT. The chemistry was a mixture of DCS, GeH_4 and HCl gases with H_2 as carrier gas. The SiGe layers were grown at a total pressure of 20 Torr at 630°C. As soon as the as-deposited morphology is studied, it is essential to avoid any post-deposition thermal treatments on the sample that can lead to morphological evolution. To do so, the DCS is left in the chamber after the growth process i.e. during the post-growth purge and the temperature decrease before the wafer unloading. This allows a very thin Si-passivation layer to be grown reinforcing the SiGe layer to thermal budget. Therefore, the observed morphology corresponds to the as-deposited state.
Then the films are characterized in terms of thickness and Ge content by means of ellipsometry and XRD. Finally, top-view SEM and AFM are used to study the morphology in several patterns. To note that all the given dimensions are the active area's dimension, i.e. before any growth.

The first pattern corresponds to large boxes (100 x 50 µm²) in which the epitaxial growth behaves like on blanket wafer. Most of the measurements (ellipsometry and XRD) are performed in these boxes. The term morphology is not suited in these structures thus the Root-Mean-Square roughness (R_{RMS}) will be the main parameter. Whatever the wafer's orientation, the {001} surface is observed with a typical R_{RMS} smaller than 0.15 nm as shown by the AFM image in ***Fig. III-11*** below. In this figure, a 20 nm SiGe layer was grown with a Ge concentration of 25%. The R_{RMS} is equal to 0.10 nm. The R_{max} parameter represents the difference between the minimum and the maximum values.

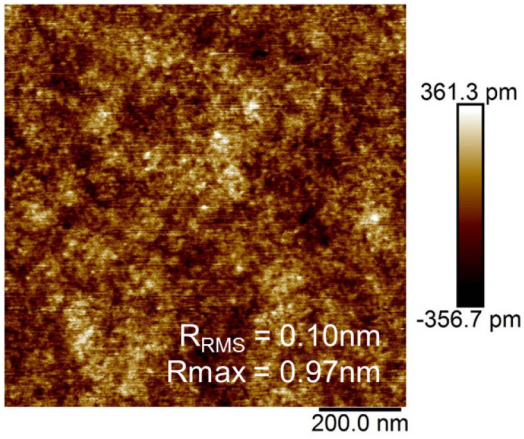

Fig. III-11*: 1 x 1 µm² tapping AFM image of SiGe 25% in a large box of 100 x 50 µm². The RMS is 0.10 nm.*

Another interesting pattern is the long rectilinear line considered as a 1D object. ***Fig. III-12*** shows the 13 nm thick SiGe as-deposited morphology in narrow lines. Different widths are shown: from 60 to 190 nm on the left and from 100 to 490 nm on the right of the figure. The two observed facets are the {111} and {001} facets. The appearance of <111> facets means that the {111} planes have low kinetics and are the most limiting plane along the <110> direction. Comparing both orientations, the morphology is very different which becomes much

more pronounced for narrow line (less than 100 nm). At these dimensions, the anisotropic faceting cannot be neglected anymore and one the contrary plays an important role on the as-deposited morphology. Indeed, having a closer look on the end of the line, the <100>-oriented pattern has cut corners (corresponding to {111} facets) which join together to form a triangle, while the <110>-oriented pattern has an angular corner having a square shape. This difference is clearly observed through the magnified AFM images on the figure (also pointed out with dashed lines). Obviously, this difference is much more amplified for 2D objects (like oval shaped pattern, as shown below) or inversely less pronounced for larger patterns or wider lines. This is the case for lines wider than 160 nm for which the small {111} facet's extension can be neglected on the whole pattern and roughly the shape can be considered as similar for both orientations.

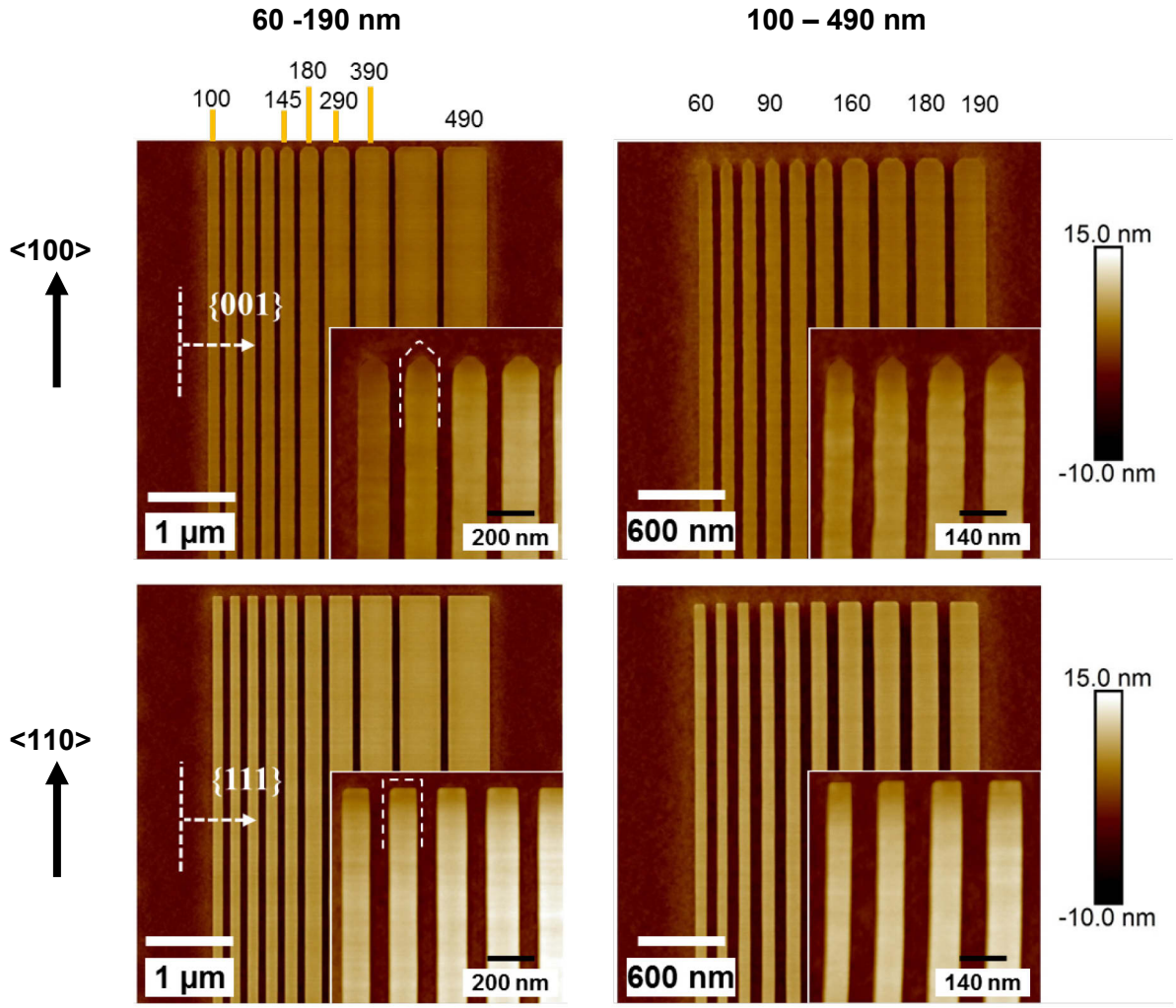

***Fig. III-12**: 5 x 5 µm² and 3 x 3 µm² AFM images of 13 nm thick SiGe as-deposited in 60 nm to 490 nm wide lines. The lines are oriented along the (top) <100> and (bottom) <110> direction.*

Finally, the spacing in between the grown lines is larger in the case of <110>-oriented lines than in the case of <100>-oriented lines. In average, the spacing measured by AFM, is 68.5 nm for the <110> orientation and is 52.8 nm for the <100> orientation. This leads to a variation of **15.7 nm**. This is due to the epitaxial lateral overgrowth (ELO) which is different for the two orientations. Indeed, as already mentioned, for the <110> orientation, the ELO is equal to 0.4

time the thickness while for the other orientation it is equal to the thickness. For a thickness of 13 nm, this means that the ELO_{110} is equal to 5.2 nm and the ELO_{100} is equal to 13 nm. Considering the spacing in between two grown lines, twice the ELO must be taken into account. As a result, for a thickness of 13 nm, the variation of the spacing should be 2 x ELO_{100} – 2 x ELO_{110} = **15.6 nm**. This is what it was experimentally obtained measuring the variation by AFM. These observations are thus in perfect agreement with what it was observed in the literature.

Three patterns are represented in ***Fig. III-13***, oriented along the <100> direction. On the top left (***Fig. III-13*** a)) part of the figure, the represented pattern (pattern 1) is a 150 nm long and 120 nm large oval; on the top right (***Fig. III-13*** b)), the second pattern (pattern 2), is a quasi-square with dimensions of 400 nm large and 420 nm long; on the bottom (***Fig. III-13*** c)) the pattern (pattern 3) is a 493 x 290 nm² rectangle. All of these dimensions correspond to the Si active zone prior to any growth, schematically depicted in the figure by dotted circles. It is worth to remind that along the <100> direction the lateral overgrowth is equal to the growth thickness while along the <110> direction it is equal to 0.4 time the thickness. Each pattern presents a regular faceted morphology with the presence of {001} and {111} facets. These facets are inclined by 90° and 54.7° to (001), respectively. The surface corresponds to the (001) plane.

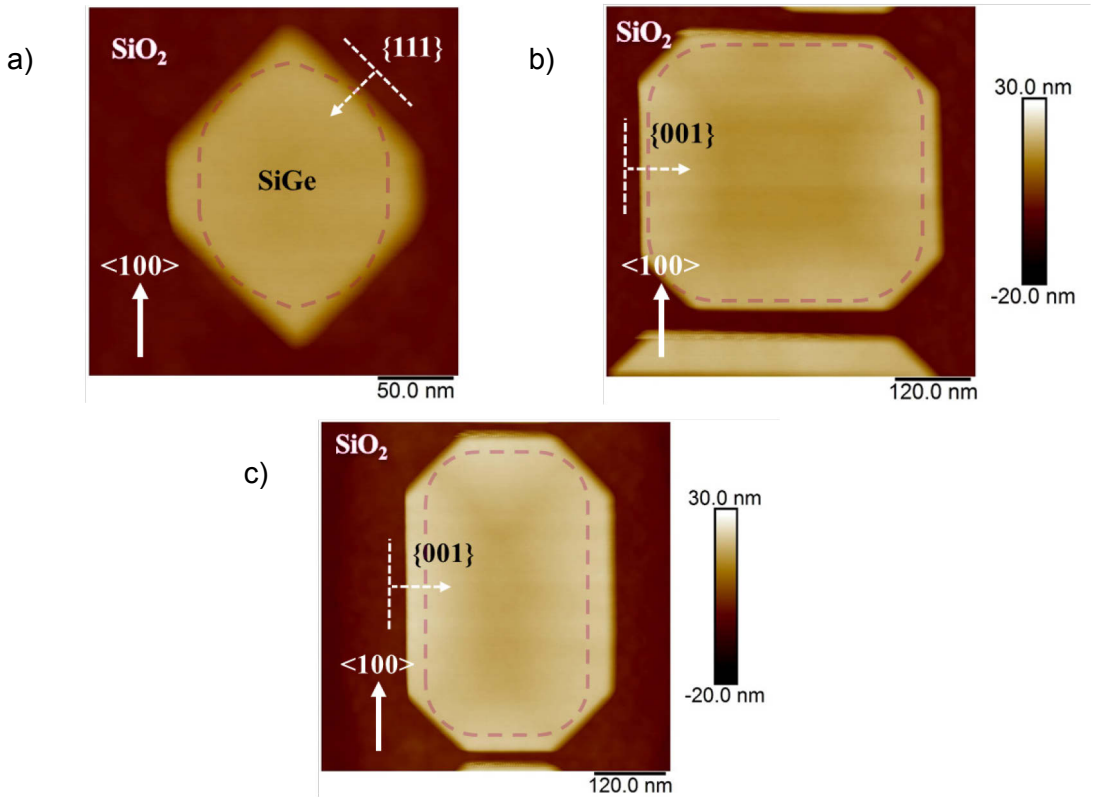

Fig. III-13*: AFM images of the SiGe as-deposited morphology in a) pattern 1, b) pattern 2 and c) pattern 3. The {111} facets are located at the corners (45°). The Si active area is schematically represented in the images by dotted circles. As reminder: the lateral overgrowth along the <100> direction is 1 x thickness and along the <110> direction it is 0.4 x thickness.*

Finally, the last investigated pattern is a circuit composed of small curved segments (340 x 105 nm²) and of lines composed of a rectilinear and an undulated side. This circuit is called SRAM and is depicted in ***Fig. III-14***. The dark parts in between the segments correspond to SiO_2 isolation. Once again, the patterns are oriented along the <100> direction since the ends of the segments show a triangular shape due to the {111} facets. The non-symmetry of the triangle is provided to the Si active zone's shape which is also not symmetric due to concave and convex parts. It was observed that the lateral overgrowth is higher on the concave edge than in convex edge.

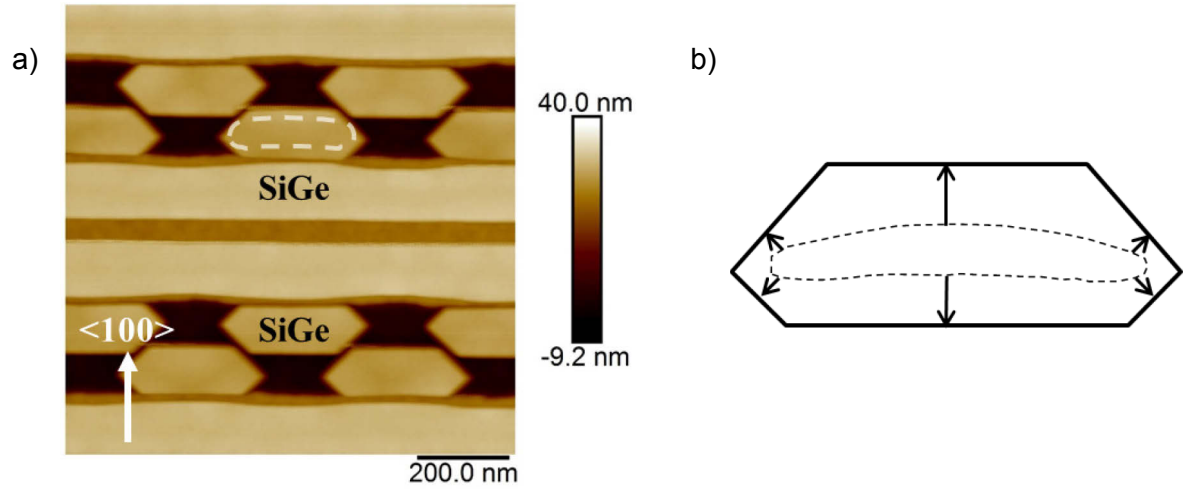

Fig. III-14*: a) 1 x 1 µm² AFM image of a <100>-oriented SRAM circuit. The morphology is once again composed of {111} and {001} facets. b) Schematic representation of the asymmetric Si active zone leading to a length's difference of the {111} facets.*

IV/ Surface passivation by Si with Dichlorosilane chemistry

IV.1) Kinetics of Si passivation

The Si passivation consists in adding a very thin (less than 5 Å) layer of Si on the SiGe epitaxy. The use of Si passivation to reduce the thermal sensitivity of Si-based epitaxy was studied by Seiss *et al*. [Seiss 13-2]. During this work, a passivation process occurring after the SiGe growth was presented in terms of growth rate and efficiency on the morphology. It consisted in a step performed at the SiGe growth's temperature (600°C), and a mixture of 26 mTorr of SiH_4 and 7.9 mTorr of HCl was used. Passivation times from 0 sec to 220 sec were investigated. It was shown that the growth rate of the Si passivation layer is not constant with time since it decreases exponentially before reaching a constant value. This was explained in terms of Si coverage on the SiGe layer. Indeed, during the Si-passivation, the Ge atoms, which are preferred desorption sites for hydrogen, at the top surface of the layer are covered increasingly by Si adatoms until no more Ge are present on the surface. Therefore, the catalytic effect decreases as soon as the Si coverage increases until it fades away. This results in a fast decrease of the growth rate before reaching a constant value. Consequently, Si-passivation by SiH_4 gas was already extensively studied. However, since almost all the growths in this work are made by DCS, it is crucial to study the Si-passivation using this gas.

In this part, the same experiments were done but the gas during the passivation was the DCS and two temperatures were studied: 610°C and 630°C. To note that these temperatures correspond once again to the SiGe growth temperature. Passivation times of 0 sec (also called reference wafer), 20 sec, 40 sec, 80 sec, 120 sec, 160 sec, 240 sec and 480 sec (only for the 610°C Si-passivation) were used.

The growth kinetics of Si-passivation was calculated thanks to XPS measurements. As soon as the thickness of the layer is less than 2 nm the XPS is more suited to measure the thickness than ellipsometry. The X-rays source was Al Kα with kinetic energy of 1486.6 eV. In order to ensure a clean and repeatable surface, XPS measurements were performed right after the SiGe growth. Therefore, the oxygen or carbon contaminations are negligible enough not to impact the final results.

The intensity of $Ge2p_{3/2}$ and Ge3d photoelectrons were measured for each wafer. They are located at theoretical binding energies of 1217 eV and 29 eV. ***Fig. III-15*** a) and b) show the $Ge2p_{3/2}$ and Ge3d lines for a passivation temperature of 630°C, respectively. ***Fig. III-15*** c) and d) show the same $Ge2p_{3/2}$ and Ge3d lines for a temperature of 610°C. The background was subtracted for each XPS measurements. Considering each graph, it is clearly observed that the peaks' intensity decreases when the passivation time increases. As already mentioned, this is due to the Si ad-atoms coverage which increases when increasing the time resulting in a decrease of the Ge signal. It is worth to add that a much higher decrease is observe when looking at the $Ge2p_{3/2}$ line. Indeed, this line is more surface sensitive since it is located at higher binding energy. On the contrary, the Ge3d line is more sensitive to thicker Si passivation layer as compared to the $Ge2p_{3/2}$ line. Also, comparing both temperatures, a significant decrease in the peaks' intensity is measured for the highest temperature. This is obviously due to the fact that at higher temperatures, the growth kinetics and thus the Si ad-atoms coverage of the SiGe layer are more efficient.

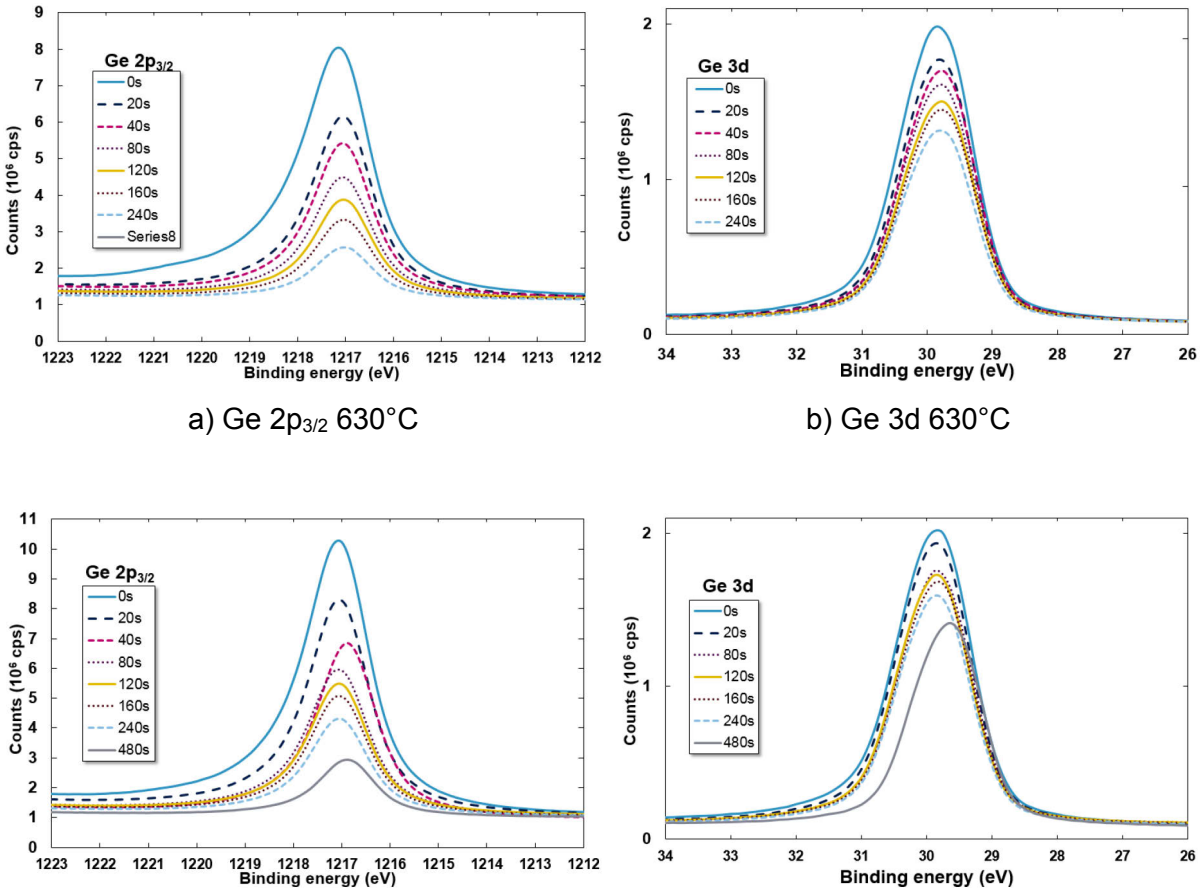

a) Ge $2p_{3/2}$ 630°C b) Ge 3d 630°C

c) Ge $2p_{3/2}$ 610°C d) Ge 3d 610°C

***Fig. III-15**: XPS spectra of the Ge $2p_{3/2}$ for a Si passivation at a) 630°C and c) 610°C, and the Ge 3d for a Si passivation at b) 630°C and d) 610°C for passivation times of 0 sec, 20 sec, 40 sec, 80 sec, 120 sec, 160 sec and 240 sec. To note that the passivation time of 480 sec was done only for the 610°C passivation layer. For all the spectra, an intensity decrease with increasing passivation time is observed due to the increase of the Si coverage.*

The Si-passivation thickness th_{passiv} is obtained thanks to the following equation:

$$th_{passivation} = -\sin(\alpha) * \lambda * \ln\left(\frac{I}{I_0}\right) \qquad \text{Eq. III-1}$$

Where α is the take-off angle with a value of 90°, λ the mean free path of the Ge photoelectrons in Si (obtained by [Tanuma 94], I and I_0 are the whole peak's areas of the passivated and reference wafers, respectively. The used λ values are 9.19 Å and 32.3 Å for the $Ge2p_{3/2}$ and Ge3d photoelectrons, respectively. The Si thicknesses, measured by Eq.III-1, are plotted in ***Fig. III-16***, for both $Ge2p_{3/2}$ and Ge3d lines and for both temperatures.
The experimentally passivation thicknesses were fitted by the following function (from [Seiss 13-4]):

$$th(t) = -A * exp\left(\frac{-t}{B}\right) + C * t + A \qquad \text{Eq. III-2}$$

The constants A, B, C have values of (respectively):

- 630°C, Ge2p$_{3/2}$: 4 Å, 14 sec, 0.050 Å/sec.
- 630°C, Ge3d: 6 Å, 35 sec, 0.035 Å/sec.
- 610°C, Ge2p$_{3/2}$: 5 Å, 27 sec, 0.025 Å/sec.
- 610°C, Ge3d: 4.1 Å, 32 sec, 0.019 Å/sec.

Finally, the GR of the Si passivation layer is obtained by deriving Eq. III-2 with respect to time:

$$GR(t) = \frac{A}{B} * exp\left(\frac{-t}{B}\right) + C \qquad \text{Eq. III-2}$$

Both the thickness fit and the GR are plotted in ***Fig. III-16***. As already observed by Seiss *et al*. [Seiss 13-2], the thickness increases non-linearly with increasing time and two regions can be distinguished. From 0 sec to a time in between 40 sec and 80 sec, there is a non-linear increase of the thickness; above this intermediate time, the dependence becomes linear. Taking the data from the Ge2p$_{3/2}$ and Ge3d lines for the short and long passivation's times, respectively, the effective thicknesses corresponding to the time dependence change can be extracted. At 610°C, the effective thickness is 4.45 Å and at 630°C, it is 5.87 Å. This effective thickness' difference comparing both temperatures, may be attributed to the tendency of the Ge to segregate at the surface to minimize the layer's surface energy (the Ge has a lower surface energy than Si) and/or simply to Ge diffusion. This segregation may be done on a distance more or less long depending on, for example, the H surface coverage or the diffusion of the H ad-atoms. A higher temperature (in this case 630°C) leads to a lower H coverage and a faster diffusion, which may result in a faster Ge segregation at the surface. This may induce that a higher effective thickness is required to suppress the Ge effects. On the contrary, at lower temperature (610°C), the Ge segregation is slower due to a higher H coverage and a slower diffusion. This may result in a lower effective thickness. In comparison with the results obtained by the author, the linear dependence appears at an equivalent thickness of 4.57 Å. These values correspond to the thickness for which the Ge catalytic effect is no more effective. This means that only few atomic layers are needed to suppress the Ge effect on the GR and to make the SiGe layer less sensitive to thermal treatments. In the following studies, the DCS was preferred since all the growths were done with a DCS chemistry and also it allows the selectivity to be maintained without adding HCl (which is the case with a SiH_4 chemistry). Second, comparing Ge2p$_{3/2}$ and Ge3d, different thicknesses and GRs are obtained. At the beginning of the passivation process at e.g. 630°C, the GR is about 19 Å/min for Ge2p$_{3/2}$ while it is about 12.1 Å/min for Ge3d. Similarly, at 610°C, the initial GR is 12.2 Å/min for Ge2p$_{3/2}$ while it has a value of 8.6 Å/min for Ge3d. Then, the GR decreases exponentially with increasing time before reaching a constant value. To note that the exponential decrease is more pronounced for the Ge2p$_{3/2}$ line at 630°C and the constant value is reached for passivation time less than 100 sec. At 630°C, the constant values obtained for the GR are 3.05 Å/min for Ge2p$_{3/2}$ and 2.10 Å/min for Ge3d. At 610°C, the GR stays constant at values of 1.53 Å/min and 1.14 Å/min for Ge2p$_{3/2}$ and Ge3d, respectively.

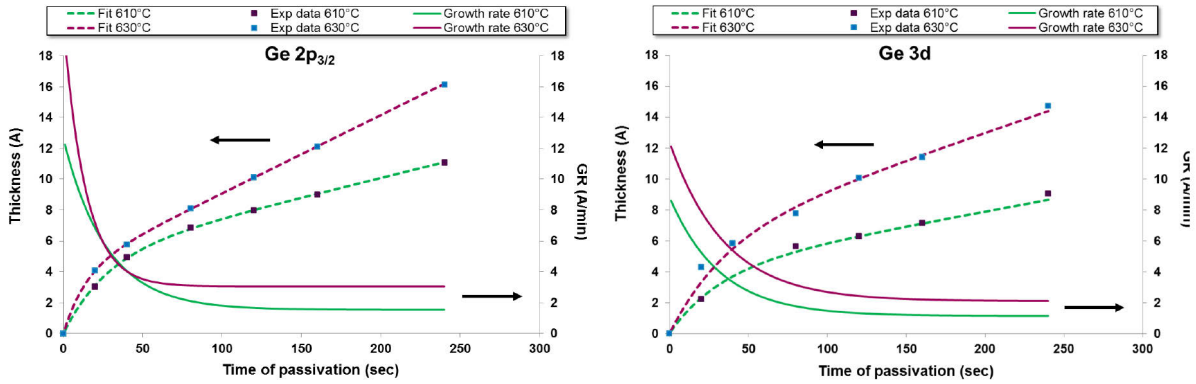

a) From Ge $2p_{3/2}$ b) From Ge 3d

***Fig. III-16**: Si-passivation thickness as a function of passivation time obtained by Eq. III-1 and the a) Ge $2p_{3/2}$ and b) Ge 3d photoelectron lines.*

A passivation time of 3600 sec at 630°C was done to verify the GR for a long passivation time. Indeed, the Si thickness after 3600 sec of passivation can be measured with good accuracy by ellipsometry allowing the "infinite" GR (GR∞) to be obtained. The measured thickness was 127.6 Å corresponding to a GR∞ of 2.13 Å/min. With the fit of the $Ge2p_{3/2}$, for a passivation time of 3600 sec, a thickness of 186.9 Å is obtained corresponding to a GR∞ of 3.05 Å/min, while for the Ge3d line, a thickness of 132.0 Å is obtained corresponding to a GR∞ of 2.10 Å/min. This may confirm the fact that the Ge3d line is more sensitive to measure thicker Si passivation layers than the $Ge2p_{3/2}$ line.

IV.2) Interest of passivation on morphology

The interest of the Si-passivation on the morphology is given in this section. To do so, a 10 nm SiGe 25% layer is grown on <110> Si blanket substrates and then passivated by DCS at temperatures of 610°C or 630°C for times comprise between 0 sec and 480 sec. Finally, to observe to influence of this passivation, the SiGe layer is annealed at 800°C for 60 sec under a 20 Torr of H_2 atmosphere. ***Fig. III-17*** shows 3 x 3 µm² AFM images of SiGe layers after the thermal treatment. For non-passivated layers (0 sec), it is observed a highly-undulated surface also called Stranski-Krastanov undulations (see *Chapter I* and *Chapter IV* for more details). These undulations are oriented along the <100> directions. Regarding the 610°C passivation, the roughness (R_{RMS}) decreases with increasing passivation time: from 6.04 nm to 0.122 nm. The ridges become less pronounced and closer from each other. For a passivation time of 480 sec the ridges disappeared completely to leave a perfectly flat surface meaning that the Si-passivation layer was thick enough to stand for the 800°C annealing. The needed thickness is comprised between 240 sec and 480 sec of passivation corresponding to a thickness comprises between 8.6 Å and 13.2 Å (from Ge3d line). For the 630°C passivation, the Si layer is already effective at 160 sec. No undulation is observed and the surface is flat with a roughness smaller than 1 nm (0.086 nm). Considering the Ge3d line in the ***Fig. III-16*** b), this passivation time corresponds to a thickness of 11.5 Å which is quite similar to what observed for 610°C.

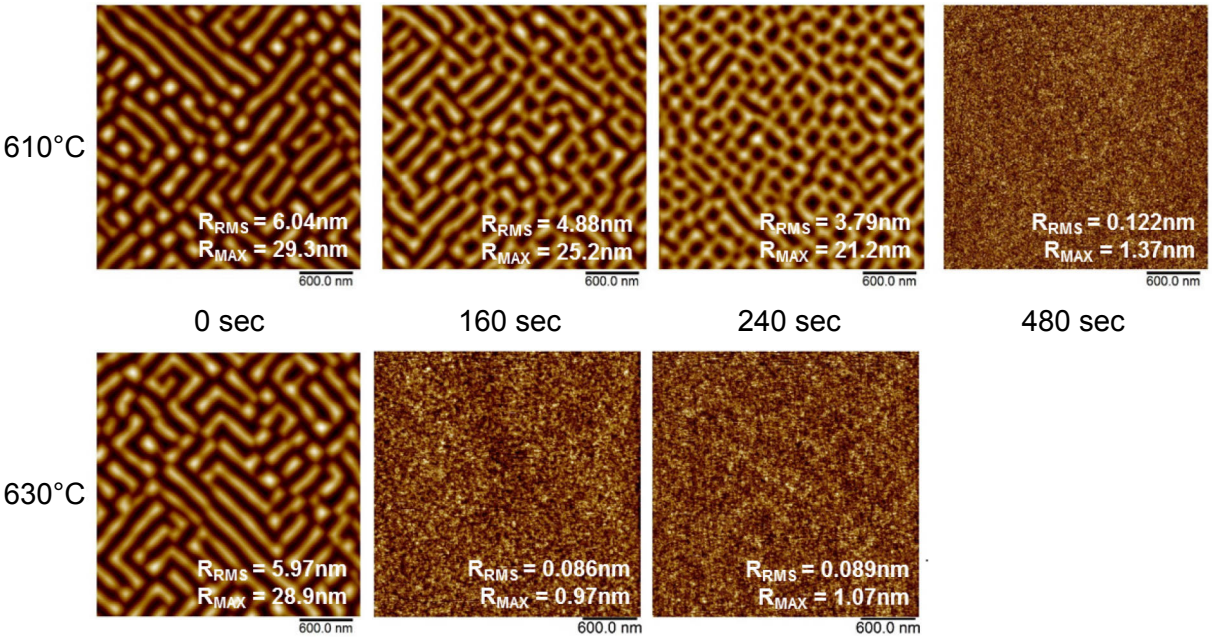

***Fig. III-17**: 3 x 3 µm² tapping mode AFM images on blanket wafer. A SiGe 25% layer was grown and annealed at 800°C for 60 sec. Before annealing, a Si-passivation by DCS gas is done at (top) 610°C or (bottom) 630°C for different passivation times: (from left to right) 0 sec, 160 sec, 240 sec and 480 sec. For both temperatures, a Si-passivation layer of about 11 Å is needed to avoid the SK undulations.*

IV.3) Application of Si-passivation

IV.3.a) During the temperature ramp process

An important application of Si-passivation of a SiGe layer is when this layer must be capped by another material, basically Si. Indeed, in most of cases, the Si growth is performed at a higher temperature than that of SiGe, and a temperature ramp is needed to attain the Si growth temperature. Moreover, few steps are added just before the Si growth, to ensure the stabilization of the pressure, the temperature and the gas. All these steps bring thermal treatments to the SiGe layer and thus may result in either thermal rounding or instabilities that must be avoided before the Si growth. The thermal rounding and the instabilities are discussed in details in the next chapter. Moreover, in the majority of cases the Si growth's temperature is higher than that of SiGe. Another example concerns the p-doped source and drain (S/D) for the 14 nm node which are grown on a SiGe channel. Here again some instabilities may appear on the SiGe channel due to thermal treatments before the S/D growth. In these cases, to avoid these morphological evolutions a Si-passivation of the surface's layer is required. This can be done during the temperature ramp or during the steps of stabilization by leaving a Si active gas like DCS during the process. A thin Si layer (< 10 Å) is grown rendering the SiGe less sensitive to thermal treatments. This section is devoted to the importance of the thin Si-passivation on the morphology of the SiGe/Si stack. The selective growth of the as-deposited SiGe was performed at 630°C using a DCS, GeH_4 and HCl mixture under a 20 Torr H_2 atmosphere. The thickness was 18 nm and the Ge content was 25%. The 4 nm Si cap is after selectively grown at 715°C using DCS gas only. The pressure during the Si epitaxy was the same as previously i.e. 20 Torr. In between the two growth processes, a temperature ramp of

2°C/sec is done to reach the Si growth temperature. During the ramp, the DCS gas is left at a pressure of 67 mTorr. This kind of ramp is also called active ramp [Dutartre 07] meaning that an active gas is present while the temperature is increasing.

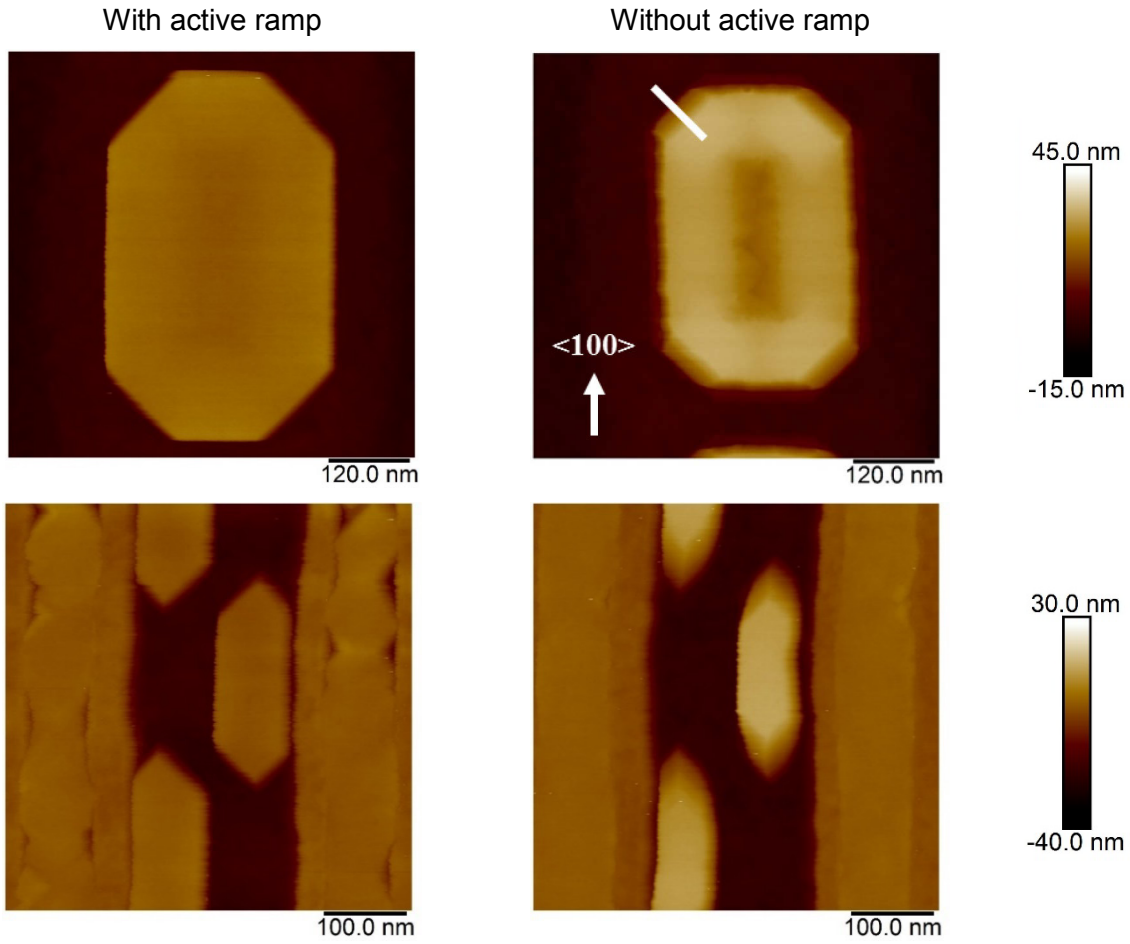

***Fig. III-18**: AFM images of Si/SiGe stack (left) with and (right) without active ramp after the SiGe growth. During the active ramp to reach the Si growth temperature, DCS is left to passivate the SiGe layer's surface with Si. Without this active ramp, the SiGe undergone thermal rounding leading to a non-acceptable morphology. On the contrary, the active ramp allows the SiGe layer to be less sensitive to temperature and the initial morphology is maintained.*

Fig. III-18 shows the influence of the active ramp of the whole stack morphology on two different patterns. When the ramp is active, the obtained morphology is similar to the as-deposited one with here again the presence of {111} and {001} facets. The growth of Si on SiGe occurred normally and the SiGe under layer does not seem to be impacted by the increase of temperature. On the contrary, without active ramp, it is clearly observed that the morphology is really different due to the fact the SiGe under layer undergone a significant thermal rounding. Indeed, for both patterns the epitaxy is smaller in dimension showing that the SiGe matter has retracted to the active zone due to thermal rounding. Also, having a closer look to the rectangle pattern, the corners are higher than the interior of the pattern and there is a long cavity in the middle. This is also characteristic of thermal rounding. Consequently,

this particular morphology leads to the conclusion that the Si cap has grown on a rounded SiGe layer which is not the case of the active ramp. The active ramp renders the SiGe layer less sensitive to temperature allowing the upkeep of the initial morphology. Finally, for a non-active ramp the stack SiGe/Si presents a succession of {111} and {113} along the <110> direction as shown in ***Fig. III-19***.

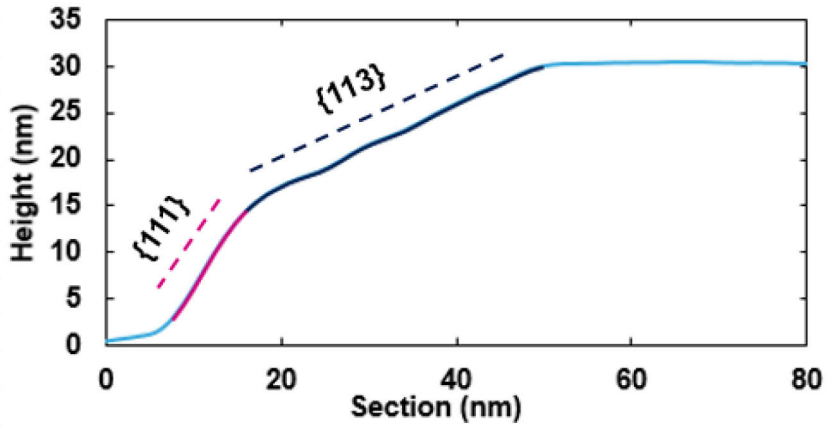

Fig. III-19*: AFM section showing the succession of {111} and {113} facets. This is taken along the <110> direction in the rectangular pattern. During the process, the temperature ramp is not active.*

IV.3.b) After the growth process – "freezing" recipe

The importance of Si passivation in the case of Si growth on SiGe layer was demonstrated in the previous part. In this section, the necessity of Si passivation after the material growth will be shown. Indeed, in the majority of cases, just after the growth a step mainly made at the growth's temperature is added. This step (typically 10 or 30 sec) is a purge step in order to remove the gases from the chamber and thus important. After this step, the temperature is decreased before wafer unloading. However, during the purge step and the decrease in temperature, the grown material undergoing a thermal treatment, could be impacted in terms of morphology. It is where the Si passivation plays once again an important role to avoid any thermal rounding. The Si passivation by e.g. DCS can be added either during the purge step or during the temperature decrease. These particular precautions were made during all this work and are called "freezing" recipe due to the fact that the morphology is in a sense, "freezing" right after the growth or the thermal budget. The experiments were realized with boron-doped SiGe (SiGe:B) layers grown at 644°C under 10 Torr of H_2 atmosphere and characterized by AFM. Three studied were performed. First, a long step of purge (120 sec) at the growth temperature during which the DCS gas was left in the chamber was done. Second, a standard purge of 10 sec without DCS was studied. Finally, the "freezing" recipe was performed. The results are shown in ***Fig. III-20***. It is clearly observed that a 10 sec standard purge is enough to change the as-deposited morphology due to thermal rounding. As observed, the SRAM has a rounded shape and the matter started to retract to the active zone. Obviously, this effect will be amplified when using a 30 sec standard purge. ***Fig. III-21*** shows the AFM sections for each case. On the contrary, the as-deposited morphology is kept when passivating the surface. Whether it is during the purge or during the "freezing" recipe, the passivation is really effective and consequently mandatory in any processes. As a result, it is very important to be aware of this possible morphology's change during the purge since, first this step is almost always used, second it could be detrimental for the devices.

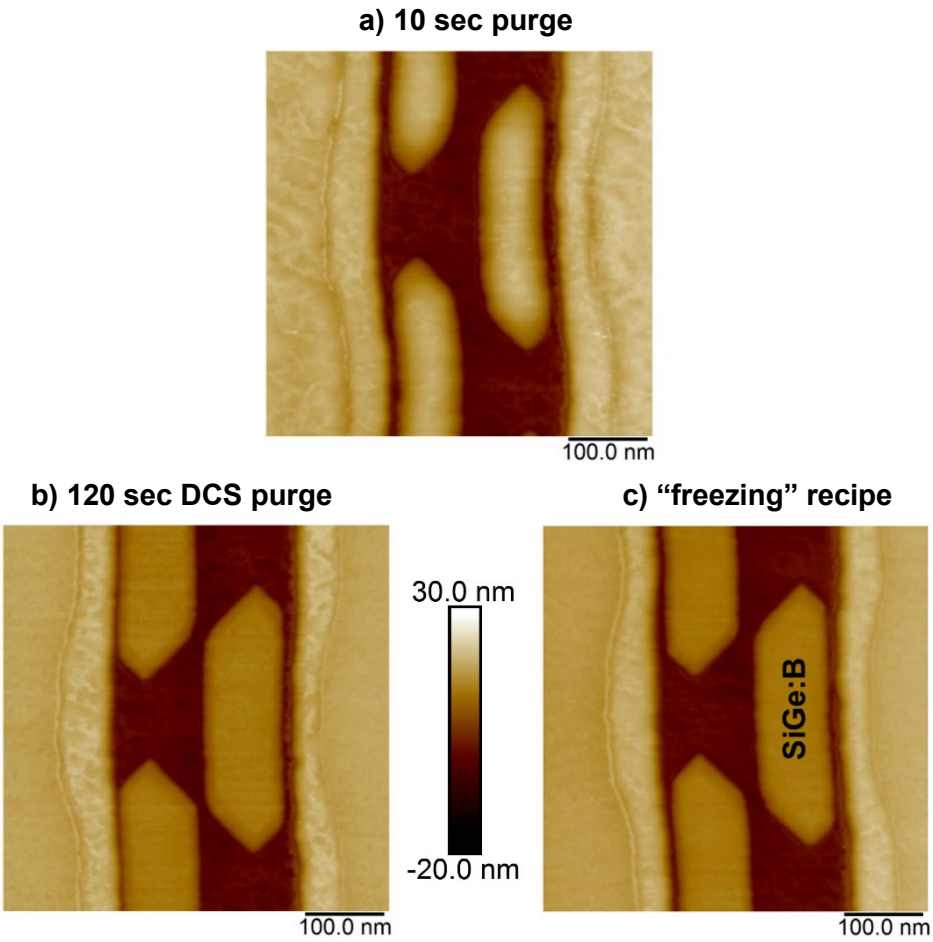

***Fig. III-20**: 0.5 x 0.5 µm² AFM images of SiGe:B in SRAM pattern. a) 10 sec of purge without passivation, b) 120 sec of purge with passivation (by DCS) and c) "Freezing" recipe.*

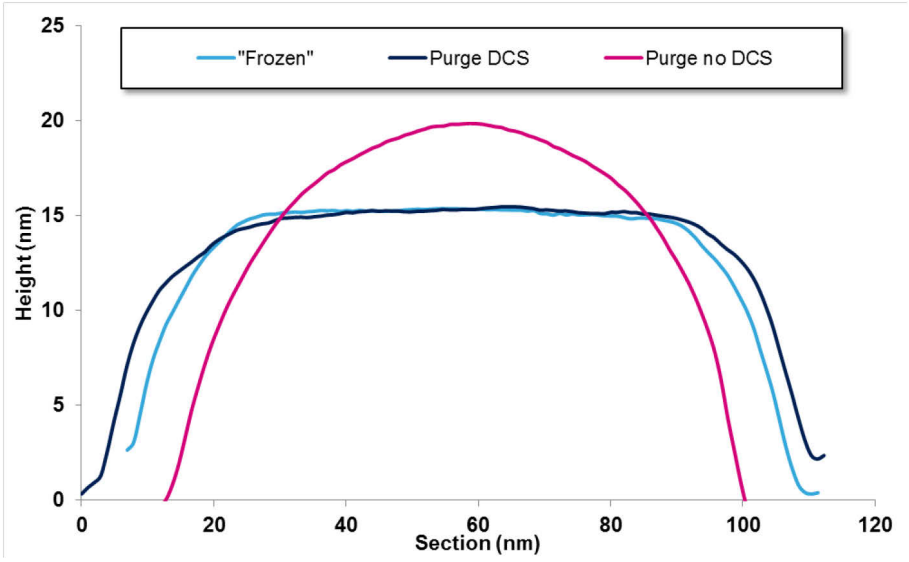

***Fig. III-21**: AFM sections of SiGe:B in SRAM circuit for each case of process. The sections are taken perpendicular to the pattern. For a purge of 10 sec without DCS, the SiGe:B layer already obtained a rounded shape due to thermal rounding.*

V/ Conclusion

In this chapter, the as-grown morphology of SiGe layers was characterized by AFM. Several patterns were studied as large boxes, lines, squares, rectangles or ovals. The large patterns were characterized by a very low roughness (lower than 0.15 nm). Concerning the small patterns, it was observed that the morphology is mainly governed by the presence of the {111}, along the <110> orientation, and the {001} facets, along the <100> orientation. These facets have theoretical angles of 54.7° and 90° with respect to the surface, respectively. Also, their corresponding lateral overgrowth were confirmed to be 1 x the growth thickness for the {001} facets and 0.4 x the growth thickness. These important differences induce that the morphology is highly affected by the substrate's orientation and even more with the continuous transistors' size scaling. For example, the lines' end presents either a triangle shape or a square shape.

The passivation of SiGe layers by Si using a DCS chemistry was investigated. The kinetics was shown to be non-linear with time: it decreases exponentially with increasing time before reaching a constant value. This is due to Ge catalytic effect that decreases with the Si coverage's increase until it completely disappears (for a thick enough Si coverage). This Si passivation was then integrated at two different process' steps: during the temperature ramp between the SiGe growth and the Si growth, or right after the growth. The importance of this passivation layer was demonstrated as soon as it is needed to maintain the as-grown morphology and to make the SiGe less sensitive to any thermal treatments. This is particularly the case, for a Si growth on a SiGe layer or during the post growth's purge. Thus, this study allowed as-grown morphologies the closest from reality to be obtained that will be further used as references for the next chapters.

Chapter 4

Post annealed SiGe epitaxy

Annealing of SiGe constitutes a research axe of great interest for many years and still is. It allows the morphology of the epitaxial objects to be modified through strain relaxation or surface diffusion or a combination of both. Since the objects' dimensions reach ten of nanometers, the epitaxy becomes more and more sensitive to any thermal treatments. Indeed, as already mentioned in the previous chapter, the morphology's control is essential for the devices' performances: depending on the technology and structure to be grown (channel, source/drain…), an annealed morphology may involve better characteristics than an as-grown one. On the contrary, a too high annealing may degrade the morphology and thus the performances.

Therefore, the chapter 4 is devoted to the study of the SiGe post annealing morphology in different size patterns. Large objects will be first discussed in terms of Stranski-Krastanov relaxation which is the main driving force of the morphology's change in the large range scale. Second, the annealing of small objects will be studied through the thermal rounding phenomenon. In this case, the main driving force is the surface energy minimization or the competition of the two previous mechanisms. This thermal rounding will be quantified in terms of kinetics. Finally, the morphological behavior of SiGe and Si caps selectively grown on an undulated surface will be studied.

I/ Stransky-Krastanov phenomenon

Annealing of SiGe under H_2 atmosphere has been extensively studied on blanket wafer by different authors. In the following, some examples will be given. Growth instabilities may occur during SiGe epitaxy on silicon surface depending on growth's conditions, substrate's orientation and also on germanium content in the layer. It may result in a change of the layer's morphology presenting highly periodic shapes. The group of Ozkan *et al.* [Ozkan 97] [Ozkan 99] has characterized SiGe films deposited on Si (001) surface and annealed under a 15 Torr of H_2 atmosphere at temperatures ranging between 700°C and 850°C. It was shown that the surface of a stressed solid is unstable with respect to variations in surface shape from a nominally flat surface. This morphologic instability results in a change of the surface's shape towards a 2D ridge shape forming an undulated surface or 3D islands. The mass transport by means of surface diffusion under the effect of the stress is the main factor of morphologic evolution. During this stress-controlled surface diffusion process, atoms move away from surface valleys toward surface peaks. During the course of surface evolution, the magnitude of the local stress in the vicinity of the valley continues to increase as well as the local curvature in the valley. During their experiments, they have first deposited a supercritical heteroepitaxial 50 nm thick film containing 22% of Ge. After a 10 sec annealing at 750°C, they observed the apparition of <100>-oriented ridges, which confirms the theory of anisotropic surface evolution. The Young modulus of Si and Ge being lower in the <100> direction, this direction is consequently softer and correspond to a minimum of energy. In their second experiment, a 10 nm subcritical SiGe film (18% Ge) was annealed at 850°C. The same formation of <100>-oriented ridges was observed after 5 minutes. While annealing time increases, the wavelength and amplitude of corrugations increases as well until only islands are observed (after 2 hours). These undulated surfaces are characteristic of Stranski-Krastanov (SK) growth mode which occurs because of elastic strain relaxation of the film (no dislocation). Indeed, when pure Ge is deposited on a (001) Si surface, the growth is initially two-dimensional (2D) and evolves rapidly (after few monolayers) to a SK growth mode characterized by the apparition of clusters. This growth mode is known to be induced by stress and allows the mechanical energy to be reduced when Ge films are deposited. In the case of the growth of SiGe with low Ge content (e.g. 20% Ge), the mismatch lattice between SiGe alloy and Si substrate is much lower compared to pure Ge growth on Si surface. Consequently, the overall stress is reduced in the epitaxial SiGe films. In the case of low enough Ge content, misfit dislocation generation may become the optimal stress relaxation mechanism. The SK relaxation is expressed in term of surface's morphology change by oriented and well defined undulations with specific wavelength. ***Fig. IV-1*** a) and b) shows AFM images of SiGe layers subjected to this SK-like relaxation due to H_2 annealing at 750°C, 10 Torr for 60 sec. The film thickness was 5 nm and the Ge concentration 25%. Both <110> and <100> orientations were used. Obviously, the ridges formed during the elastic strain relaxation are turned at 45° comparing <100> and <110> orientations. The ridges are consequently always oriented along the <100> direction, some is the substrate used. This can be attributed to the lowest Young's modulus of Si and Ge along the <100> direction: in Si the minimum value is 130 GPa which occurs in the <100> direction [Hopcroft_10]. ***Fig. IV-1*** c) shows a 20 nm thick SiGe layer annealed under 20 Torr H_2 atmosphere at 725°C for 480 sec. The orientation of the pattern is <100>. The 2-D isotropic Power Spectral Density (PSD) tool from AFM software was used to measure the wavelength of the instabilities SK. For a 5 nm thick layer, the wavelength is about 0.167 µm. For a 20 nm thick layer, the wavelength is higher and is about 0.231 µm. As a result, the growth thickness

impacts the undulation's wavelength: the thicker the growth the higher the wavelength. The system wants to relax by adopting a specific wavelength which will be the most adapted to minimize the total energy. These obtained values are specific to our case and thus will change for other materials, thicknesses…

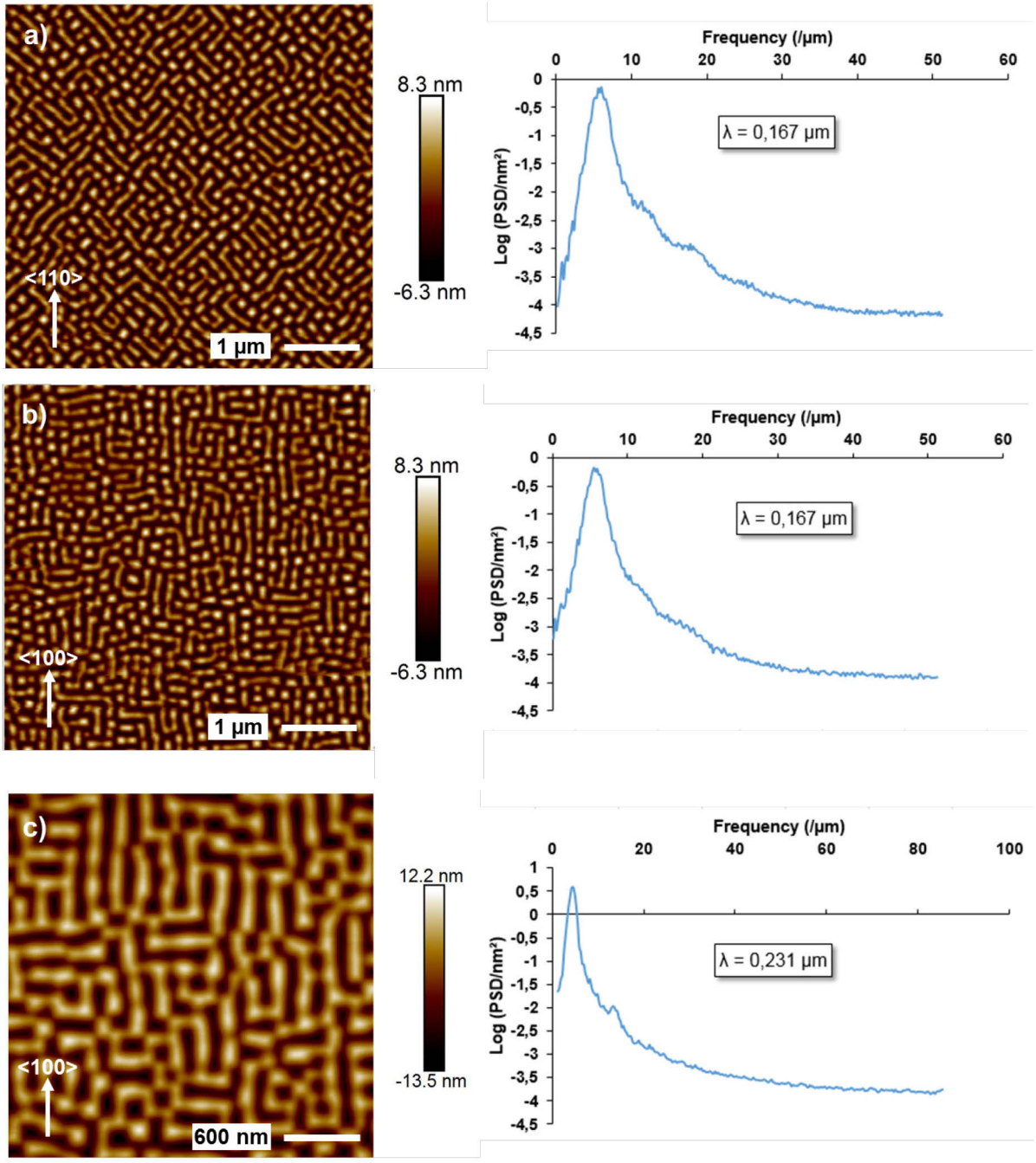

***Fig. IV-1**: 5x5 µm² AFM tapping images of a) <110> and b) <100> 5 nm thick SiGe 25% annealed at 750°C for 60 sec under 10 Torr H_2 atmosphere. c) 3x3 µm² AFM image of <100> 20 nm thick SiGe 25% annealed at 725°C for 480 sec under 20 Torr of H_2. The corresponding 2-D Isotropic Power Spectral Densities are represented on the right. Spatial frequency of 0.167 µm and 0.231 µm are measured for the thin layer and thick layers, respectively.*

The PSD is an analysis complementary tool that gives information on roughness and spacing. It performs a decomposition of the surface profile into its spatial wavelengths and allows comparison of roughness measurements over different spatial frequency ranges. In a case of surface analysis, PSD can be described as follow [Gavrila 07]:

$$PSD(f_x, f_y) = \lim_{L\to\infty} \frac{1}{L^2} \left\{ \int_{-\frac{L}{2}}^{+\frac{L}{2}} dx \int_{-\frac{L}{2}}^{+\frac{L}{2}} dy \,.\, z(x,y).\exp\left[2\pi i(f_x.x + f_y.y)\right] \right\}^2 \qquad \text{Eq. IV-1}$$

With L being the scan length, supposed to be equal in x and y directions, f_x and f_y are the spatial frequencies for x and y directions, respectively, and i the complex number defined by $i^2 = -1$. Z(x,y) describes the surface profile in terms of height as a function of x and y. This expression describes the PSD for an infinite scan length. However, during an AFM scan a finite number N of values are measured. These values are assumed to be equidistantly spaced in x; y directions at distances $\Delta x = \Delta y = L/N$. Eq. IV-1 is then reduced to:

$$PSD(f_x, f_y) = L^2 \left[\frac{1}{N^2} \sum_{n=0}^{N} \sum_{m=0}^{N} z(x_m, y_n).\exp(2\pi i.x_m.f_x)\,.\exp(2\pi i.y_n.f_y) \right]^2 \qquad \text{Eq. IV-2}$$

Where $x_m = m.\frac{L}{N}$, $y_n = n.\frac{L}{N}$.

SK-like strain relaxation is also displayed in ***Fig. IV-2***. The SiGe films being grown on patterned wafers, the structures must be large enough to obtain the formation of SK <100>-oriented ridges. This is the case of box structures with dimensions of 100x52µm². Two different steps of SK are shown here. The films are 8 nm thick with Ge concentration of 25%. Both films are annealed at 850°C under 20 Torr of hydrogen but different times are used: in a) 60s and in b) 180s. The ***Fig. IV-2*** a) shows a SiGe film that has undergone an elastic strain relaxation with formation of ridges oriented along <100>. In ***Fig. IV-2*** b), the film has also been subjected to a strain relaxation but more important in a way the ridges have disappeared for the benefit of domes.

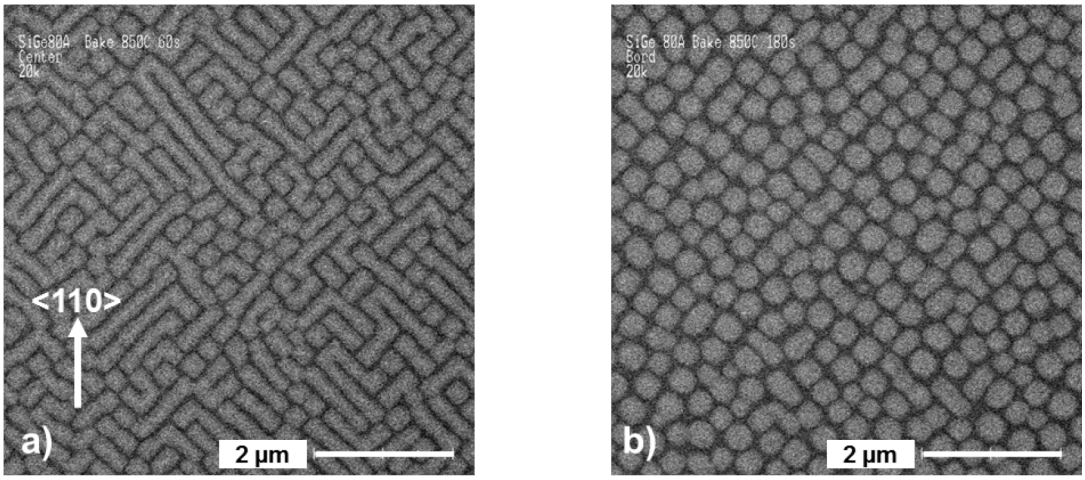

Fig. IV-2*: Top view SEM images of 8nm thick SiGe layer annealed at 850°C under 20 Torr of H_2 for a) 60 sec and b) 180 sec.*

I.1) The apparition of SK-like relaxation undulation

The first study deals with the study of the SK undulation as a function of temperature and time of annealing. To do so, 20 nm SiGe layers with 25% of Ge were grown on Si <100>-oriented patterned wafers. Annealing temperatures from 650°C to 725°C and durations from 30 sec to 1920 sec were used under 20 Torr of hydrogen atmosphere. The undulations were characterized in terms of roughness (R_{RMS}) measured by AFM. The measurements were done in the sub-micron scaled boxes. ***Fig. IV-3*** shows the evolution of the roughness as a function of time for the 4 investigated annealing temperatures.

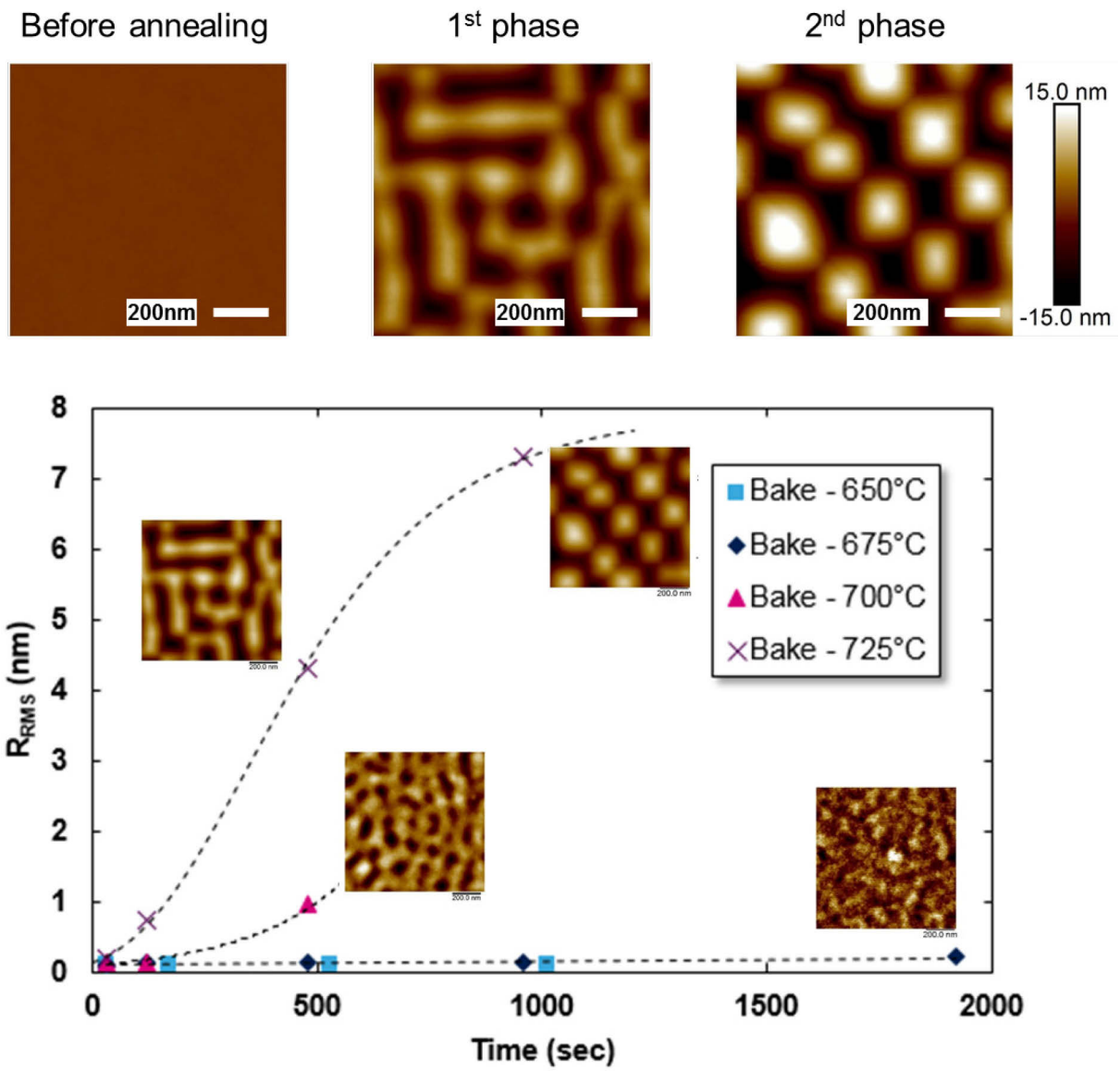

Fig. IV-3*: R_{RMS} evolution as a function of annealing duration for 4 investigated temperatures: 650°C, 675°C, 700°C and 725°C. 1 x 1 µm² AFM images taken at specific moments are also depicted in the graph. They show the evolution of the surface morphology. The undulations take a long time before appearing. Since the ridges start to propagate the roughness exponentially increases until a saturation value. At this point all the ridges transformed into domes. To note: the data obtained at 650°C were shifted of 50 sec for clarity.*

It is observed that the undulation's mechanism takes a long time to appear at least for temperatures of 650°C and 675°C. Indeed, even after 1920 sec of 675°C annealing, the R_{RMS} is low (0.219 nm) and no undulations are visible. On the contrary, at 700°C the undulations appear after 480 sec (R_{RMS} = 0.952 nm) and at 725°C they appear after 120 sec (R_{RMS} = 0.726). The surface is undulated but the rounded ridges are not yet completely formed and the <100> preferred orientation is not well defined. At the moment when the mechanism starts the roughness exponentially increases: it reaches a value of 4.3 nm after 480 sec at 725°C. At this roughness value, the ridges are well defined as well as their <100> orientation. By still increasing annealing time or temperature the rounded ridges break into several parts and transform into single domes. The domes have a square base dimensions comprise between 200 and 350 nm. At this point, the roughness slowly increases until reaching a constant value of about 8 nm. To note that the data obtained at 650°C were shifted of 50 sec for clarity purpose. This shift does not change the results since the roughness does not evolve at this annealing temperature.

I.2) The wetting layer in the SK relaxed surface.

The existence of the wetting layer in SK relaxed surfaces is investigated in this part. To put the existence in evidence, an 8 nm SiGe 25% layer grown on blanket wafer was annealed at 850°C during 180 sec so that almost all the ridges have broken into single domes. The annealed layer is then etched with HCl gas in the chamber (see annex etching by HCl). An average thickness of 5 nm was removed. This step is required to entirely remove the wetting layer in between the domes. Indeed, the wetting layer is supposed to be few Angstroms thick. Finally, the same wafer is again annealed at 800°C for 60 sec (named Bake 2) in order to see if the wetting layer is reformed during the second bake. The flow of the experiment is given in ***Fig. IV-4***.

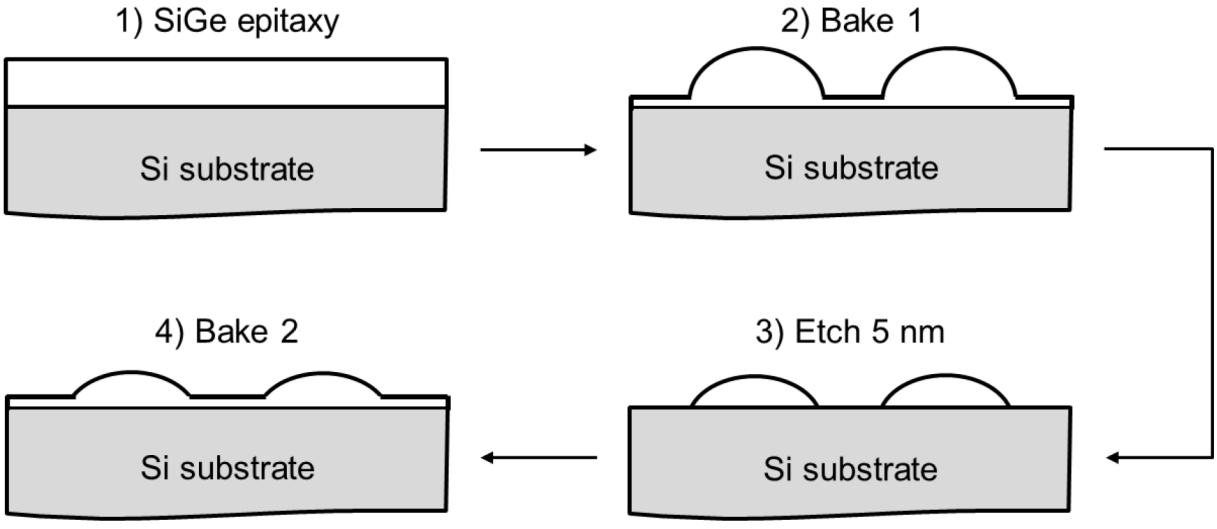

Fig. IV-4*: Schematic representation of the experiment. (1) The 8 nm thick SiGe epitaxy is first (2) annealed at 850°C for 180 sec under 20 Torr H_2 atmosphere. (3) Then, the same sample is etched under HCl; 5 nm in average is etched. (4) Finally, the sample is once again annealed at 800°C for 60 sec. To note that after the anisotropic etching the domes may be transformed into pyramids.*

Primarily results were obtained by characterizing the samples by XPS to obtain the Ge signal, and by AFM to measure the roughness. It is important to note that for the XPS measurements, the same wafer was characterized post etch and post bake 2, which is not the case for the AFM characterization. Since The AFM is not located in clean room, three wafers were prepared corresponding to the three steps of the experiment. The XPS measurements were done on the wafer that endured all the different steps, i.e. from the epitaxy to the bake 2.

XPS measurements are given in ***Fig. IV-5***. XPS was performed right after the 5 nm etch and after the post bake 2. Both Ge3d and $Ge2p_{3/2}$ are represented and the peaks' area is given in **TABLE IV-I**. When looking both ***Fig. IV-6*** and **TABLE IV-1**, it is clear that the Ge signal increases after the second bake. Regarding the Ge3d line, it changes from 1.12 x 10^6 counts.eV/sec to 1.49 x 10^6 counts.eV/sec, i.e. a 33% increase is observed. The effect is even more pronounced for the $Ge2p_{3/2}$ line since it is more surface sensitive due to higher binding energy: the peak's intensity evolves from 8.31 x 10^6 counts.eV/sec to 15.08 x 10^6 counts.eV/sec. This behavior can be explained by the formation of a new wetting layer between each dome. Indeed, after the SiGe etch, the layer is composed of SiGe domes surrounded by Si, decreasing in average the Ge signal. However, if the wetting layer is formed after the 2nd annealing, the whole surface is composed of SiGe which can explain the increase of Ge peak's intensity. During the annealing, different mechanisms can be proposed. First, during the annealing, the Si ad-atoms tends naturally to diffuse from the top of the domes where the SiGe is relaxed, towards the most favorable zones where the lattice parameter is the closest from Si (i.e. the substrate). Through this diffusion, they fill the space in between the domes. However, this behavior does not allow to explain the increase of the Ge signal. Second, during the annealing, the Ge atoms may inter-diffuse in the Si substrate, decreasing in the same way the Ge content of the formed domes. This would result in a decrease of the Ge signal which is not the case. Third, the Si diffusion towards the space in between the domes may lead to a homogeneity of the surface. Since its surface energy is lower than that of Si, the Ge tends to stay at the surface in order to minimize the whole system's surface energy. This leads to a lateral segregation of Ge atoms or most probably to the diffusion of both Ge and Si atoms from the domes' top towards the peripheral zones. As a result, the combination of the Si diffusion and Ge segregation in between the domes will lead to the formation of the wetting layer (or at least to an important domes' expansion reducing their thickness and thus going flat) and to an increase of the SiGe surface. These mechanisms are described in ***Fig. IV-6***.

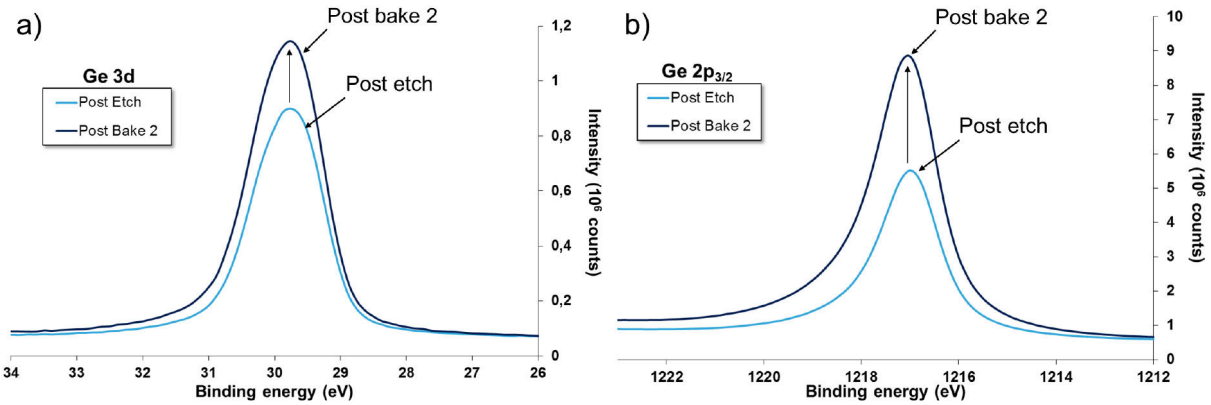

Fig. IV-5*: XPS spectra post etch and post bake 2 of the a) Ge3d and b) $Ge2p_{3/2}$ photoelectron lines. The peak's intensity increases after the bake 2 which may be explained by the formation of a SiGe wetting layer between the domes.*

TABLE IV-1. Peaks' area (in 10^6 counts.sec^{-1}.eV) calculated from XPS measurements for each layer conditions: post 5 nm etch and post bake 2.

Conditions	Ge3d	Ge2p$_{3/2}$
Post etch	1.12	8.31
Post bake 2	1.49	15.08

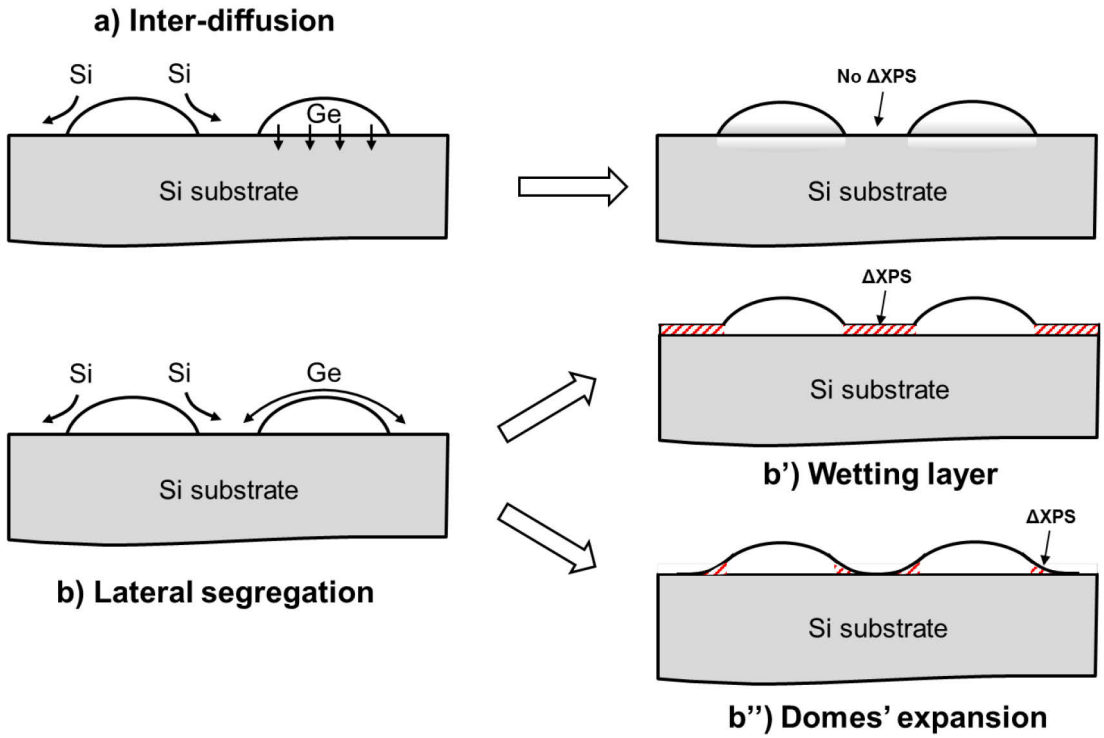

***Fig. V-6**: Schematic representation of the different mechanisms that may occur during the annealing. The Si tends to diffuse on the strained surface from the domes' top to the peripheral zones. a) The **Ge inter-diffusion** does not explain the Ge signal's increase since it may on the contrary decrease the signal. However, b) the **lateral segregation** of Ge atoms in addition to the Si diffusion may lead to the b') **wetting layer**'s formation or to the b'') **domes' expansion**. Both the domes' expansion and the wetting layer may explain the XPS signal increase.*

Fig. IV-7 below shows 5 x 5 µm² and 1 x 1 µm² AFM images of SiGe layers after the first bake (post bake 1), the 5 nm etch and the second bake (post bake 2). The reference layer exhibits a roughness of 8.72 nm which decreases to a value of 7.80 nm after the 5 nm etch. After the second annealing, the roughness strongly decreases and has a value of 5.33 nm. This behavior was also expected and supports the XPS measurements in a sense that the wetting layer is creating (or the domes expand) during the 2nd bake. Indeed, the SiGe matter from the domes diffuse on the Si surface to form the wetting layer. This can lead in average, to a decrease of the roughness. This may also be due to the re-organization of the morphology. Indeed, the anisotropic etching may have transformed the domes into more or less faceted pyramids. In this case, the system is not in an equilibrium state and wants to minimize its energy by forming again domes through surface diffusion.

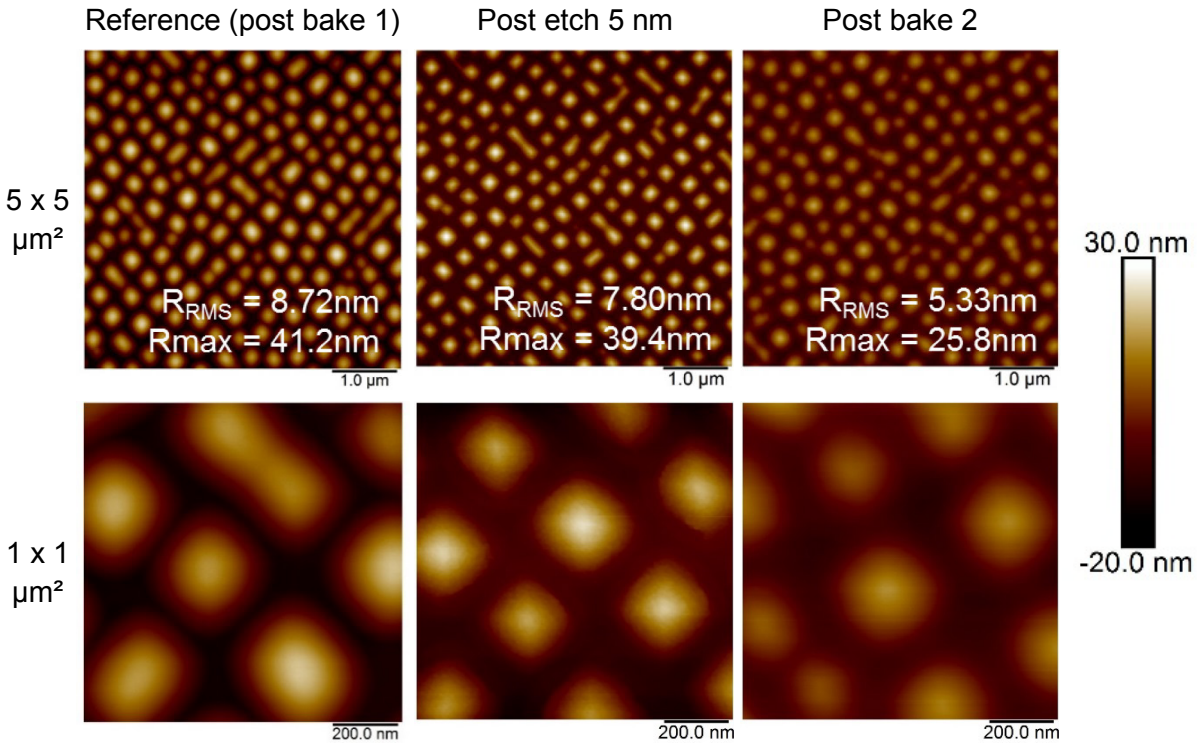

***Fig. IV-7**: AFM images of SiGe layers (from left to right) post bake 1 (reference), post 5 nm etch and post bake 2. The roughness (R_{RMS}) decreases of 33% after the second bake.*

II/ Thermal rounding phenomenon

As already mentioned, most of the experiments of SiGe annealing were performed on non-patterned wafers. Consequently, this part is dedicated to annealing made on patterned wafers. In small patterns, the SiGe films after annealing evolve in a way that the as-deposited facets disappear for the benefit of a rounding shape. This morphological evolution is called thermal rounding and was studied by Seiss *et al.* [Seiss 13-1]. This mechanism is possible as soon as the atoms' mobility is large enough, which is the case at elevated temperatures during an annealing. The main driving force of this thermal rounding activation is the surface energy's reduction. Indeed, it is well known that any system tends to minimize its internal energy. In other words, as the chemical potential is related to the local curvature, the atoms tend to move towards zones with lower curvature, thus leading to a global reduction of the local curvature. ***Fig. IV-8*** below shows the morphological evolution of a 19 nm SiGe (27%) layer before (left) and after (right) annealing at 650°C under H_2 atmosphere.

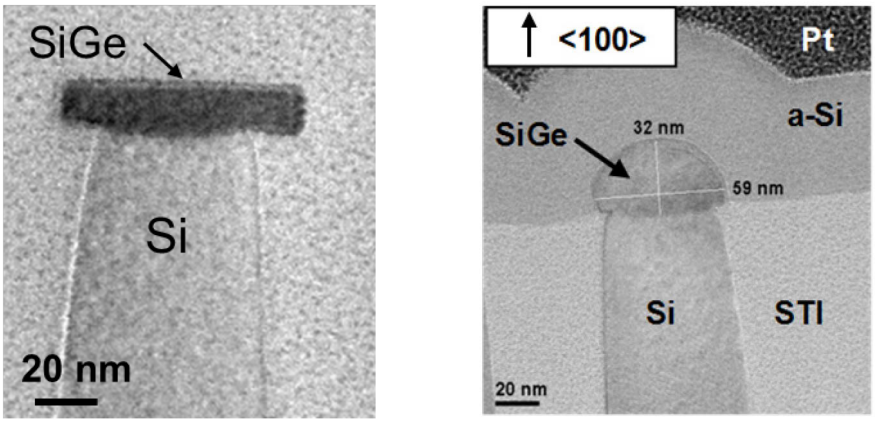

***Fig. IV-8**: TEM cross-section of SiGe deposited in 45 nm <100>-oriented wide lines (left) before and (right) after annealing at 650°C. The facets {001} and their corresponding overgrowths fade away completely until obtain a rounded-shape. Taken from [Seiss 13-1].*

II.1) Instabilities in lines

II.1.a) Annealing of SiGe's lines

The SK instabilities in epitaxial lines were studied by Seiss *et al*. It was shown that these instabilities change with deposited material (Si or SiGe), deposited thickness, lines width and orientation (<100> or <110>). Moreover, for a unique material and considering the post annealed epitaxy perfectly rounded (arc of circle), it was seen that these instabilities appear for a critical central angle equal to 180° [Seiss 13-3]. Instabilities have been widely studied in <100> oriented Si and SiGe epitaxial lines but not extensively in <110> oriented lines. Then, the purpose of this section is to properly study this orientation and to compare the morphology of the lines for the different orientations. For this study, the SiGe layers were annealed under H_2 atmosphere at 750°C. ***Fig. IV-9*** and ***Fig. IV-10*** below show AFM images done in <100> and <110> SiGe oriented lines with different thicknesses and widths: epitaxies of 5 and 19 nm thick and lines widths varying between 60 and 490 nm.

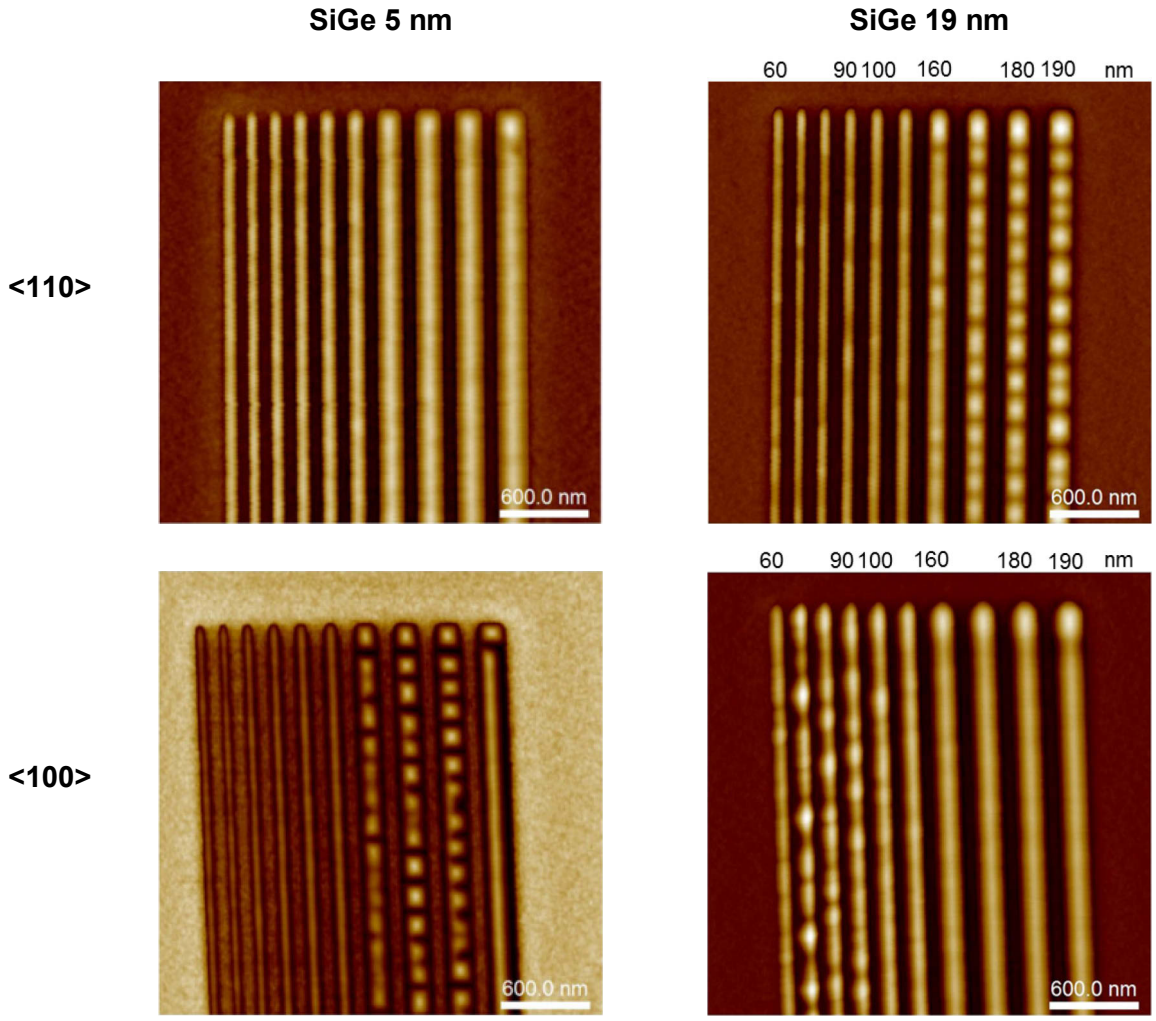

***Fig. IV-9**: AFM images of <100> and <110> oriented lines with different thicknesses and lines widths. The lines were annealed at 750°C under H_2 atmosphere. The morphology strongly depends on the thickness, the width (60-190nm range) and the orientation.*

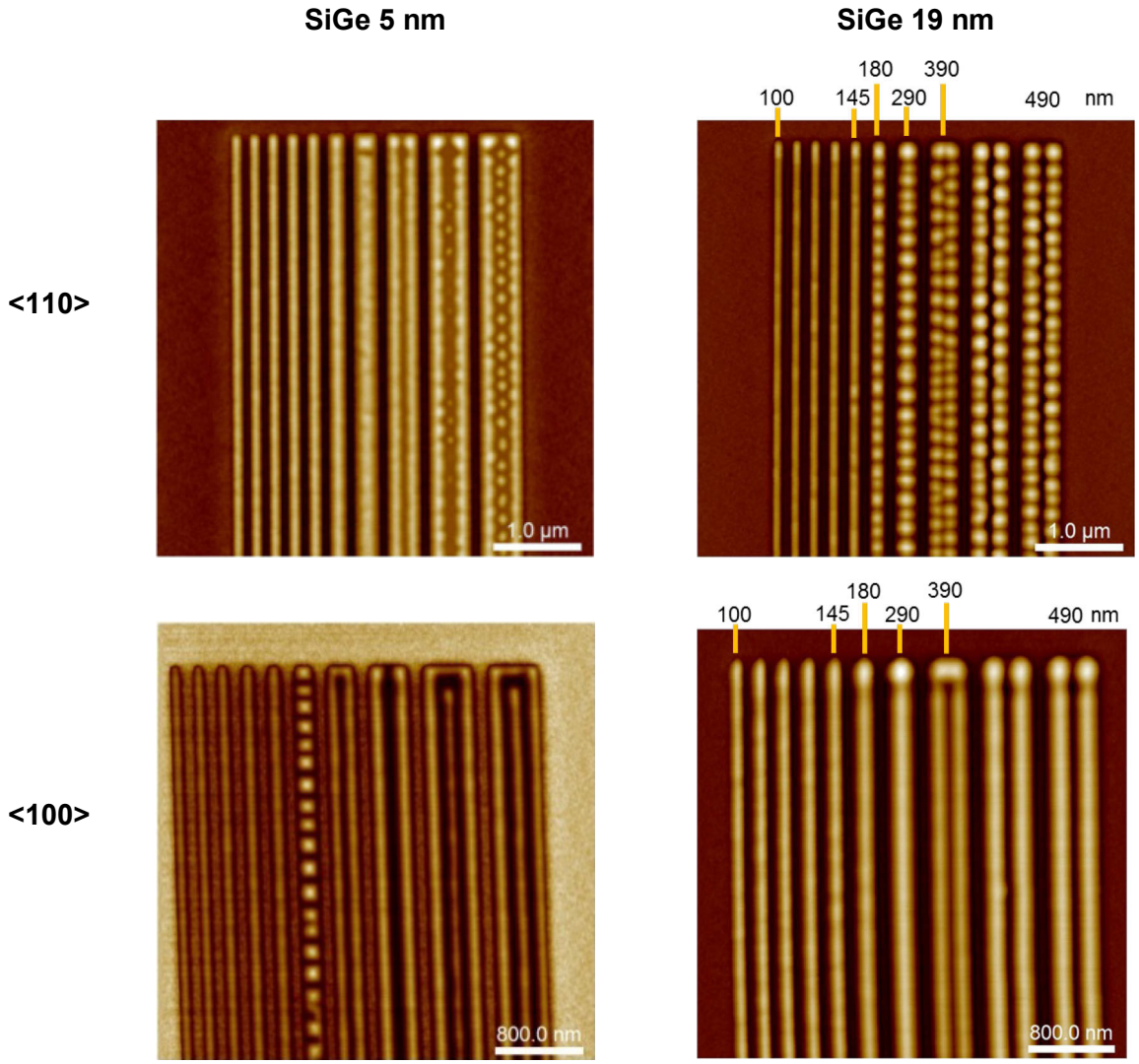

***Fig. IV-10**: AFM images of <100> and <110> oriented lines with different thicknesses and lines widths. The lines were annealed at 750°C under H_2 atmosphere. The morphology strongly depends on the thickness, the width (100-490 nm range) and the orientation.*

In any cases, similarities can be found comparing the morphology of both line orientations in the 60-490 nm width range. For both orientations, stable and instable regions appear, named as rounded and islands (or ridges), respectively, as shown in **Table IV-1**. In the table, several lines' width ranges (60-85 nm, 100-145 nm…) are represented as well as their corresponding morphology.

For the 5 nm thick SiGe, it appears that the <110> oriented lines are stable in a larger range of line's width than the <100> oriented lines. This is clearly seen in the case of a thickness of 5 nm where no instabilities are observed in the narrowest <110> oriented lines, i.e. 60-190 nm compared to <100> oriented ones (islands apparition occur for 160 nm wide lines). Also, for the same thickness but wider lines (290-490 nm), the instabilities in <110> lines appear for a width of 390 nm whereas in <100> lines the instabilities appear sooner, i.e. 180 nm wide lines. The instabilities in wide lines are characterized by the separation of the line into two (or three) separated lines. For the <100> direction, the line separates for a width of 290 nm; for the <110> orientation, it appears at a width of 390 nm. Comparing both orientations, the <100> lines are smooth and rounded whereas the inside of the <110> lines is undulated. Finally, the <100>

and <110> 490 nm wide lines separate in three lines. Along the <100> direction, the instabilities are characterized by the presence of an inner smooth line surrounding by two outer smooth lines. The two outer lines are linked at the end of the pattern. Along the <100> direction, the instabilities are characterized by the presence of inner successive islands all along the line, surrounded by two undulated outer lines. As a result, for thin films, the <110> oriented lines seem to be more stable.

For 19 nm thick films, the instability region for lines' widths comprised between 60 nm and 190 nm, is inversed comparing both orientations. Along the <100> direction, the lines are unstable (presence of bulges) in the 60-100 nm range, whereas the <110> oriented lines are stable in the same width range. In the 160-190 nm range, the <100> oriented lines stabilized, whereas along the <110> orientation, the lines broke into islands, thus are no more stable. Moreover, considering wider lines, i.e. in the 180-490 nm range, the <110> lines reveals the formation of instabilities sooner (180 nm) than <100> lines (390 nm). Considering both the <100> and <110> orientations, the lines separate in two lines for a width of 390 nm. However, along the <100> orientation, the two separated lines are perfectly rounded and smooth which is not the case for the <110> orientation. Indeed, along this direction, the two separated lines are in the form of successive islands. In this case, two instabilities appear: the separation of the lines into two separated lines and the formation of islands along the lines. For thick films and at these lines' widths, the system does not tend to form three lines as observed in thin films. Finally, the lines' ends present for the two orientations, a local thickening of the film due to additional matter caused by epitaxial lateral overgrowth. This local thickening is also observed for the 5 nm tick lines but it is less pronounced.

TABLE IV-1. Summary of the annealed SiGe morphology as a function of line width and line orientation.

	Width (nm)	**60-85**	**100-145**	**160-180**	**190**
<100>	**5 nm**	Rounded	Rounded	Islands	1 ridge
	19 nm	Bulges	Rounded	Rounded	Rounded
<110>	**5 nm**	Rounded	Rounded	Rounded	Rounded
	19 nm	Rounded	Rounded	Islands	Islands

	Width (nm)	**290**	**390**	**490**
<100>	**5 nm**	2 ridges	2 ridges	3 ridges
	19 nm	Rounded	2 ridges	2 ridges
<110>	**5 nm**	Rounded	2 ridges	3 ridges
	19 nm	Islands	2 ridges + Islands	Islands

The phenomenon of islands and ridge formation parallel to the line orientation is attributed to the superposition of two effects occurring during annealing: thermal rounding and SK-like undulations [Dutartre 12]. First, the rounded and smooth shape obtained during the annealing is due to the surface diffusion giving rise to the thermal rounding. Second, this mechanism is assisted by the SK undulation phenomenon which leads for example to the separation of the wide lines in two parts. Indeed, the wavelength of the separated lines formation for the 5 nm thick SiGe is about 160 nm and for the 19 nm thick SiGe it is about 230 nm. These two values are very close to the ones obtained by PSD in very large patterns. This means that depending

on the line's width and the thickness, the line will not or will separate in several parts, which is driven by the SK undulation mechanism. This phenomenon is schematically represented in ***Fig. IV-11***. It gives the number of separated lines that can exist, in theory, as a function of the line's width, for 5 nm and 19 nm thick layers. This graph shows the number increases by discrete values which are shifted to higher line's widths when increasing the growth thickness. For line's width in the order of the wavelength the system does not have enough space to form two undulations but the line may appear very unstable. In order to obtain two lines, the line's width must be in the order of twice the wavelength. In the same manner, three separated lines will be possible for a line's width equivalent to 3 time the wavelength.

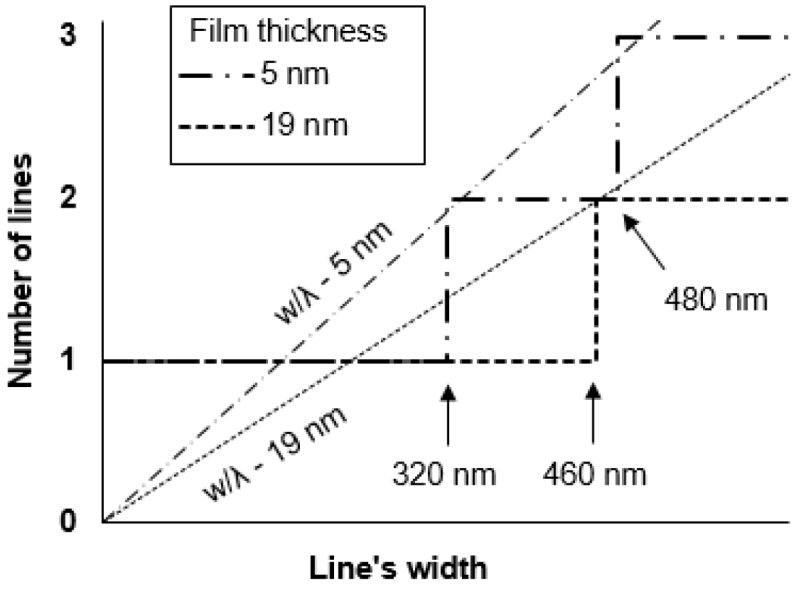

Fig. IV-11*: Schematic representation of the number of separated lines as a function of the line's width. This representation is a theoretical illustration of the above discussion. The number of separated lines that will be formed will depend first on the preferential SK wavelength for a given thickness and thus to the line's width. As example, for a film thickness of 5 nm, the line will separate in two for a width equivalent to twice the SK wavelength, i.e. in this theoretical case 320 nm. The width over the wavelength is also represented by the straight lines.*

Another important observation was done on the instabilities specifically in <110> oriented lines where the islands formation is more pronounced. Having a closer look on the islands, facets apparition was seen as shown in ***Fig. IV-12***. Different line widths were studied: 180, 290 and 490 nm. To note that the x-scale is different for each line width. Two dominant facets were retained from AFM profiles which are {113} and {119} facets. Their experimental and theoretical angles are given in **Table IV-2**. Several differences can be seen in the AFM profiles for the three lines widths given in ***Fig. IV-12***. First the extension of the {119} facets seems to be increased with the line width in comparison to the {113} facets for which the contrary is evidenced. This is due to the fact that the line's width being higher, the mean curvature radius is also higher that favors the presence of facets with lower angles. That is why the system will prefer to form large {119} facets rather than large {113} facets. Also, the profile in wider lines that separated in two (>290 nm) is asymmetric (see ***Fig. IV-12*** d)), i.e. the extension of the outer {119} facets is higher than the inner {119} facets. In average, the outer and inner

extensions are 88 nm and 68 nm, respectively. This may be explained by three hypotheses and probably by a combination of both. First, the outer side of the line is trapped by the interface between the SiO_2 and the Si active zone which is not the case for the inner part. Thus, the morphological behavior of both sides may be different. Second, the line's separation, mainly due to the SK mechanism, presents a narrow valley with a local curvature radius very low. This leads to a relatively steep inner slop which leaves few spaces for the {119} facet. Third, the strain in the Si is different at the line's edges and at the center (line's separation) leading to an asymmetric SiGe relaxation.

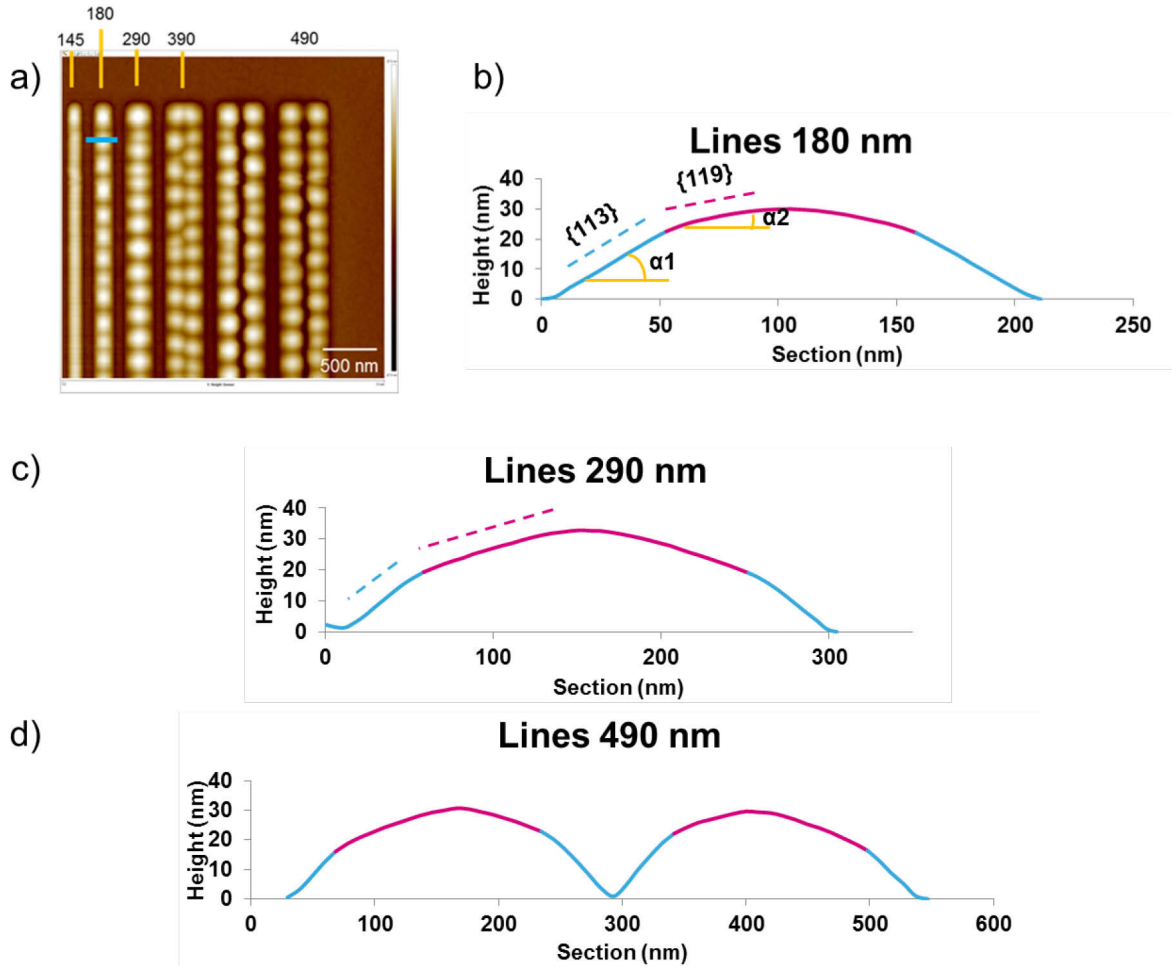

***Fig. IV-12**. a) 3x3 nm² AFM images of <110> oriented lines. The widths are given above the image in nm. b) Horizontal AFM profile of one island (in blue line on the AFM picture) in a 180 nm wide line. α1 and α2 are the facets angles and are equal respectively to 24.6° ± 1.1° and 9.1° ± 0.8° corresponding to {113} and {119} facets. c), d) are AFM profiles of instabilities respectively in 290 and 490 nm wide lines.*

TABLE IV-2. Angles with (001) plane of the {hkl} facets formed in the instabilities in <110> oriented lines. The experimental angles were determined by AFM scans.

Miller indices	Theoretical angle (°)	Measured angles
{113}	25.24	24.6°+/-1.1°
{119}	8.93	9.1°+/-0.8°

II.1.b) Stabilization of instabilities in lines

In the previous part of this chapter, the effects of the thermal rounding in narrow lines was pointed out. It was shown that depending on the active area dimensions and the epitaxy's thickness, the lines can exhibit instabilities with the presence of bulges or islands, or stabilities with a stable and rounded morphology. Both the SK relaxation and the surface energy minimization are the main mechanisms that allow the instabilities or the stabilities to be formed. This part aims at stabilizing the <100> oriented lines that present instabilities with bulges. To do so, 22 nm thick SiGe 25% layers were grown in 70 nm wide lines and annealed at 725°C for 960 sec under 20 Torr of H_2 atmosphere. This annealing will be named anneal 1. The morphology of lines post anneal 1 is displayed in ***Fig. IV-13***.

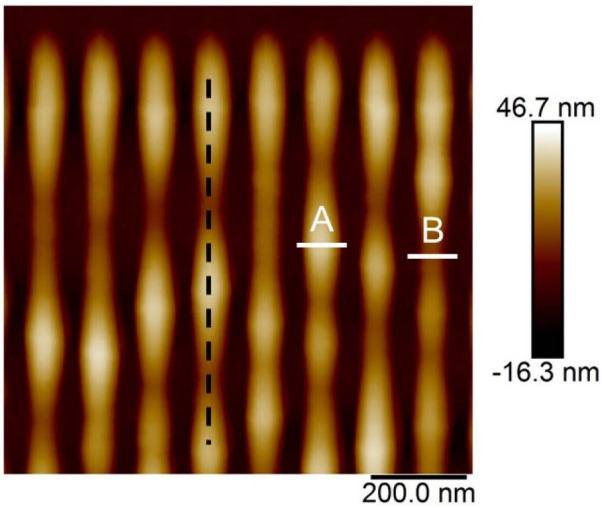

Fig. IV-13*: 3 x 3 µm² AFM height image of 22 nm thick SiGe after anneal 1. The lines are <100> oriented and 70 nm wide. The instabilities characterized by the bulges are observed. The black dash line represents the direction of the height profile used further.*

The lines present huge bulges. The observed height variations of annealed SiGe are quantified by a height profile taken along the middle of each line as indicated by dashed line in ***Fig. IV-13***. The peak-to-valley values are measured for each line and then averaged. The average roughness R_{RMS} is also measured. The bulges have an average peak-to-valley value of 16.3 nm and along the line the roughness is 5.8 nm. The same lines are then thinned in order to reach in average a thickness of 10 nm (i.e. 12 nm is etched) and to get back a stabilization zone. Finally, they are once again annealed at the same temperature and duration as previously. This annealing will be named anneal 2. All the steps of the experiment are schematically represented in ***Fig. IV-14***. The scheme was drawn in cross-section perpendicularly to the lines.

Fig. IV-15 shows SEM images of the 70 nm wide lines after each step of the experiment: post anneal 1, post etch and post anneal 2. AFM images post anneal 1 and post anneal 2 are also depicted. To note that after each step of the experiment, the same wafer was characterized by SEM. However, the AFM images correspond to two different wafers that were processed one after the other. It is clearly observed that post anneal 2, the instabilities that were present after the anneal 1 (and post etch) have been almost completely removed, leaving

stable lines. The height variations are measured as illustrated in ***Fig. IV-15***. A peak-to-valley value of 1.1 nm and a roughness along the lines of 0.6 nm were obtained. These values are 16 times and 10 times lower than the ones measured post anneal 1. All the results are summarized in ***Table IV-3***. The AFM profiles after each step are displayed in ***Fig. IV-16***. The profile given after etching is not an experimental profile since no AFM measurements could be performed at this step.

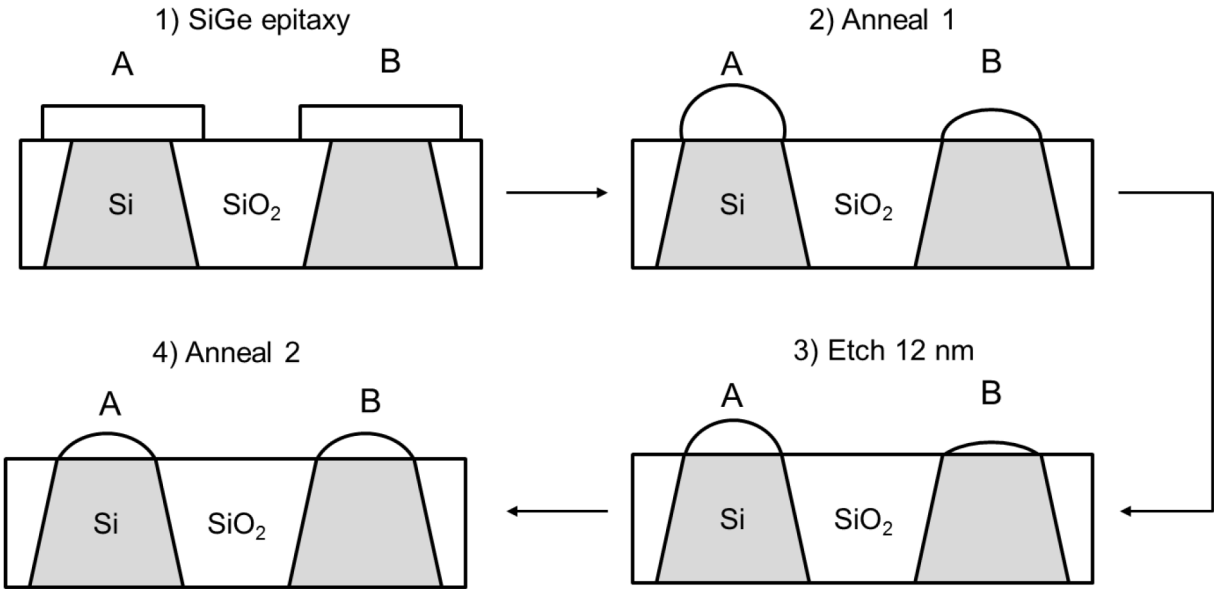

Fig. IV-14*: Schematic representation of the experiment. It represents a cross-section perpendicular to the lines (A = maximum and B = minimum of undulations in* ***Fig. IV-13****). (1) First, a 20 nm thick SiGe epitaxy is done. (2) Second, the layer is annealed at 725°C for 960 sec under 20 Torr of H_2 atmosphere (anneal 1). (3) Third, the lines are thinned by 12 nm (10 nm is left in average). (4) Finally, the layer is again annealed (anneal 2). To note: anneal 1 = anneal 2.*

TABLE IV-3: Height variations and roughness R_{RMS} in SiGe's lines after anneal 1 and after anneal 2. The lines width is 70 nm. It is important to remind that between anneal 1 and anneal 2, a 12 nm etch was done. The peak-to-valley value is described by ΔH_{avg} in the table.

step	th (nm)	ΔH_{avg} (nm)	R_{RMS} (nm)
Post anneal 1	22	16.3	5.8
Post anneal 2	10	1.1	0.6

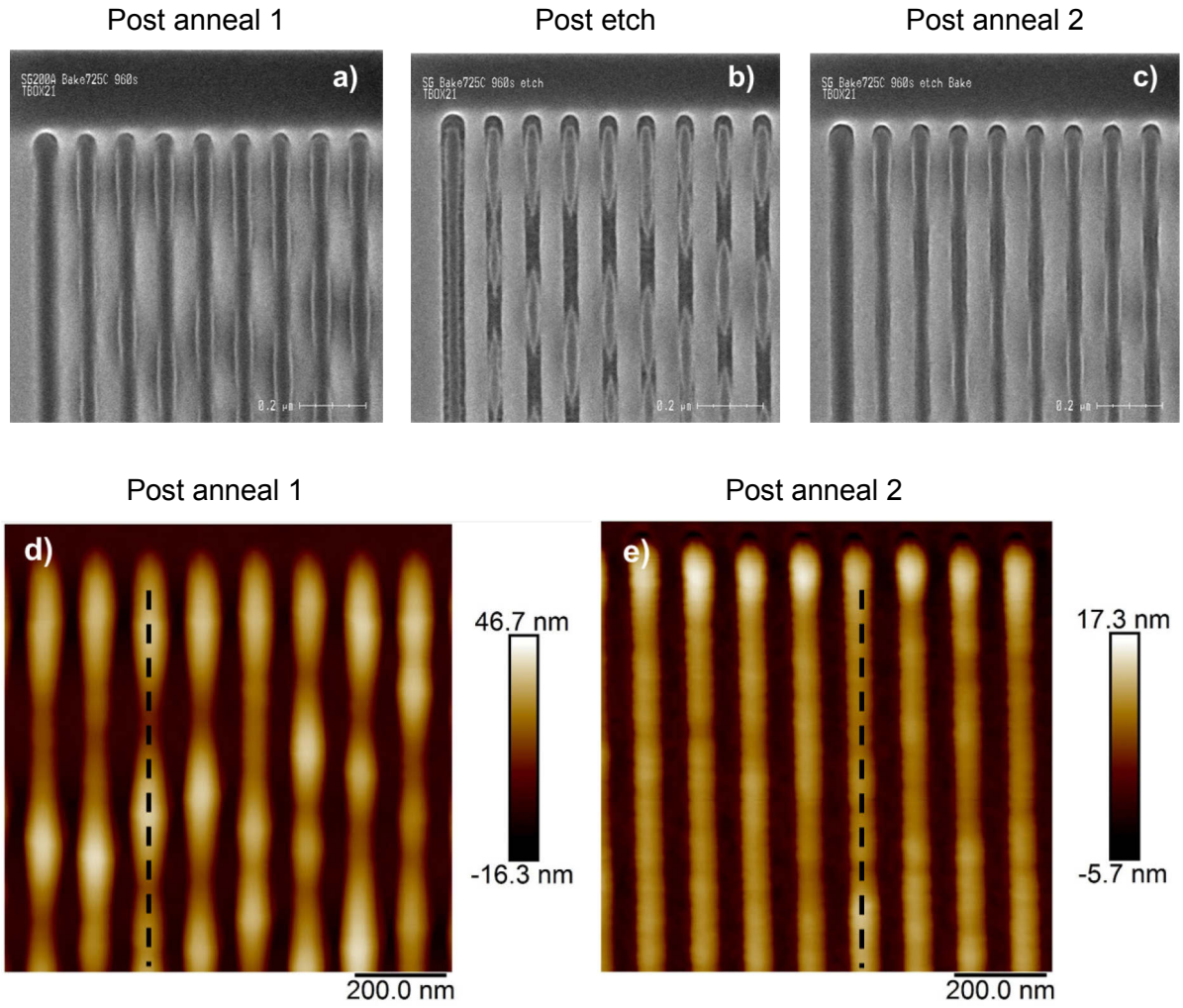

***Fig. IV-15**: a), b) and c) Top-view SEM images of SiGe in 70 nm wide lines after anneal 1, etch and anneal 2, respectively. The SEM images correspond to the same wafer. d) and e) 3 x 3 µm² AFM height images of the same lines post anneal 1 and anneal 2, respectively. **To note that the Z-scale is different for the AFM images**. Two different wafers (processed one after the other) were used for the AFM characterization. After the anneal 2, the instabilities were removed leaving stable lines.*

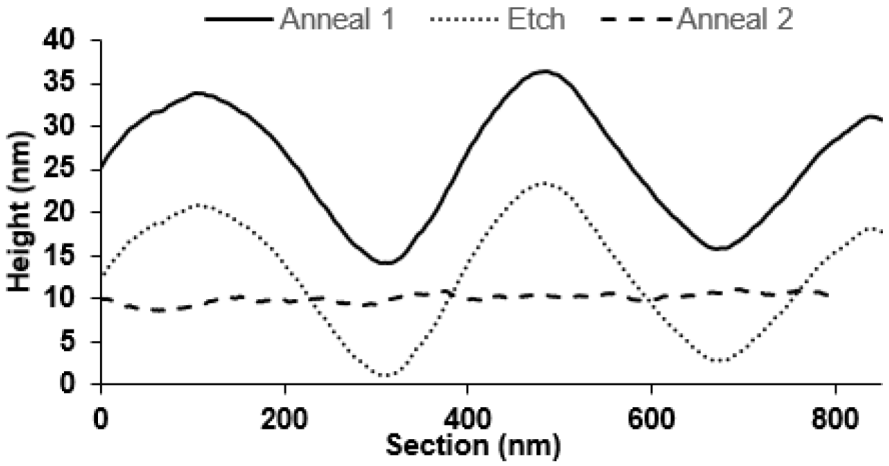

Fig. IV-16*: AFM profiles along the middle of the line after each step of the experiment as shown in* ***Fig. IV-15****. The huge instabilities are clearly removed after the anneal 2. To note that the profile after the etching is not experimental. It is a subtraction of the profile after anneal 1 of the removed matter quantity.*

II.2) Thermal rounding kinetics in SiGe epitaxy

For this study, 20 nm SiGe depositions were made. The Ge content for these layers was about 25%. The initial (as-deposited) morphology is given in *Chapter 3*. Two patterns are studied here: the oval and the quasi-square patterns. For simplicity purposes, the oval and quasi-square patterns will be called pattern 1 and pattern 2, respectively.

II.2.a) Influence of annealing under a hydrogen atmosphere of 20 Torr

In this section, the influence on the SiGe morphology of the temperature and time during annealing under a 20 Torr (i.e. 2660 Pa) H_2 atmosphere is studied. Since several annealing temperatures were used during this study, cautious cares were taken especially during the ramp in temperature to avoid any excessive thermal budget between for example, 650°C and 725°C. The ramp's duration should be similar for any temperature and the overshoot must be as lower as possible. To do so, the temperature ramp was adjusted for all the annealing temperature as well as the PID values as demonstrated in the *Chapter 2*.

Morphology

Four annealing temperatures and durations were used, which are 650, 675, 700 and 725°C, and 30, 120, 480 and 960 sec. The morphological evolution of patterns 1 and 2 as a function of annealing temperatures and durations are given in ***Fig. IV-17*** and ***Fig. IV-18***, respectively. It is easy to see that the pattern 1 evolves very rapidly to its final morphology and obtains a dome-shape with extended facets. The final shape of this pattern is obtained for a thermal budget of 650°C, 480 sec. At 675°C for 30 sec, the pattern 1 has already a dome-shape. ***Fig. IV-19*** gives a magnified AFM image (amplitude error) of the final shape obtained for the patterns 1 and 2. Several facets are observed. In the <110> direction, {111} and {113} facets are measured with theoretical angles with respect to (001) plan, of 54.74° and 25.24° respectively. Along (or close to) the <100> direction, it is observed {715}, {15 3 23} and {105}

facets which are inclined by 67.99° or 54,7°, 33.63° and 11.31° to (001) [Brehm 11] [Vescan 98]. The dome has a typical height of 38 nm and diameter lengths equal to the dimensions of the Si active zone (150 nm long and 120 nm large). This kind of pattern is then more suited for kinetics at lower temperatures (650°C or less). In contrast, the pattern 2 is larger and in this way less sensitive to thermal budget and more suited for higher temperatures. When subjected to different thermal budget, its morphology changes progressively passing through a large panel of steps. First, the edges begin to retract to the active zone. In this step, the facets {001} and {111} and their corresponding overgrowths fade away completely. This is clearly seen during the annealing at 650°C. This phenomenon is called thermal rounding and it gives rise to the formation of rounded ridges all around (annealing at 675°C for 120 sec). These ridges are higher than the interior of the pattern and relatively smooth. A closer look at the corners shows that they are higher than the edges of the pattern. These two observations are named edge and corner effects during which there is a transport of matter coming from the lateral overgrowths towards the pattern's edges and corners [Seiss 13-1]. Then, the corners start to approach towards each other until they collapse to form a single large faceted dome. This final dome is 53 nm high and a diameter of 410 nm, and is obtained for a temperature of 725°C (for a time comprises between 120 sec and 480 sec). Different facets are identified with relatively low miller indices and are the following. In the <110> direction, {113} and {119} facets are observed. The last facet has an angle of 8.93°. In the <100> direction (or close to this direction), the dome presents {105} and {15 3 23} facets.

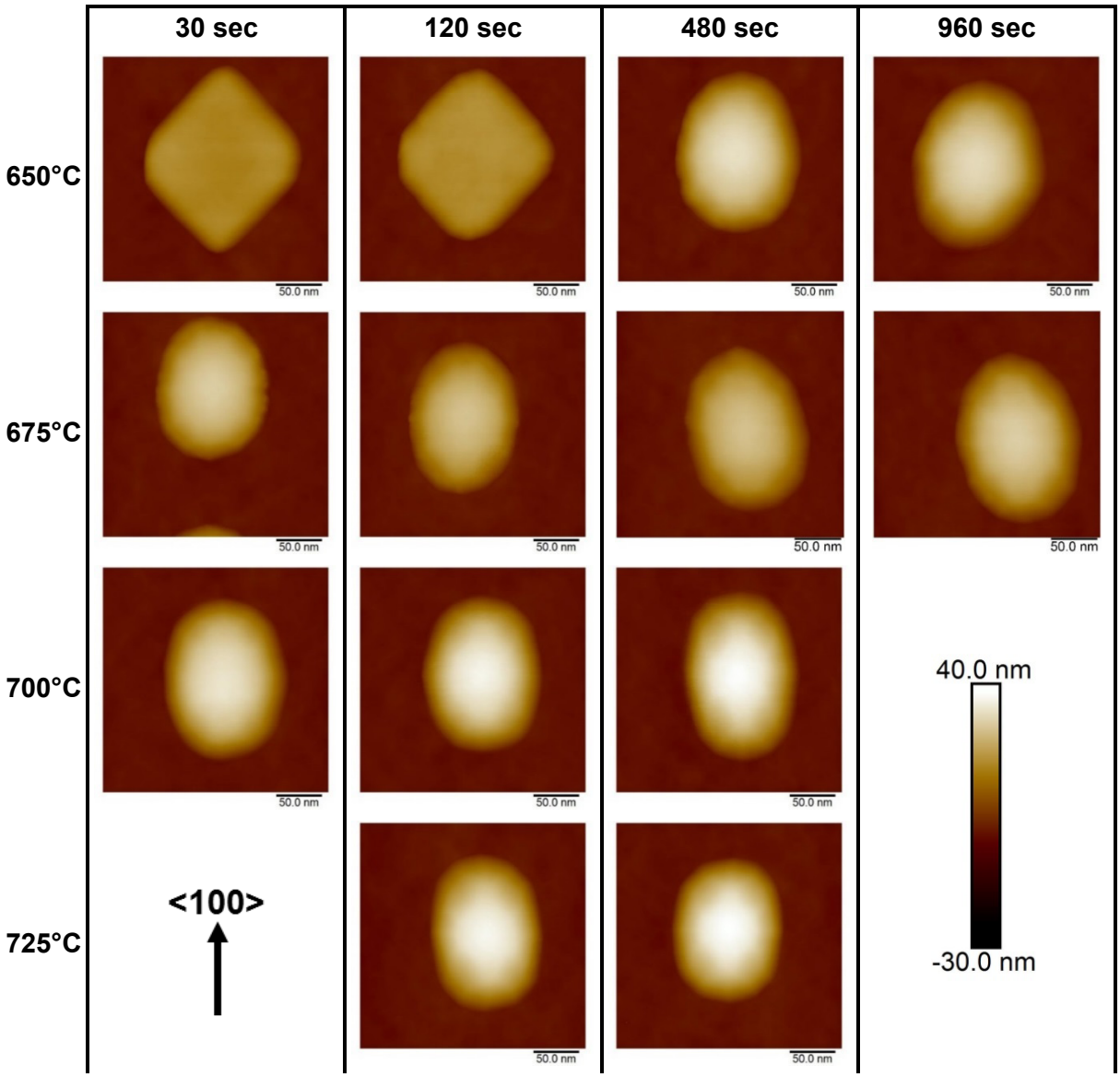

***Fig. IV-17**: AFM images of pattern 1 subjected to different thermal budgets. The temperatures and times used during the annealing are given in the pictures. They range from 650°C to 725°C for temperatures and from 30 sec to 960 sec for times. The final morphology is rapidly obtained since a thermal budget of 650°C, 480 sec is enough to round the pattern.*

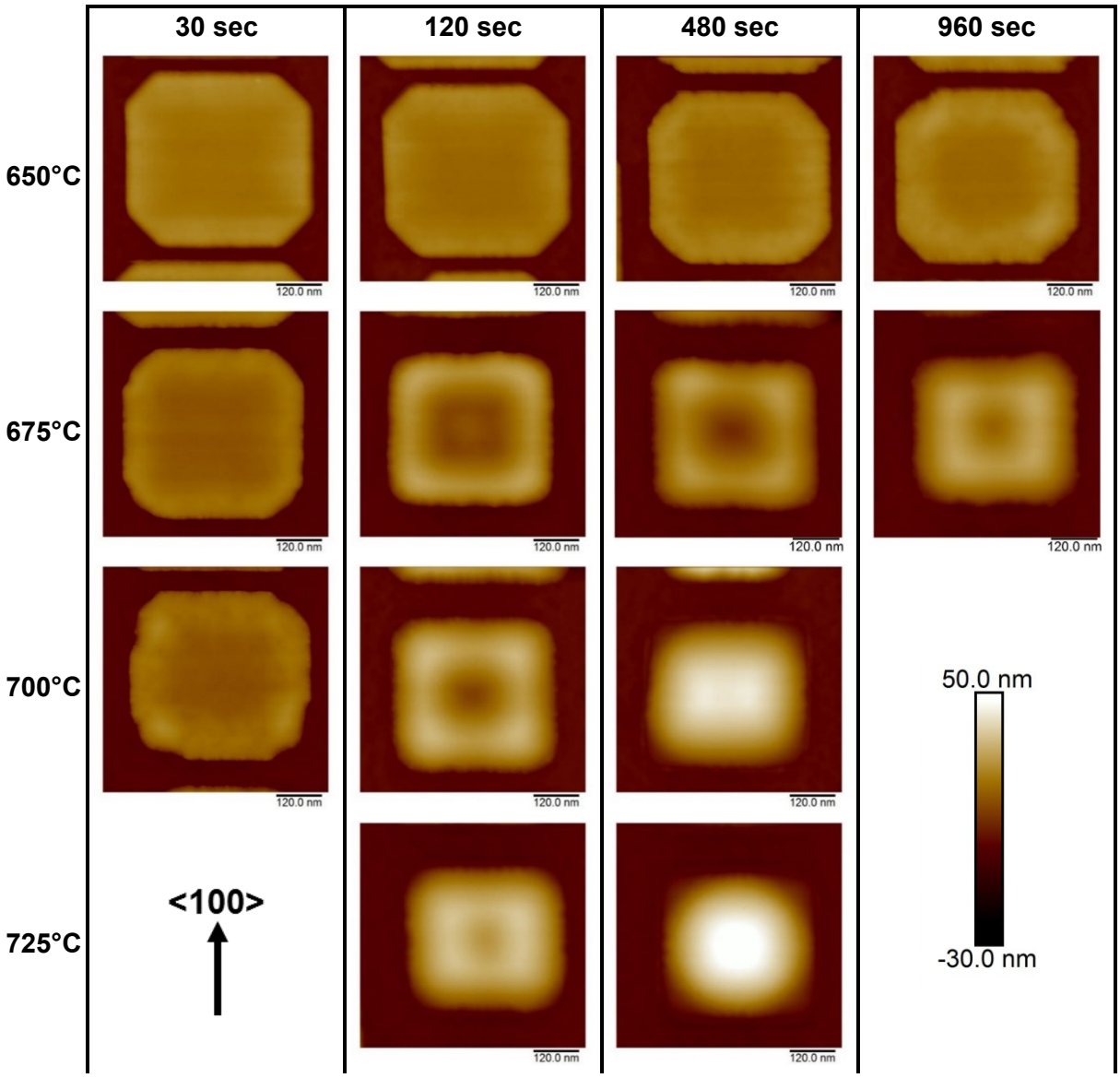

***Fig. IV-18**: AFM images of patterns 2 subjected to different thermal budgets. The temperatures and times used during the annealing are given in the pictures. They range from 650°C to 725°C for temperatures and from 30 sec to 960 sec for times. The pattern 2 being larger, it is less sensitive to thermal budget and a clear screening of its evolution is possible. The final shape is obtained for a thermal budget of 725°C, 480s (or less, meaning between 120s and 480s).*

The final morphology of both patterns and the location of all facets are shown more in details in ***Fig. V-19***. The images are the amplitude error of the AFM. The amplitude image shows how the tip deflected as it encountered the sample's surface; in other words, it is the image of the signal error of the AFM. This kind of image is well suited to have a clear view of the topography. An important point to note is that the z-scale in amplitude error is completely meaningless in terms of the sample's structure, which explains why the z-scale is not represented in the images. For assignment of miller indices, the measured angles were then compared to the theoretical inclination of a large number of {*hkl*} surfaces, and the ones with the best match and reasonable low miller indices are listed in **Table IV-4**. As proved in this table, for these

facets, the theoretical angle value θ is within the experimental error bars or at least within 1° of the experimental values. In **Table IV-4**, the {*hkl*} facets are ordered from top to bottom according to increasing inclination angle θ. It is worth to note that the higher the thermal treatment, the more visible the facets. This means that the small facets appear progressively during the thermal rounding until the final equilibrium shape is reached. At this step, the facets are well visible.

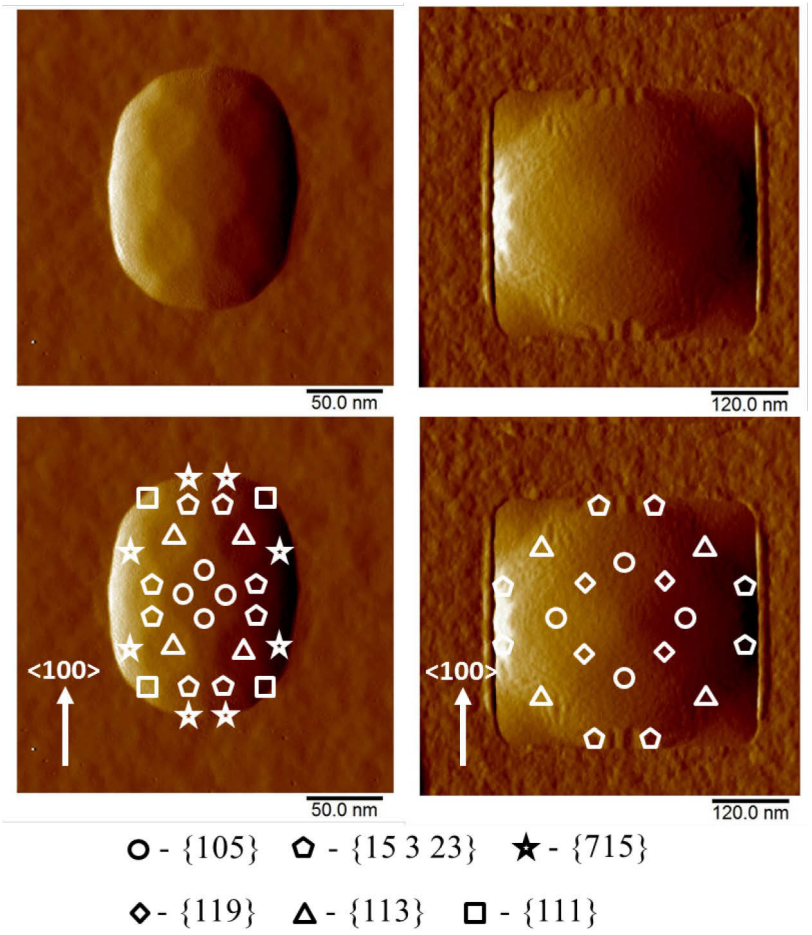

***Fig. IV-19**: AFM amplitude error image showing the final shape of (left) pattern 1 and (right) pattern 2. The surface orientation was measured by AFM. The majority of the facets are marked by the small white symbols and listed below the pictures.*

TABLE IV-4. List of facets with their corresponding experimental and theoretical angle θ. The error bars are also given here.

Facet	Θ_{th} (°)	Θ_{exp} (°)
{119}	8.93	9.0 ± 0.3
{105}	11.31	11.6 ± 0.5
{113}	25.24	25.7 ± 0.6
{15 3 23}	33.63	34.0 ± 0.4
{715}	54.74	54.6 ± 0.3
{111}	54.74	54.3 ± 1.2

Rounding kinetics

Pattern 2 is used to compute the rounding kinetics. To do so, the displaced volume of matter is measured by an AFM tool called “bearing analysis”. This method allows the volume to be calculated by integrating the data above a given threshold value. Taking an AFM section, it can be schematize as shown in ***Fig. IV-20*** below. The gray parts in this figure represent the integrated part of the pattern. Integrating above the entire pattern, it is possible to obtain the displaced volume of matter. To note, only the first points were used to compute the kinetics since the displaced volume cannot run to infinite (evolution towards a final faceted dome). The displaced volume as a function of the annealing times is plotted in ***Fig. IV-21***. As observed, the displaced volume is roughly linear with time until a certain value is reached corresponding to the moment where no more matter can be displaced. The linear dependence of the volume with time allows to obtain three different slopes: (2479 ± 159) $nm^3.s^{-1}$ for 650°C, (31737 ± 1742) $nm^3.s^{-1}$ for 675°C and (80317 ± 6509) $nm^3.s^{-1}$ for 700°C. Finally, the slopes for each annealing temperature are displayed in the same figure (bottom) as a function of reverse absolute temperature (Arrhenius plot). From this last graph, it is possible to extract two different energies: (2.9 ± 0.5) eV and (7.7 ± 0.5) eV, corresponding to two different regimes. In the figure, the dashed line gives the activation energy of the Si surface diffusion.

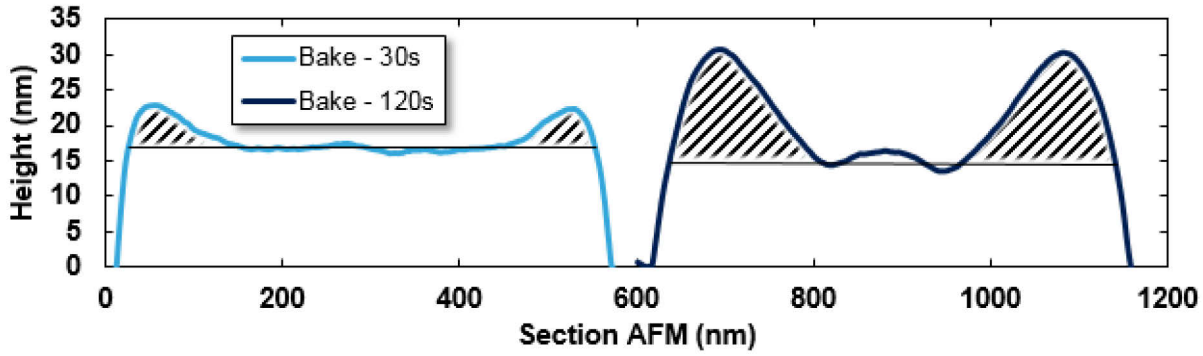

Fig. IV-20*: AFM sections of pattern 2 annealed at 675°C for 30 sec and 120 sec (from left to right). The grey parts correspond to the integrated zone.*

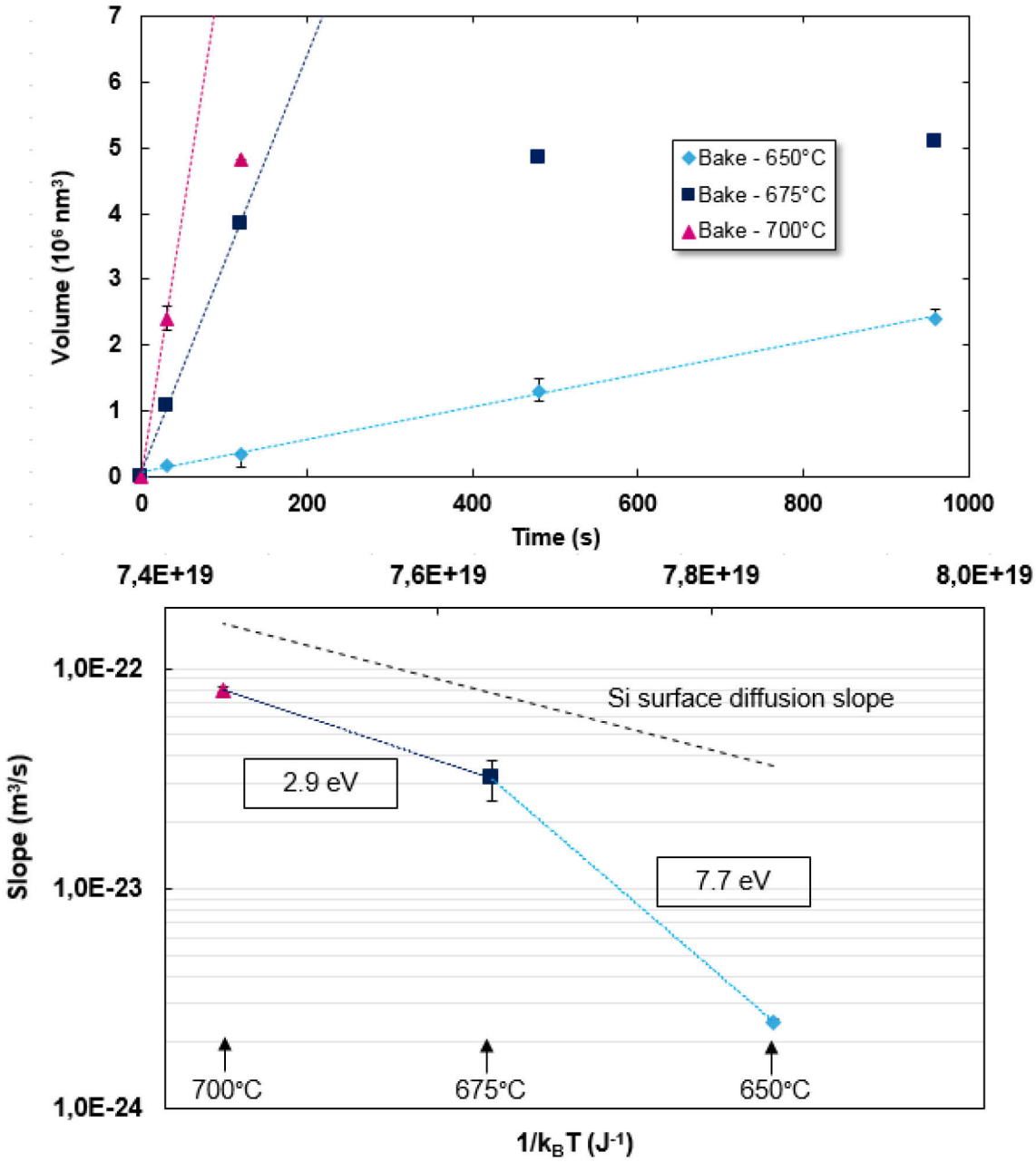

***Fig. IV-21**: Top: Evolution of the displaced volume of matter as a function of time for different annealing temperature (650°C, 675°C and 700°C). Bottom: Slopes of the previous graph as a function of the reverse absolute temperature (Arrhenius plot). Two energies can be extracted: 2.9 eV and 7.7 eV.*

The energy of 2.9 eV is close to the activation energy of the Si surface diffusion which is 2.3 eV [Keeffe 94]. This means that at relatively high annealing temperature, the rounding kinetics is mainly driven by the Si surface diffusion. On the contrary, the high apparent energy measured for lower temperature is probably due to the apparition of another mechanism, in addition to the surface diffusion. Indeed, at low temperature, the H coverage increases preventing the surface diffusion to be effective and thus the thermal rounding occurs slower. Thus the “apparent” activation energy of 7.7 eV would correspond to the combination of the surface diffusion activation and the evolution of the H surface coverage.

II.2.b) Influence of pressure during anneal

The study of pressure influence during annealing is given in this section. Identical depositions as the ones presented in the previous part are annealed under various pressures of H_2 atmosphere. Pressures of 5 Torr (665 Pa), 10 Torr (1330 Pa) and 200 Torr (26600 Pa) are used. The recipes are adjusted in order to get exactly the same temperature in each condition. Indeed, if no corrections are done, the actual temperature of the wafer changes when the pressure is modified (see *Chapter 2 II/ Epitaxy chambers*). A dummy wafer is firstly processed and annealed at the desired temperature. The temperature is then measured by the top pyrometer and adjusted directly in the recipe. This manipulation is performed for each pressure change. The morphology after annealing at 650°C during 120 sec is displayed in ***Fig. IV-22***. It is observed that the H_2 pressure has a huge influence on the post annealed morphology. Indeed, at high pressure, the as-deposited morphology is kept at this temperature meaning that the SiGe layer can handle much higher thermal budget. For similar thermal budget and at lower pressures (10 Torr and 5 Torr), thermal rounding occurs much faster: pattern 1 has already reached its equilibrium dome shape, and pattern 2 presents rounded ridges which were observed for an annealing of 675°C for 120 sec at 20 Torr.

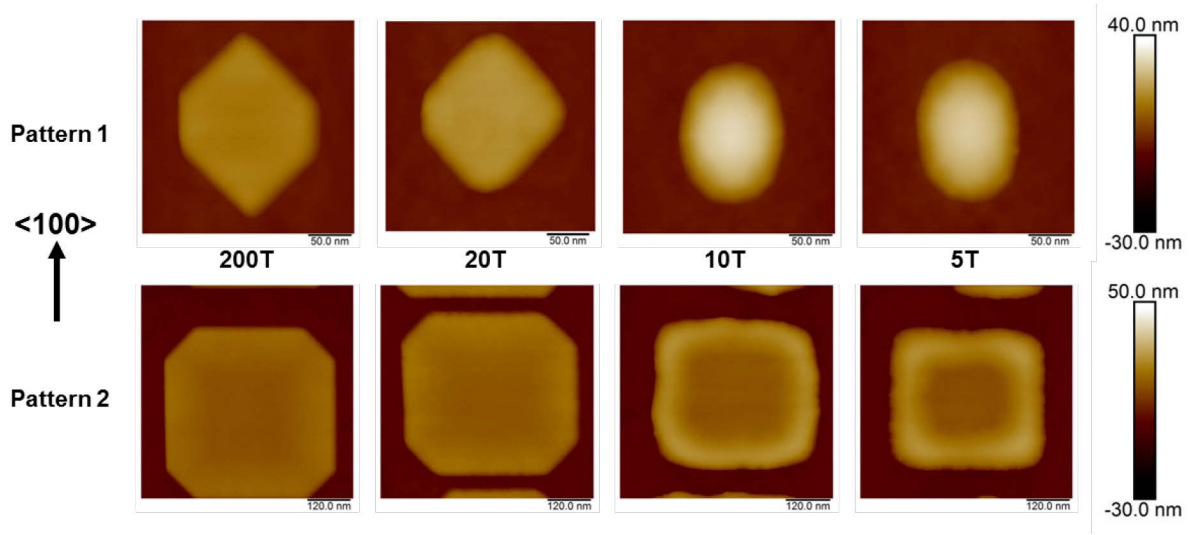

Fig. IV-22*: AFM images of pattern 1 and 2 annealed at various pressures: from 200 Torr to 5 Torr (left to right). The thermal budgets are the same, i.e. 650°C for 120 sec.*

Fig. IV-23 shows AFM images of pattern 1 annealed at temperatures from 700°C to 750°C for 120 sec under 200 Torr. Even at 750°C, pattern 1 did not reach its final morphology. This can be explained in terms of Si ad-atoms surface diffusion which is very affected by the pressure due to the fact that hydrogen atoms stick to the surface more or less efficiently. For low pressure, hydrogen coverage is decreased allowing Si ad-atoms to diffuse on the surface increasing the thermal rounding's efficiency. On the contrary, for high pressure, the H coverage is high as well impeding the Si ad-atoms to diffuse and thus the thermal rounding.

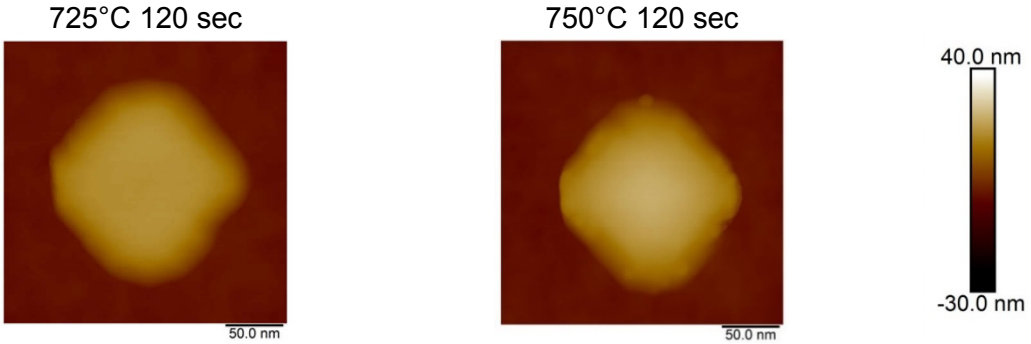

***Fig. IV-23**: AFM images of pattern 1 annealed under H_2 atmosphere of 200 Torr for 120 sec at (left) 725°C and (right) 750°C. Under high pressure annealing, the pattern can handle a much higher thermal budget due to a slower Si ad-atom diffusion.*

II.2.c) Influence of carrier gas during anneal: N_2

In this part, the influence of the carrier gas during the annealing is studied. The gas is replaced by N_2 at the same pressure of 20 Torr. The wafers were annealed for 120 sec at 650°C. ***Fig. IV-24*** shows AFM height images of both pattern 1 and pattern 2 after annealing; on the left, the patterns were annealed under N_2 atmosphere and on the right, the patterns were annealed under H_2 atmosphere. Comparing both cases, a clear morphological difference is visible. Indeed, when using N_2 carrier gas, the pattern 1 has obtained its final rounded faceted shape whereas it is not the case for annealing under H_2 atmosphere. This difference is even more visible regarding to the pattern 2. Under N_2 atmosphere, the edge and corner effects have already occurred with the formation of smooth rounded ridges all around the pattern and higher corners than the ridges. Also, the {111} and {001} facets with the corresponding overgrowth completely disappeared. On the contrary, under H_2 atmosphere, the post-annealed morphology is similar to that of as-deposited meaning that the thermal budget was not sufficient enough to lead to thermal rounding. This difference between both carrier gases can be explained by the fact that nitrogen atoms do not adsorb on the surface, or at least very weakly as compared to hydrogen atoms. As a result, the Si ad-atoms are less stopped by adsorbed atoms and can diffuse on the surface much easier. The thermal rounding is consequently more efficient when using N_2 as carrier gas instead of H_2. Finally, comparing the morphology of pattern 1 and pattern 2 after N_2 annealing with the one obtained after H_2 annealing (*see Fig. IV-17 and Fig. IV-18*), a thermal treatment under 20 Torr of N_2 at 650°C for 120 sec is almost similar to a thermal treatment under 20 Torr of H_2 at 700°C for 120 sec. As a result, and at this temperature range, an annealing temperature decrease of 50°C is sufficient to obtain the same morphology when passing from H_2 to N_2 atmosphere. This could be very important for devices since low thermal budgets are required to avoid any degradations.

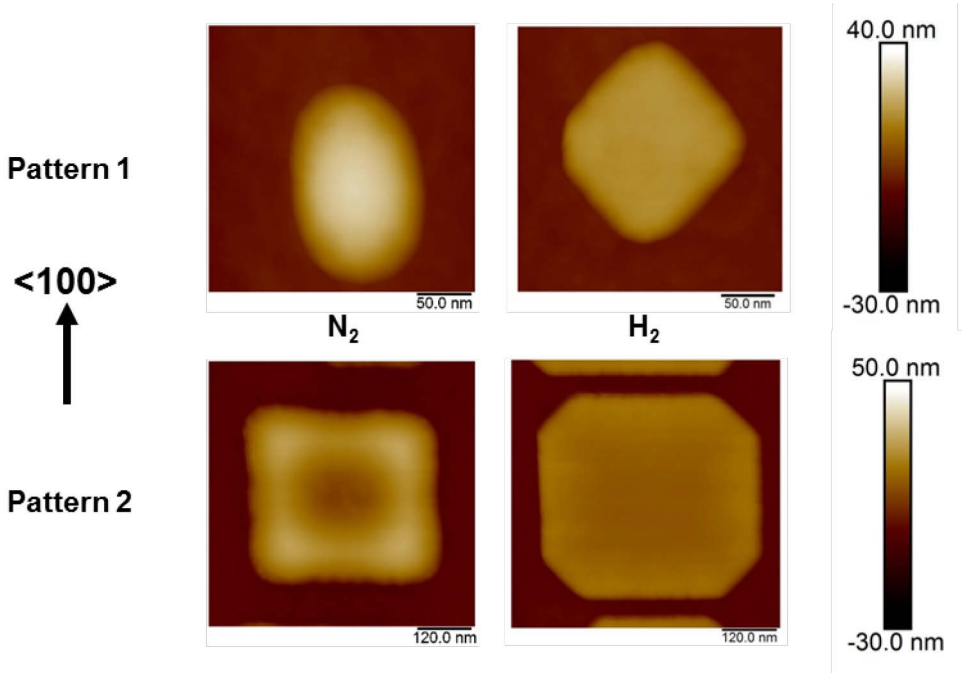

***Fig. IV-24**: AFM images of pattern 1 and 2 annealed under 20 Torr of (left) N_2 and (right) H_2 atmosphere. The thermal budgets are the same, i.e. 650°C for 120 sec. A clear morphological difference between both N_2 and H_2 annealing is observable. This means that nitrogen atoms hardly adsorb on the surface allowing an easy Si diffusion.*

III/ Si-based epitaxies on non-flat surface

The morphological behavior of Si-based cap layers grown on a non-flat surface is investigated in this part. The use of caps is more and more used in microelectronics mainly to improve the performances or to avoid some degradations. This is the case, for instance, in SiGe RSD, a Si cap layer has been defined as a solution to avoid morphological degradation when the metal contact is formed. Indeed, the salicidation of the SiGe top layer creates a large number of defects causing severe contact punch-through [Kasim 14]. These degradations are mainly due to Ge segregation at elevated temperatures leading to a non-stable metal germanosilicide contact [Liu 05] [Lai 99]. The nickel silicide contact formed by adding a Si capping shows better characteristics [Yang 03] [Wu 03]. This part allows the understanding under the scenes of how Si-based epitaxy behaves on a non-flat surface.

The non-flat under layer was made of 8 nm annealed SiGe (25%) selectively grown on Si active zones. The annealing conditions are 850°C for 60 sec under a 20T of H_2 atmosphere. The post anneal morphology is displayed in ***Fig. IV-25***. Three different patterns were investigated: a large box (100 x 52 µm²), a rectangle (493 x 290 nm²) and a SRAM (340 x 105 nm²). The dimensions of the box being very large, it could be considered as a full sheet wafer resulting in SK-like relaxation due to the stress presents in the SiGe layer. The formation of domes and lines, oriented along <100> direction, are consequently observed. The smallest patterns (rectangle + SRAM) have reached their equilibrium shape due to thermal rounding.

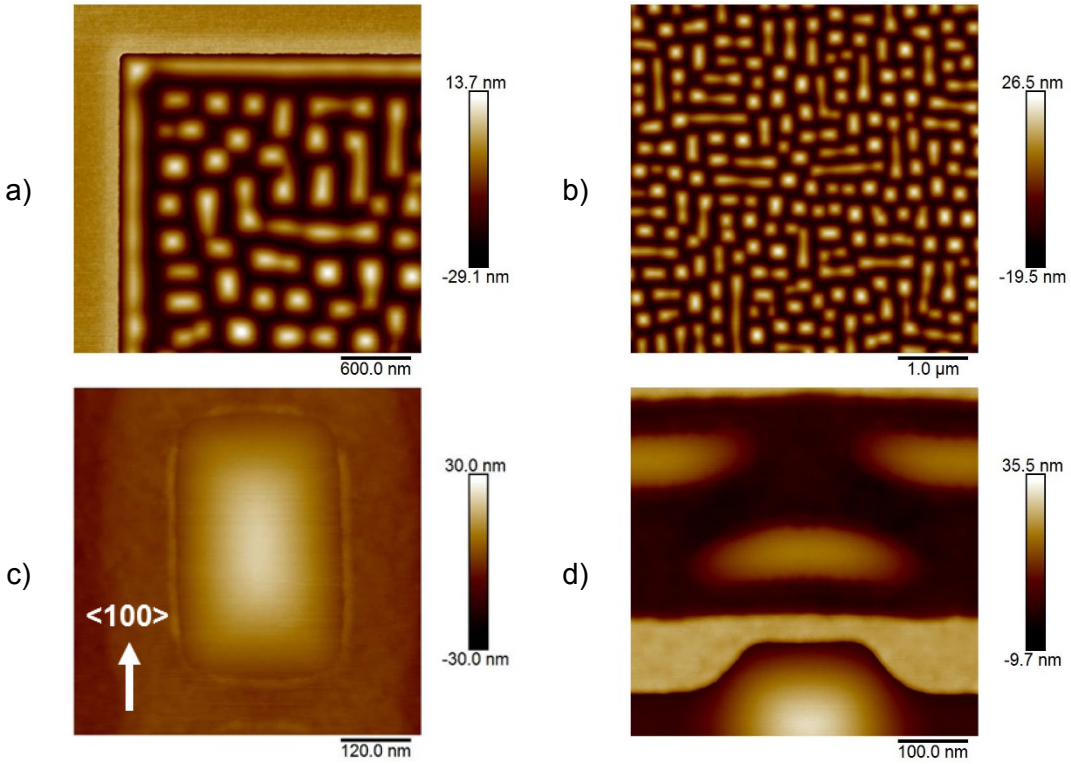

***Fig. IV-25**: AFM tapping images of the 8 nm annealed SiGe under layer. The annealing was performed at 850°C for 60 sec under H_2 atmosphere. The investigated patterns are a) and b) large box (100 x 52 µm²), c) rectangle (493 x 290 nm²), and d) SRAMs (340 x 105 nm²).*

Different Si-based cap layers of different thicknesses (8 or 16 nm) are grown on the above structures: either the cap is made of Si or it is made of SiGe. Also, the influence of the growth rate and of the Ge content on the capping morphology are studied. For the Si caps, GR from 2.2 nm/min to 4 nm/min are studied. For the SiGe caps, Ge contents of 25% and 31% were used. The growth conditions for each cap are listed in **Table IV-5**. Since the Si growth temperature is higher than that of SiGe, the morphology of the annealed SiGe under layer is frozen in order to be comparable for each cap.

TABLE IV-5. Growth conditions for Si-based cap layers

Material	Carrier gas	Chemistry	Growth temperature
Si	H_2	DCS only	715°C
SiGe 25%	H_2	DCS + HCl + GeH_4	630°C
SiGe 31%	H_2	DCS + HCl + GeH_4	610°C

In the following, the different caps are listed, containing information about the GR and layer thickness.

- Si caps; 2.2 nm/min, 3.4 nm/min and 4.0 nm/min; 8 and 16 nm.
- SiGe (25%); 1.8 nm/min; 8 and 16 nm.
- SiGe (31%); 2.7 nm/min; 8 nm.

For simplicity, in the following, the terms lowGR, medGR and highGR will be used to defined low Growth Rate (2.2 nm/min), medium Growth Rate (3.4 nm/min) and high Growth Rate (4.0 nm/min), respectively.

III.1) Comparison between Si and SiGe caps

III.1.a) In large pattern (box)

Fig. IV-26 shows 5 x 5 µm² AFM images of the morphology in the large boxes for each cap layer. The vertical scale is the same for all the images. The reference layer (SiGe under layer) is shown on the top of the figure and a roughness (R_{RMS}) of 8.01 nm is measured. Independently of the cap, a very specific behavior is observed when a cap is added on the SK surface, especially in the case of domes: some very geometrically regular and repeatable platforms are created. Each platform can be considered as a pyramid more or less truncated, with a squared base, for which the edges are oriented along the [110] and [-110] directions. Considering Si caps, it is observed that the roughness decreases when the GR decreases. Therefore, a high GR, accelerating the capping by Si, favors a conformal growth. However, the thickness does not impact the roughness since similar values are measured. R_{RMS} values from 7.45 nm to 6.41 nm for 8 nm thick caps, and from 7.37 nm to 6.72 nm for 16 nm thick caps are obtained. When regarding 8 nm thick SiGe caps, it is clear that the adding of Ge impacts considerably the morphological behavior of the caps since a smaller roughness (5.79 nm) is measured for SiGe 25% caps. Moreover, when increasing the Ge content to 31% the roughness is almost decreased of a factor of 2 and reached a value of 3.29 nm. In addition to that, the thickness has an influence of the roughness which is not the case for Si cap layers. Indeed, for a SiGe 25% cap with a thickness of 16 nm, the roughness is equal to 3.57 nm which is quite similar as the 8 nm thick SiGe 31% cap. This means that a top surface with a roughness comparable to the one of an as-deposited epitaxy (~ 0.1 nm) can be reach increasing the SiGe cap thickness. This behavior seems not to be possible with Si caps.

The mechanisms occurring during the caps' growth are similar to the one already discussed during the wetting layer formation (*see chapter 4*). During the cap's growth, the Si ad-atoms may diffuse from the domes' top to the wetting layer. In addition, the Ge segregation and/or the inter-diffusion may lead to a flattening of the post annealed SiGe domes. Furthermore, a low GR and thus a longer growth's duration, may enhance the inter-diffusion resulting in flatter domes. Consequently, it would be easier to grow a Si cap with a lower roughness since the roughness of the SiGe layer is lower as well. This may explain the roughness' decrease when decreasing the Si cap's GR. On the contrary, a high GR with the high H coverage will lead to a conformal cap's growth since the Si does not have enough time to diffuse. This explains the high roughness of the Si caps having a high GR.

As observed the SiGe levels the surface well better that the Si cap. This may imply that the Si and Ge ad-atoms surface diffusion is higher than that of Si ad-atoms alone in the case of Si caps. The leveling of the surface is more efficient with increasing Ge content, meaning that Ge acts as a diffusion catalyzer. This may be due to an enhancement of the strain's gradient between the top and the bottom of the domes and a lower H coverage. Indeed, in between the domes, the SiGe cap is compressively grown on the wetting layer increasing the strain's gradient. As a result, the Si ad-atoms would diffuse faster towards the domes' bottom in order to relax this compressive layer.

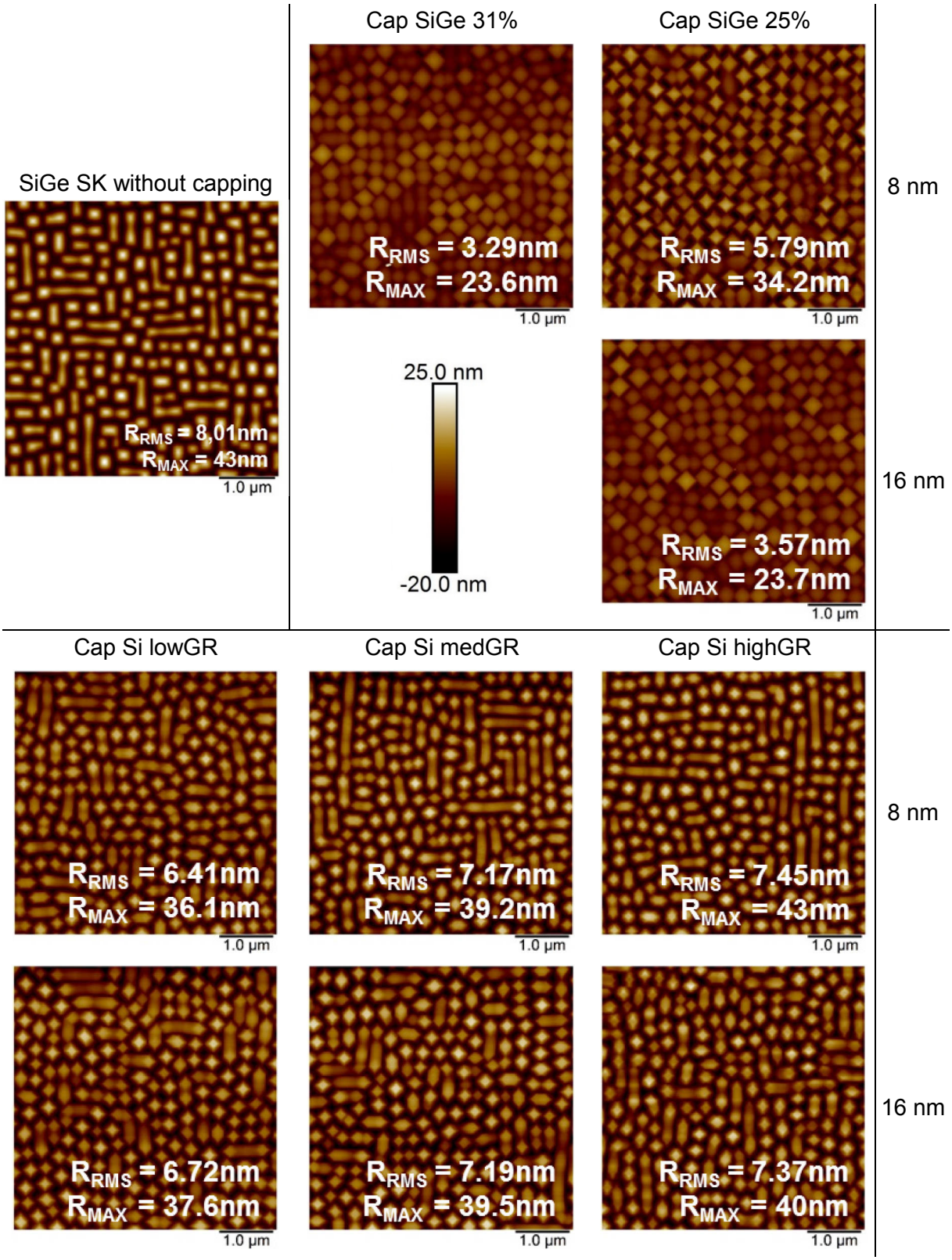

***Fig. IV-26**: AFM images of SiGe (25% and 31%) and Si caps deposited on SK-like relaxation surface (top right image). The roughness is reported directly on the figure. A much higher decrease of the roughness for SiGe caps than for Si caps is observed. Moreover, the thickness has an influence on the roughness only for SiGe caps, meaning that a top surface with a roughness comparable to the one of an as-deposited epitaxy (~ 0.1 nm) can be reach increasing the SiGe cap thickness.*

Fig. IV-27 gives higher-magnification AFM amplitude error images of domes created by SK-like relaxation in the same large patterns capped with Si (GR = 2.2 nm/min) or with SiGe 25%; both thicknesses are given. Complementary HRTEM images are given in ***Fig. IV-28***.

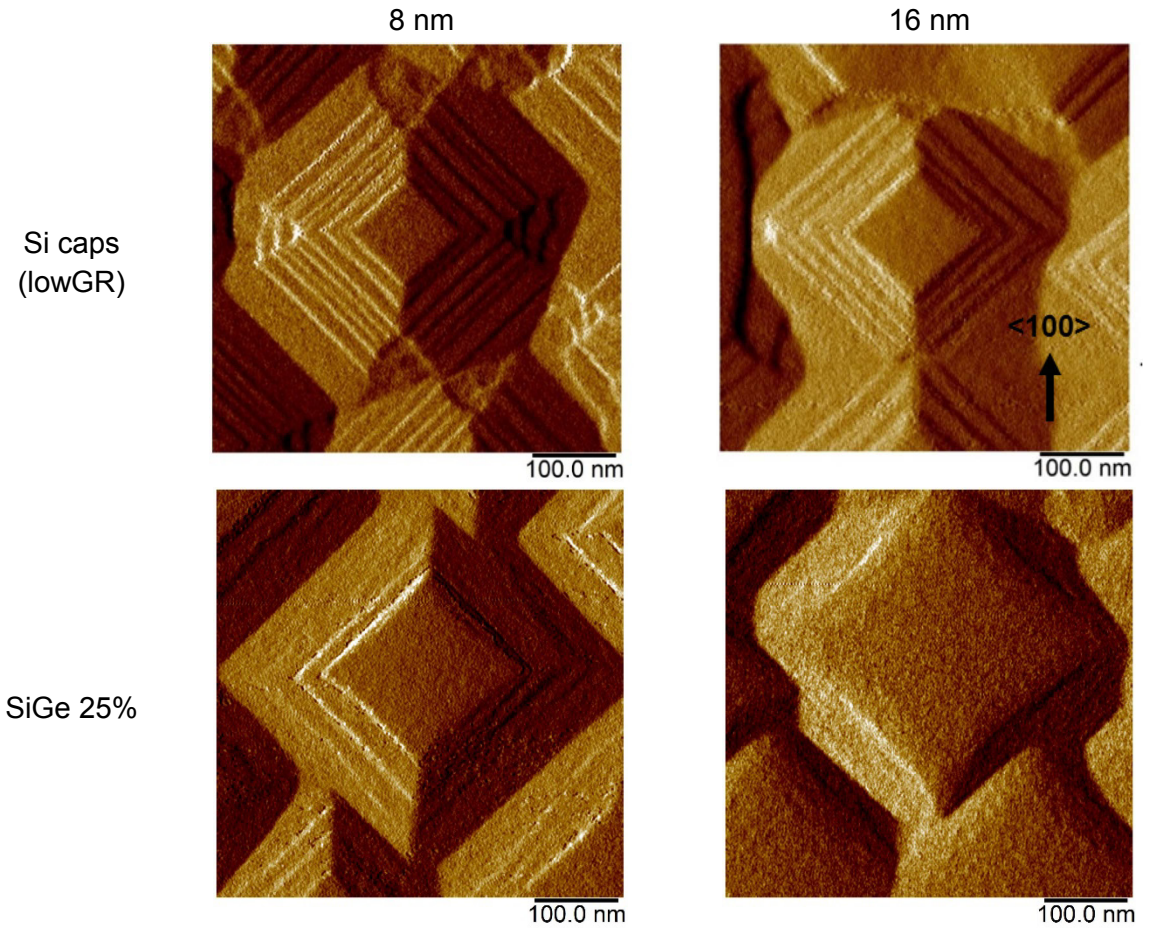

Fig. IV-27*: Amplitude error images made by 0.5 x 0.5 µm² AFM. On top, (left) 8nm and (right) 16nm Si cap (GR = 2.2 nm/min); on bottom, (left) 8nm and (right) 16nm SiGe 25% grown on a dome of SiGe 25%. Successive terraces are clearly observed. The number of terraces is higher for thin Si cap than for thicker caps. No terraces are observed for SiGe caps.*

The images show that the Si capping consists in truncated pyramids made of a succession of terraces. For both thicknesses of Si caps, the terraces are constituted by steep and less inclined facets. The number of terraces may be different according to the thickness or the material deposited on the dome. The largest number of terraces is clearly seen on domes capped with thin Si layer. The terraces being oriented along the <110> direction (45° with respect to <100>), the facets are described as {11h}, with h being comprised between 2 and 9 (or more). {112} facets are in this case the steepest ones, and {119} the least inclined. The facets identified by TEM are {113} and {119}; {112} and {117} are maybe also present but the low measurement accuracy does not allow to conclude. Completely flat facets (inclined by 0°) are also observed corresponding to the (001) plane. Another observation that can be extracted from these images is that the most extended facets (lateral extension) are the ones with the weakest inclination (< 25° with respect to (001)). In average, the length of less inclined facets is 13.6 nm as compared to 4.7 nm for steep facets. This step bunching already observed on epitaxial growth of Si/Si (111) vicinal surfaces with misorientations [Berbezier 09], was

attributed to a faceting instability and can be explained in terms of minimization of the total surface energy of a vicinal surface. The surface profile can be schematically represented by the diagram presented in ***Fig. IV-29***. On the contrary, the SiGe caps consists only in an undulated surface without terraces. The squared base of the pyramid is still visible but seems to disappear while increasing the cap's thickness (or increasing the Ge concentration).

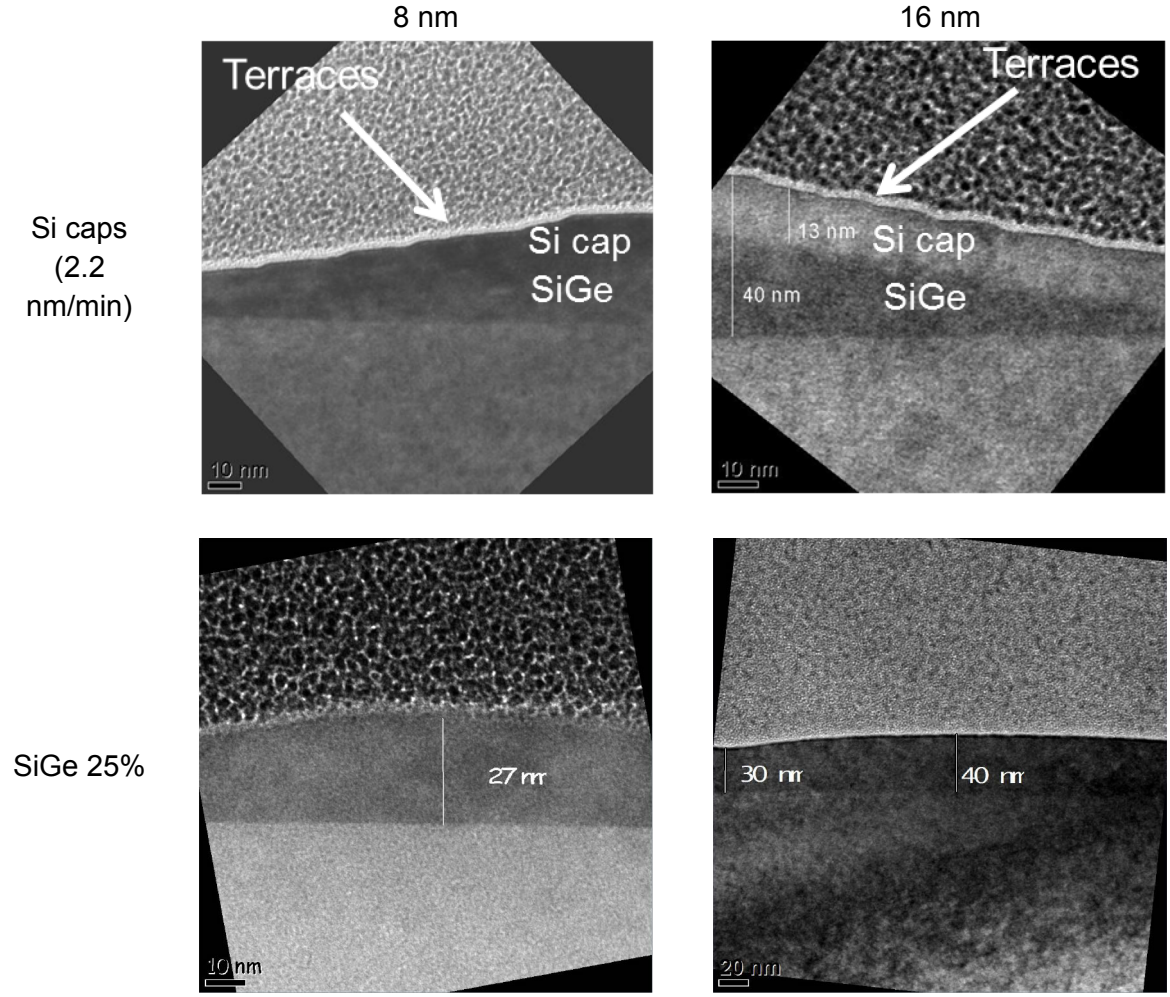

Fig. IV-28*: TEM images of (top) Si and (bottom) SiGe caps grown on rounded SiGe epitaxy. The image shows the succession of flat and steep facets in Si caps. An undulated surface is observed for SiGe caps.*

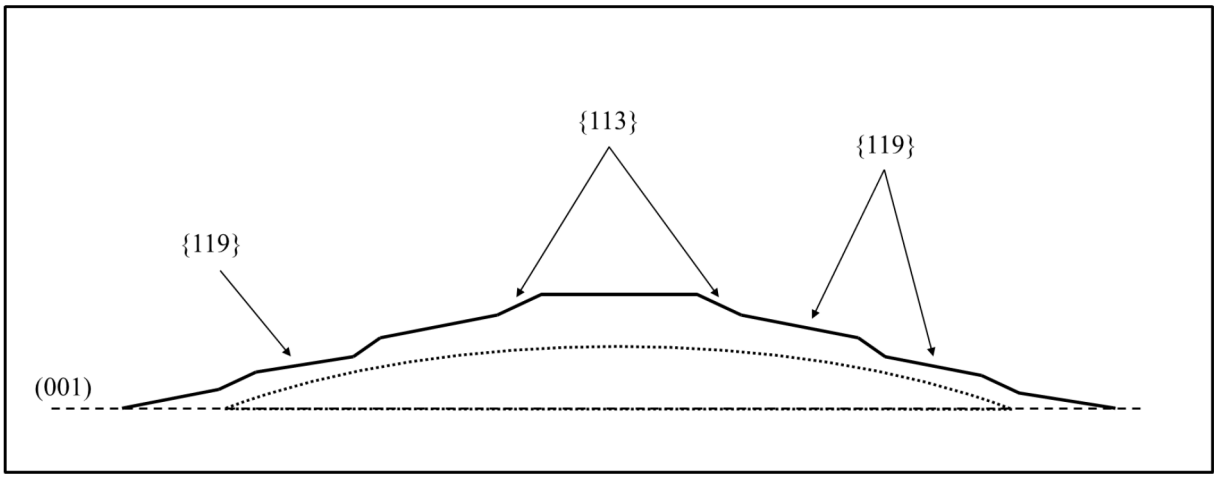

Fig. IV-29*: Schematic representation of successive terraces grown on one dome deduced from HRTEM and AFM images.*

III.1.b) In small patterns (rectangle + SRAM)

Similar observations are made for smaller patterns (***Fig. IV-30*** and ***Fig. IV-31***). First, regarding the rectangle shaped pattern, it is evidenced that the SiGe caps are more effective to recover an as-deposited morphology than Si caps. Indeed, the morphology of the 16 nm SiGe 25% and of the 8 nm SiGe 31% is very close to the one obtained by a regular SiGe epitaxy deposited on a flat surface, i.e. with {111} and {001} facets. It is worth to note that at these investigated thicknesses the morphology is almost the same as the as-deposited morphology but not exactly since the top surface is not totally flat. On the contrary, Si cap regardless of the thickness, has a very special morphology with the presence of non-standard facets: besides {111} and {001} facets, there is also {5 3 15} facet with theoretical angle of 21.2° [Brehm 11]. The cross-section TEM images in ***Fig. IV-31*** give also similar results. It is clear that the 16 nm SiGe cap presents a flat top surface which can be attributed to the (001) plane, whereas both 8 nm and 16 nm Si caps present a rounded top surface. To quantify more accurately the influence of all the different caps, the top surface's curvature radius of the pattern is measured and given in **Table IV-6**. The under layer (written as Reference) has a curvature radius of (271 ± 7) nm. Thanks to the radius, it is clear that the SiGe caps level the top surface much better than Si caps. Indeed, for thin caps (8 nm), the radius is multiplied by a factor of 7 for SiGe and by a factor of 5 for Si lowGR; for thick caps (16 nm), the radius is multiplied by a factor of almost 12 for SiGe as compared to a factor of only 6 for Si lowGR. These results also show, once again, that the thickness increase is even more effective for SiGe caps than for Si caps. As a second observation, the Si cap's GR has also an influence on the morphology. Indeed, when decreasing the GR, the curvature radius decreases as well. For thin Si caps, the curvature radius changes from 950.4 nm (highGR) to 1518.0 nm (lowGR); for thick Si caps, it changes from 1212.4 nm (highGR) to 1621.2 nm (lowGR). Furthermore, the facets {111} and {001} become more pronounced for lower GR. This can be seen in the AFM sections where the sides along the <100> direction are much steeper for Si cap lowGR (in dark blue) than for Si cap highGR (in light blue). In addition to that, thanks to these AFM sections, the top surface is more extended for Si lowGR than for Si highGR. These results demonstrate that decreasing the GR significantly, even the Si cap would allow a change in morphology of the rounded surface towards an as-deposited and faceted morphology.

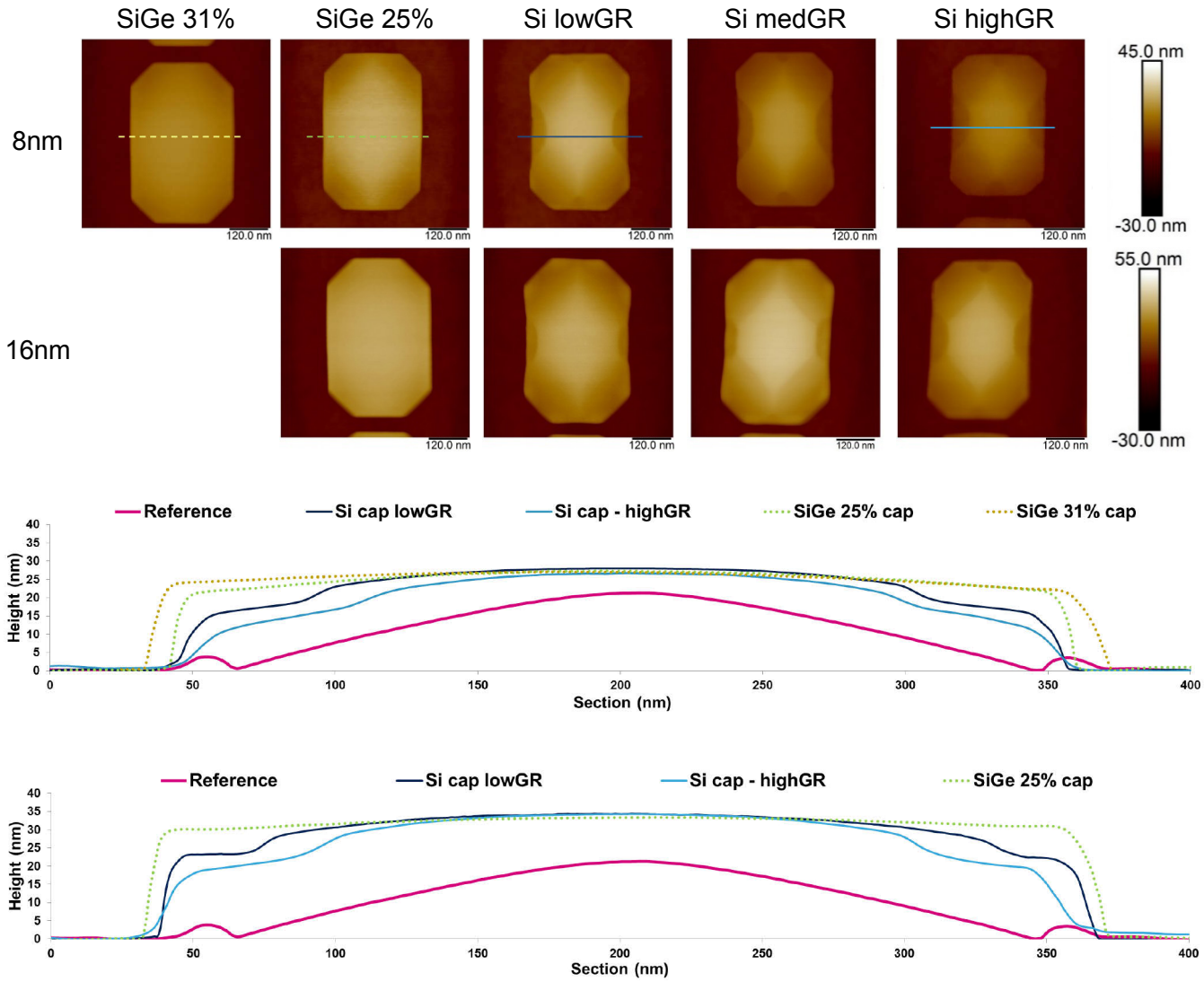

***Fig. IV-30**: 0.6 x 0.6 µm² AFM images and sections of a rectangle pattern capped with Si and SiGe. The capping thicknesses are either 8 nm or 16 nm. The sections are made across the center of the pattern as shown by the lines drawn on the images. The reference (in pink line on the graph) is the 8 nm rounded SiGe without capping. The morphology in patterns is really different depending on the material and thickness of the cap.*

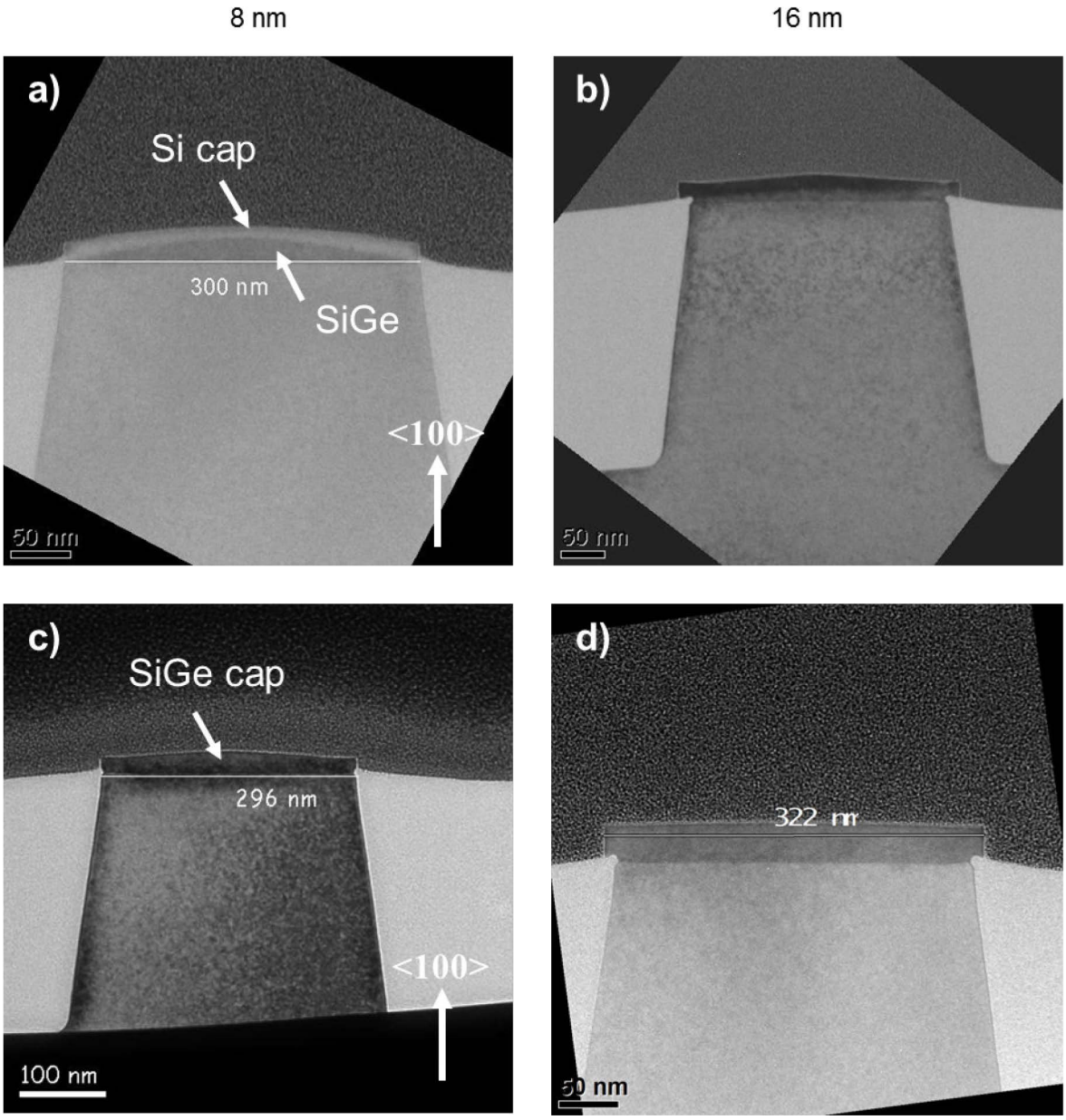

***Fig. IV-31**: Cross-section TEM images of a) 8 nm Si cap, b) 16 nm Si cap, c) 8 nm SiGe cap and d) 16 nm SiGe cap grown in the rectangle patterns. The top surface's curvature depends on the cap's thickness and material. For the SiGe caps, the top surface presents a curvature radius higher than for Si caps, leading to a rather flat surface as observed for the 16 nm SiGe cap.*

TABLE IV-6. Curvature radius of the rectangle's top surface in nm. The radius is higher for SiGe caps than Si caps. This means that a SiGe cap is more efficient to find back a regular morphology than a Si cap.

Samples/cap	Thickness (nm)	Radius (nm)
Reference	8	271 ± 7
Si highGR*	8	950.4 ± 33
	16	1212.4 ± 22
Si medGR**	8	1117 ± 44
	16	1515,4 ± 74
Si lowGR***	8	1518.0 ± 31
	16	1621,2 ± 19
SiGe 25%	8	1946,3 ± 71
	16	3202,4 ± 71
SiGe 31%	8	2442,2 ± 41

*highGR = high Growth Rate = 4 nm/min
**medGR = medium Growth Rate = 3.4 nm/min
***lowGR = low Growth Rate = 2.2 nm/min

Second, regarding to SRAM patterns which are smaller than the rectangles (***Fig. IV-32***), it is even more evident that the SiGe cap layers allows the as-deposited morphology to be recovered since the top surface of both 8 nm SiGe 31% and 16 nm SiGe 25% caps is totally flat. This allows to say that the dimensions of the pattern is an important factor on the capability of the SiGe cap to level a rounded surface: the smaller the pattern, the more rapidly the SiGe will adopt an as-deposited morphology. Considering Si caps, the SRAMs present successive terraces as already observed in large boxes. These terraces are located along the <110> direction and begin by {111} facets. ***Fig. IV-33*** shows AFM sections made along this <110> direction for SiGe 31% and 8 nm Si medGR cap layers. As already mentioned, the SiGe 31% cap present {111} facets along this direction, from the bottom to the top of the SRAM. This is the characteristic morphology of a regular epitaxy made of this kind of pattern. For the Si medGR cap, the {111} facet is also visible but its extension is not completed. Indeed, the facet disappears for the benefit of terraces made of less inclined facets, i.e. succession of {113} and {11h}, h being higher than 3.

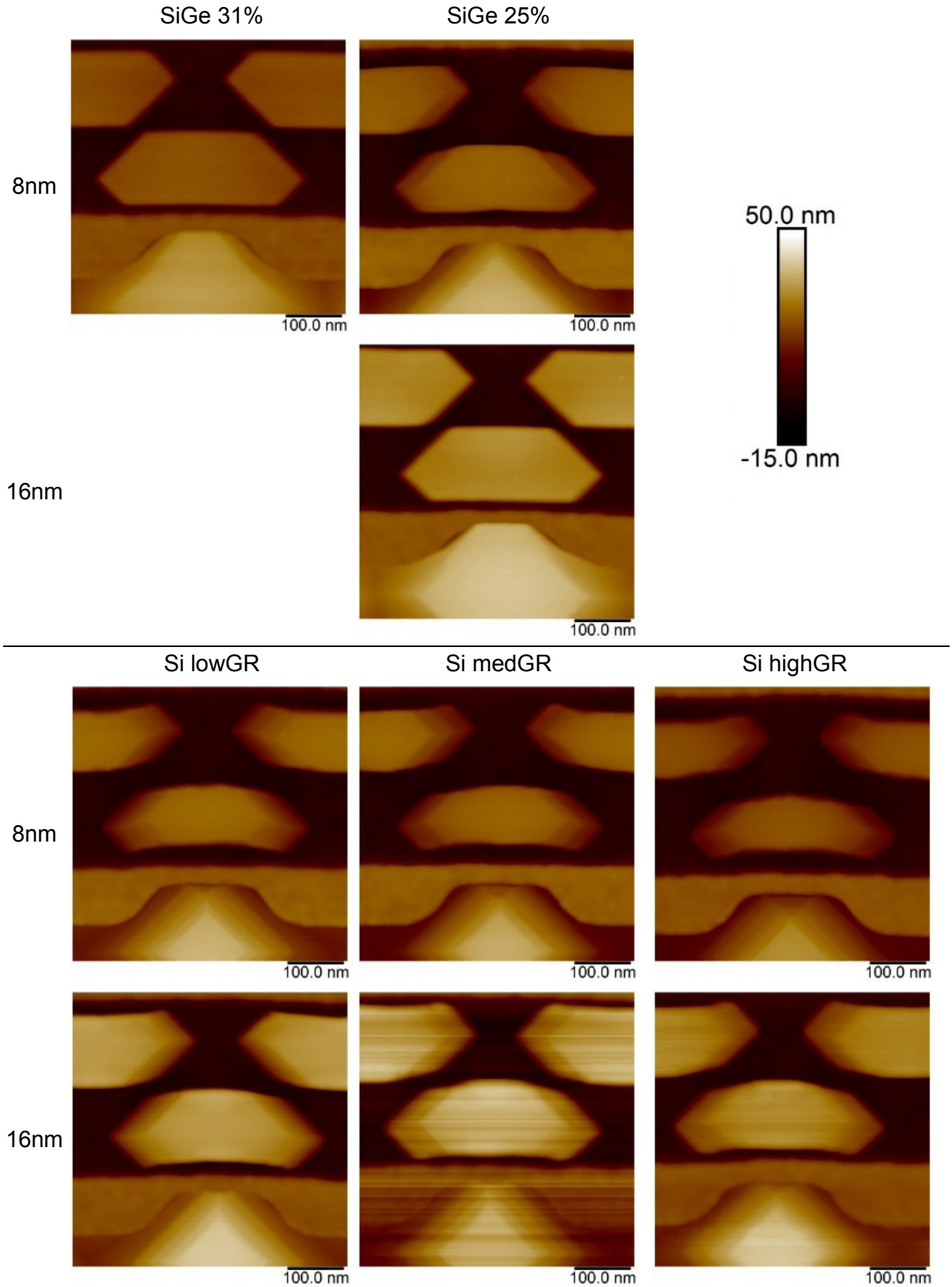

***Fig. IV-32**: 0.5 x 0.5 µm² AFM images of SRAMs capped with Si and SiGe. The capping thicknesses are either 8 nm or 16 nm. For Si cap layers, the presence of successive terraces is observed along the <110> direction independently of the thickness. For SiGe cap layers, the as-deposited morphology can be recovered for thick cap or higher Ge content. Thus, the SRAM pattern is made of {111} and {001} facets*

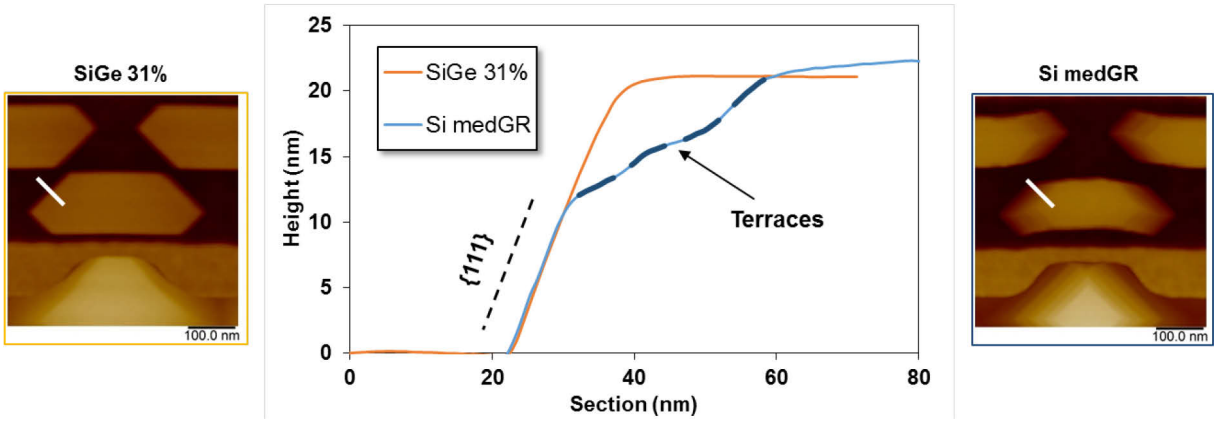

***Fig. IV-33**: AFM section along the <110> direction for 8 nm SiGe 31% and 8 nm Si medGR cap layers. For the SiGe cap, the presence of the {111} facet is well visible from the bottom to the top of the SRAM. For Si cap, the {111} facet is also visible but disappears for the benefit of terraces made of less inclined facets, i.e. succession of {113} and {11h}, h being higher than 3.*

III.2) Anneal of Si caps

In order to understand more in detail the presence of successive terraces in Si caps, especially to know if these terraces correspond to an equilibrium morphology or if they are due to kinetics effects, the 8 nm low growth rate Si cap (2.2 nm/min) was annealed at 850°C for 60 sec under 20 Torr of H_2 atmosphere. ***Fig. IV-34*** and ***Fig. IV-35*** show the results in large and small patterns, respectively. First, in the large box, a significant decrease of the roughness is clearly observed: it goes from 6.41 nm to 3.10 nm in R_{RMS}. Second, and most important result, the successive terraces and their several facets disappeared completely. Indeed, the multi-faceted pyramids transformed into smaller domes leaving an undulated surface without any terraces. Only the square base is still present after the annealing. This morphological behavior was not expected since the terraces' presence was attributed to a minimization of the surface energy [Berbezier 09] and thus the system would prefer to stay in the faceted state, which is not the case.

The annealing allows to bring the sufficient energy to the system to relax the strain and to go towards an equilibrium state which was not achieved due to the high Si cap growth kinetic. The strain loosening can be attributed to an important Ge inter-diffusion between the SiGe domes and the Si cap.

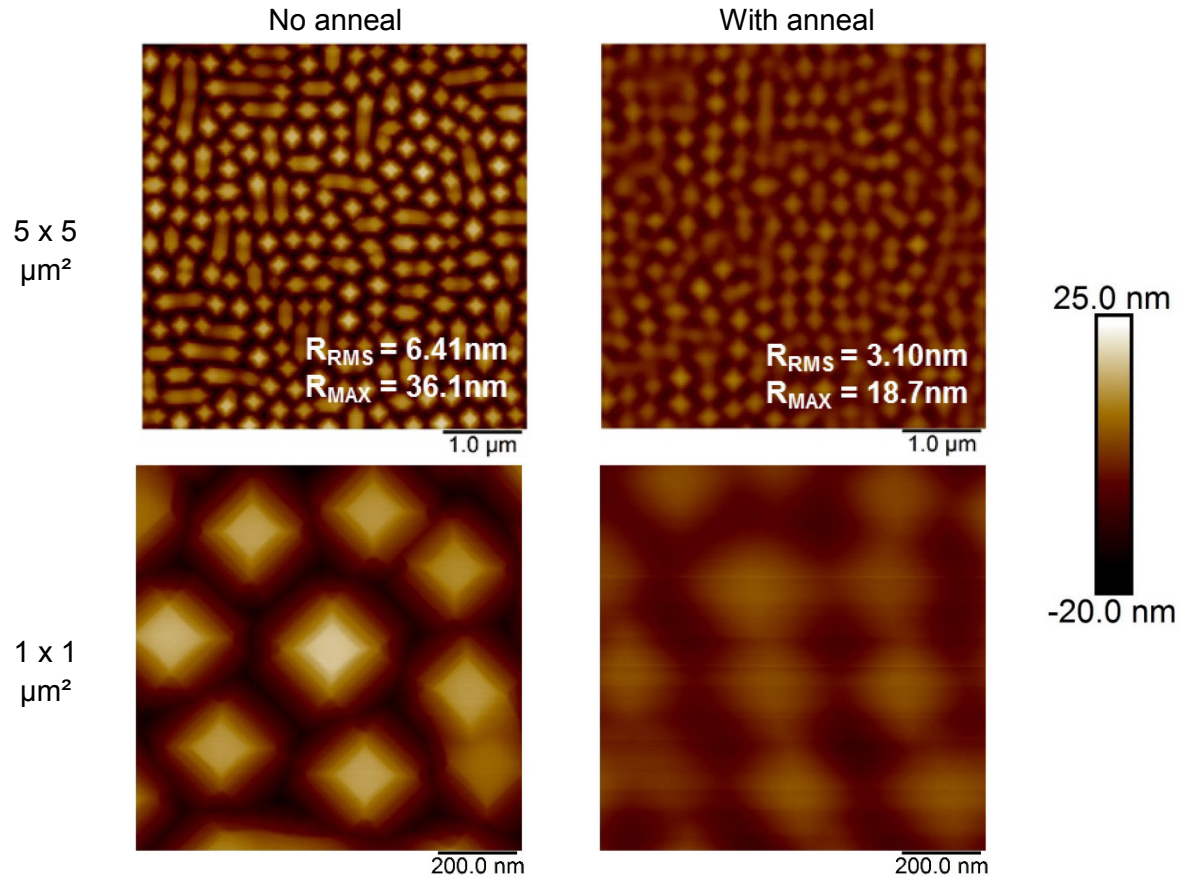

***Fig. IV-34**: AFM images in large box of 8 nm Si IGR cap layer before and after annealing at 850°C for 60 sec under 20 Torr of H_2 atmosphere. The roughness decreases after annealing and the terraces fade away completely.*

In SRAMs (***Fig. IV-35***), the terraces also disappeared giving rise to a morphological evolution towards a rounded shape similar to the one observed before adding the caps. In rectangles, the morphology also evolved towards a morphology much more rounded shape on the edges and with a flat top surface. These results are not in accordance with the hypothesis of the creation of facets to minimize the total surface energy of a vicinal surface since after annealing the facets disappear. As a result, and conclusion, in this case, the observed terraces are probably due to kinetic effects.

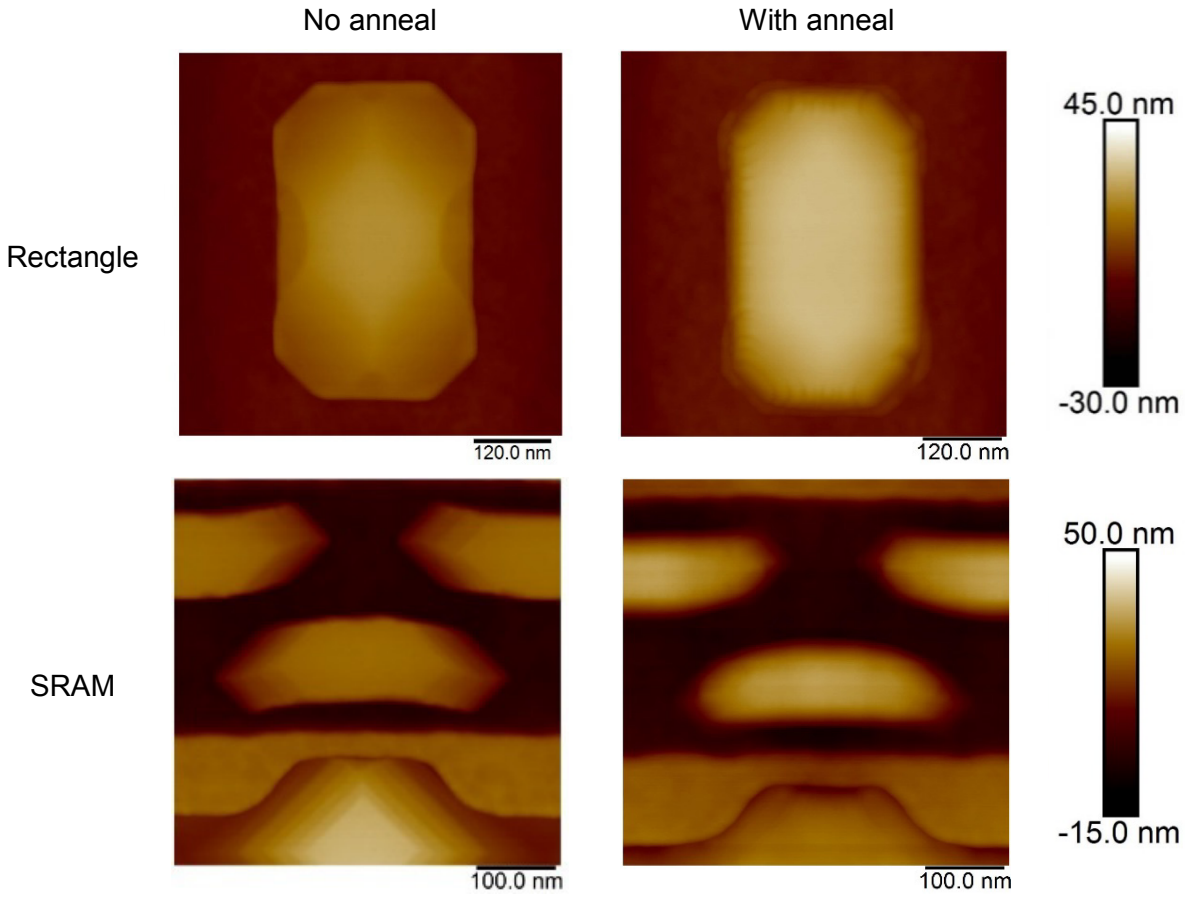

***Fig. IV-35**: AFM images in rectangle and SRAM patterns of 8 nm Si IGR cap layer before and after annealing at 850°C for 60 sec under H_2 atmosphere. The terraces disappeared for the benefit of a rounded morphology.*

IV/ Conclusion

In this chapter, the influence of the SiGe layers' annealing was extensively studied. First, in large patterns, the thermal treatments lead to a surface's morphology change through the SK-like relaxation. This is characterized by the apparition of undulations more or less pronounced depending on the annealing. These undulations are always oriented along the <100> directions and have a specific wavelength. The preferred orientation is attributed to the lowest Young's modulus along this direction (130 GPa). In our specific cases, the measured wavelengths were 0.167 µm for a 5 nm thick SiGe 25% layer, and 0.231 µm for a 20 nm thick SiGe 25% layer. Thus, the wavelength depends on the growth thickness and on the material. The SK undulations' evolution is produced step by step. First, the energy given to the system must be high enough for the undulations to appear. Indeed, for relatively low temperatures (650°C and 675°C), a duration of 1920 sec is not enough to observed undulations. However, when they appear, the roughness increases exponentially, slows down before stabilize. In this particular case, i.e. 20 nm thick SiGe 25%, the roughness stabilized at about 8 nm. In the first step of the undulations' apparition, the <100> preferred orientation and the specific wavelength are not well defined still. For high thermal treatments, e.g. 725°C for 960 sec, the <100>

oriented undulations break to form single domes, with square base's dimensions comprise between 200 nm and 350 nm.

The wetting layer presents between the domes (high thermal treatments) was characterized by XPS. The post annealed SiGe layer was etched in a way that left only domes surrounded by Si. It was shown that after a second annealing, the Ge signals increase that may explain the re-formation of the wetting layer or at least the domes' expansion through the surface diffusion. This leads to a decrease of the domes' thickness which was confirmed by AFM measurements.

The annealing was then studied in small patterns considered as 1D objects as it is the case of very long lines. When subjected to annealing, the lines are characterized by the presence of instabilities. These instabilities depend on the growth thickness, the lines' width and orientations. They appear with the presence of either bulges, or domes along the lines or a separation of the line in two, three or more lines. The lines' instabilities are due to the superposition of the thermal rounding and the SK-like undulations. The last mechanism allows the lines to be separated in two or three (or more) lines. Indeed, the wavelengths obtained in the lines are similar to the ones obtained for the SK undulations in large patterns. It was also demonstrated that an unstable line can be stabilized ensuring that the system rediscovers in a stabilization zone. This was performed by thinning an unstable line and by annealing this line. It was shown that the line stabilized after the annealing.

The study was then focused on 2D objects like squares or ovals. During the thermal rounding, it was shown that the patterns evolve towards a final faceted (low angle) shape. The as-grown facets and their corresponding overgrowth disappear leading to an excess of matter at the pattern's edges and corners. Finally, this excess grows and collapse to form the dome. The rounding's kinetics was quantified measuring the volume of displaced matter. Two regimes were obtained: at high temperatures, the rounding is mainly driven by the surface diffusion (activation energy of 2.9 eV) while at low temperatures, another mechanism is added to the surface diffusion ("apparent" activation energy of 7.7 eV). The high obtained energy was supposed to be due to a higher H coverage slowing down the thermal rounding.

The influence of the H_2 pressure and the carrier gas' nature during the annealing were highlighted. Concerning the H_2 pressure, the higher the pressure, the slower the thermal rounding. This is attributed to the H coverage which increases with increasing the pressure. On the contrary, when changing the carrier gas to N_2, the rounding was found to occur faster due to the fact that the N atoms do not stick efficiently to the surface.

Finally, the morphological behavior of Si and SiGe caps grown on a non-flat surface was studied. It was observed that the SiGe cap allows a leveling of the surface more efficiently than Si caps. The Ge may act as a diffusion catalyzer due to a better H desorption and thus to a lower H coverage. Moreover, the cap's growth rate seems to have an influence on the surface leveling. Indeed, a high GR with a high H coverage will lead to a conformal cap's growth since the Si does not have enough time to diffuse. A last observation was the presence of facets ({113} or {119}) arranged as successive terraces. These terraces completely disappeared after an annealing meaning that their presence is probably due to kinetics' effects.

Chapter 5

Industrial applications

Nowadays, the incorporation of boron as dopant in epitaxies of CMOS technology is mainly used in the p-type sources and drains. These elements constitute important parts of the transistor and thus the study of their morphology is essential. One way to enhance the devices' performances is to considerably increase the doping concentration. However, the required concentrations have reached (and in some case exceeded) the limits of solubility which can lead to important morphological degradations. These degradations are even worse in objects with size in the range of tens nanometers. Here again, the small size effects are present in boron-doped SiGe and depends on the boron concentration.

In this chapter, the boron-doped SiGe epitaxy is discussed as a function of the boron concentration. First, the kinetics of grown boron-doped SiGe, as well as the boron and germanium incorporation are given. Then, the morphological aspect of boron-doped SiGe layers is studied. The epitaxy quality and the faceting will be the main axes of research of this part. Finally, all the preliminary results obtained will be used to integrate these epitaxies in "real" source/drain structures.

In structures like the source/drain (S/D), in-situ boron-doped SiGe raised sources and drains (RSD) are needed to thicken the access region and lower the contact resistance of high-performance pMOSFETs. In addition, it is desirable to have high germanium composition to increase the stress. However, high Ge concentration and boron doping may be detrimental for the morphology of epitaxial growth and as a consequence, for transistor's performances. This chapter is devoted to the influence of boron doping in SiGe layers. In a first part, the kinetics of grown boron-doped SiGe is given, as well as the boron and germanium incorporation. Second, the morphology of the grown layers is studied in term of crystalline quality and faceting as a function of boron doping. Also, the behavior of SiGe:B when subjected to a thermal budget is shown.

I/ Boron doped SiGe characteristics

In this first part, the kinetics is studied as a function of boron partial pressure. The boron and germanium incorporation is also given. Growth of the-as-deposited samples was realized in the EPI Centura 300. The chemistry used for the epitaxial growth was a mixture of DCS, HCl, and germane gases with H_2 as carrier gas. The partial pressures of the active gases were adjusted to ensure a selective growth. The growth was performed at 644°C at a total pressure of 10 Torr. In this process, the morphology was "frozen" by leaving in the chamber the DCS gas during the cooling of the substrate. The partial pressure of the active gas was chosen so that no more than 0.5 nm of Si (preferably 0.2 nm) is deposited. To know more about the "freezing" recipe, see *Chapter 2*. After this step, a very short H_2 purge, without heating, at low temperature is done before the wafer unloading.
The films were characterized by spectroscopic ellipsometry and by XRD to obtain the thickness and the growth rate. The boron concentration was measured by SIMS. MBIR measurements were also performed to obtain the carriers' concentration.
The SiGe:B films were grown on <100> oriented patterns.

I.1) Growth rate

Initially, the growth rates (GR) of SiGe:B films were studied as a function of boron partial pressure. To do so, 6 different boron pressures were used: 0.033, 0.065, 0.098, 0.196, 0.293 and 0.389 mT. These pressures take into account the dilution of gases, thus correspond to the actual pressures. ***Fig. V-1*** below gives the growth rates of SiGe:B for 5 different pressures and for two masks with different Si coverage (13.59% and 16.21%). The Si coverage in this case is the percentage of Si active zone on the whole wafer. As example, a 13.59% Si coverage means that there is 13.59% of active zones on which epitaxy can be done. The GR in the case of 0.389 mT of B_2H_6 was not possible with regard to the poor growth and bad morphology of the film (see top-view SEM in ***Fig. V-2***). The film growth was not achieved correctly probably due to surface saturation by B atoms or B making precipitates with Si or Ge at the interface. In ***Fig. V-2***, the high doping level is compared with intermediate doping level.

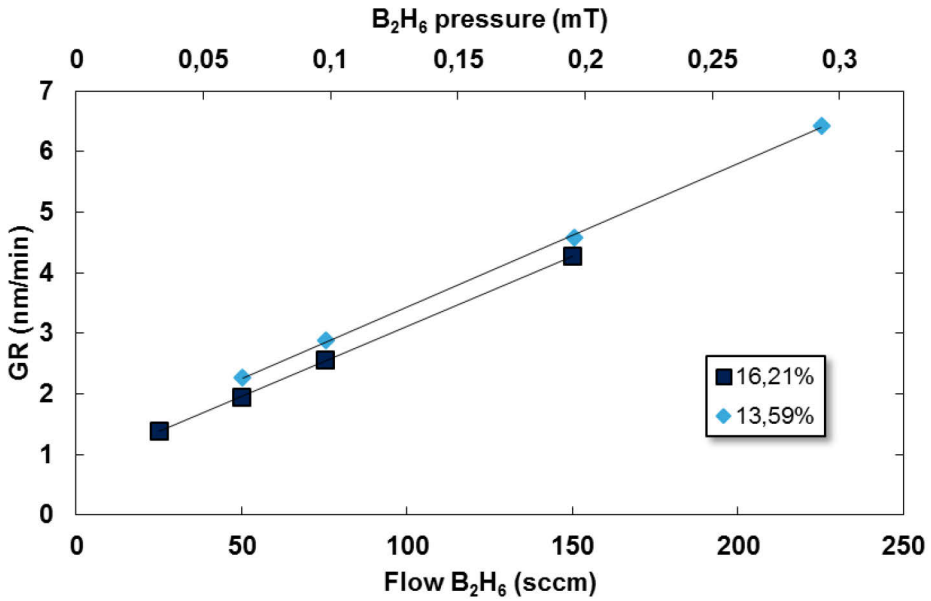

***Fig. V-1**: Boron-doped SiGe growth rate as a function of the B partial pressure. Si coverages on the substrate of 16.21% and 13.59% were used.*

It is quite easy to see, in these process conditions, that the GR increases linearly with increasing B_2H_6 partial pressure, and more than that, it drastically increases: the GR can triple for a B concentration increase of few percent (for example from 0.2% to 4%). Indeed, for a Si coverage of 13.59%, it varies from 2.3 nm/min to 6.2 nm/min when increasing diborane partial pressure from 0.065 to 0.293 mT; for a Si coverage of 16.21%, the GR increases from 1.39 to 4.28 nm/min when the partial pressure increases from 0.033 to 0.196 mT. It is well known that B_2H_6 is a precursor enhancing the GR of Si and SiGe. This phenomenon can be explained in terms of increase of free surface sites due to an enhanced H desorption when B atoms are present on the surface. Then, the adsorption of Si or Ge precursors is easier since more free surface sites are created. As a second observation, for a certain value of partial pressure, the GR is not the same for both masks. Indeed, there is an increase of the GR of 0.3 nm/min when the Si coverage decreases. This phenomenon is called the global loading effect. We can define loading effect as the modification of the characteristics (thickness, composition…) of an epitaxial layer depending on the mask of the substrate. Global loading effect refers to differences obtained for a same process at the wafer's scale. The explanation is the number of available active molecules which is higher for a smaller active Si area (precursor consumption decreases with total Si area). These available active molecules enhancement results in an increase of the growth rate. [Dutartre 08]

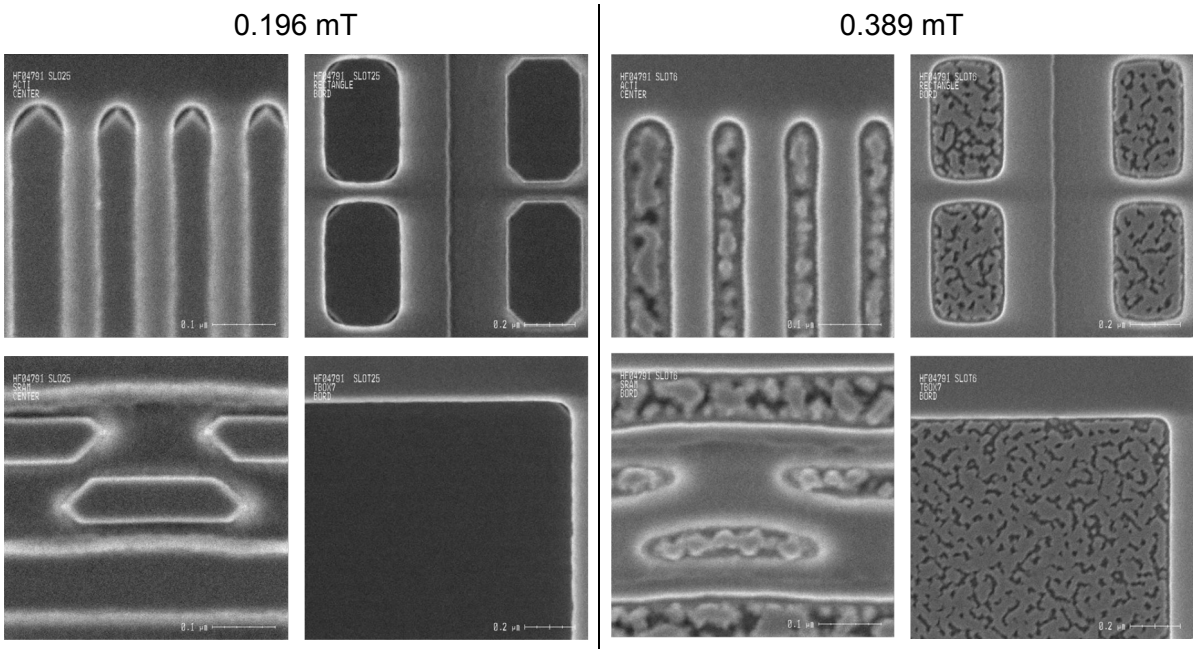

Fig. V-2*: Top-view SEM images of in-situ B-doped SiGe with a B partial pressure of (left) 0.196 mT and (right) 0.389 mT in different patterns. From top to bottom and left to right: lines, rectangles, SRAMs and large box. The high doing presents a very bad morphology, the growth does not occur correctly.*

I.2) Boron incorporation

Fig. V-3 shows TOF SIMS profiles of three boron-doped SiGe layers corresponding to three different B_2H_6 partial pressures (mask with 13.59% of Si coverage): 0.065, 0.196 and 0.293 mT (in the graph, 50, 150 and 225 sccm, respectively). The average B concentrations for both 0,065 and 0.196 mT are respectively 1.23 x 10^{20} at/cm^3 and 6.57 x 10^{20} at/cm^3, and seem to be constant on the entire film. However, for the heavily B-doped SiGe the concentration reduces from the interface between SiGe:B and Si to the surface of the layer and even more there is a peak at the interface. Then, the B concentration varies from 3.14 x 10^{21} at/cm^3 for the peak to 1.08 x 10^{21} at/cm^3 at the surface. This peak for highly B-doped SiGe has already been seen in the literature [Zhu 13] and is not totally understood. It can be interpreted as a saturation of the initial surface by B atoms and/or the boron atoms make precipitates with Si or Ge on the surface.

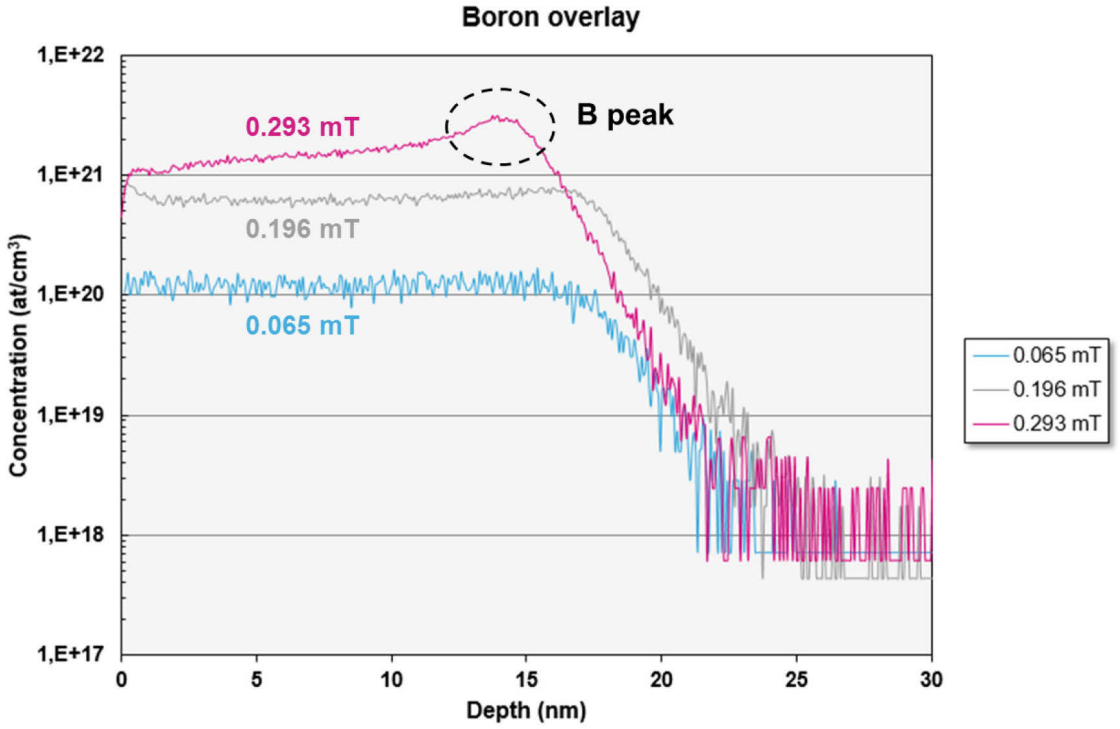

***Fig.V-3**: ToF SIMS analyses of B concentrations for different B_2H_6 partial pressure: 0.065 mT (blue), 0.196 (grey) and 0.293 (purple) mT.*

The ***Fig. V-4*** gives the Boron concentrations as a function of the diborane partial pressure. These concentrations were extracted from XRD for the deposited thickness and Model Based Infrared Reflectometry (MBIR) thanks to the formula:

$$Boron\ conc\ (at/cm^3) = \frac{Dose\ (at/cm^2)}{Thickness\ (cm)} \qquad \text{V-1}$$

As comparison, we have plotted in the same graph the B atoms concentrations obtained by TOF SIMS in the boron-doped layers as a function of B partial pressure. In a general point of view the concentrations obtained thanks to MBIR are lower than those obtained by TOF SIMS. It even worse for high doping: the concentration measured by TOF SIMS is almost 8 times higher than the one measured by MBIR. This behavior has already been observed by Hatmann *et al.* [Hartmann 07]. Since MBIR measures carrier concentration while TOF SIMS, a number of atoms, the explanation of this difference is probably the fact that some B atoms are incorporated in interstitial sites and do not participate in strain compensation. By the way, these atoms are not measured by MBIR. Indeed, at these important concentrations, all the B atoms cannot be located in substitutional sites. Also, this huge difference can be explained by an overestimation of the SIMS measurement at elevated doping level. Moreover, considering the SIMS measurements, the highest doping level correspond to a 4% B incorporation which may in some point no more be considered as a doping. Indeed, such a concentration can be considered as a compound like $Si_{1-x-y}Ge_xB_y$.

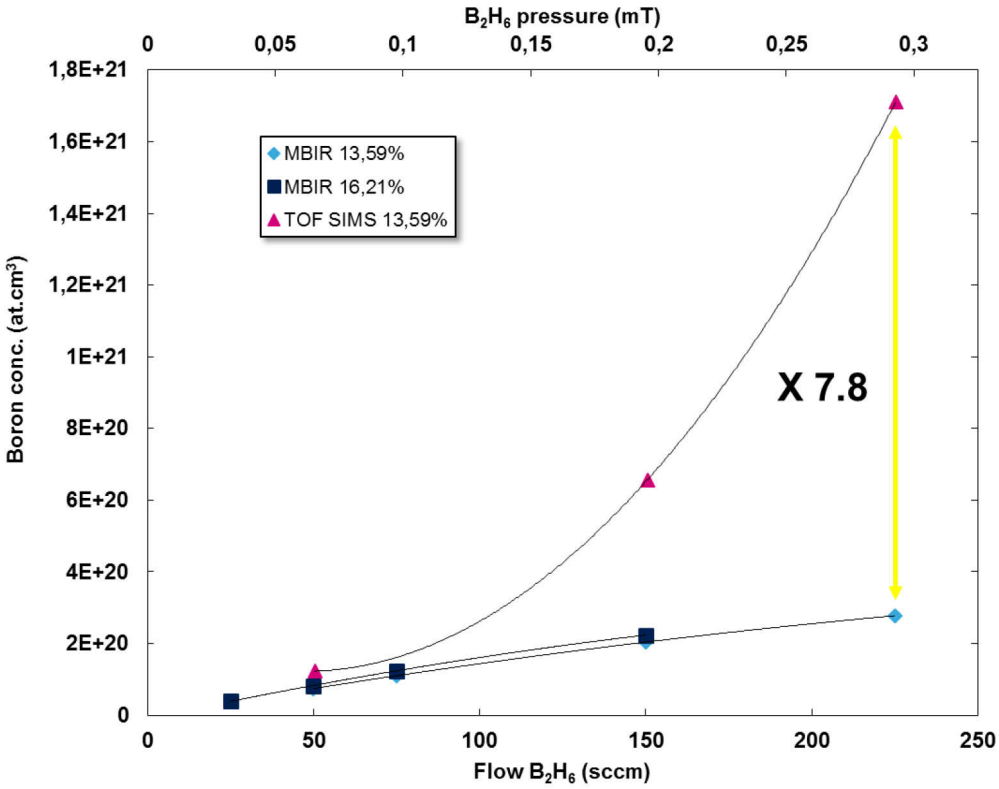

***Fig. V-4**: Boron concentration as a function of the B_2H_6 partial pressure.*

I.3) Ge content

An X-Ray Diffraction was used to gain access to the “apparent” Ge concentration in the boron-doped SiGe layers. The notion of “apparent” is used because the Ge concentration is calculated assuming that boron-doped SiGe layers behave like a binary SiGe alloy with a lattice parameter given by [Dismukes 64]:

$$a\left(Si_{1-x_{app}}Ge_{x_{app}}\right) = 5.431 + 0.2x_{app} + 0.027x_{app}^2$$

Moreover, it is well known that the silicon lattice contracts as a fact that B atoms are smaller than Si and Ge atoms: a_B = 3.852 Å ⇔ a_{Si} = 5.43105 Å and a_{Ge} = 5.65785 Å (the compressive strain in SiGe layers is compensated by substitutional B atoms). Therefore, XRD is only sensitive to the substitutional (active) B. The presence of B has to be taken into account for XRD interpretation. The plot in ***Fig. V-5*** gives XRD diagrams for four B-doped SiGe layers with different B concentrations. The curves in ***Fig. V-5*** are shifted vertically to improve the clarity. As the B concentration increases, a shift to higher angles of the SiGe:B layer peak is well visible. This is obviously linked to a decrease in the “apparent” Ge concentration, which is in fact due to strain compensation by small B atoms. As a second observation, the SiGe peak intensity decreases with increasing the B concentration and in the same way the fringes vanish and almost none of them can be seen for the most heavily B-doped SiGe layer. In a first hypothesis, this can be explained by a decrease of epitaxy quality. The quality of the epitaxial

growths is shown in the second part of this chapter (*see Chapter V-II/ Morphological aspect of SiGe:B*).

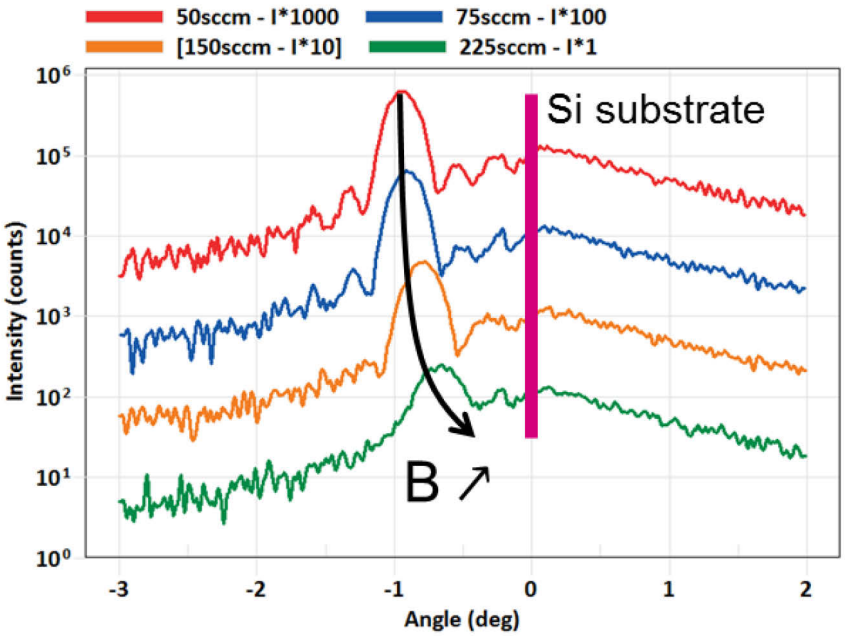

***Fig. V-5**: XRD diagram of B-doped SiGe layers grown at 644°C, 10 Torr, for different B_2H_6 partial pressures: 0.065 mT (50 sccm), 0.098 mT (75 sccm), 0.196 mT (150 sccm) and 0.293 mT (225 sccm). Curves are shifted vertically (I x 1, I x 10, I x 100, I x 1000) for clarity. The most heavily B-doped SiGe layer is characterized by a broadened, far less intense peak, and by a disappearance of fringes.*

Thanks to this diagram, the "apparent" XGe can be measured as a function of B partial pressure (see ***Fig. V-6***). The "apparent" Ge concentration decreases from 36% to almost 27% for B_2H_6 partial pressures varying from 0.065 to 0.325 mT (mask with 13.59% of Si coverage) and from 36% to 30% for B_2H_6 partial pressures varying from 0.033 to 0.196 mT (mask with 16.21% of Si coverage). A growth without boron (i.e. removing the B_2H_6 gas) was also performed in the same conditions. The value of the XGe, measured by XRD, is found to be about 38%. However, since the incorporation of boron enhance the GR, when no boron is added the GR is reduced a lot. Thus, the thickness was not high enough to obtain very accurate measurements. However, other growths were performed without B_2H_6 but decreasing the HCl partial pressure during the epitaxy. This allows the GR to be increased in order to be able to grow thick enough layers. Finally, measuring these layers by XRD, an average XGe of 38.8% was found which is very close to the value obtained previously.

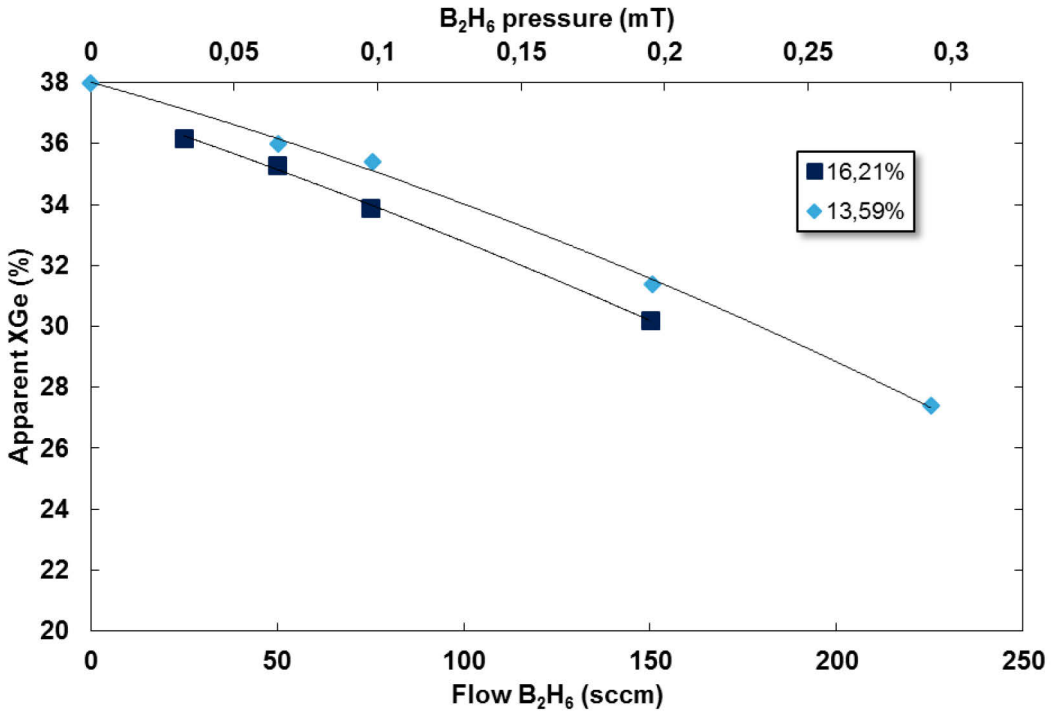

***Fig. V-6**: Apparent XGe as a function of the B_2H_6 partial pressure.*

The “real” Ge concentrations were calculated thanks to two different methods and plotted in ***Fig. V-7***. Since TOF SIMS measures the total number of species in the layer, it is easy to extract the Ge concentration (in blue line in ***Fig. V-7***). The second method was to use XRF in order to extract the Ge dose from the intensity of the peak and thus the percentage of Ge can be calculated (red curve in ***Fig. V-7***). The decrease of XGe is less pronounced considering TOF SIMS analysis with values varying from 34% to 31% and it is quite similar considering XRF calculations with values ranging between 36 and 31%. As already mentioned, the “apparent” XGe measured by XRD is directly linked to the lattice contraction due to boron atoms, thus to the out-of-plane lattice constant ($a^{\perp}$). This results in the relatively high difference between the “apparent” and “real” XGe obtained at high doping levels. Furthermore, the “real” XGe seems to decrease a little. This can be attributed to the incorporation competition between the dopants, i.e. the Ge and the B. As a result, the higher the boron doping the less the Ge incorporation. Also, this can be attributed to the large GR increase. Indeed, XGe tends to decrease with increasing the GR (e.g. effect of the temperature).

Comparing the difference between the “apparent” XGe measured by XRD and the “real” XGe measured by XRF, it is possible to measure the lattice contraction corresponding to the boron and verify the accordance with the literature. Indeed, it was shown by Horn *et al.* [Horn 55] that one single boron atom exerts a 0.26% lattice contraction per atomic percentage of boron in silicon. Equivalently, the Ge exerts a 0.04% lattice increase per atomic percentage of Ge in silicon. For example, taking the highest doping, the difference of Ge content measured by both techniques is about ΔXGe = 4%. This value would correspond to a 0.16% lattice contraction due to boron atoms, and equivalently to 0.6% of boron in the lattice. Finally, it corresponds to a boron concentration of about 2.9×10^{20} at/cm^3 which is very close to the value obtained by MBIR (~2.8×10^{20} at/cm^3). The same exercise can be done for the intermediate doping for which the ΔXGe is equal to 2.7%. This would correspond to 0.41% of boron or equivalently, to a boron concentration of 1.99×10^{20} at/cm^3. This value is also very close to one

obtained by MBIR which is 2.04x10^{20} at/cm^3. This method to find back the boron concentration comparing the XRD and XRF techniques may reinforce the judgement of the “overestimated” SIMS values.

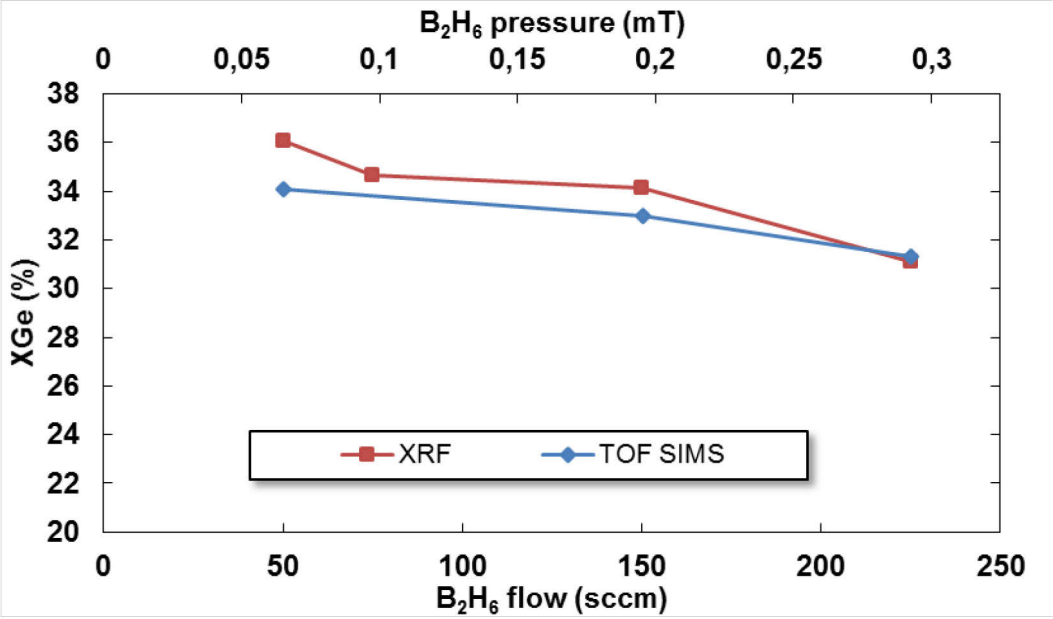

***Fig. V-7**: “Real” XGe as a function of the B_2H_6 partial pressure. No significant influence of B_2H_6 partial pressure on “real” XGe is observed.*

II/ Morphological aspect of SiGe:B

II.1) Roughness in large box (100 x 50 µm²)

In this second part, the quality of the epitaxial growths and the faceting are studied as a function of boron doping. The epitaxies’ thickness is the same for all the samples to be comparable and is 20 nm. Each film is characterized and then compared by AFM and SEM.

First, the roughness as a function of the B_2H_6 partial pressure was studied in large pattern (100 x 50 µm²), as shown in ***Fig. V-8*** and ***Fig. V-9***. For low and intermediate boron doping (from 0.065 to 0.196 mT) the roughness is comparable and rather low: it is comprised between 0.112 nm and 0.154 nm as R_{RMS}. However, for higher boron doping, the roughness increases significantly and attains values of 0.226 nm for 0.293 mT and 0.855 nm for 0.389 mT. Note that the color scale is different for layer with the highest B concentration (6.2 nm compared to 1 nm). As a reminder, the Z sensitivity of the AFM is less than 0.1 nm, thus all the raw data are considered to be very accurate. This last layer is characterized by a very rough and undulated surface as if the boron makes precipitates with Si or Ge.

The two most heavily B-doped SiGe films are consequently respectively 2 and 8 times rougher than the less heavily doped layers. This may explain the reason why almost no fringes were observed on the XRD diagrams (***Fig. V-5***) and why the peak intensity decreases drastically for high B concentrations. To note that for a diborane partial pressure of 0.293 mT, the roughness is relatively good: R_{RMS} lower than 0.250 nm is acceptable for the devices. However, this SiGe:B layer contains many defects as shown by cross-section TEM images

depicted in ***Fig. V-10***. An example is given in the magnified TEM image in ***Fig. V-10***, which is characterized by its burger vector (shown by the white arrow). These dislocations may be due to boron precipitates close to the Si/SiGe:B interface leading to defects in the lattice. This observation reinforces the bad epitaxy quality hypothesis done during the study of the XDR diagrams. Indeed, this kind of defects lead to a decrease of the peak intensity.

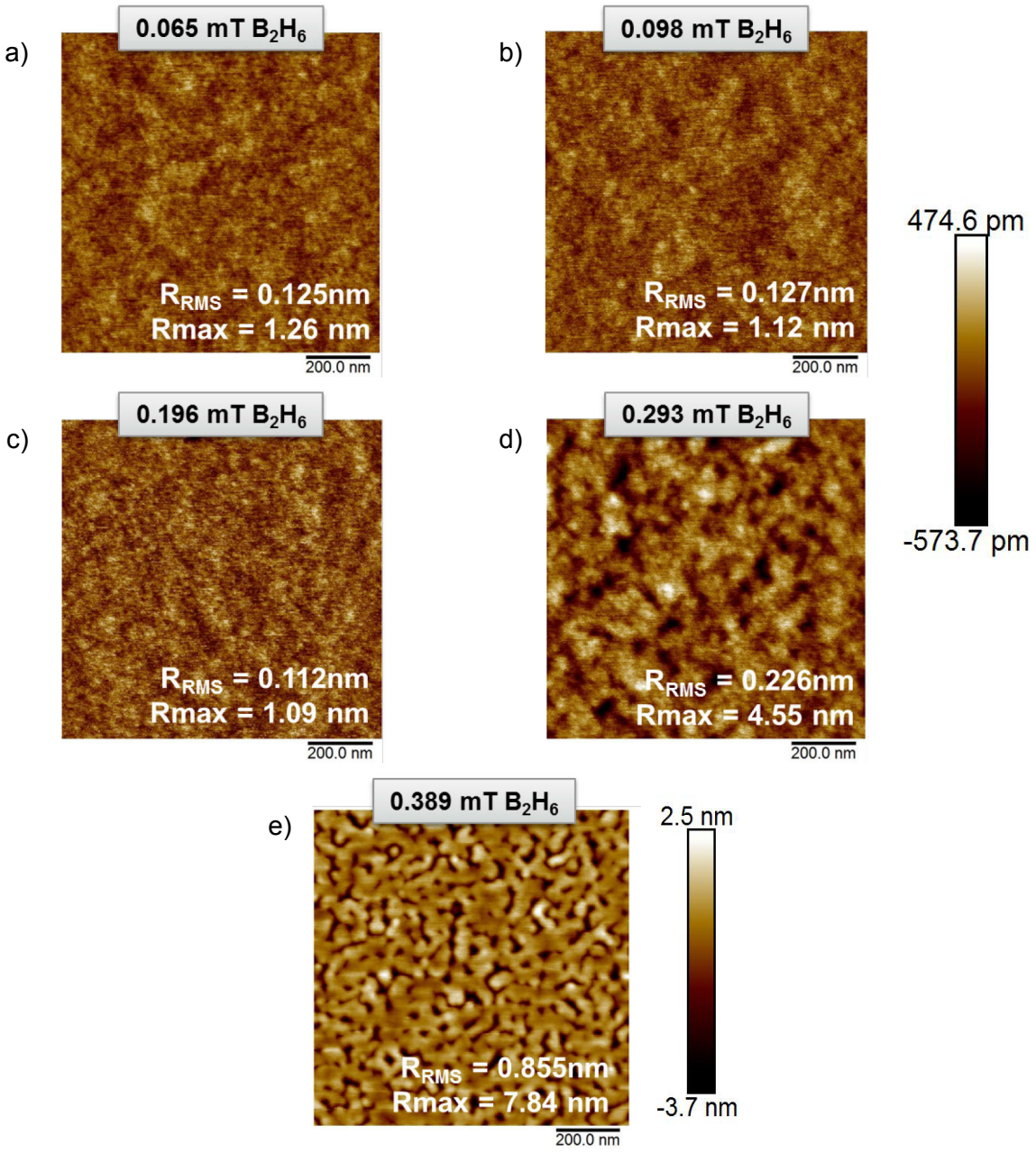

Fig. V-8*: 1 x 1 µm² tapping mode AFM images on large pattern a) 0.065 mT b) 0.098 mT c) 0.196 mT d) 0.293 mT and e) 0.389 mT of B_2H_6. To note that the color scale is the same for the pressures from 0.065 mT to 0.293 mT but changes for the pressure of 0.389 mT.*

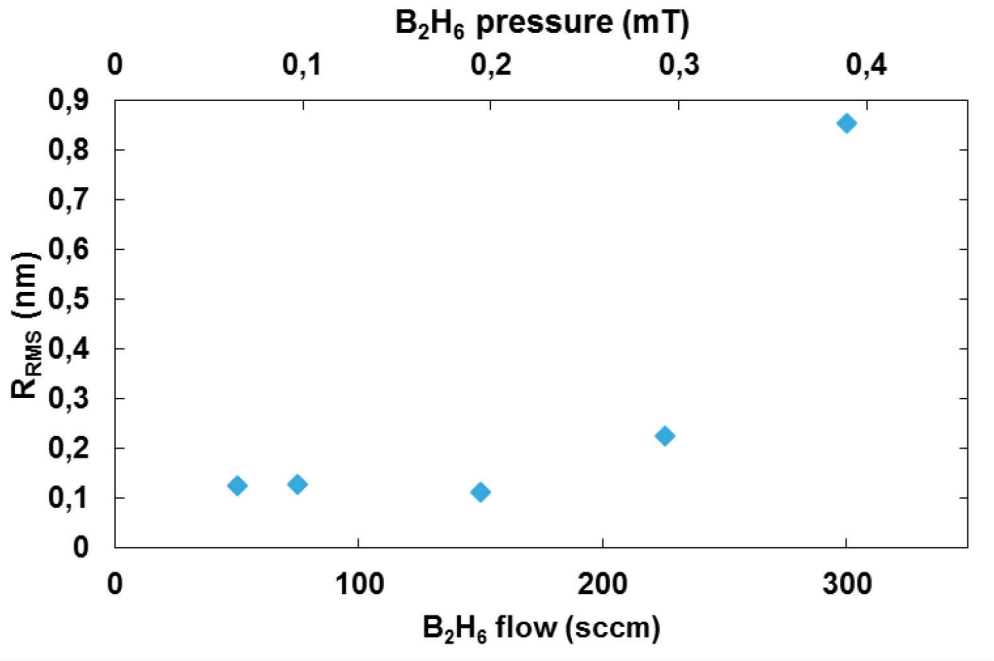

***Fig. V-9**: Roughness as a function of the B_2H_6 partial pressure dependence of the roughness.*

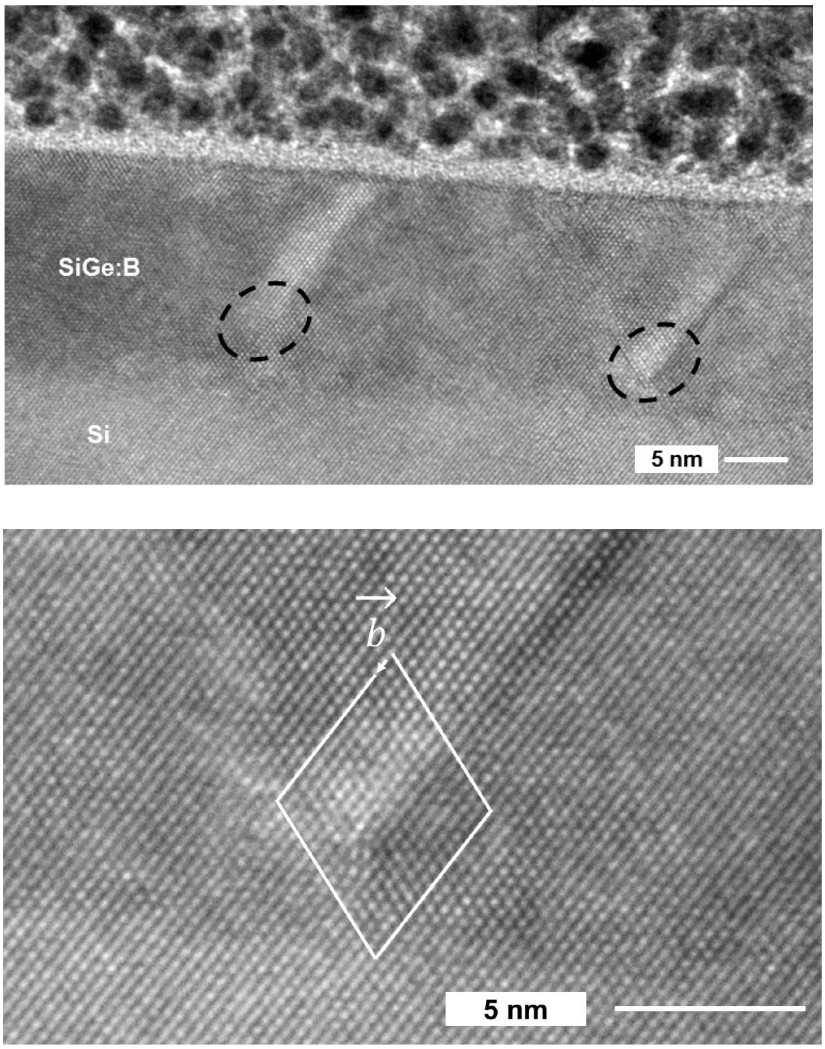

***Fig. V-10**: Cross-section TEM and magnified TEM images of highly doped (0.293 mT of diborane) epitaxial SiGe:B performed in a large box (100 x 50 µm²). Many defects (shown by black dotted circles) are observed in this layer explaining the decrease of the diffraction peaks and fringes' intensity. In the magnified TEM image, a dislocation is defined by its burger vector.*

II.2) Faceting as a function of boron concentration

The morphology of SiGe:B epitaxy in small pattern was also studied. To begin with, intermediate boron doping (0.196 mT) with good epitaxy quality was taken. The ***Fig. V-11*** shows AFM images of SiGe:B epitaxy in small patterns. Thanks to this analysis, a regular facetted morphology is evidenced with the observation of {001} and {111} facets. Indeed, the faceting led to a triangular shape with sides located at 45° from the pattern orientation of <100>. As a consequence, the sides are oriented perpendicular and parallel to the <110> direction and present facets belonging to the {111} planes family. To make sure that {111} facets are clearly identified, an AFM section along <110> direction was done (see ***Fig. V-11*** b). An angle of 54.1° with respect to the (001) plane is measured which is typically the angle of {111} facets (to be compared with theoretical angle 54.74°). The vertical {001} walls cannot be measured by AFM due to the shape of the tip, but it is obvious that they belong to this family plane due to the fact that they are oriented perpendicular to the <100> direction. This kind of

morphology is well-known and is the same as for un-doped SiGe epitaxy (as already shown in *Chapter III*).

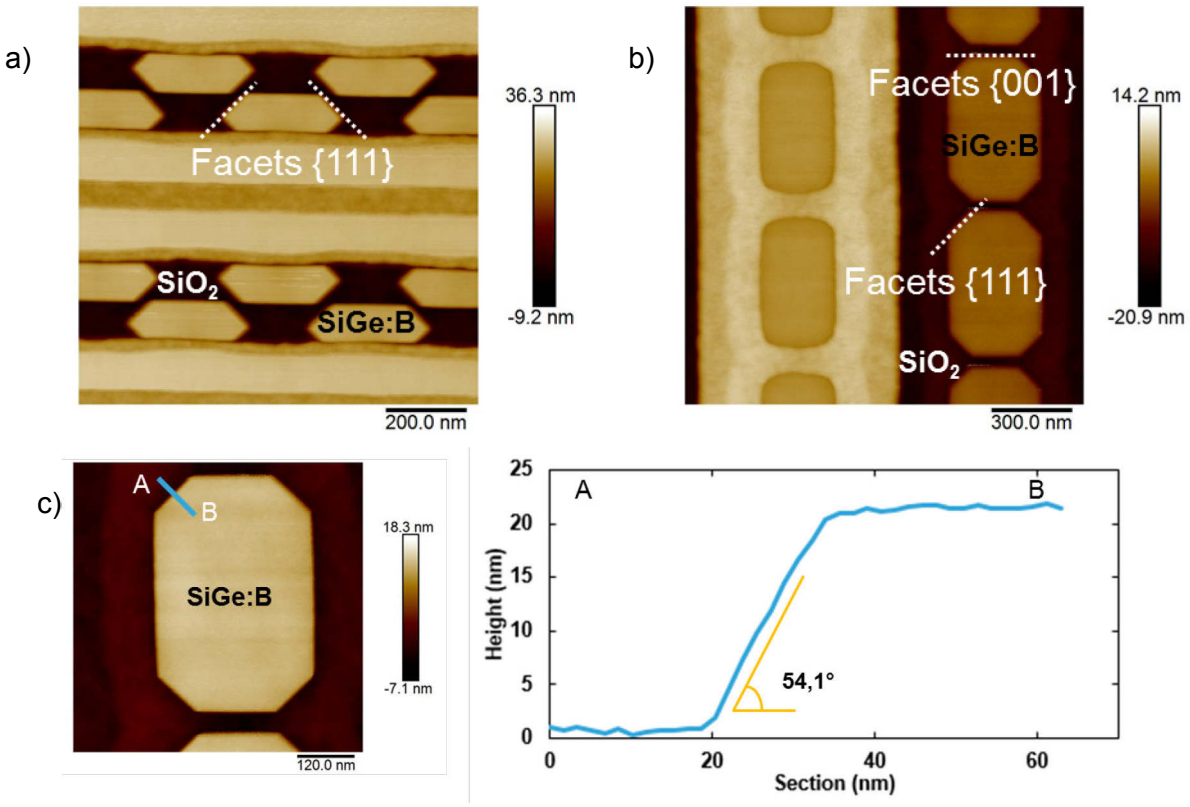

***Fig. V-11**: AFM images in patterns for a B_2H_6 partial pressure of 0.196 mT. a) SRAM b) Rectangle and c) AFM section in the cut corner showing the {111} facet.*

The influence of diborane partial pressure on the epitaxial morphology is given in ***Fig. V-12***. The observed patterns are the active zone of SRAM circuits with dimensions of 36.8 x 276 nm² and an oval with dimensions of 120 x 150 nm². Pressures from 0.033 mT to 0.293 mT were investigated. As observed in the top view SEM images, for intermediate doping (from 0.065 mT to 0.196 mT) the patterns present a regular facetted morphology which is the same as already shown previously. For both patterns, the {111} and {001} facets are well visible. Second, when increasing the diborane pressure to 0.293 mT, the epitaxial growth is very poor resulting in a degradation of the morphology. The patterns' edges are highly rough and irregular and no more facets are observed. This kind of morphology is very detrimental for the devices and must be avoided. It is worth to compare this morphology with the one obtained in the large box for the same pressure. Indeed, in the large box, the roughness corresponding to this doping was relatively good since the fit of XRD diagram was possible and a R_{RMS} value lower than 0.250 nm is acceptable. However, in small patterns the morphology is unacceptable for the devices. As a consequence, the pattern's dimensions impact the quality of the SiGe:B layers. The smaller the pattern's size, the more important the effects due to large B doping. Finally, for very low doping (0.033 mT), the morphology in both patterns is different, especially along the <110> direction. Besides the {111} facets, it seems that another facet appeared as shown in white dotted circles in ***Fig. V-12***. To characterize this change in morphology, AFM images and sections in the <110> direction were performed in SRAMs and depicted in ***Fig. V-13***. Having a closer look on the facets, it is clearly observed that a more extended facet inclined

by 35.32° with respect to (001) plane is present. Along this direction, this angle is the signature of the {112} facet with theoretical angle of 35.26°.

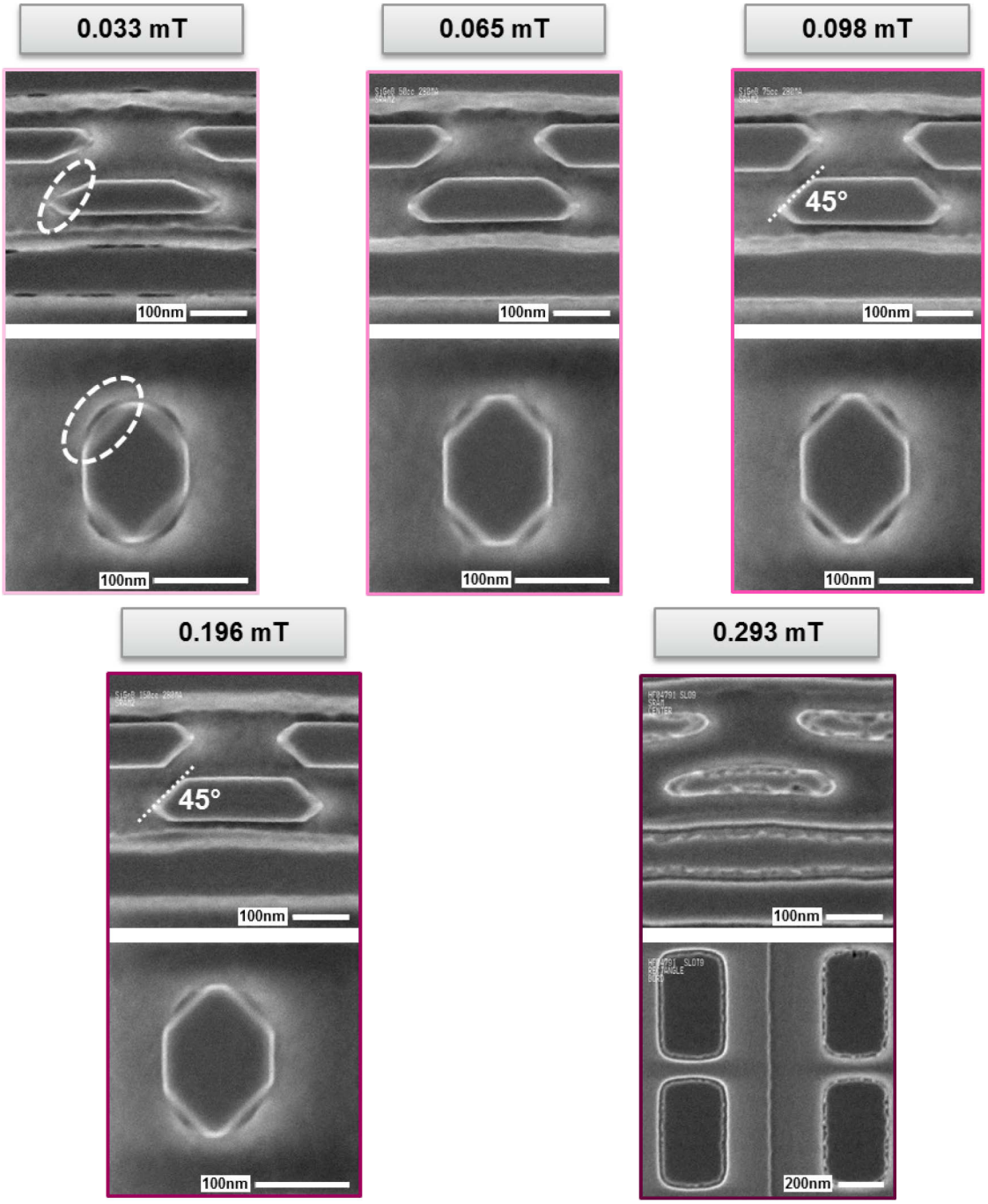

***Fig. V-12**: Top view SEM images of SiGe:B for different partial pressures : 0.033, 0.065, 0.098, 0.196 and 0.293 mT. For low doping, the faceting changes with the apparition of {112} facets (dotted white circles). For intermediate doping, SiGe:B epitaxy in small patterns presents a regular morphology. For high doping, the growth is very poor, no more facets are present.*

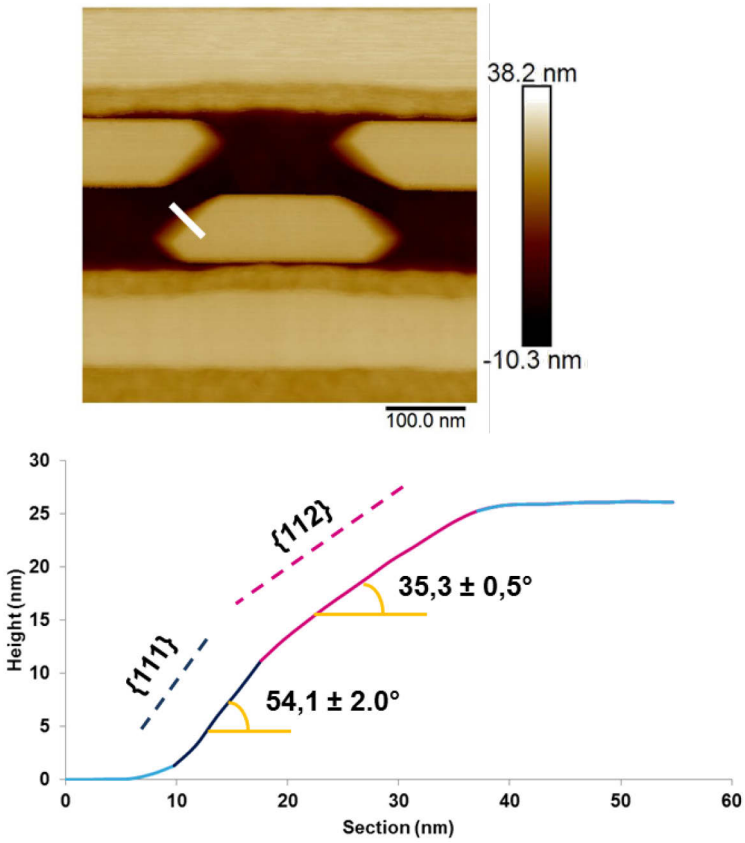

***Fig. V-13**: Top: AFM images in SRAM for a B_2H_6 partial pressure of 0.033 mT. Bottom: AFM section along <110> direction. Apparition of the {112} facet. The {111} facet is still observable.*

II.2) Epitaxial Lateral Overgrowth

In this section, the epitaxial lateral overgrowth (ELO) is studied as a function of B_2H_6 partial pressure. Pressures from 0.033 mT to 0.196 mT are used. Two SRAMs with different dimensions, named SRAM 1 and SRAM 2 are taken for this study. The morphology of both patterns prior to epitaxial growth is given by top view SEM in ***Fig. V-14***. The dimensions are 276 x 36.8 nm² and 299 x 46 nm², respectively. The as-deposited morphology is also shown in this figure. L1 and L2 are the two investigated lengths which will allow the ELO to be studied. L1 is also called the transversal ELO and L2 the longitudinal ELO. To note that L1 and L2 are not exactly the ELO since by definition, ELO is the overgrowth of the epitaxy out of the active zone (on the SiO_2). L1 and L2 can then be defined as:

$$L = 2 * ELO + AZ \qquad \text{Eq. V-1}$$

Where ELO is the lateral overgrowth, AZ is the dimension of the active zone in the direction of the measured length.

Fig. V-15 gives cross-section TEM images of SRAM 2 along the <100> direction (along L1) for 0.065 mT and 0.196 mT of diborane. As a first observation, the ELO seems to be lower for low doping than for high doping. The reason of this difference in ELO will become clear by comparing each B_2H_6 partial pressure in the following. Second, the observed thickness in this pattern is higher than the one measured in large boxes: a thickness of 24 nm is observed as

compared to the 20 nm measured by ellipsometry and XRD. This difference is due to the loading effect. Consequently, it is worth to remind that the ELO could be underestimated: as already observed by Seiss *et al*. in the same patterns [Seiss 13-4], the overgrowth on the convex edges is smaller than the deposited thickness. Moreover, the ELO measured by Eq.V-1 is the average between the two ELOs corresponding to the concave and the convex edges resulting in a smaller calculated ELO. ***Fig. V-16*** shows the evolution of L1 and L2 as a function of the B_2H_6 partial pressure for both SRAM 1 and SRAM 2. Concerning the transversal ELO, it is observed that an increase of diborane flow leads to an increase of L1. For SRAM 1, it evolves from 58.5 nm to 70.0 nm when increasing the partial pressure from 0.033 to 0.196 mT; for SRAM 2, L1 increases from 73.2 nm to 85.7 nm. This means that the ELO's observations made on an un-doped layer are impacted when the boron is incorporated inside the lattice, or at least by the change in the growth kinetics due to boron incorporation. The calculation of ELO in SRAM 2 by Eq.V-1, shows that the layers with high B concentrations behave like an un-doped layer. Indeed, the ELO is equal to 19.9 nm (for 0.196 mT) and to 19.4 nm (for 0.098 mT) which is equivalent to the growth thickness (20 nm). In these cases, a certain deposited thickness results in the same amount of overgrowth. However, when decreasing the diborane partial pressure to 0.033 mT, ELO is no more than 13.6 nm meaning that a certain deposited thickness results in an overgrowth's amount of only 68% of the thickness (0.68 x the growth thickness). The same trend is observed for SRAM 1. Concerning the longitudinal ELO, no influence of the boron incorporation on L2 is observed. L2 seems to stay constant around 278 nm for SRAM 1 and around 295 nm for SRAM 2 independently on the diborane partial pressure.

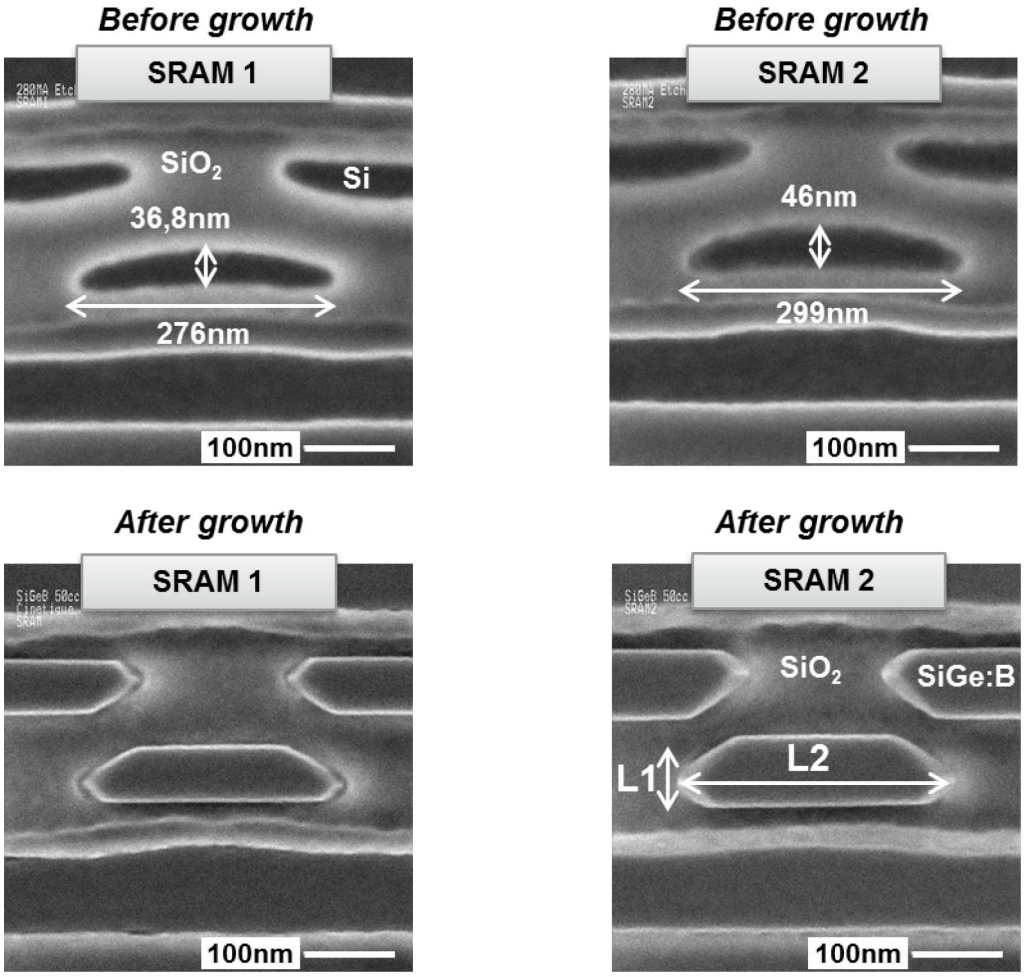

***Fig. V-14**: Top view SEM images of SRAM 1 and SRAM 2 before and after SiGe :B growth. The SRAM 1 has dimensions of 276 x 36.8 nm² and the SRAM 2 has dimensions of 299 x 46 nm².*

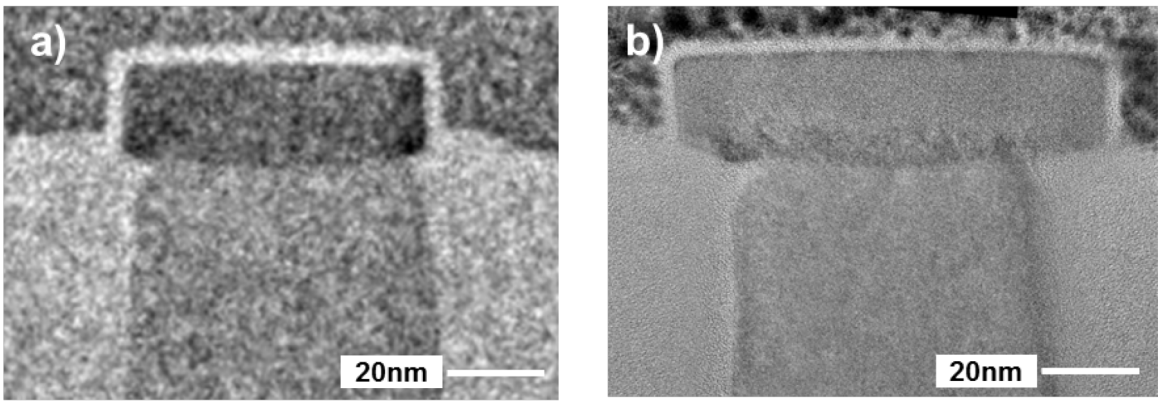

***Fig. V-15**: Cross-section TEM images of SRAM 2 along the <100> direction. a) 0.065 mT of diborane. b) 0.196 mT of diborane.*

a)

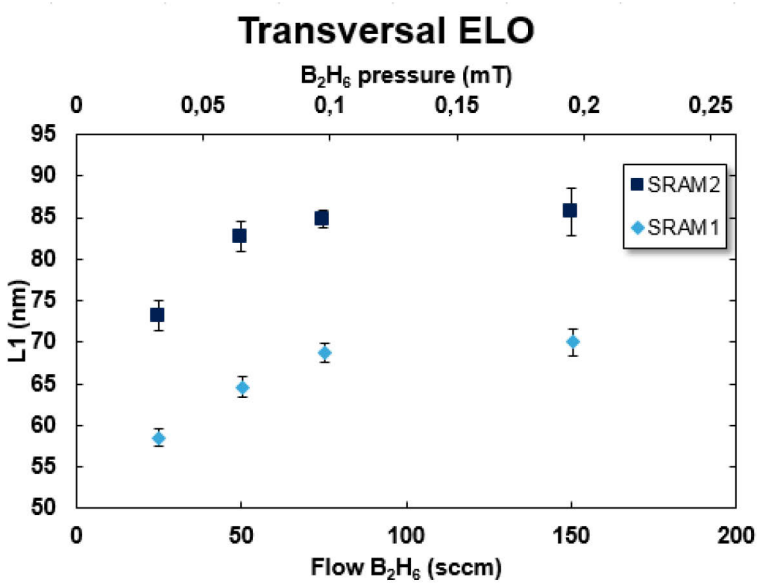

b)

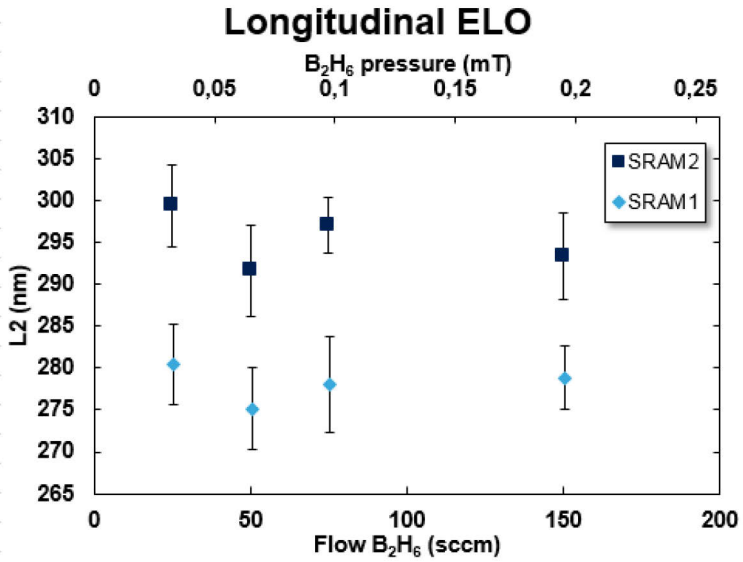

***Fig. V-16**: Evolution of the a) transversal and b) longitudinal ELO as a function of diborane partial pressure.*

III/ Morphology of SiGe:B after annealing

The influence of annealing on the SiGe:B films' morphology is studied in this section. The SiGe sample with a boron concentration of 6.57 x 10^{20} at/cm^3 (equivalent to 0.196 mT of diborane) is annealed at temperatures equal or lightly higher than the growth temperature, i.e. 644°C and 650°C for 0 s to 60 sec under a hydrogen atmosphere of 10 Torr. This part was used to characterize the influence of the purge step after the growth on the samples' morphology. The morphological evolution is given in ***Fig. V-17***. The morphology of the annealed samples is characterized by AFM.

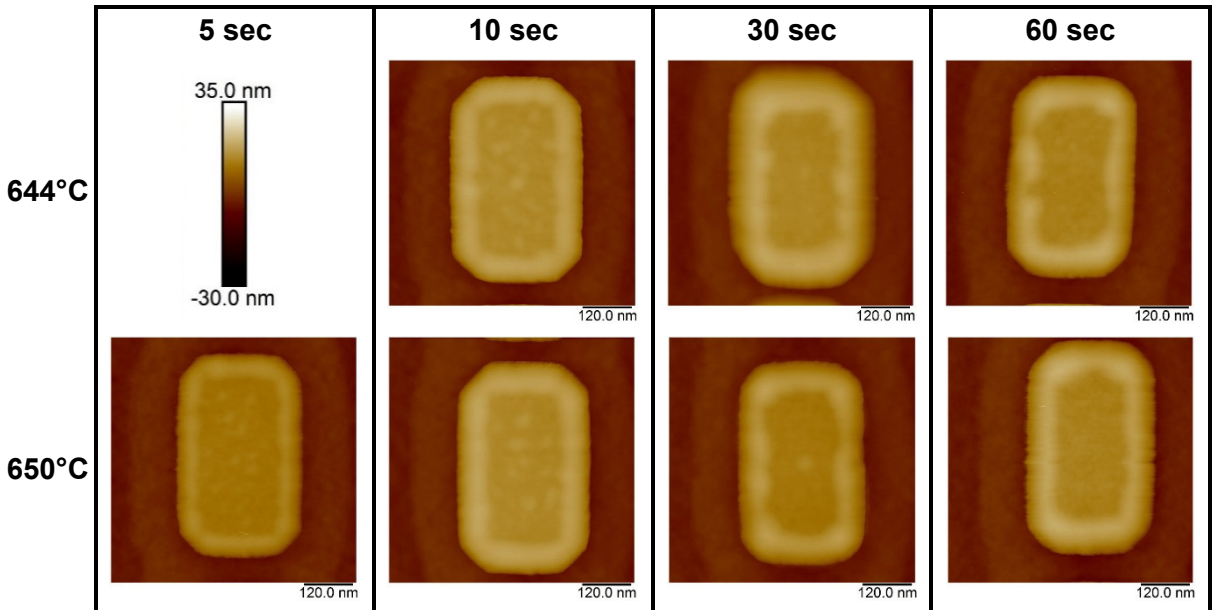

***Fig. V-17**: AFM tapping images of SiGe:B layers annealed either at 644°C or 650°C for durations comprise between 5 sec and 60 sec. The thermal rounding is very effective even for short durations: the ridges already formed all around the pattern.*

As already mentioned for un-doped layers, during thermal rounding the matter entirely retracts to the active zone leading to the formation of rounded ridges all around the pattern. The as-grown facets and their corresponding lateral overgrowth disappear during this step. For B doped layers, similar observations are made but there are some significate differences. First, for annealing at 650°C and 644°C, only 5-10 sec is enough for the thermal rounding to be effective which was not the case for un-doped layers. Indeed, the rounded ridges already formed all around the pattern. An un-doped SiGe layer was grown and then annealed at 650°C for 10 sec under a 10 Torr of H_2. The annealing was performed in the same conditions as for the SiGe:B layers. The comparison is given in ***Fig. V-18***. It is clearly observed that the thermal rounding is much more pronounced in the case of B doped SiGe layer. Regarding the un-doped layer, the morphology is similar to the as-grown one meaning that 10 sec of annealing (at 10 Torr and 650°C) is not sufficient for the thermal rounding to be observed. This faster thermal rounding may be provided by first, the Ge concentration which is higher in the boron doped layers (33% versus 25%) second, the boron incorporation. Indeed, as already mentioned the B incorporation increases the GR by decreasing the H coverage. This allows a faster surface diffusion and thus a faster thermal rounding. Second, the rounded ridge around the pattern is not smooth and regular as already observed and the interior of the pattern is highly rough as compared as what it was observed for an un-doped layer. In addition, the matter seems to retract to the active zone really slowly and even more it seems to be trapped. Indeed, in some cases, the corners are still cut at 45° while the {111} facets disappeared. This may be due to the boron that makes precipitates with Si atoms impeding the epitaxy to retract. Another interpretation can be that the B makes the Si (or Ge) adhere to the SiO_2.

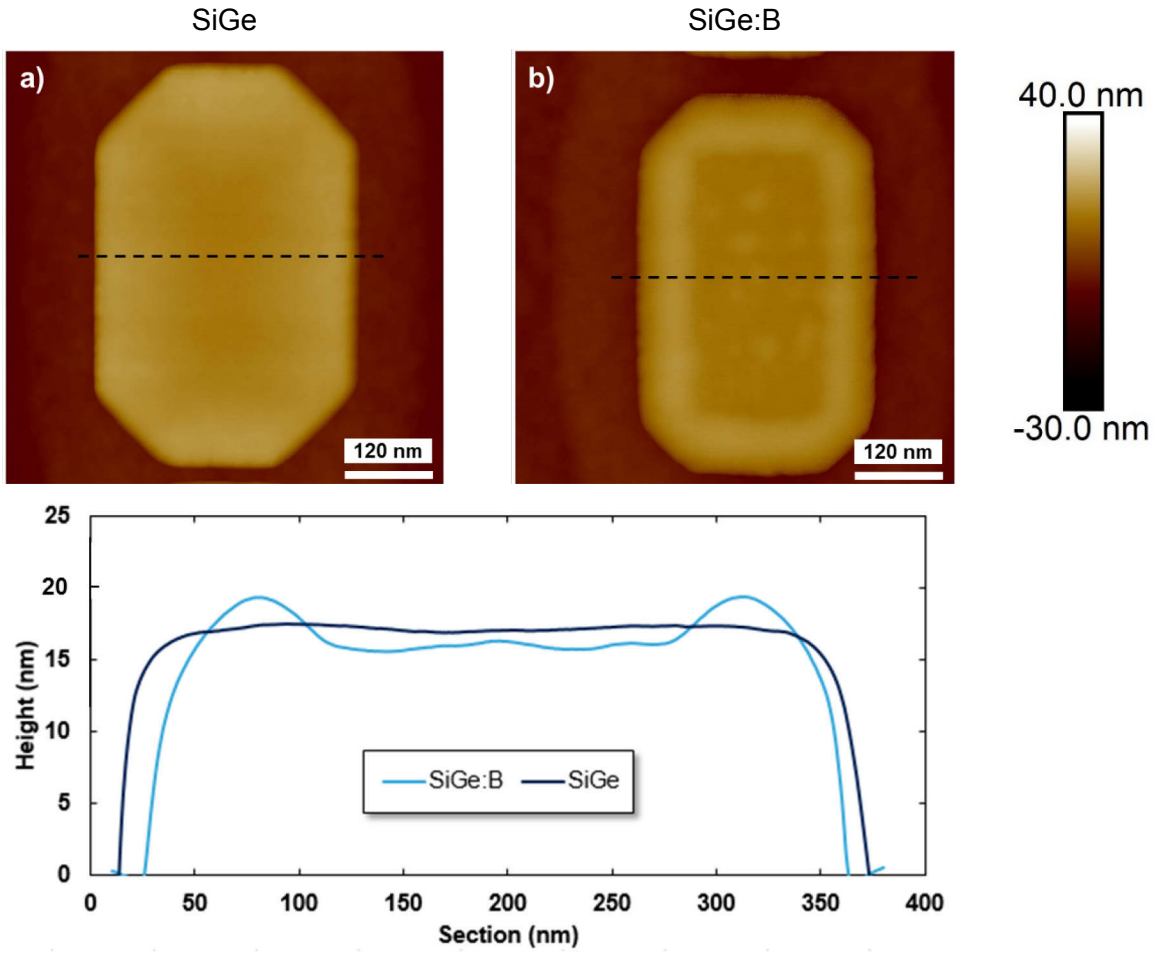

***Fig. V-18**: 0.6x0.6 µm² AFM images of a) SiGe and b) SiGe:B layers annealed at 650°C for 10 sec under 10 Torr of H_2. The AFM sections for both layers is also given. The rounding is much more efficient when the layer is doped with boron. This can be explained by the decrease of H coverage due to an enhancement of the GR when boron is added in the layer. The decrease of H coverage results in a faster thermal rounding.*

1x1 µm² AFM images made in large patterns is also given in ***Fig. V-19***. The difference is once again clearly evidence. The roughness is much higher is the case of SiGe:B: it is equal to 0.465 nm for SiGe:B and 0.111 nm for the SiGe layer. The SiGe:B layer presents a highly rough surface with the formation of randomly organized islands. This means also that the SiGe:B is more sensitive to thermal treatment than the un-doped SiGe layer. However, it seems that for the doped layers, the formation of the <110> oriented ridges (already observed for n-doped layers) does not occur maybe due to the fact that very rapidly the B makes precipitates with Si or Ge avoiding the SK undulations to be formed. Moreover, comparing the SK undulations with the formation of islands in SiGe:B layers, the wavelength measured by the Power Spectral Density is very different. Indeed, it was observed an undulations' wavelength of 0.231 µm for a 20 nm thick un-doped layers. In the case of SiGe:B, the wavelength is roughly equal to 0.08 µm, which is 3 times lower than that of SiGe

.

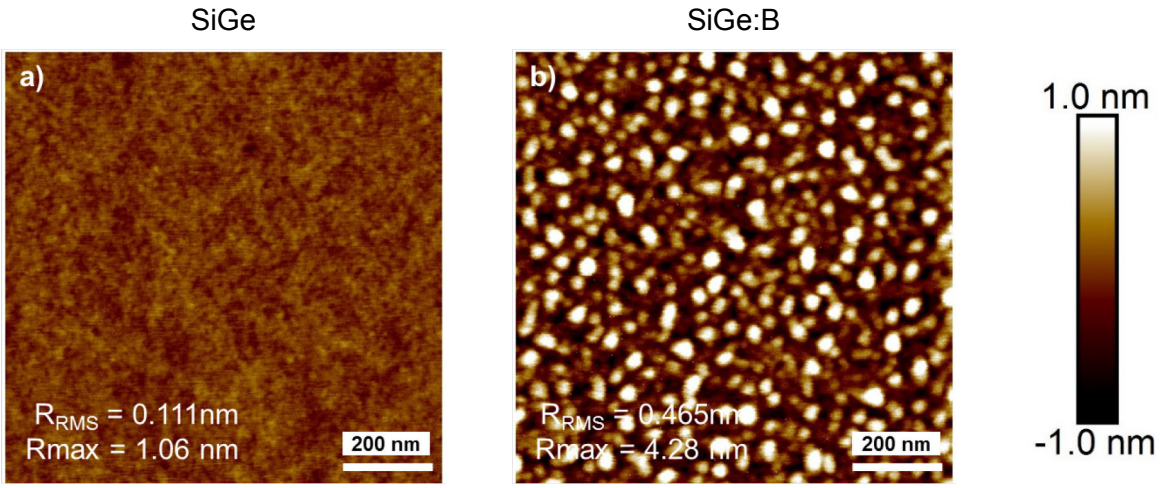

***Fig. V-19**: 1x1 µm² AFM images made in large patterns of a) SiGe and b) SiGe:B layers. Both layers were subjected to the same thermal treatment: 10 sec at 650°C and 10 Torr. The SiGe:B layer presents a highly rough surface with randomly organized islands.*

Fig. V-20 shows AFM images of SiGe:B layers in large boxes after 850°C annealing for 60 sec under 20 Torr of hydrogen. Both B_2H_6 partial pressures of 0.065 mT and 0.196 mT are used. First, comparing the doped and the un-doped layers, one can see that the observed <100>-oriented ridges and regular domes normally formed during the annealing are no more present when adding boron dopants inside the layer. At least, the preferred direction and the regularity in the domes' size and shape is no more respected. Indeed, the morphology seems to be randomly organized and the patterns' size and shape in the large box are very different from one to another. In terms of faceting, the doped islands are faceted but they appear to contain multiple twin planes or simply irregular shape (see ***Fig. V-21***). This has to be compared with the high degree of symmetry as already observed in un-doped SiGe domes. This behavior can be explained in terms of defects due to boron precipitations with Si or Ge avoiding the strain relaxation to propagate. Second, comparing both doped layers, it is observed that the doping level as a significant impact of the post-anneal morphology. Indeed, the islands that are formed during the annealing are more abundant in the case of the lowest doping. Furthermore, considering the high doping, the islands seems to be trapped by the highly rough surrounded surface and their corresponding facets appear clearer. This is well observed in ***Fig. V-21*** showing the magnified AFM amplitude error images of the islands. In this figure, some small bubbles surrounding the islands are visible which can be the foresaid boron precipitates.

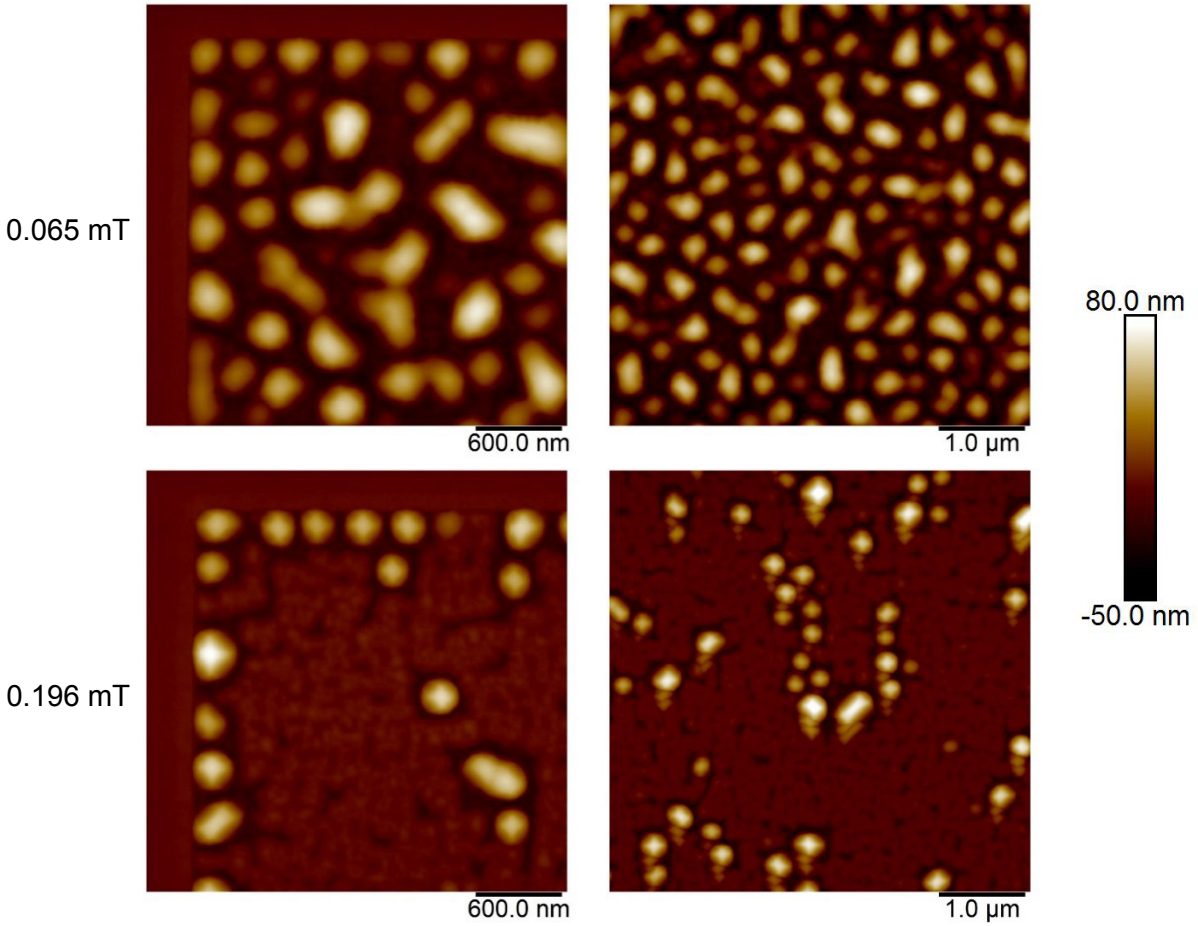

***Fig. V-20**: AFM images of annealed boron doped SiGe layers in large boxes. The annealing was performed at 850°C for 60 sec under 20 Torr of hydrogen. B_2H_6 partial pressures of 0.065 mT (top) and 0.196 mT (bottom) are represented. Boron prevents the SK undulations to be formed creating agglomerates.*

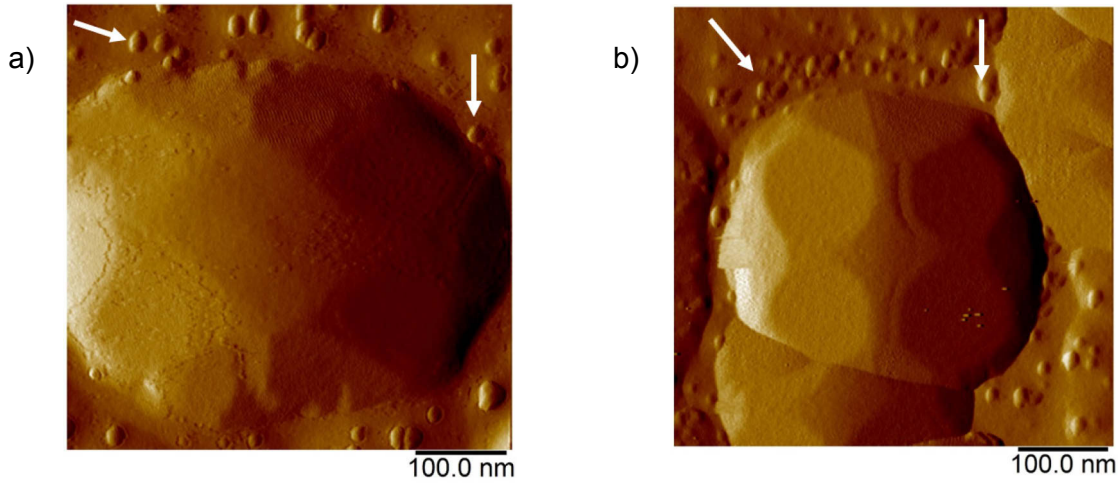

***Fig. V-21**: Magnified AFM amplitude error images of islands in the large boxes for a) low doping (0.065 mT of B_2H_6) and b) high doping (0.196 mT of B_2H_6). The islands are less faceted for the lowest doping. For both, the islands show asymmetries probably due to defects or boron precipitates. The small bubbles (shown by white arrows) can be the aforesaid boron precipitates.*

Similar results are obtained when looking at smaller patterns as shown in ***Fig. V-22***. For the low doping, the matter separated into two parts forming two separated islands, one located on the top of the patter and the other on the bottom. For the highly-doped layer, two islands also formed but they are not separated. Moreover, these islands are faceted in a way they appear as asymmetric pyramids. The pyramid's top is not centered and the four facets all around are not exactly similar. This can be explained by the fact that the highest B doping induces a higher strain's decrease resulting in an increase of the instabilities' wavelength, thus to bigger pyramids. Consequently, a small strain may induce larger wavelength and larger pyramids. The pyramids being larger cannot fit inside the pattern and consequently organize in an asymmetric way. Finally, both doped layers show corners cut at 45° as if the matter has difficulties to retract to the active zone. Here again, this can be attributed to boron precipitates impeding the atoms to diffuse correctly on the surface, or to the fact that B makes the Si (or Ge) adhere to the SiO_2. It is clearly observed with the amplitude error images where the small bubbles are well visible all around the pattern.

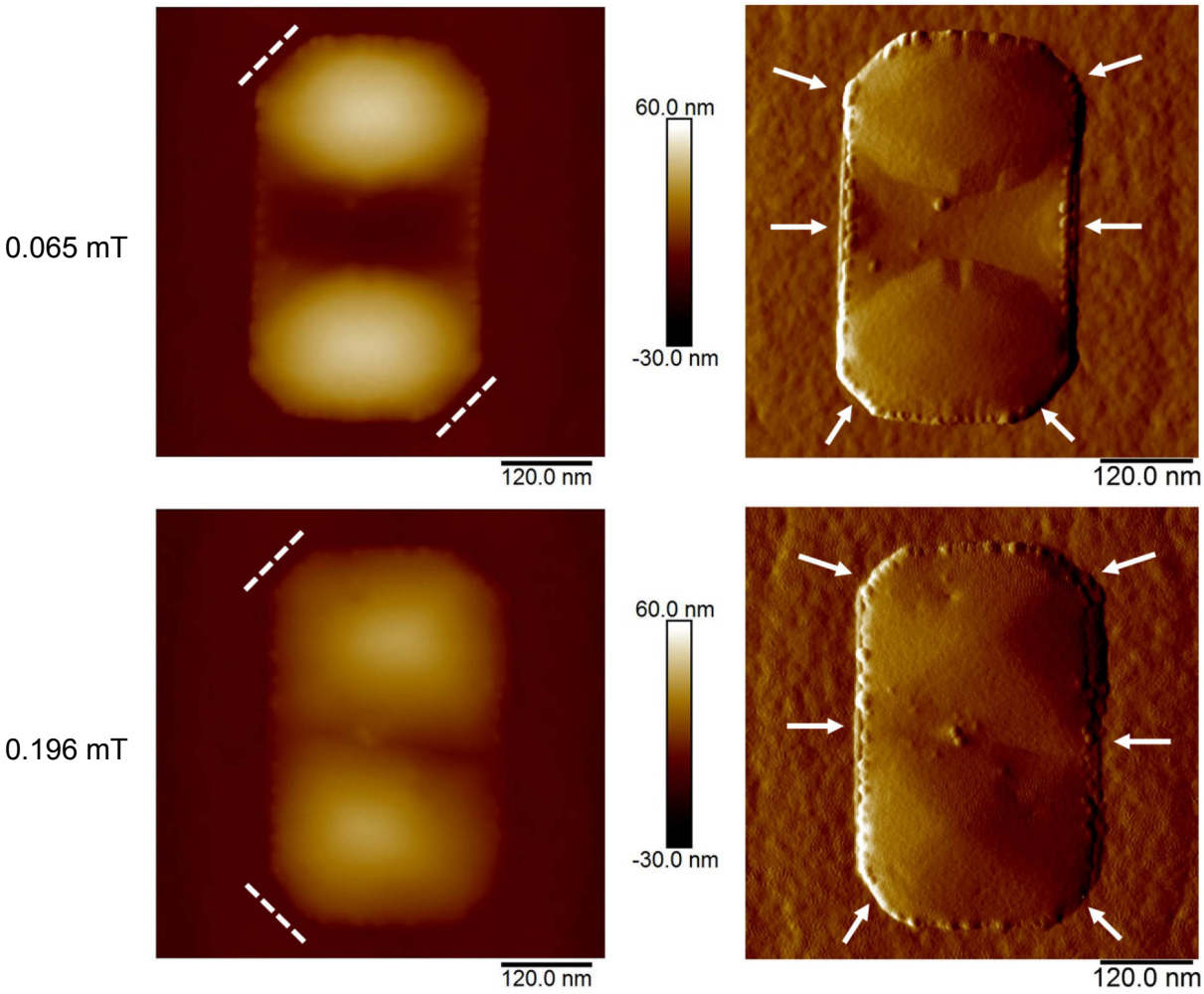

***Fig. V-22**: 0.6 x 0.6 µm² AFM images of SiGe:B layers in rectangle pattern after 20 Torr of H_2 annealing at 850°C for 60 sec. Diborane partial pressure of (top) 0.065 mT and (bottom) 0.196 mT were used. For the low concentration, two distinctive parts broke away which is not the case for the high concentration which shows two asymmetric pyramids. The right part of the image show the same images but in amplitude error mode. The small bubbles all around the pattern are shown by white arrows.*

As a conclusion of this part, it was evidenced that the incorporation of B in the layers induces at least four consequences. First, the B increases the GR due to a decrease of the hydrogen coverage. This results in an enhancement of the thermal rounding as observed for annealing (purge) at 10 Torr. Second, the B seems to pin the Si on the SiO_2 which results in an efficiency loss of the matter's retraction during the thermal rounding. This was observed in rectangle patterns for which the corners at still cut at 45°. Third, the B makes precipitates with Si or Ge atoms which may trap the as-grown morphology. Finally, the B decreases the layer's strain.

IV/ Industrial applications in S/D

This last part deals with the integration of the investigated boron doped layers in the 14 nm node source and drain devices. The wafers are <110>-oriented. The aim was to grown p-doped SiGe layers in between two gates to create the S/D with the adequate facetted

morphology. Indeed, a faceted morphology can decrease the parasitic resistance and a capacitance gain of 40% can be reached, as shown in ***Fig. V-23*** below [Lacord 12].

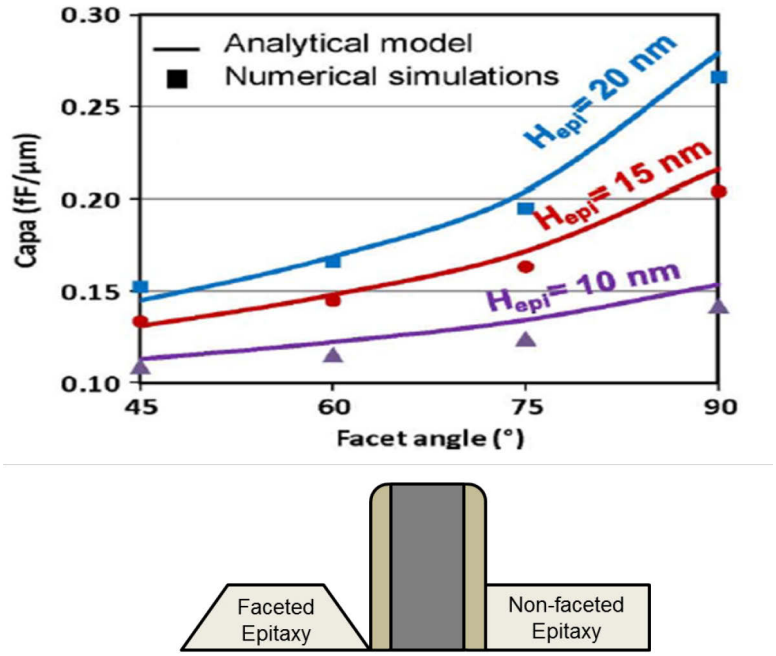

Fig. V-23*: Capacitance as a function of the facet angle for different thicknesses' layer. For a faceted epitaxy, a capacitance gain of 40% can be reached as compared to a non-faceted morphology.*

However, some difficulties were found when growing boron doped SiGe layers. First, since a high doping level is required for the device's performances, the morphology was degraded as already observed for as-deposited SiGe:B layers whose effect is intensified for the 14 nm node. Second, the B doped SiGe layers are grown selectively on a SiGe channel, which is more thermally sensitive than the Si channel. This means that cautious cares must be done before growing the B doped layer: the SiGe channel is passivated with Si atoms during the temperature ramp to reach the SiGe's growth temperature. Finally, even for an acceptable quality of epitaxy, the SiGe:B layers were flat without any facets. This morphology is given in ***Fig. V-24***. As a first interpretation of this result could be that the epitaxial growth was not faceted. However, another and preferred interpretation is that the SiGe:B layer was subjected to thermal rounding before wafer unloading leading to the disappearance of the facets and a leveling of the surface. Indeed, in the majority of the process a small purge (10 – 30 sec) is added after the growth (*see Chapter 3 IV.3) Application of Si-passivation*) that can be long enough for the ad-atoms to diffuse on the surface. As a result, the "freezing" recipe was added to validate the hypothesis of thermal rounding during the purge. ***Fig. V-25*** show top-view SEM images in the device for a standard process (with 10 sec of purge) and for the optimized process (with "freezing" recipe). In the figure, the boron concentration measured by MBIR (in large patterns TBOX) is equal to 1.4 x 10^{20} at/cm^3. Having a look on each device's structure, the morphological difference between the two processes is evident. For the "freezing" process, the morphology presents facets all around. These facets are the {111} facets because of the <110> orientation of the patterns on the (001) surface. However, for the standard process, the

facets almost disappeared and the corners have a rounded shape. This is even more visible when the dimensions of the active zone decrease.

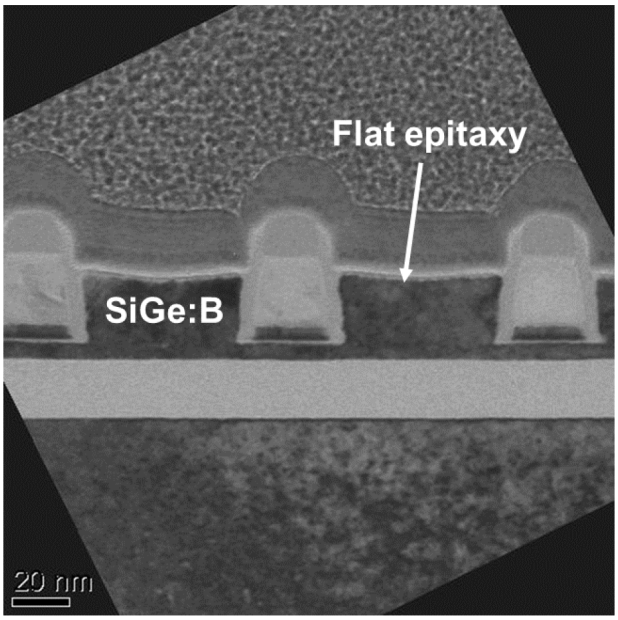

***Fig. V-24**: TEM cross-section image of S/D SiGe:B epitaxy. The layer presents a flat morphology without any facets. Image from STMicroelectronics.*

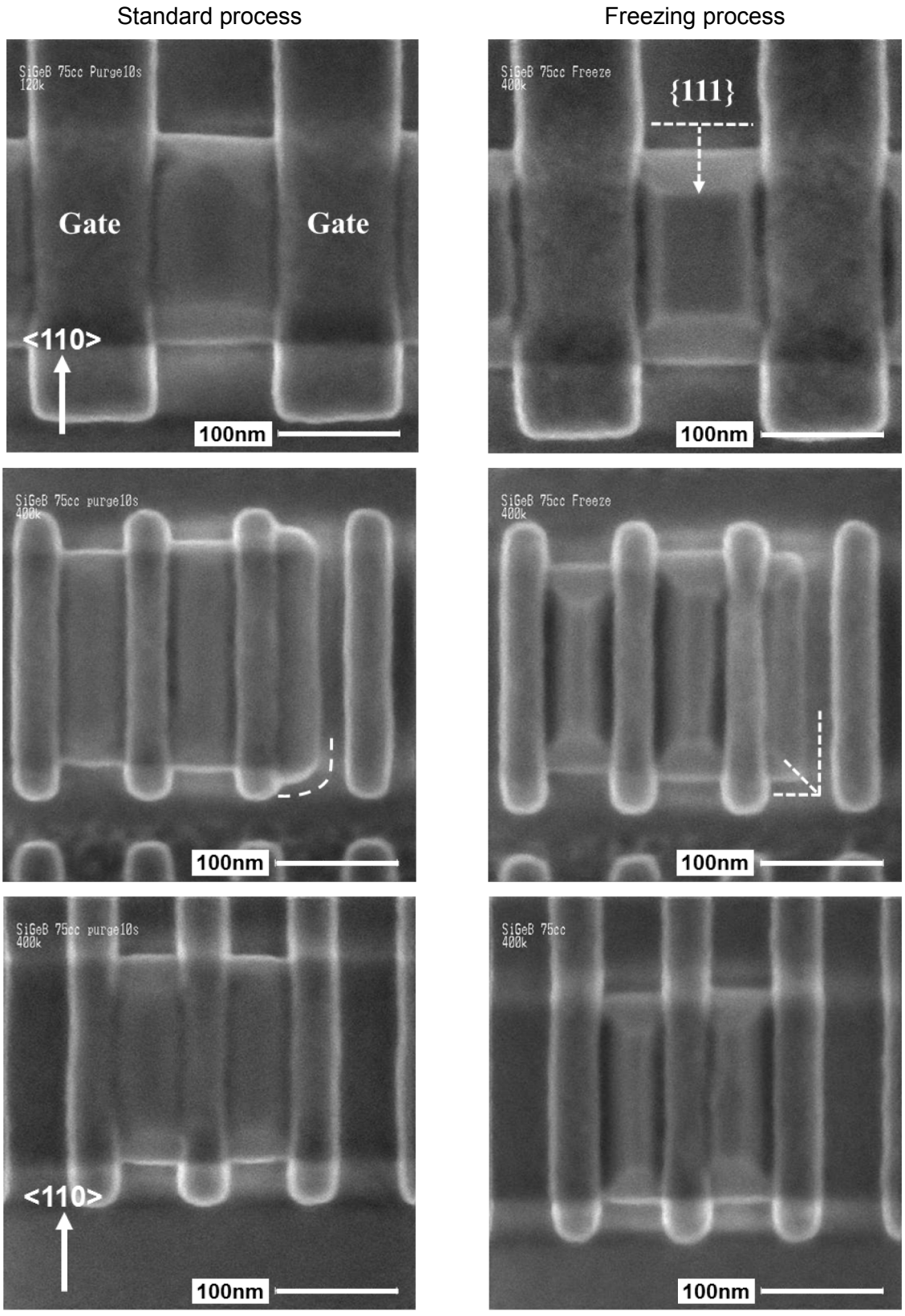

***Fig. V-25**: Top-view SEM images of SiGe:B in difference device's structure for (left) a standard process with a 10 sec purge and (right) the "freezing" process. It is clear that during the standard process the SiGe:B layer endured the thermal rounding since the facets disappeared as shown by the dotted lines.*

A more quantitative study was performed in these structures by AFM. ***Fig. V-26*** shows AFM images of the SiGe:B layers grown by the standard process and by the "freezing" recipe. Thanks to the AFM profile displayed in this figure, with the "freezing" recipe, the {111} facets are clearly identified and the top's surface of the epitaxy is perfectly flat which corresponds to the {001} facet. On the contrary, with the 10 sec purge, the profile shows a rounded shape with no more facets. The profiles were done as shown by the white dash line. AFM profiles perpendicular to this direction were also performed (black lines) but it is rather difficult to identify the {111} facets: only angles of 50° were measured and not the theoretical angle of 54.7°. However, the rounded aspect in the case of the purge, is well present. This study confirms the usefulness of the "freezing" recipe to maintain the as-grown morphology.

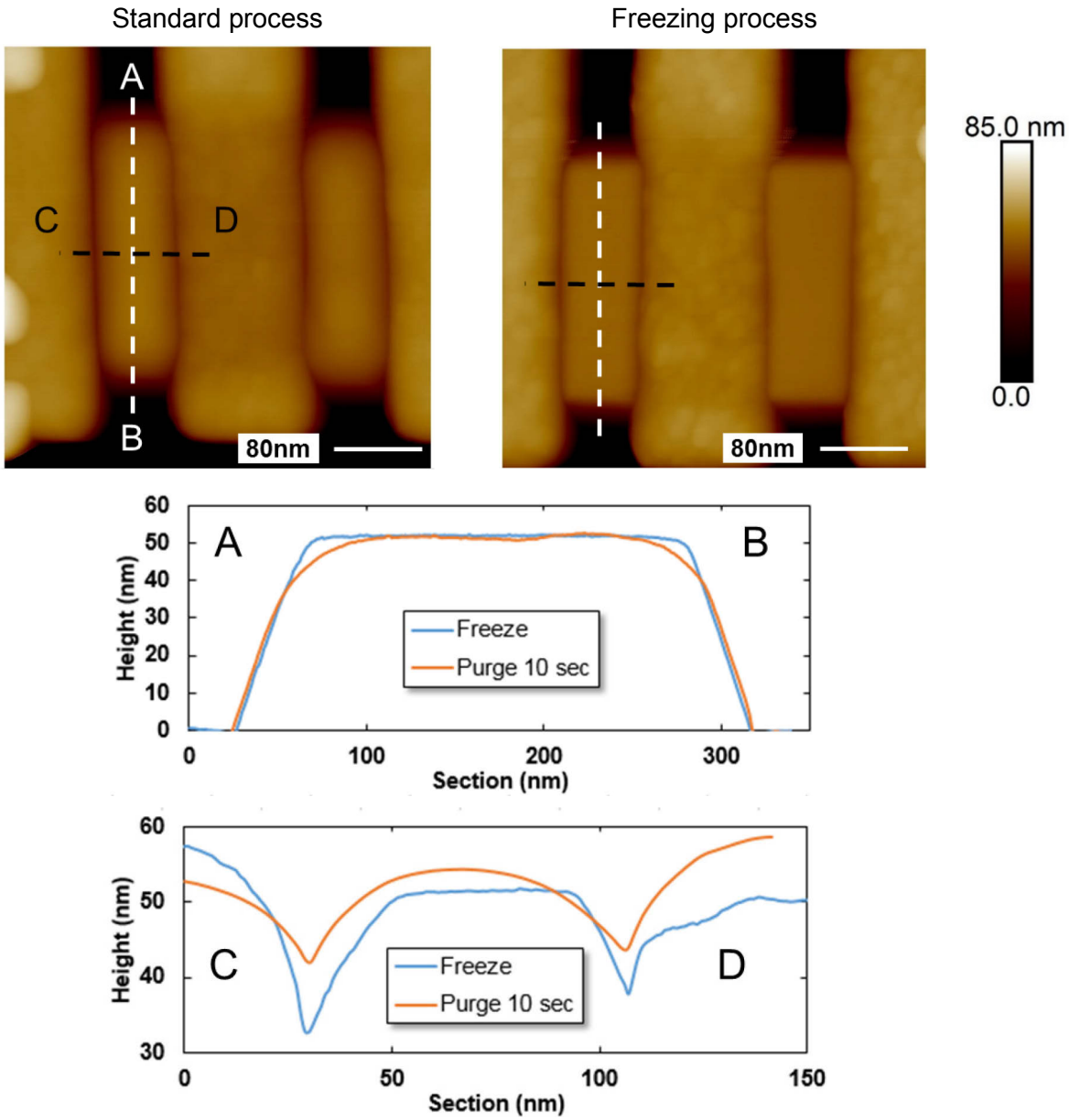

Fig. V-26*: AFM images of SiGe:B for (left) a standard process with a 10 sec purge and (right) the "freezing" process. The profiles are shown in the graph. It is clear that for the standard process the corners adopted a rounded shape and the top surface is not flat as observed for the "freezing" recipe.*

The efficiency of the “freezing” process was again demonstrated and the integration of the process in the circuit’s structures was successfully achieved. A regular {111} faceted morphology was rediscovered would allow better a capacitive/resistance trade off to be reached in certain integration schemes. Some electrical measurements would be interesting to perform in these structures to verify the hypothesis.

V/ Conclusion

This chapter was focused on the SiGe:B layers and especially, the influence of the B on the kinetics and the morphology. First, the GR increases with increasing the B concentration. This is due to an enhanced H desorption freeing the surface sites faster. It was observed, for high doping levels, that the B concentration presents a huge peak at the interface, then decreases and stabilizes at a lower value close to the surface. This may be attributed to a B saturation at the interface which can make some precipitates. The XRD technique was shown to be not sufficient to measure the “real” XGe because it measures, in one hand, the lattice dilatation due to Ge, and in the other hand, its contraction due to the small B atoms. As a result, the XRF was used to measure the XGe, since it measures the amount of Ge.

The morphology was studied as a function of the B concentration. It was shown that the epitaxies’ quality decreases significantly for high doping levels. Dislocations were observed which may be resulted to B precipitates at or near the interface. Furthermore, the B may induce differences on the faceting. For intermediate doping, the faceting is similar to the un-doped layers with the presence of {111} and {001} facets. For low doping, the {112} facet appeared in addition to the {111} facet. The epitaxial lateral overgrowth in the <100> direction was also investigated in SRAM’s the active zones. For intermediate doping, the ELO is equal to 1 x the growth thickness. It decreasing when decreasing the B concentration and reaches, in our case, a value of about 0.68 x the thickness.

Annealing of SiGe:B layers was studied and compared to un-doped SiGe layers (for a same thermal treatment). First, the thermal rounding occurs faster for SiGe:B than for un-doped layers. This may be provided by first, the Ge concentration which is higher in the boron doped layers (33% versus 25% for the un-doped layers) second, the B. Indeed, as already mentioned the B incorporation increases the GR by decreasing the H coverage. This allows a faster surface diffusion and thus a faster thermal rounding. However, the retraction to the active zone seems not to be produced as fast as what observed for un-doped layers. This can be attributed to boron precipitates impeding the atoms to diffuse correctly on the surface, or to the fact that B makes the Si (or Ge) adhere to the SiO_2. In large boxes, SiGe:B layer presents a highly rough surface with the formation of randomly organized islands while the un-doped layer presents a flat surface (low roughness). However, the SK undulations do not seem to appear in the case of SiGe:B layers, maybe due to B precipitates that avoid the undulations to propagate.

The integration of the Si passivation in the SiGe:B S/D process for the 14 nm node was successfully done. It was compared, in terms of morphology, to the standard process which contains a post growth purge. With the “freezing” recipe, a well faceted morphology was obtained, while with the standard process, the morphology had a rounded shape. This showed once again the importance to take cautious cares when dealing with any thermal treatments.

Conclusion

The improvement of the epitaxy's processes and their integration in CMOS technologies allowed to solve many different problems conceived by the unremitting transistor's scaling. Nowadays, epitaxy is one of the major steps for the devices' development and is a key factor to continuously improve the performances of these devices. It is used to realize, for example, high mobility SiGe channel or in-situ doped sources and drains. Moreover, the very accurate control of the epitaxial growths' morphology is crucial for the devices' performances especially with the continuous decrease of the transistor's size. Third, with transistor's dimensions reaching tens of nanometers, the thermal effects are very pronounced and can have a real impact on the morphology and thus on the devices' performances. The effects that were neglected in the past are no more and must be taken into account. In addition, the increase of the structures' complexity, for example, the growth around the gate of the boron doped sources and drains on SiGe channel, makes the epitaxial growths and their morphological control very critical. Consequently, the morphology's study and more precisely the influence of thermal treatments on the morphology of Si-based epitaxies is the main aim of this thesis. To do so, selective epitaxial growths (Si, SiGe and SiGe:B) performed by RT-CVD were characterized first, right after the growth, second, after different thermal treatments.

Before any experiments, it was very useful to take cautious cares, especially when thermal treatments will be done on the layers. Indeed, preliminary studies on PID constants and lamp ratios showed the importance of these values on the temperature's control. For example, the optimization of the PID values allows to obtain very repeatable and faster temperature ramp, and also to minimize the overshoots (inversely the under-shoots) at the end of the ramp. This part is fundamental since the temperature is the main factor leading to morphological changes and thus must be controlled with high accuracy. Moreover, since the thermal treatments are very important in this thesis, these last ones must be repeatable for each processed wafer. In these preliminary studies, the influence of the pressure on the temperature was also given. It was shown that the wafer's temperature changes when the pressure in the chamber changes. Indeed, depending on the lamp ratio the temperature can increases or decreases significantly. It was proved that there is a certain lamp ratio for which the wafer's temperature is equal to the susceptor's temperature and does not depend on the pressure.

The un-doped as-grown epitaxial layers were studied in a first part in terms of kinetics. The Si and SiGe growth rate was studied as a function of the DCS and GeH_4 partial. The Ge content was also given as a function of the GeH_4 partial pressure. Concerning the SiGe's growth, the GR increases with increasing GeH_4 partial pressure. This is attributed to the catalysis of H

desorption from the surface by Ge atoms, freeing sites for growth. In a second part, the as-grown morphology was characterized by AFM. Different patterns were observed as references for the following studies. Therefore, larges boxes, lines, rectangles, squares, ovals and SRAM circuits were studied in terms of roughness, faceting and epitaxial lateral overgrowth. For example, it was observed that the roughness of the as-grown layers is typically less than 0.15 nm. Also, it was confirmed the formation of {001} facets along the <100> orientation and {111} facets along the <110> orientation. The epitaxial lateral overgrowth is different for each facet: it is roughly equal the grown thickness for the {001} facets and to 0.4 time the thickness for the {111} facets.

The SiGe layers' passivation by Si atoms was investigated. First the kinetics of the Si passivation made by DCS was quantified by XPS for two temperatures: 610°C and 630°C. It was shown that the growth rate of the Si passivation layer is not constant with time since it decreases exponentially before reaching a constant value. This was explained in terms of Si coverage on the SiGe layer. The passivation was then integrated at different process' steps and its impact on the morphology after thermal treatments was also studied. In a first part, it was integrated during the temperature ramp between the SiGe growth and the Si growth. Both material are grown at different temperatures, being higher for the Si (630°C for SiGe and 715°C for Si). Then, it was integrated either during the post growth purge or right after the growth removing the purge ("freezing" recipe). It was demonstrated the importance of adding a passivation to maintain the as-grown morphology by rendering the SiGe layer less sensitive to any thermal treatment. This passivation is particularly essential when a Si cap must be grown on SiGe layers or for the 14 nm node technology for which the channel under the p-doped source and drain is made of SiGe.

Since the as-grown morphology was characterized for specific patterns, the study was then focused on the thermal treatments' influence on the morphology. First, the Stranski-Krastanov phenomenon's apparition was investigated in large patterns as a function of time and temperature. It was shown that the SK undulations take a long time to appear but since they start to propagate, the roughness exponentially increases until the undulations transform into islands. At this moment, the roughness stabilizes. This work has led to the characterization of the wetting layer created between the domes. It was observed by XPS that a wetting layer of few angstroms is formed due to the diffusion. Second, the thermal rounding was studied in small patterns. In the lines, it was observed that the instabilities' behavior is different according to the lines' orientation, lines' thickness and lines' width. The instabilities increase by changing the lines' orientation from <110> to <100>, increasing the thickness or the width. The instabilities' morphology is characterized by the apparition of islands, ridges or a combination of both. The phenomenon of islands and ridge formation parallel to the line orientation is attributed to the superposition of two effects occurring during annealing: thermal rounding and SK-like undulations. Thickness being an important parameter leading to the instabilities, the question of the stabilization of an unstable line can be addressed. To do so, unstable <100> oriented lines were thinned and finally annealed at relatively high temperature. The AFM observations showed that the lines stabilized after the second annealing which allowed to confirm the role of the curvature radius on the instabilities.

The thermal rounding was also studied in oval and square patterns. First, it was observed that the patterns evolve toward a final equilibrium rounded dome which present low angle facets. Facets like {105}, {15 3 23}, {715}, {119} and {113} were measured by AFM. Second, the rounding kinetics was quantified by measuring the displaced volume of matter. In an Arrhenius plot, two regimes were obtained corresponding to two distinctive slopes: 2.9 eV and

7.7 eV. In the high temperature regime (low energy) the rounding is mainly driven by the surface diffusion since the activation energy of the silicon surface diffusion is very close to the extracted energy. In the low temperature regime, the high “apparent” activation energy is probably due to the apparition of another mechanism occurring in the same time as the surface diffusion. At low temperature, the hydrogen coverage increases leading to a slower surface diffusion and thus the thermal rounding occurs slower as well. Third, the pressure during the annealing was modified from 5 Torr to 200 Torr. It was showed that the highest the pressure the less efficient the thermal rounding. This effect is very pronounced between 5 Torr and 200 Torr. At 200 Torr, the patterns did not evolve and present an as-grown morphology. This is attributed to the fact that hydrogen atoms stick to the surface more or less efficiently due to the annealing pressure affecting the Si ad-atoms surface diffusion. For low pressure, hydrogen coverage is decreased allowing Si ad-atoms to diffuse on the surface increasing the thermal rounding’s efficiency. Finally, the influence of the carrier gas during the annealing on the thermal rounding was studied. It was shown that changing the gas from H_2 to N_2, the thermal rounding is much more effective meaning that the N atoms do not (or at least much less than H atoms) stick to the surface. Also, this work reinforces the hypothesis of the H coverage’s role on the rounding.

The morphological behavior of Si and SiGe caps grown on a non-flat surface was investigated in another set of experiments. This part is important since talking about metal contact on SiGe S/D. Indeed, a cap is often used to avoid degradations on the SiGe S/D. During this work, it was demonstrated that the Si and SiGe caps behave very differently. The SiGe caps allows to obtain an as-grown morphology and to level the top surface much easier than for Si caps. This effect is even more pronounced when the Ge content is increased in the SiGe cap. Moreover, it was observed that the Si cap’s growth rate seems to have an impact on the morphology. Indeed, a lower growth rate would allow to find back an as-grown morphology more easily than a high growth rate. Different mechanisms were proposed to explain these effects, such as the inter-diffusion, the Ge segregation or the catalyzer’s aspect of the Ge due to an increase of the strain’s gradient between the domes’ top and the wetting layer. Third, the smaller the pattern the easiest the as-grown morphology to be found back. Finally, the Si caps present successive terraces which is not the case for SiGe caps. These terraces observed by TEM are made of {113} and {119} facets. The {112} and {117} facets (observed by AFM) are maybe also present but the low measurement accuracy does not allow to conclude. The presence of terraces is attributed to kinetic effects. Indeed, after annealing of the Si/SiGe stack, the terraces completely disappeared which is contradictory with a surface’s energy minimization hypothesis.

The last chapter of this manuscript was dedicated to the boron-doped SiGe layers. In a first part, it was demonstrated that the growth rate increases with the B_2H_6 partial pressure. This phenomenon can be explained in terms of increase of free surface sites due to an enhanced H desorption when B atoms are present on the surface. Then, the adsorption of Si or Ge precursors is easier since more free surface sites are created. The boron incorporation was measured by MBIR and Tof SIMS. The boron concentration is constant in the SiGe layer for the low doping but is no more when increasing the doping. Indeed, for the heavily B-doped SiGe the concentration reduces from the interface between SiGe:B and Si to the surface of the layer and even more there is a peak at the interface. Then, the B concentration varies from 3.14×10^{21} at/cm^3 for the peak near the interface, to 1.08×10^{21} at/cm^3 at the surface. It can be interpreted as a saturation of the surface by B atoms and/or the formation of boron precipitates on the surface. The Ge content was also studied as a function of B_2H_6 partial

pressure. XRD was used to obtain the “apparent” Ge content which decreases when increasing the B_2H_6 partial pressure. This is due to the lattice contraction exerted by the B atoms (smaller than the Si and Ge atoms). Consequently, XRD is not sufficient to obtain the real Ge content. This one was obtained by XRF showing a more constant Ge content as a function of B_2H_6 partial pressure. The small decrease of Ge content can be attributed to the incorporation competition between the dopants, i.e. the Ge and the B. As a result, the higher the boron doping the less the Ge incorporation.

The SiGe:B as-grown morphology was then characterized by AFM. The roughness as a function of the B_2H_6 partial pressure was studied in large pattern and it was observed that it increases when for the high doping levels. For the highest doping, the surface is very rough and undulated. It was observed by HRTEM the presence of many dislocations. This B effect on the epitaxies’ quality is even more pronounced for the small patterns, characterized by a very poor epitaxy with no facets. For intermediate doping levels, the faceting is similar to the one obtained with an un-doped SiGe layer: we observed the {111} and {001} facets. However, for low doping levels, the {112} (measured by AFM) appeared in addition the {111} facet. This results in a succession of (from the bottom to the top of the pattern) the {111} and the {112} facets. Finally, the lateral overgrowth was shown to decrease with decreasing the B concentration.

This work was followed by the influence of the annealing on the SiGe:B layers. It was demonstrated that the thermal rounding is faster in the case of SiGe:B that in the case SiGe. First, this can be attributed, to the higher Ge concentration. It is worth to remind that the process used to grow the SiGe:B layers leads to higher Ge content compared to the un-doped SiGe layers. Second, to the B incorporation may also explain the faster rounding. Indeed, the B increases the GR which may result in a decrease of the H coverage and thus to an enhancement of the thermal rounding. However, the thermal rounding is not produced in the same way in the case of SiGe:B. The rounded ridges around the pattern are not smooth and present bulges. Moreover, the pattern’s interior is very rough and it can be observed the apparition of some islands. Higher thermal treatments were done on SiGe:B layers. In large patterns, it was observed the islands’ formation randomly organized in comparison to the well-organized rounded ridges for un-doped layers. In terms of faceting, the doped islands are faceted but they appear to contain multiple twin planes or simply irregular shape. This can be due to B precipitates with Si or Ge. Considering small patterns, the matter does not seem to entirely retract to the active zone but is like trapped on the SiO_2 surface. Here again, this can be attributed to boron precipitates impeding the atoms to diffuse correctly on the surface, or to the fact that B makes the Si (or Ge) adhere to the SiO_2. As a result, the B incorporation induces many mechanisms. First, the B increases the GR leading to a decrease of the hydrogen coverage. This results in an enhancement of the thermal rounding. Second, the B seems to pin the Si on the SiO_2 which results in an efficiency loss of the matter’s retraction during the thermal rounding. Third, the B makes precipitates with Si or Ge atoms which may trap the as-grown morphology. Finally, the B decreases the layer’s strain.

In the last part, the industrial application on the S/D of the 14 nm node was done. The aim was to grown p-doped SiGe layers in between two gates to create the S/D with the adequate facetted morphology. This was achieved by integrating the previous investigated SiGe:B layers and the “freezing” recipe. Comparing the standard process presenting a 10 sec purge (at the growth temperature) and our process with the “freezing” recipe, it was possible to obtain a regular faceted morphology instead of the flat epitaxy. This work confirms once again the importance of the Si passivation to maintain the desired morphology.

In summary, the works done on the morphological evolution of SiGe and SiGe:B layers have led to the understanding of the main mechanisms occurring during the thermal treatment. This represents a real advantage since it allows to improve significantly the control of the epitaxies' morphology and to further enhance the devices' performances. Furthermore, the advanced researches on the Si passivation allowed to maintain the as-grown morphology and to avoid the instabilities' formation for every future technology which is a real interest since the objects' dimension is very small. In addition to that, it allowed to solve some problems remained unanswered, especially concerning the flat SiGe:B epitaxy for the 14 nm S/D. Also, the successful integration of this step in different processes will be advantageous for many other applications requiring Si-based epitaxies, such as sensors or CMOS future nodes.

Annex A

Etching by HCl

In epitaxy by RT-CVD, the HCl gas is mainly used to obtain selectivity versus dielectrics. Gaseous HCl is directly injected inside the chamber either with Si(Ge) precursor gases or alone in successive steps alternating between growth step and etch step also called cyclic epitaxy. In cyclic epitaxy, the HCl allows the removal of amorphous Si(Ge) grown on the dielectrics without (or very weakly) etching the monocrystalline Si(Ge) grown on Si active areas. However, increasing the temperature or the HCl partial pressure, the monocrystalline Si(Ge) can be easily etched. One important application of etching by HCl is the defects' revelation in epitaxies. At the defect level, the material is etched faster than all around leading to a significant magnification of the defects. This technique is very used to know the epitaxy quality in very large areas. In this study, some etch steps were used to remove the SiGe wetting layers after a relatively high temperature annealing without etching the Si substrate. Second, it was used in lines after an annealing to re-stabilize the lines which present Plateau-Rayleigh like instabilities. Some developments were required to selectively etch the SiGe layer and to know the kinetics of the etching. To be selective and effective, the temperature as well as the HCl partial pressure must be chosen low enough not to etch the Si substrate but high enough to etch the SiGe in an effective way. By the way, the etch process was performed under a 200 Torr of H_2 atmosphere at 600°C with an HCl partial pressure of 58.5 mT. In these conditions, the SiGe etch rate (ER) was in average 12.0 nm/min with a total range of about 0.7 nm/min (see ***Fig. A-1***). To know the Si ER, the process was done on Si substrate for 1200 sec and an average ER of about 3.7 x 10^{-2} nm/min was measured corresponding to an excellent selectivity of about 300.

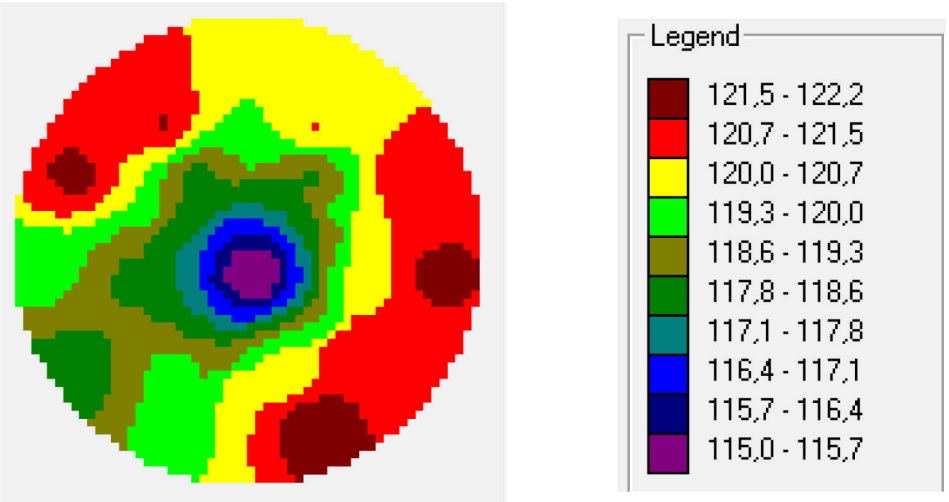

Fig. A-1*: Wafer mapping after the SiGe etch. The legend corresponds to the ER in Å/min. In average the ER is equal to 12.0 nm/min with a total range of 0.7 nm/min.*

Annex B

Simulation with COMSOL®

COMSOL® simulations were done in large patterns to study the elastic energy gain between an as-grown SiGe and a post-annealed SiGe presenting SK-like undulations. To do so, a 20 nm SiGe 25% layers were simulated on a Si substrate. Both Si and SiGe are simulated as anisotropic materials defined by their 6 x 6 orthotropic stiffness matrices. For silicon, the matrix with three axes at [100], [010] and [001] is [Wortman 65] [Hopcroft 10]:

$$\begin{bmatrix}\sigma_1\\ \sigma_2\\ \sigma_3\\ \sigma_4\\ \sigma_5\\ \sigma_6\end{bmatrix} = \begin{bmatrix}165.7 & 63.9 & 63.9 & 0 & 0 & 0\\ 63.9 & 165.7 & 63.9 & 0 & 0 & 0\\ 63.9 & 63.9 & 165.7 & 0 & 0 & 0\\ 0 & 0 & 0 & 79.6 & 0 & 0\\ 0 & 0 & 0 & 0 & 79.6 & 0\\ 0 & 0 & 0 & 0 & 0 & 79.6\end{bmatrix} \begin{bmatrix}\varepsilon_1\\ \varepsilon_2\\ \varepsilon_3\\ \varepsilon_4\\ \varepsilon_5\\ \varepsilon_6\end{bmatrix}$$

(in GPa).

For SiGe, the elastic constants were obtained as followed [Schaffler 01], x being the Ge content in the $Si_{1-x}Ge_x$ layer, in this case 0.25:

$c_{11}(GPa) = 165.7 - 37.3x$

$c_{12}(GPa) = 63.9 - 15.6x$

$c_{44}(GPa) = 79.6 - 12.8x$

The SK-like undulations were taken from an AFM profile corresponding to a 20 nm SiGe 25% layer annealed at 725°C during 480 sec. As mentioned in the Chapter 3, the ridges formed during the SK relaxation, are always oriented along the <100> orientations may be due to the lower Yong's modulus along this direction: 130 GPa against 169 GPa (along the <110> direction) [Hopcroft 10]. Therefore, the study was focused on the elastic energy gain obtained for <100>-oriented undulations, compared to <110>-oriented undulations. The elastic energies were computed, first, for a non-undulated 20 nm thick SiGe (25%) layer, second, for undulated SiGe layers, simulated along the <110> and along the <100> orientations. Also, the surface energies were analytically calculated through the equation:

$$E_{surface} = \gamma . S$$

With γ the surface energy density and S the surface of the SiGe layer. The value of γ (for Si) for the {100} planes is the following [Jaccodine 63]:

γ_{100} = 2.13 J.m^{-2}. The surface energy density is supposed isotropic in the {100} plane.

Fig. B-1 shows the 3D model of the non-undulated SiGe (before annealing). The SiGe system was chosen as a rectangular cuboid with dimensions of 1815 x 20 x 2000 nm^3 (length

x width x depth). The values given by COMSOL are the elastic density energies in $J.m^{-3}$. From COMSOL these values are computed for both the SiGe and Si and the sum is taken. Finally, the elastic energy is calculated by multiplying the densities' sum by the rectangular cuboid's volume. To note that the volume (7.26×10^{-20} m^3) is kept constant for each system. The elastic energy obtained for this object is 1.236×10^{-12} J and the surface energy is $\gamma_{100}S_{noSK} = 7.732 \times 10^{-12}$ J. These values correspond to this specific object. In order to be comparable to other system it is more interesting to consider the energies in J/m^2. This leads to:

$E_{el,noSK} = 0.340$ J/m^2

$\gamma S_{noSK} = 2.130$ J/m^2

For the following, the energies will be directly given in J/m^2.

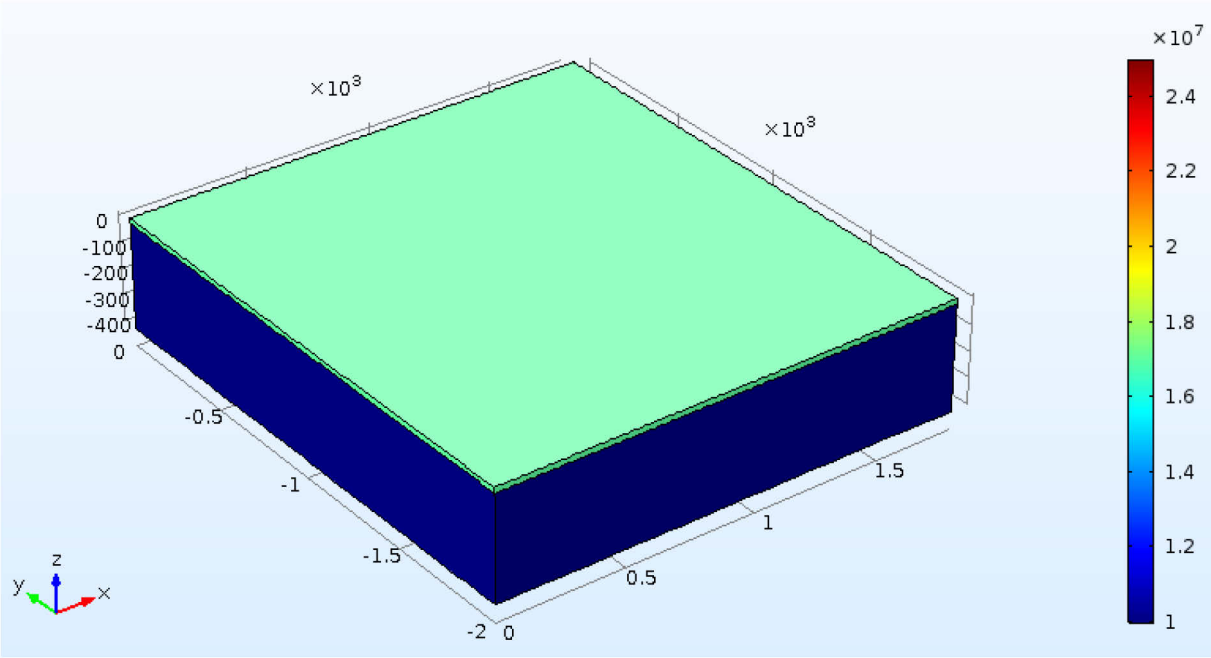

***Fig. B-1**: Elastic strain density of an as-grown SiGe 25% layer on a Si substrate. Both materials are taken anisotropic. The elastic energy is $E_{el,noSK} = 0.340$ J/m^2 and the surface energy is $\gamma S_{noSK} = 2.13$ J/m^2.*

Fig. B-2 gives the computation's results for both orientations. To compute the <110> orientation, the whole system is rotated to 45° and the elasticity matrices of Si and SiGe are the same. Along the <100> directions, the computed elastic energy is $E_{el,100} = 0.311$ J/m^2 and the surface energy is $\gamma_{100}S_{100} = 2.149$ J/m^2. The sum of the elastic and surface energies gives, in comparison with the non-undulated SiGe, an energy difference of -0.40 %. This means that the system prefers to adopt an undulated surface. Along the <110> orientations, $E_{el,110} = 0.314$ J/m^2 and the surface energy is the same as for the <100> directions. This corresponds to an energy difference of -0.28%. The energy gain is consequently higher in the case of <100>-oriented undulations.

These results show that the system minimizes its energy first by forming an undulated surface and second, by orienting these undulations along the <100> orientation.

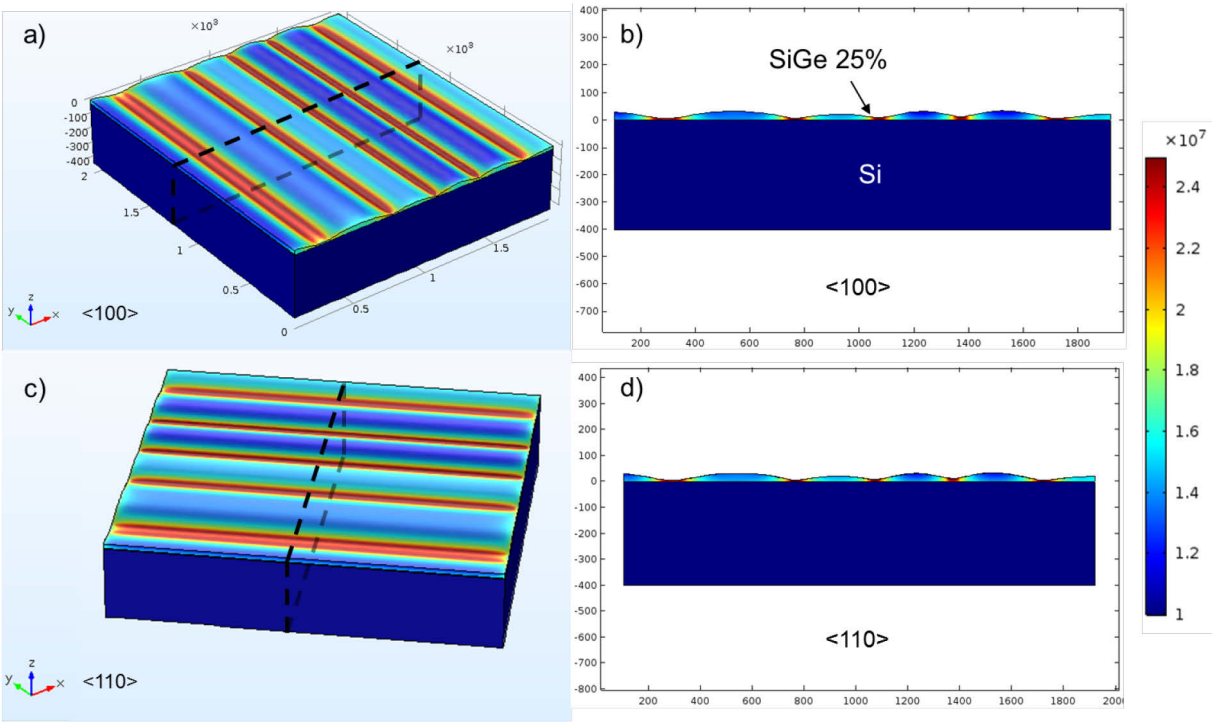

***Fig. B-2**: Elastic strain density of post-annealed SiGe 25% on a Si substrate for a) b) <100> and c) d) <110> orientations. The 2D representations b) and d) are taken perpendicular to the undulations as shown by the black dashed lines in a) and c). The Si and SiGe are taken anisotropic materials and defined by their elasticity matrix. Along the <100> direction, the energy difference as compared to the non-undulated surface, is higher than the <110> direction.*

The results are summarized in **Table B-1**.

TABLE B-1. Elastic and surface energy computed for the non-undulated and undulated SiGe. The ΔE (as compared to the non-undulated surface) is given in percentage.

Sample	Elastic energy (J/m^2)	Undulations (nm)	Surface energy (J/m^2)	ΔE (%)
As-grown	0.340	1815	2.130	0
<100>	0.311	1831	2.149	-0.40
<110>	0.314	1831	2.149	-0.28

Similar computations were done by arbitrarily multiplying the undulations' amplitude by a factor comprises between 0.25 and 2. The surface is kept constant while increasing the amplitude as shown in ***Fig. B-3***.

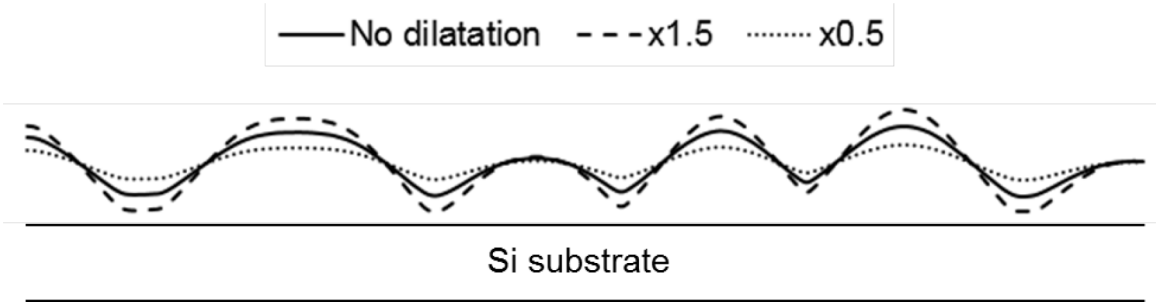

Fig. B-3**: Schematic representation of the undulations' dilatation while keeping the same surface. The multiplying factor varies from 0.25 to 2. Only the factor 0.5, 1 (no dilatation) and 1.5 are represented.* ***To note that in the figure, the vertical and horizontal axis are not at the same scale.

The elastic and surface energies are computed for each multiplying factor and are shown in **Table B-2**. The absolute value of the energy difference |ΔE| as a function of the multiplying factor is displayed in ***Fig. B-4***. To note that the γ variation due to the strain is not taken into account. It is observed that |ΔE| increases with increasing the undulations' amplitude and seems to stabilize and then decreases: in our particular case, for the <110> orientation, it decreases for a factor higher than 1.5; for the <100> orientation, it decreases for a factor higher than 1.7. This behavior is similar to the one obtained for the formation of the SK undulations. This means that the increase of the undulations' amplitude allows an energy gain which is possible when annealing the SiGe layer. It is worth to remind that the apparition of the SK undulations is due to the SiGe layer's relaxation to reduce the overall stress and thus to a minimization of the energy. However, this gain cannot run to infinity and then stabilize which may be related to the domes' apparition and to the fact that no more atoms can be displaced. For example, for <100>-oriented undulations, an amplitude factor higher than 1.7 cannot be possible since the system has a minimum energy for a factor of 1.7.

TABLE B-2. Elastic and surface energy computed for each multiplying factor. The ΔE (as compared to the non-undulated surface) is given in percentage. The γ variation due to the strain is not taken into account.

Factor	Elastic energy (J/m^2)		Surface energy (J/m^2)	ΔE (%)	
	<100>	<110>		<100>	<110>
x0.25	0.338	0.339	2.131	-0.010	-0.005
x0.5	0.333	0.334	2.135	-0.090	-0.061
x1	0.311	0.314	2.149	-0.400	-0.280
x1.2	0.298	0.302	2.157	-0.590	-0.420
x1.5	0.276	0.283	2.173	-0.890	-0.603
x1.7	0.267	0.276	2.181	-0.908	-0.524
x2	0.253	0.265	2.196	-0.848	-0.359

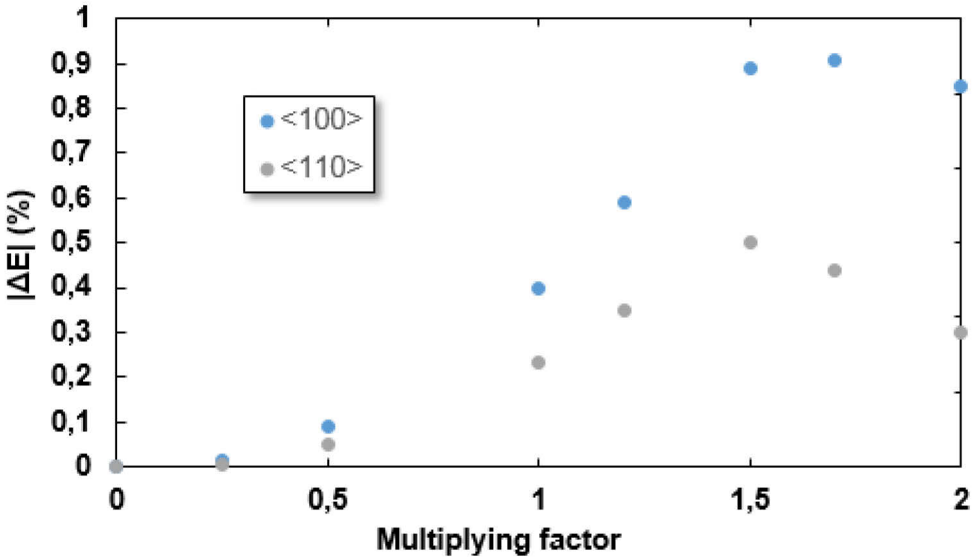

***Fig. B-4**: The absolute energy difference as a function of the multiplying factor. The absolute difference increases with increasing the undulations' amplitude and stabilizes for factor higher than 1.5 (or goes down). This behavior is very similar to the SK undulations and domes' apparition.*

References

A

[AMAT 04] Applied materials. Epi 300 Centura, 2 and 4 Chamber Systems, Process Manual, 2004

[Auth 12] C. Auth, C. Allen, A. Blattner, D. Bergstrom, M. Brazier, M. Bost, M. Buehler, V. Chikarmane, T. Ghani, T. Glassman, R. Grover, W. Han, D. Hanken, M. Hattendorf, P. Hentges, R. Heussner, J. Hicks, D. Ingerly, P. Jain, S. Jaloviar, R. James, D. Jones, J. Jopling, S. Joshi, C. Kenyon, H. Liu, R. McFadden, B. McIntyre, J. Neirynck, C. Parker, L. Pipes, I. Post, S. Pradhan, M. Prince, S. Ramey, T. Reynolds, J. Roesler, J. Sandford, J. Seiple, P. Smith, C. Thomas, D. Towner, T. Troeger, C. Weber, P. Yashar, K. Zawadzki, K. Mistry, *Symposium VLSI Technology Digest*, pp.131-132, **2012**.

B

[Bean 84] J. C. Bean, L. C. Feldman, A. T. Fiory, S. Nakahara, and I. K. Robinson, *Journal of Vacuum Science & Technology A*, vol. 2, p. 436, **1984**.

[Berbezier 09] I. Berbezier and A. Ronda, *Surface Science Report*, vol. 64, n° 2, pp. 47-98, **2009**.

[Binnig 86] G. Binnig, C. F. Quate and C. Gerber, *Physical Review Letters*, vol. 56, n° 9, p. 930, **1986**.

[Brehm 11] M. Brehm, H. Lichtenberger, T. Fromherz and G. Springholz, *Nanoscale Research Letters*, vol. 6, p. 70, **2011**.

C

[Chau 04] R. Chau et al., *IEEE Electron Device Letters*, vol. 25, n° 6, p.408, **2004**.

[Coon 92] P. A. Coon, P. Gupta, M. L. Wise, and S. M. George, *Journal of Vacuum Science & Technology A*, vol. 10, p. 324, **1992**.

[Coon 93] P. A. Coon, M.L Wise and S.M. George, *Journal of Crystal Growth*, vol. 130, n° 1-2 pp. 162-172, **1993**.

[Cunningham 91] B. Cunningham, J. O. Chu, and S. Akbar, *Applied Physics Letters*, vol. 59, p. 3574, **1991**.

[Currie 04] M. T. Currie, *Proceedings of 2004 International Conference on Integrated Circuit Design and Technology*, pp. 261-268, **2004**.

D

[Damlencourt 10] J. F. Damlencourt, *ECS Transactions*, vol. 28, n° 1, pp. 343-348, **2010**.

[Dismukes 64] P Dismukes, L. Ekstrom and R.I. Paff. *Journal of Physical Chemistry*, vol. 68, n° 10, pp. 3021-3027, **1964**.

[Duru 13] R. Duru, D. Le-Cunff, T. Nguyen, D. Barge, Y. Campidelli, N. Laurent, J. Hoglund, *IEEE*, pp. 237-242, **2013**.

[Dutartre 92] D. Dutartre, P. Warren, I. Berbezier and P. Perret, *Thin Solid Films*, vol. 222, n° 1-2, pp. 52-56, **1992**.

[Dutartre 01] D. Dutartre *et al, Semiconductors and Semimetals*, vol. 72, p. 397-457, **2001**.

[Dutartre 06] D. Dutartre, A. Talbot, N. Loubet, *ECS Transactions*, vol. 3, n° 7, p. 473, **2006**.

[Dutartre 07] D. Dutartre, Patent US2007/0074652 (A1), **2007**.

[Dutartre 08] D. Dutartre, F. Deléglise, C. Fellous, L. Rubaldo, A. Talbot, Chapter 5 in “SiGe and Si strained-Layer Epitaxy for Silicon Heterostructure Devices”, J.D. Cressler, CRC Press, **2008**.

[Dutartre 12] D. Dutartre, B. Seiss, Y. Campidelli, D. Pellissier-Tanon, D. Barge, R. Pantel, *Thin Solid Films*, vol. 520, n°8, pp. 3163-3169, **2012**.

[Dutartre 16] D. Dutartre, *ECS Transactions*, vol. 75, n° 8, pp. 303-323, **2016**.

F

[Ferguson 01] B. A. Ferguson, C. T. Reeves, D. J. Safarik, and C. B. Mullins, *Journal of Applied Physics*, vol. 90, p. 4981, **2001**.

[Fitzgerald 89] E. A. Fitzgerald, G. P. Watson, R. E. Proano, D. G. Ast, P. D. Kirchner, G. D. Pettit, and J. M. Woodall, *Journal of Applied Physics*, vol. 65, p. 2220, **1989**.

[Fossum 07] J. G. Fossum, *Solid-State Electronics*, vol. 51, pp. 188-194, **2007**.

[Frank 06] D. J. Frank, W. Haensch, G. Shahidi, O. H. Dokumaci. *IBM Journal of Research and Development*, vol. 50, n° 4-5, **2006**.

G

[Gavrila 07]

R. Gavrila, A. Dinescu, D. Mardare, *Romanian Journal of Information Science and Technology*, vol. 10, n° 3, pp. 291-300, **2007**.

[Greenlief 95] C. M. Greenlief and M. Armstrong, *Journal of Vacuum Science & Technology B*, vol. 13, p. 1810, **1995**.

[Greve 93] D. W. Greve, *Materials Science and Engineering B*, vol. 18, n° 1, pp. 22-51, **1993**.

H

[Hartmann 07] J. –M. Hartmann, F. Gonzatti, J. –P. Barnes, F. Fillot, T. Billon, *ECS Transactions*, vol. 6, n° 1, pp. 397-400, **2007**.

[Hartmann 11] J. M. Hartmann, A. Abbadie, and S. Favier, *Journal of Applied Physics*, vol. 110, n° 8, p. 3529, **2011**.

[Hartmann 13] J.M. Hartmann, V. Benevent, J. P. Barnes, M. Veillerot, D. Lafond, J. F. Damlencourt, S. Morvan, B. Prévitali, F. Andrieu, N. Loubet, and D. Dutartre, *Solid-State Electronics*, vol. 83, pp. 10-17, **2013**.

[Herzog 95] H. J. Herzog, *IEEE*, p. 49, **1995**.

[Hierlemann 95] M. Hierlemann, A. Kersch, C. Werner, and H. Schäfer, *Journal of the Electrochemical Society*, vol. 142, n° 1, pp. 259-266, **1995**.

[Hoeneisen 72] B. Hoeneisen and C. A. Mead, “Limitations in microelectronics—II, Bipolar technology 1”, *Solid-State Electron*., vol. 15, n° 8, pp. 891–897, **1972**.

[Holt 08] J. R. Holt Eric C. Harley, T. N. Adam, S. –J. Jeng, K. Tabakman, R. Pal, H. M. Nayfeh, L. R. Black, J. J. Kempisty, M. W. Stoker, A. Dube, and D. J. Schepis, *ECS Transaction*, vol. 16, n° 10, pp. 475-483, **2008**.

[Hopcroft 10] M. A. Hopcroft, W. D. Nix and T. W. Kenny, *Journal of Microelectromechanical Systems*, vol. 19, n° 2, **2010**.

[Horn 55] F. H. Horn, *Physical Review*, vol. 97, n° 6, p. 1521, **1955**.

[Houghton 90] D. C. Houghton, C. J. Gibbings, C. G. Tuppen, M. H. Lyons, and M. A. G. Halliwell, *Applied Physics Letters*, vol. 56, p. 460, **1990**.

I

[Ibach 09] H. Ibach, H. Lüth, *Solid-State Physics*, **2009**.

J

[Jaccodine 63] R. J. Jaccodine, *Journal of The Electrochemical Society*, vol. 10, n° 6, pp. 524-527, **1963**.

[Jang 91] S. -M. Jang and R. Reif, *Applied Physics Letters*, vol. 59, pp. 3162-3124, **1991**.

K

[Kao 05] C. –T. Kao, J. –P. Chou, C. Lai, S. Umotoy, J. Huston, S. Trinh, M. Chang, X. Yuan, Y. Chang, X. Lu, W. Wang, S. –E. Phan, *United States Patent*, US 20050230350 A1, **2005**.

[Kasim 14] J. Kasim, C. Reichel, G. Dilliway, B. Bai, N. Zakowsky, *IEEE*, pp. 153–154, **2014**.

[Kasper 75] E. Kasper, H. -J. Herzog and H. Kibbel, *Applied Physics*, vol. 8, p. 199, **1975**.

[Keeffe 94] M. E. Keeffe, C. C. Umbach, J. M. Blakely, *Journal of the Physics and Chemistry of Solids*, vol. 55, n°10, pp. 965-973, **1994**.

[Kim 93] K. J. Kim, M. Suemitsu, and N. Miyamoto, *Applied Physics Letters*, vol. 63, p. 3358, **1993**.

[Kuppurao 08] S. Kuppurao, Y. Kim, Y. Cho, S. Chopra, Z. Ye, E. Sanchez, and S. Chu, *ECS Transaction*, vol. 16, n° 10, pp. 415-425, **2008**.

L

[Lacord 12] J. Lacord, G. Ghibaudo, and F. Boeuf, *IEEE Transactions on Electron Devices*, vol. 59, n°5, pp. 1332-1344, **2012**.

[Lai 99] J. B. Lai and L. J. Chen, *Journal of Applied Physics*, vol. 86, p. 1340, **1999**.

[Liehr 90] M. Liehr, C. M. Greenlief, S. R. Kasi and M. Offenberg, *Applied Physics Letters*, vol. 56, n° 7, pp. 629-631, **1990**.

[Liu 05] J. Liu and M. C. Ozturk, *IEEE Transactions on Electron Devices*, vol. 52, p. 1535, **2005**.

[Lo 97] S.H. Lo, *IEEE Electron devices letter*, vol. 18, **1997**.

[Loubet 10] N. Loubet *et al.*, *Conference on Solid State Devices and Materials*, **2010**.

[Luryi 86] S. Luryi and E. Suhir, *Applied Physics Letter*, vol. 49, p. 140, **1986**.

M

[Maiti 98] C.K. Maiti, L. K. Berra, S. Chattopadhyay, *Semiconductor Science and Technology*, vol. 13, pp. 1225-1246, **1998**.

[Matthews 74] J. W. Matthews and A. E. Blakeslee, *Journal of Crystal Growth*, vol. 27, pp.118-125, **1974**.

[Merwe 63] J. H. Van der Merwe, *Journal of Applied Physics*, vol. 34, p. 123, **1963**.

[Meyerson 88] B. S. Meyerson, K. J. Uram, and F. K. LeGoues, *Applied Physics Letters*, vol. 5, n° 3, p. 2555, **1988**.

[Mistry 07] K. Mistry, et al., *IEDM Technology Digest*, pp. 247-250, **2007**.

[Moore 75] G. Moore, *IEDM Tech. Dig.*, p. 11, **1975**.

[Moore 03] "No exponential is forever," *in ISSCC*, San Francisco, CA, **2003**.

N

[Nowak 02] E. J. Nowak, *IBM Journal of R&D*, vol. 46, n° 2, pp. 169-180, **2002**.

[Noble 90] D. B. Noble, J. L. Hoyt, C. A. King, J. F. Gibbons, T. I. Kamins, and M. P. Scott, *Applied Physics Letters*, vol. 56, p. 51, **1990**.

O

[Oura 99] K. Oura, V. G. Lifshitsb, A. A. Saranina, A. V. Zotova, M. Katayama, *Surface Science Reports*, vol. *35*, pp. 1-69, **1999**.

[Ozkan 97] C. S. Ozkan, W. D. Nix, H. Gao, *Applied Physics Letters*, vol. 70, p. 2247, **1997**.

[Ozkan 99] C. S. Ozkan, W. D. Nix, H. Gao, *Journal of Materials Research*, vol. 14, n° 8, pp. 3247-3256, **1999**.

P

[People 86] R. People, J. C. Bean, *Applied Physics Letter*, vol. 49, p. 229, **1986**.

[Pribat 10] C. Pribat, PhD Thesis, STMicroelectronics, **2010**.

[Pribat 11] C. Pribat, D. Dutartre, *Journal of Crystal Growth*, vol. 334, n° 1, pp. 138-145, **2011**.

R

[Racanelli 90] M. Racanelli and D. W. Greve, *Applied Physics Letters*, vol. 56, p. 2524, **1990**.

[Reichel 12] C. Reichel, J. Schoenekess, S. Kronholz, G. Beernink, A. Zeun, A. Dietel, T. Kammler, *Thin Solid Films*, vol. 520, n° 8, pp. 3170–3174, **2012**.

[Ribot 02] P. Ribot, S. Monfray, T. Skotnicki, D. Dutartre, *Materials Science and Engineering: B*, vol. 89, n° 1-3, pp 125–128, **2002**.

[Robbins 91] D. J. Robbins, J. L. Glasper, A. G. Cullis, and W. Y. Leong, *Journal of Applied Physics*, vol. 69, p. 3729, **1991**.

S

[Schaffler 01] F. Schaffler, in *Properties of Advanced SemiconductorMaterials GaN, AlN, InN, BN, SiC, SiGe*. Eds. Levinshtein M.E., Rumyantsev S.L., Shur M.S., John Wiley & Sons, Inc., p.p. 149-188, **2001**.

[Seiss 13-1] B. Seiss, D. Dutartre, *Solid-State Electronics*, vol. 83, pp. 18-24, **2013**.

[Seiss 13-2] B. Seiss, D. Dutartre, *ECS Transactions*, vol. 53, n° 3, pp. 33-43, **2013**.

[Seiss 13-3] B. Seiss, G. Brémond, D. Dutartre, *MRS Proceedings*, vol. 1551, pp. 87–92, **2013**.

[Seiss 13-4] B. Seiss, PhD Thesis, STMicroelectronics, **2013**.

[Sinniah 89] K. Sinniah, M. G. Sherman, L. B. Lewis, W. H. Weinberg, J. T. Yates, Jr., and K. C. Janda, *Physical Review Letters*, vol. 62, n° 5, p. 567, **1989**.

[Suda 90] Y. Suda, D. Lubben, T. Motooka, and J. E. Greene, *Journal of Vacuum Science & Technology A*, vol. 8, p. 61, **1990**.

T

[Talbot 04] A. Talbot, J. Arcamone, C. Fellous, F. Deléglise, D. Dutartre, *In SiGe Materials, Processing and Devices, ECS*, **2004**.

[Tanuma 94] S. Tanuma, C. J. Powell and D. R. Penn, *Surface and Interface Analysis*, vol. 21, n° 3, pp.165-176, **1994**.

[Tyagi 07] S. Tyagi, *Proc. of 14th Intl. Symposium on the Physical and Failure Analysis of Integrated Circuits*, pp. 10-15, **2007**.

V

[Vegard 21] L. Vegard, Z. Phys., vol. 5, n° 1, pp. 17-26, **1921**.

[Vescan 98] L. Vescan, K. Grimm, C. Dieker, *Journal of Vacuum Science & Technology B*, vol. 16, p. 1549, **1998**.

W

[Wormington 11] M. Wormington, B. Yokhin, D. Berman, A. Krokhmal, I. Mazor, P. Ryan, J. Wall and R. Bytheway, *AIP Conference Proceedings*, vol. 1395, p. 198, **2011**.

[Wortman 65] J. J. Wortman and R. A. Evans, *Journal of Applied Physics*, vol. 36, n° 1, **1965**.

[Wu 03] W. W. Wu, S. L. Cheng, S. W. Lee, and L. J. Chen, *Journal of Vacuum Science & Technology B*, vol. 21, p. 2147, **2003**.

Y

[Yang 03] T.-H. Yang, G. Lou, E. Y. Chang, T.-Y. Yang, H.-C. Tseng, and C.-Y. Chang, *IEEE Electron Device Letters*, vol. 24, p. 544, **2003**.

Z

[Zhu 13] Z. Zhu, Z. Cong, B. Ramachandran, *ECS Transactions*, vol. 50, n° 9, pp. 999–1006, **2013**.

Résumé français

Introduction

Depuis l'invention du transistor en 1947 par William Shockley, John Bardeen et Walter Brattain, une incroyable course a commencé pour améliorer ses performances entraînant de façon inéluctable une diminution croissante de ses dimensions. Il y a de cela seulement une quarantaine d'années, la longueur du canal des transistors faisait plusieurs micromètres alors que maintenant des dimensions de l'ordre de la dizaine de nanomètre ont été atteintes. Tout cela fut possible grâce à l'avènement et à l'amélioration des techniques de fabrication telles que la lithographie. Cette réduction de la taille des transistors a suivi pendant de nombreuses années la fameuse loi empirique de Gordon E. Moore qui stipule que le nombre de dispositifs sur une puce de silicium double tous les deux ans. Cette loi qui n'est qu'une extrapolation empirique s'est avérée extrêmement exacte. Ainsi, de nombreuses industries de semi-conducteurs ont fait de cette loi leur principal plan d'action afin d'améliorer leur productivité et la performance des dispositifs, et avant de réduire leur coût. Cependant, les récents progrès technologiques sur les dispositifs avancés ont atteint leurs limites principalement lorsque les canaux ont été réduits à des dimensions inférieures à 90 nm. De nombreux problèmes sont alors apparus qui se sont révélés être nuisibles pour les performances des transistors. Parmi ces problèmes, les effets de canaux courts sont les plus importants et les plus critiques. Il va sans dire que la miniaturisation ne s'est pas arrêtée ici et a continué sa progression en contournant quelque peu la loi de Moore. Ceci fut possible grâce aux multiples efforts qui ont été fournis pour introduire de nouveaux procédés, matériaux et architectures. Ainsi des matériaux comme les diélectriques à faible permittivité (dits matériaux low-K) ou des matériaux ayant un paramètre de maille supérieur au silicium ont été progressivement intégrés dans les dispositifs. Concernant ces derniers, c'est le cas du $Si_{1-x}Ge_x$ (SiGe) qui présente des propriétés cristallographiques, mécaniques et électroniques particulièrement intéressantes. Historiquement, l'épitaxie de SiGe a été introduite pour la fabrication de la base du transistor bipolaire. Plus tard, elle fut intégrée en tant qu'amplificateur de la mobilité des trous dans les canaux, sources/drains des pMOSFET de type p.

Dans le Transistor à effet de champ à grille métal-oxyde (ou MOSFET en anglais), le courant est contrôlé par l'application d'un champ électrique perpendiculaire à la surface du semi-conducteur et à la direction du courant. Il existe deux types de MOSFET : le type n et le type p aussi nommés transistors nMOS et pMOS. Dans le cas des transistors nMOS, sur le substrat de type p il y a deux régions de type n fortement dopées. Ces régions sont appelées source et drain. Au contraire, pour les transistors de type p, le substrat est dopé n alors que les sources et drains sont dopés p.

Comme déjà mentionné, la diminution continue des transistors malgré le développement et l'introduction de nouveaux matériaux, a entraîné de nombreuses dégradations et ce depuis que la taille des canaux est passée sous la barre des 90 nm. Il est devenu alors difficile de complétement arrêter le transistor, ce qui augmente fortement les courants de fuite et par conséquent la consommation de puissance. Ainsi afin de maintenir les performances, de nouvelles architectures ont été introduites fournissant une meilleure stabilité électrostatique et

supprimant les effets de canaux courts. La première architecture remplace le silicium bulk par une fine couche de Si (< 10 nm) construit sur une couche isolante (SiO_2) aussi appelé SOI (pour silicon-on-insulator) Ceci permet d'augmenter le couplage capacitif entre la grille et le canal et de diminuer le couplage entre la source et le drain. D'autre part, cette technologie est assez facile à fabriquer du fait de son aspect planaire et est facilement compatible avec les anciennes technologies à base de silicium. La deuxième approche consiste à créer un transistor non-planaire à multi-grilles (double-gate or Tri-gate) construit soit sur substrat de silicium simple soit sur substrat SOI. Dans cette structure, le canal dépasse l'isolant formant comme un aileron (« fin FET » en anglais). La grille est alors déposée tout autour du canal lui donnant presque le total contrôle de ce dernier. Ceci permet de rendre le contrôle de la tension de seuil beaucoup plus facile, réduisant les fuites entre la source et le drain

Pour récapituler, de nos jours, l'amélioration des performances des transistors repose principalement sur le développement de nouvelles structures et architectures ainsi que sur le remplacement et/ou l'ajout de nouveaux matériaux présentant de meilleures caractéristiques comme c'est le cas pour le SiGe. Celui-ci permet un meilleur contrôle de la tension de seuil et de la contrainte en augmentant la mobilité des porteurs dans le canal. De même, le dopage, par exemple de type p, dans les sources/drains est de grand intérêt puisqu'il permet d'obtenir de meilleures caractéristiques, notamment des plus faibles résistances d'accès. Pour ces applications, ces épitaxies se doivent d'être sélectives par rapport aux diélectriques (SiO_2 ou Si_3N_4). De nombreuses études ont été menées sur ces procédés sélectifs et sont maintenant très bien maîtrisés. Toutefois, ces épitaxies sont faites dans des domaines instables que ce soit chimique (limite de solubilité), mécanique (présence de fortes contraintes) ou même morphologique (les motifs les plus petits peuvent atteindre quelques nm) ce qui les rend particulièrement difficiles. Concernant l'aspect morphologique, de nombreux effets ont fait leur apparition du fait de la petitesse des motifs. Ces effets morphologiques jusqu'alors négligés doivent être pris en compte dans les technologies CMOS actuelles ce qui peut rendre les procédés industriels compliqués. Ainsi, le facettage, les anisotropies et les effets thermiques sont à compter parmi les plus importants. Par ailleurs, ces derniers sont particulièrement critiques et des précautions doivent être faites pour ne pas dégrader la morphologie. C'est pour cela que cette thèse s'est focalisée sur les aspects morphologiques des épitaxies sélectives « petites dimensions » à base de silicium.

Le chapitre 1 expose les bases de l'épitaxie et de l'hétéro-épitaxie, en introduisant les notions d'épaisseur critique, de relaxation et de contrainte bi axiale en compressions. Les propriétés des matériaux Si et SiGe sont également présentées. Ensuite, les différents modes croissance sont décrits. Une partie est dédiée aux principes de la technique de dépôt chimique en phase vapeur et des réactions mises en jeu lors des croissances de Si ou SiGe(B). Enfin, une revue des croissances sélectives et des effets de charge est donnée.

Les détails expérimentaux sont décrits dans le chapitre 2. Après une brève introduction sur le nettoyage de surface avant épitaxie, l'équipement d'épitaxie est exposé en détail. Quelques résultats concernant l'influence des *PID* et des « *lamp ratio »* sur la température du procédé sont donnés. Dans une troisième partie, les techniques de caractérisation sont introduites. La technique AFM est présentée plus en détails étant le principal outil des caractérisations morphologiques.

Le chapitre 3 est consacré à la morphologie des épitaxies post croissance. Différents types de motifs de différentes tailles sont étudiés et discutés en termes de rugosité (pour les motifs très larges) et de facettage. Concernant ce dernier, des motifs en forme de lignes « infinies »,

de carrés et de rectangles sont utilisés. Les notions de passivation Si et de rampes actives ainsi que leur importance sur les études qui vont suivre sont adressées.

Dans le chapitre 4, la morphologie des épitaxies après recuit dans ces mêmes motifs est étudiée en détail, en introduisant les notions de relaxation de type Stranski-Krastanov et d'arrondissement thermique. L'influence de la température et du temps de recuit ainsi que la pression et le gaz porteur sur la morphologie est donné. L'arrondissement thermique est ensuite quantifié en termes de cinétique. Dans cette section, les motifs de grandes dimensions et les petits motifs sont discutés séparément. Ensuite, le comportement morphologique de l'encapsulation par du Si et du SiGe d'une surface ondulée ou arrondie est étudié. Différents paramètres comme la concentration de germanium ou la cinétique de croissance des encapsulations ont été modifiés et se sont révélés influer sur la morphologie.

Les applications industrielles du SiGe dopé bore sont données dans le chapitre 5. Tout d'abord, la cinétique de croissance des couches dopées et l'incorporation des dopants sont préalablement étudiées. Deuxièmement, la morphologie de ces épitaxies est caractérisée. L'influence du dopage sur la qualité de l'épitaxie, le facettage et la surcroissance latérale est présentée. Ensuite, l'aspect d'arrondissement thermique est également étudié. Enfin, les principaux résultats obtenus dans les chapitres précédents sont appliqués dans les dispositifs et plus particulièrement dans les sources/drains. Le but était de trouver un procédé permettant de réunir les aspects de morphologie facettée et de concentration de bore acceptable.

Chapitre 1 – Les propriétés du silicium, silicium-germanium et silicium-germanium dopé bore

Les propriétés cristallographiques

Le silicium et le germanium ont la même structure cristallographique que le diamant, avec comme paramètre de maille, respectivement, 5.431 Å et 5.658 Å. Leur similarité de structure et de propriété chimique fait qu'ils peuvent former un alliage binaire SiGe. Cependant, le SiGe ayant un paramètre de maille 4.18% plus grand que le Si, une couche de SiGe épitaxiée sur un substrat Si est en compression. Cette contrainte est d'autant plus importante que la concentration en germanium augmente. La conséquence de cette contrainte est que soit le film de SiGe est sans défaut, la déformation reste élastique et alors l'épitaxie est pseudomorphe, soit le film se relaxe par déformation plastique en formant des dislocations. Dans le cas d'hétéro-épitaxies comme c'est le cas pour du SiGe sur Si, trois principaux modes sont nommés : Frank-van der Merwe, Volmer-Weber et Stranski-Krastanov.

Procédés d'épitaxie

Les techniques de croissance de matériaux sont multiples et variées mais celle utilisée de façon majoritaire du fait de ces nombreux avantages par rapport à tous ces compétiteurs est la technique de RT-CVD (*Rapid Thermal Chemical Vapor Deposition* en Anglais). Elle permet notamment une bonne flexibilité en termes de pression, de température, ou encore de chimie. Des rampes en température très rapides peuvent être atteintes augmentant considérablement la productivité.

L'épitaxie est l'habilité d'ajouter et d'arranger de façon ordonnée les atomes sur une surface cristalline afin de faire croître une couche monocristalline. L'épitaxie peut être soit une homo-épitaxie, c'est-à-dire une croissance d'un matériau sur un même matériau, soit une hétéro-épitaxie, dans ce cas le matériau qui doit croître est différent de celui du substrat. Les principaux mécanismes rentrant en jeu lors d'une épitaxie sont le transport des précurseurs, l'adsorption sur les sites libres du substrat, la diffusion jusqu'à un site de nucléation et enfin la désorption des produits de réaction. Il existe de nombreux précurseurs pour la croissance du Si ou SiGe(B) mais ceux utilisés lors de ces études sont le SiH_2Cl_2, GeH_4 (avec HCl) et le B_2H_6.

De façon générale, les paramètres tels que la température, le débit des gaz, la pression et le choix des gaz actifs et porteurs affectent la cinétique de croissance. Deux régimes en CVD sont clairement identifiés. On distingue alors le régime à haute température où la cinétique de croissance est limitée par le transport des précurseurs gazeux au substrat. Dans ce cas, la cinétique tend à saturer et ne dépend plus (ou faiblement) de la température. Au contraire, la cinétique de croissance dans le régime à basse température, dépend fortement de la température et est limitée par la disponibilité des sites libres et par la désorption des espèces présentes en surface.

Les croissances d'épitaxie sélectives sont depuis longtemps utilisées en microélectronique, notamment dans les technologies CMOS, les transistors bipolaires ou encore l'optoélectronique. Par définition, l'épitaxie sélective est une épitaxie qui s'effectue uniquement sur des zones spécifiques, principalement sur Si (ou SiGe selon la technologie). En général, il est question de sélectivité par rapport aux matériaux diélectriques (SiO_2). Pendant une épitaxie non sélective, il y a croissance sur toutes les zones de la plaquette, monocristalline sur le Si et polycristalline sur les zones diélectriques. Il existe différentes méthodes pour atteindre la sélectivité. En premier, l'ajout d'une certaine quantité de HCl pendant la croissance le permet. Aussi, le précurseur SiH_2Cl_2 est très souvent utilisé puisqu'il permet d'être sélectif sans ajout de HCl. Enfin, l'épitaxie cyclée est également très utilisée. Elle est basée sur le fait que le polycristal se grave beaucoup plus rapidement que le monocristal et est donc composée d'une succession d'étape de croissance et de gravure.

Les effets de charge peuvent être définis par la modification des caractéristiques (épaisseur, concentration) d'une couche épitaxiée dépendant du masque utilisé. L'effet de charge local se définit par le changement de caractéristiques sur une même plaque quand la taille des motifs change. L'effet de charge global quant à lui réfère aux différences obtenues pour un même procédé mais sur des plaques ayant des rapports de zones actives différents.

Chapitre 2 – Détails expérimentaux

Préparation de la surface par SiCoNi

L'obtention d'une surface parfaitement propre avant épitaxie est une condition primordiale. En effet, une couche dont la croissance se fait sur une surface contaminée entraînera la formation de défauts à l'intérieur du matériau. Ainsi, la plaque doit être nettoyée pour retirer l'oxyde et les éventuels contaminants. Il existe plusieurs méthodes mais celle utilisée pendant cette thèse est un nettoyage plasma réalisé dans une chambre SiCoNi. Le très grand avantage de cette technique est qu'elle est directement intégrée au bâti d'épitaxie permettant un passage de plaque rapide. De plus, entre les deux étapes, il n'y a aucun contact avec l'air ambient. Le

principe se base sur la réaction des produits du plasma avec le SiO_2 en créant une fine couche de $(NH_4F)_2SiF_6$, qui est ensuite facilement retirée en chauffant le substrat à 200°C.

La chambre d'épitaxie

Lors de cette étude, les épitaxies ont été réalisées dans un réacteur RTCVD EPI Centura 300 de Applied Materials. Cet équipement industriel peut traiter des plaques de 300 mm. C'est un équipement composé de plusieurs modules interconnectés entre eux par une chambre de transfert. Il y a deux chambres d'épitaxie ayant chacune des rôles distincts et précis pour éviter toute contamination. Une chambre est ainsi utilisée pour les dopages n et l'autre pour les dopages p. Les deux peuvent être utilisées pour les épitaxies intrinsèques (sans dopage). Les murs des chambres sont en quartz. Le substrat est placé sur un suscepteur en graphite revêtu de SiC qui est en rotation pour améliorer l'uniformité (épaisseur et concentration). Le chauffage par le haut et par le bas de la plaque se fait par des lampes tungstène halogène dont leur puissance peut être ajustée. Deux pyromètres permettent la mesure de la température au centre de la plaque (par le haut) et du suscepteur (par le bas). La température dans la chambre est contrôlée par le pyromètre bas et par une boucle PID (Proportionnel, Intégral, Dérivée).

L'impact de la valeur des constantes PID sur la température du procédé d'épitaxie a été mis en évidence en termes de stabilisation de température et d'overshoot (dépassement de la température de consigne). Deux valeurs ont été choisies : 0,2/0,1 et 0,1/2. L'expérience consiste en une succession de rampes ascendantes et descendantes en température avec des temps de stabilisation de 60 s et 120 s. Il a été vu que pour une valeur de constante PID rapide, i.e. 0,2/0,1, un gain de 38% sur le temps de stabilisation de la température peut être obtenu en comparant avec une constante PID de 0,1/2. De la même manière, un gain de 50% sur l'overshoot a été atteint en prenant un PID de 0,2/0,1.

Techniques de caractérisation

Tout au long de ce travail, plusieurs techniques ont été utilisées pour caractériser les épitaxies. Concernant les caractéristiques des couches, l'ellipsométrie spectroscopique et la diffraction des rayons X ont toutes les deux permis les mesures d'épaisseur et de concentration en germanium des épitaxies de SiGe. Pour les couches de Si et notamment pour connaître la cinétique de croissance du Si dans certaines conditions, une sous couche de SiGe dont on connaît l'épaisseur (généralement 8 nm) est rajoutée. La spectrométrie de fluorescence des rayons X a permis la mesure de la concentration en germanium dans les couche de SiGe dopées bore. Quant au dopage bore dans le SiGe, il a été mesuré par réflectométrie infrarouge et par spectrométrie de masse à ionisation secondaire. La spectrométrie photoélectronique X a été utilisée pour quantifier la cinétique de la passivation Si des couches de SiGe. Concernant la morphologie des épitaxies, l'équipement principal de cette thèse est la microscopie à force atomique (AFM). Il a permis d'obtenir des informations sur la rugosité et sur la topographie de la plupart des échantillons. La microscopie électronique à balayage en vue de dessus a été également fortement utilisée pour effectuer une première vérification de l'aspect morphologique des épitaxies avant de pouvoir les observer en AFM. Enfin, quand l'AFM ne suffisait pas, des coupes transversales en microscopie électronique en transmission ont été faites, notamment pour caractériser la morphologie des encapsulations par du silicium.

Chapitre 3 – L'épitaxie après croissance

Le phénomène de facettage

Morphologie des épitaxies à base de silicium

La morphologie des épitaxies dans des motifs particuliers est montrée dans cette section pour être utilisée comme référence. En effet, la plupart de ces motifs vont être soumis à différents recuits qui vont changer considérablement la morphologie. Il est donc essentiel de connaître avec précision la morphologie après croissance. Les principaux motifs utilisés sont les suivants. Le premier motif est une large boîte ayant comme dimensions 100 x 50 µm². Ces boîtes, plus communément appelées TBOX, sont généralement des boîtes utilisées pour les mesures d'épaisseur ou de concentration. Leurs dimensions étant très grandes, le comportement des épitaxies dans ces boîtes est similaire à celui des épitaxies sur pleine plaque. Par conséquent, après croissance dans les TBOX, l'étude est portée sur la rugosité. Une épitaxie de qualité va montrer une rugosité inférieure 0,15 nm indépendamment de l'orientation de la plaque. Les lignes « infinies » font aussi parties des motifs étudiés. Elles se sont avérées très intéressantes notamment après recuit puisque la morphologie est très dépendante de l'orientation et de la largeur de ces lignes. Des largeurs allant de 60 nm à 490 nm ont été montrées. Après croissance, ces lignes présentent une surface plane qui représente le plan (001). Selon l'orientation <110>, les extrémités des lignes sont droites (en forme de carré) et selon l'orientation <100>, les extrémités sont coupées à 45° formant une forme triangulaire quand la ligne est suffisamment étroite. Cette forme triangulaire est due à l'apparition des facettes {111} faisant un angle théorique de 54,7° par rapport au plan (001), et de 45° par rapport aux orientations <100>. Trois autres motifs sont représentés dans ce manuscrit : un oval (150 x 120 nm²), un quasi-carré (400 x 420 nm²) et un rectangle (493 x 290 nm²). Chacun de ces motifs ont les coins coupés à 45°, encore une fois due à la présence des facettes {111}. Ces motifs sont orientés selon la direction <100>. Enfin, le dernier motif examiné, appelé SRAM, correspond à un circuit composé de petits segments incurvés (340 x 105 nm²) et de lignes asymétriques, ayant un côté rectiligne et un côté ondulé. A noter que les dimensions données sont les dimensions de la zone actives avant la croissance.

Passivation silicium de la surface par DCS

L'étude de la passivation Si a déjà été étudiée par Seiss *et al*. Cette passivation a été quantifiée en termes de cinétique et d'efficacité sur le maintien de la morphologie. Elle n'a été cependant faite qu'avec une chimie SiH_4 mais pas DCS. Le but de cette section est donc l'étude la cinétique et de son importance dans les procédés d'épitaxie en utilisant une chimie DCS. Cette chimie est avantageuse dans notre cas, puisque le DCS est le principal précurseur des épitaxies de ce manuscrit. D'autre part, elle permet une croissance sélective de la couche de passivation qui n'est pas le cas pour une chimie SiH_4. La cinétique a été mesurée juste après la croissance à l'aide de la technique de spectrométrie photoélectronique X (XPS). En effet, grâce à cette technique, les épaisseurs des couches de passivation pourront être calculées afin de remonter à une cinétique. Plusieurs plaques ont été préparées sur lesquelles une même couche de SiGe a été déposée avant d'être passivée. La passivation Si se fait à la température de croissance en coupant juste le GeH_4. Les températures de passivation sont 610°C et 630°C avec des durées allant de 0 s à 480 s. Les intensités des pics du $Ge2p_{3/2}$ and

Ge3d ont été mesurées pour chaque plaque. Il est évident que l'intensité de ces pics diminue avec l'augmentation du temps de passivation ce qui signifie que les atomes de Si recouvrent progressivement la surface du SiGe. Evidemment, il est observé, à temps égaux, que l'intensité des pics est plus importante pour la température la plus faible, suggérant que la cinétique est plus faible. Ce qui est plus important est que la cinétique n'est pas constante en fonction du temps et diminue de façon quasi exponentielle entre 0 s et 150 s avant d'atteindre une valeur constante. Ceci s'explique par la diminution de l'effet catalytique du Ge pendant la passivation. Un temps de passivation de 3600 s à 630°C a aussi été fait afin de pouvoir valider les mesures de la cinétique à valeur constante. En effet, l'épaisseur de Si peut être mesurée par ellipsométrie du fait du long temps de passivation et donc de l'épaisseur suffisamment élevée de la couche de passivation. Il s'est alors avéré que le pic du Ge3d est plus sensible pour mesurer des épaisseurs plus importantes, du fait de son énergie cinétique plus importante.

Ce principe de passivation a été mis en place sur différentes étapes du procédé d'épitaxie et son importance pour le maintien de la morphologie a été mise en évidence. Effectivement, la couche de passivation a déjà prouvé son utilité afin d'augmenter la stabilité thermique des couches de SiGe. Tout d'abord, la passivation a été mise en place lors de rampes en température (appelée dans ce cas, rampe active). Ceci notamment dans le cas d'un cap de Si sur SiGe, la température de croissance du Si étant généralement plus élevée que celle du SiGe. Il a été vu lors de cette étude que la rampe active permet une stabilité thermique accrue de la couche de SiGe comme exposé dans la ***Fig. R.1***. Ici, la température de croissance du SiGe est 630°C et celle du Si, 715°C. Il est observé qu'avec la rampe active la morphologie obtenue est très similaire à celle qu'on obtient après croissance, le SiGe n'a pas été affecté par l'augmentation de la température. A l'inverse, sans cette rampe active, la morphologie est complétement différente et le SiGe a subi un fort arrondissement thermique. Ceci peut être vu sur la figure par le fait que les coins du motif sont plus hauts que l'intérieur, et par la fente qui se trouve au milieu. Ceci prouve que les rampes actives sont essentielles pour stabiliser thermiquement une couche de SiGe, surtout dans le cas où il est nécessaire de réaliser une épitaxie de Si par-dessus.

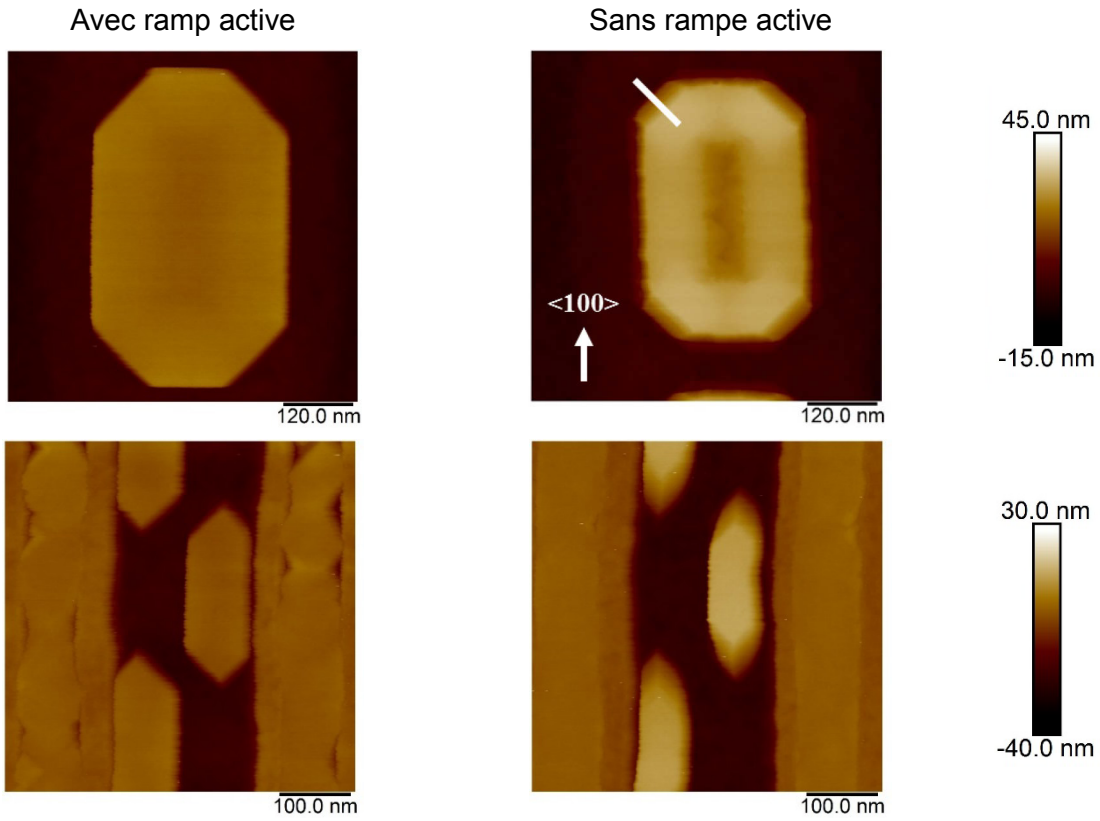

***Fig. R.1**: Images AFM d'un stack de Si/SiGe (gauche) avec et (droite) sans rampe active après la croissance du SiGe. Pendant la rampe active pour atteindre la température du Si, le flux de DCS est conservé de façon à passiver la surface en Si. Sans cette rampe active, le SiGe a subi un arrondissement thermique. Au contraire, avec la rampe active le SiGe ne présente pas d'arrondissement et la morphologie initiale est conservée.*

Deuxièmement, la passivation a été ajoutée après la croissance pour éviter tout changement morphologique qui pourrait se produire juste après la croissance pendant l'étape de purge. Cette purge permet l'évacuation des gaz après la croissance et se fait généralement à la même température que celle-ci pendant un temps compris en 10 s et 30 s. Ce temps de purge peut parfois être suffisant pour arrondir de façon significative les motifs. Une passivation avant ou pendant la purge est donc nécessaire pour éviter ceci, appelé aussi recette de figeage. Pour mettre en évidence l'influence de la passivation sur la morphologie, 3 plaques ont été préparée avec du SiGe dopé bore : une avec une purge standard de 10 s sans passivation, une autre avec une purge DCS de 120 s et une dernière avec la recette de figeage. Les résultats AFM sont montrés dans la ***Fig. R.2***. Il est clairement démontré que 10 s de purge a suffi pour arrondir les motifs, alors qu'avec une passivation Si, les motifs ont gardé leur morphologie après croissance. Ceci prouve encore une fois l'importance des passivations pour maintenir la morphologie d'après croissance. Il est à noter que toutes les épitaxies effectuées lors de cette thèse ont été précautionneusement préparée afin de caractériser la « bonne » morphologie.

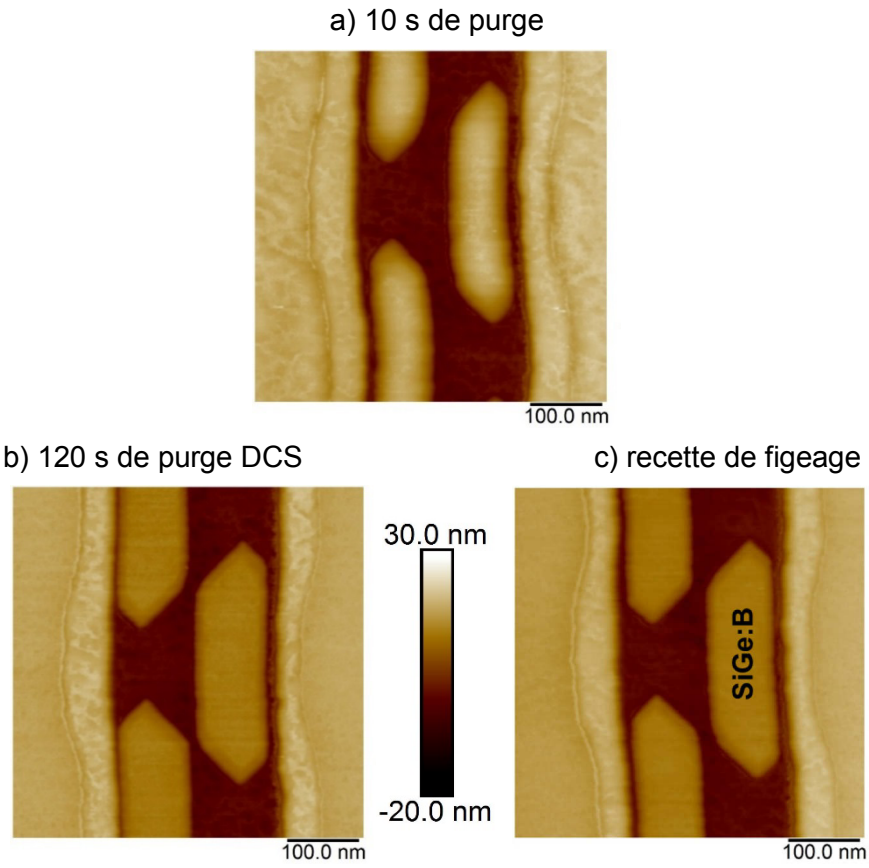

***Fig. R.2**: 0.5 x 0.5 µm² images AFM de SiGe:B dans les circuits SRAM. a) 10 s de purge sans passivation, b) 120 s de purge avec passivation (au DCS) et c) recette de figeage.*

Chapitre 4 – L'épitaxie après recuit

Dans cette partie, les motifs larges de type TBOX et les motifs de petites dimensions vont être discutés séparément.

Le phénomène de relaxation de type Stransky-Krastanov

Dans un premier temps il sera question de recuit dans les motifs larges considérés comme des plaques sans motifs. Dans ce type de motifs, les recuits se caractérisent par l'apparition d'ondulations de surface provenant de la relaxation élastique (sans défauts) de la couche contrainte, plus communément appelée relaxation de type Stransky-Krastanov. Ceci permet au système de réduire son énergie mécanique globale. Ces ondulations sont par conséquent visibles uniquement dans le cas d'hétéro-épitaxie à désaccord de maille où le matériau est sous contrainte. Elles se caractérisent par une longueur d'onde qui leur est propre et par la présence de lignes segmentées et toujours orientées selon les directions <100>. Ces ondulations ont été observées pendant notre étude sur des couches SiGe 25% recuites à des températures de plus de 700°C. Concernant cette étude spécifique, la longueur d'onde de ces instabilités quelle que soit l'orientation du substrat varie entre 0,167 µm et 0,231 µm selon que l'épaisseur du SiGe (25%) est 5 nm ou 20 nm, respectivement. Si le recuit est plus important (plus long ou à plus haute température), les lignes continuent de se segmenter pour ne former

à la fin une multitude d'îlots. L'apparition des instabilités est étudiée dans cette partie. Pour cela, des épitaxies de 20 nm de SiGe ont été faites qui ont ensuite été recuites in situ sous H_2. Différents recuits (de 650°C à 725°C) ont été effectués puis les ondulations ont été caractérisées par AFM en termes de rugosité. C'est ce qui est montré dans la ***Fig. R.3***. Les ondulations prennent un certain temps avant d'apparaître. A partir de ce moment, la rugosité augmente exponentiellement puis plus lentement avant de saturer à une valeur d'environ 8 nm. Cette étape correspond à la cassure des lignes en petits dômes qui ne bougeront plus même avec un recuit plus important. A noter que les points obtenus à 650°C ont été arbitrairement décalé de 50 s pour plus de clarté. Ceci ne change pas les résultats puisque la rugosité ne varie pas à cette température de recuit.

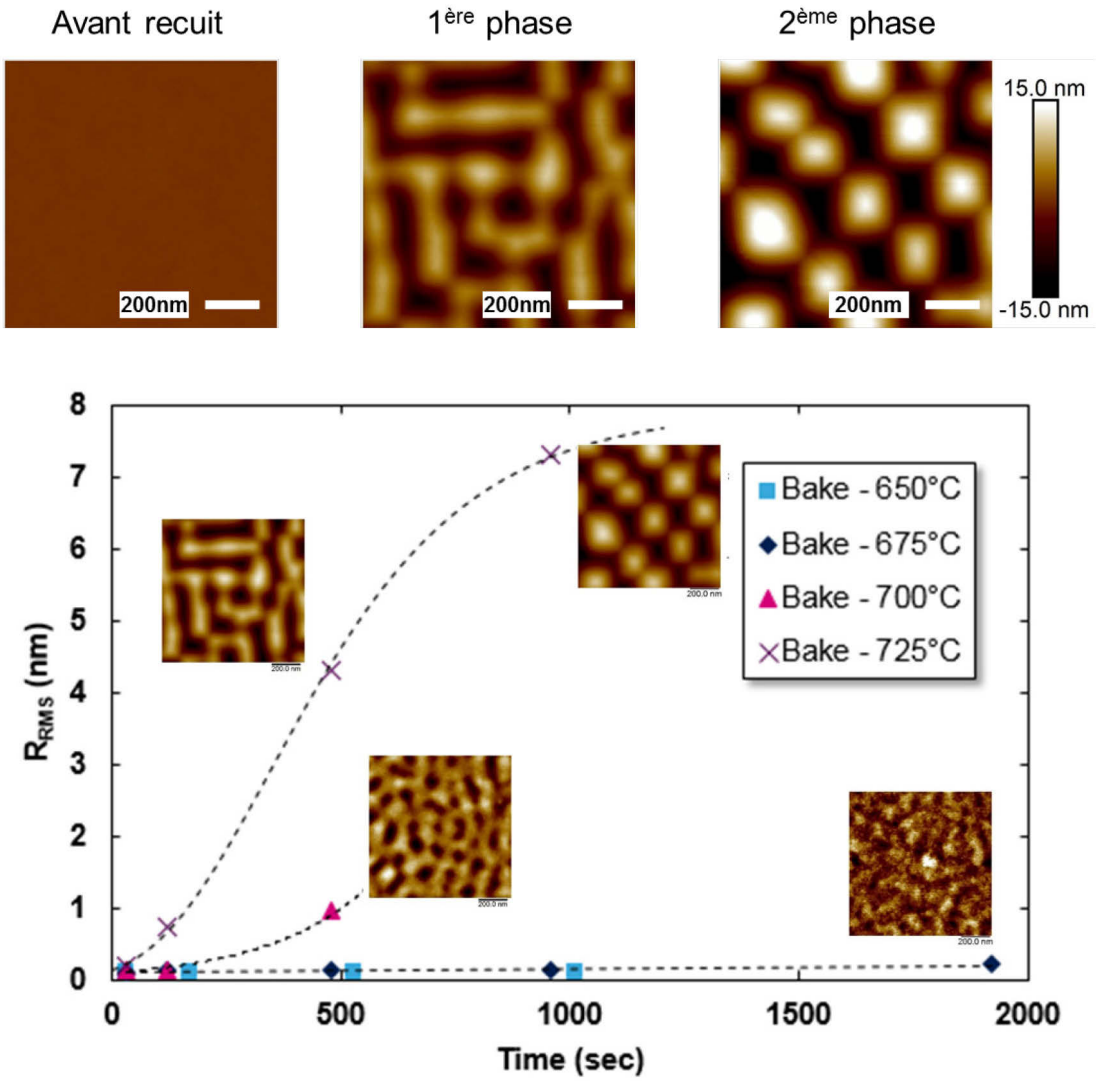

Fig. R.3*: Evolution de la rugosité en fonction de la durée des recuits pour 4 températures différentes : 650°C, 675°C, 700°C et 725°C. Des images AFM 1 x 1 µm² prises à des moments spécifiques de la formation des instabilités sont montrées sur le graphe. Les ondulations prennent un certain temps avant d'apparaître. A partir de ce moment, la rugosité augmente de façon exponentielle avant de saturer autour de 8 nm. Cette saturation provient de l'apparition des dômes. A noter : les points obtenus à 650°C ont été arbitrairement décalés de 50 s pour plus de clarté.*

Le phénomène d'arrondissement thermique

Dans les petits motifs, les couches épitaxiées subissant un recuit évoluent de telle sorte que les facettes d'après croissance disparaissent en grande partie pour donner une forme beaucoup plus arrondie. Pendant cette évolution, la matière se retire entièrement dans la zone active, faisant de ce fait disparaître les croissances latérales. Ce phénomène s'appelle arrondissement thermique et est possible lorsque la mobilité des atomes est suffisamment large. Ceci se traduit par la volonté du système à évoluer vers une morphologie ayant un minimum d'énergie de surface. Un schéma explicatif est donné dans la ***Fig. R.4***.

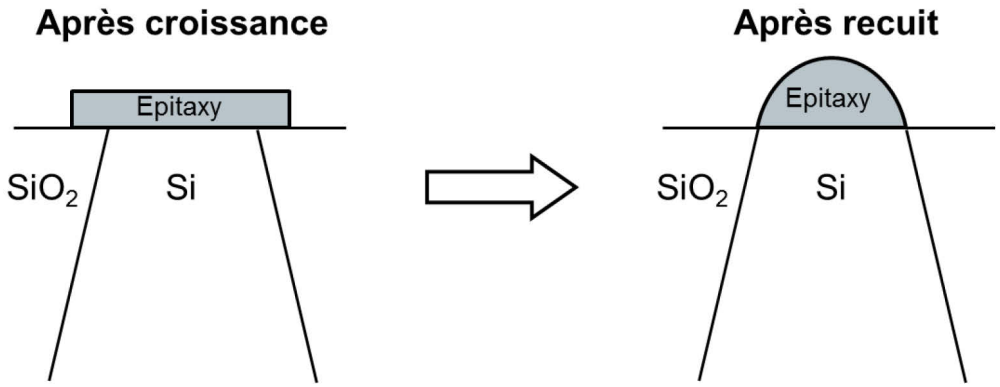

Fig. R.4*: Représentation schématique de l'arrondissement thermique se produisant lors d'un recuit. Les croissances latérales se retirent dans la zone active de Si et les facettes d'après croissance disparaissent. L'épitaxie après recuit se retrouve avec une forme arrondie.*

Les instabilités dans les lignes

Les instabilités dans les lignes ont été étudiées en détails, par Seiss *et al*, selon l'orientation <100> mais très peu selon l'orientation <110>. Cette étude s'est donc focalisée sur les lignes orientées <110> ayant subies un recuit et ensuite la morphologie obtenue a été comparée aux lignes <100>. Pour cela, deux épaisseurs de SiGe ont été utilisées : 5 nm et 19 nm, ainsi que des lignes de largeurs allant de 60 nm à 490 nm. Les couches de SiGe ont été recuites sous hydrogène à 750°C. Comparant les deux orientations, des zones stables et instables sont observées. Les zones stables se caractérisent par une morphologie bien arrondie et des lignes uniformes sur toute la longueur, tandis que les zones instables se caractérisent par la présence d'îlots, d'ondulations et de bosses le long de la ligne. En première observation, et pour une épaisseur de 5 nm, il apparaît que les lignes orientées <110> sont stables sur une plus grande variété de largeur de lignes que celles orientées selon la direction <100>. En effet, les instabilités des lignes <110> apparaissent pour une largeur de ligne de 390 nm (la ligne se partage en deux) alors que pour l'orientation <100> elles sont visibles déjà pour des lignes de 160 nm de largeur. En revanche, pour une épaisseur de 19 nm, l'inverse peut être observé. Tout d'abord, pour les lignes étroites (60 – 190 nm), la présence des instabilités est inversée selon l'orientation. Concernant l'orientation <110>, les lignes paraissent stables entre 60 et 100 nm et les instabilités font leur apparition à partir de 160 nm. Selon l'orientation <100>, les lignes sont instables dans un premier temps mais deviennent stables à partir de 160 nm avant de perdre à nouveau leur stabilité pour une largeur de 390 nm où la ligne se scinde en deux.

Il est maintenant évident que les domaines de stabilités ou d'instabilités varient non seulement en fonction de l'épaisseur de l'épitaxie ou de la largeur de la ligne mais également en fonction de l'orientation de ces mêmes lignes. Ce phénomène de formation d'îlots et de séparation de lignes sur la longueur est attribué à la compétition entre deux mécanismes se produisant pendant le recuit : la relaxation de type Stranski-Krastanov et l'arrondissement thermique.

Connaissant les différents facteurs jouant sur l'instabilité des lignes, l'idée de vouloir stabiliser une ligne instable est alors envisageable. C'est le but de cette expérience qui met en jeu des lignes de largeur 70 nm orientée <100> et d'épaisseur 22 nm. Ces lignes sont recuites une première fois à 725°C pendant 960 s sous H_2 de telle sorte que les instabilités soient présentes. Elles sont ensuite amincies par HCl pour obtenir une épaisseur moyenne de 10 nm et finalement recuites à nouveau dans les mêmes conditions que précédemment. Il a été montré qu'après le deuxième recuit les lignes qui étaient instables au début sont redevenues stables.

La cinétique d'arrondissement thermique

La cinétique d'arrondissement thermique a été calculée en étudiant l'évolution morphologique de différents motifs ayant subis des recuits différents. Les recuits ont été faits sous hydrogène à 20 Torr. Des plaques avec motifs ont donc été préparées avec du SiGe 25% d'épaisseur 20 nm. Quatre différents temps et températures de recuit ont été utilisés pour cette étude : 650°C, 675°C, 700°C et 725°C ; 30 s, 120 s, 480 s et 960 s. L'évolution de la morphologie pour un certain motif (quasi-carré) est montrée dans la ***Fig. R.5***. Il est clairement visible que pendant l'arrondissement thermique différentes étapes se produisent avant que le motif n'atteigne sa forme finale. Tout d'abord, la matière des croissances latérales se replie entièrement dans la zone active faisant disparaitre les facettes d'après croissance. Les surépaisseurs qui en résultent entraînent la formation de bourrelets lisse et uniforme tout autour du motif. Elles continuent alors à croître progressivement, se rapprochent les unes des autres avant de se rejoindre pour ne former à la fin qu'un seul et unique dôme.

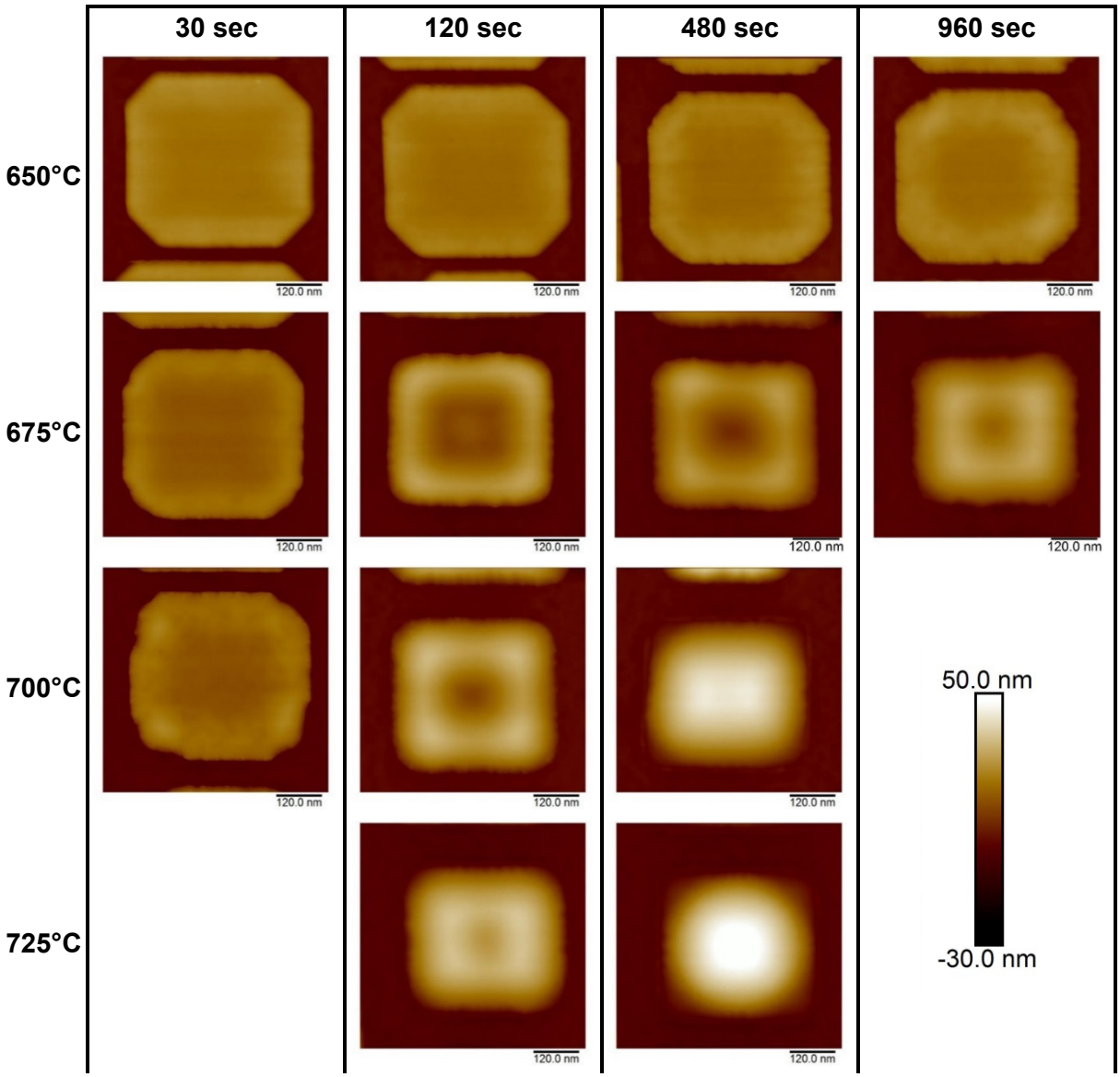

***Fig. R.5**: 0.6 x 0.6 µm² images AFM du motif quasi-carré ayant subi différents recuits. Les températures et temps de recuit sont écrits sur la figure. L'évolution complète du motif est bien visible : la matière se retire progressivement dans la zone active, les surépaisseurs qui en résultent s'accroissent avant de se rejoindre pour former un large dôme. Ce dôme représente la forme finale du motif recuit.*

Cette évolution du motif a permis par la suite le calcul de la cinétique d'arrondissement. En effet, en calculant le volume de matière déplacée pendant le recuit, il a été possible de tracer ce volume en fonction du temps de recuit pour les 4 températures. De ce graphe, les pentes ont été extraites afin de tracer l'Arrhenius de la cinétique comme montré dans la ***Fig. R.6***. Deux pentes distinctes ressortent de ce graphe correspondant à des régimes de haute et basse température : 2.9 eV et 7.7 eV. La première énergie se rapproche de la value de la diffusion de surface du Si qui est égale à 2.3 eV (en pointillé sur la figure). Ceci signifie qu'aux températures de recuit relativement élevées, le principal mécanisme de l'arrondissement thermique est la diffusion de surface. Aux plus faibles températures, un autre mécanisme (en plus de la diffusion de surface) apparaît augmentant grandement l'énergie. Ceci peut être dû

au fait qu'à plus basses températures, la couverture de H est plus élevée ce qui diminuerait la diffusion de surface et par conséquent la rapidité de l'arrondissement thermique, d'où la forte énergie d'activation apparente dans ce régime.

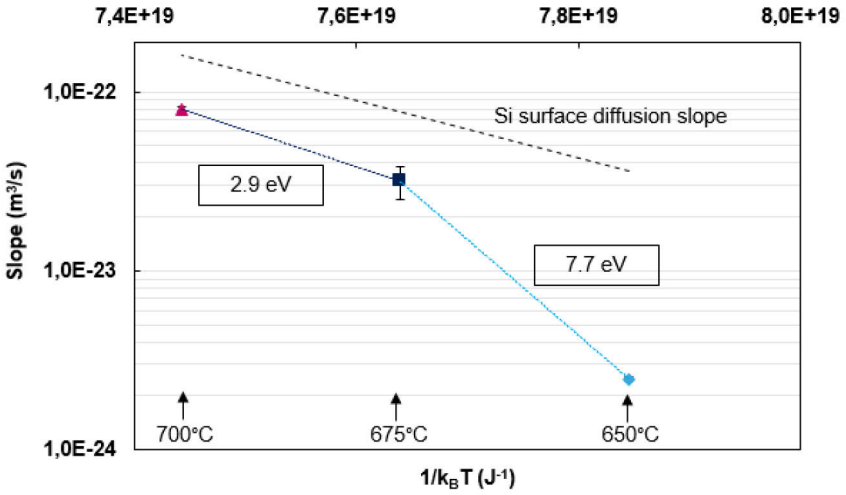

***Fig. R.6**: Arrhenius de la cinétique d'arrondissement thermique. Deux énergies ont été extraites : 2.9 eV and 7.7 eV.*

L'influence de la pression lors du recuit a également été mise en évidence. Pour cela, les mêmes couches de SiGe que précédemment ont été recuites sous H_2 à 650°C pendant 120 s à différentes pressions totales : 5 Torr, 10 Torr, 20 Torr et 200 Torr. La différence morphologique dans le motif quasi-carré est montrée dans la ***Fig. R.7***. Il est observé que l'arrondissement thermique est beaucoup plus rapide à basse pression. En effet, à 5 Torr, le motif est bien arrondi avec la présence des bourrelets tout autour. Au contraire, à 200 Torr, le motif ne semble avoir subi aucun arrondissement puisque sa morphologie est très similaire à celle d'après croissance (les facettes sont toujours présentes ainsi que leur surcroissance latérale correspondante). Ceci s'explique par la couverture d'hydrogène en surface qui varie en fonction de la pression totale. A faible pression, la couverture d'hydrogène est plus faible ce qui rend la diffusion des ad-atomes de Si en surface plus facile. A l'inverse lorsque la pression augmente, la couverture augmente aussi, empêchant les atomes de Si de diffuser rapidement.

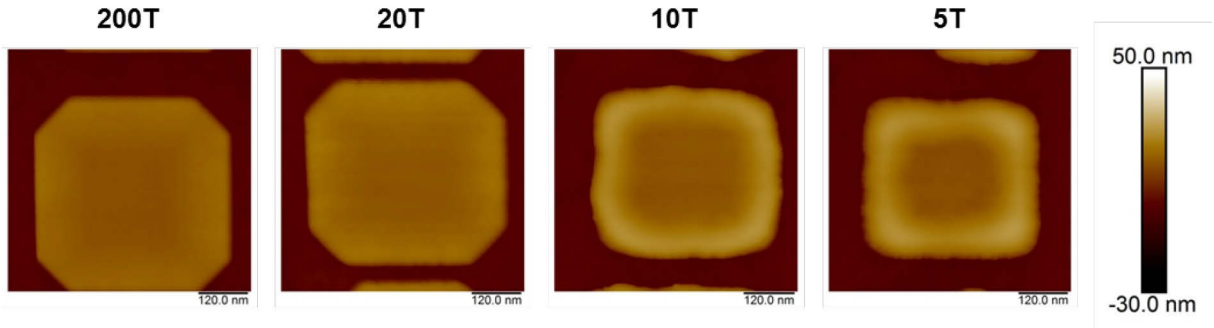

***Fig. R.7**: 0.6 x 0.6 µm² images AFM du motif quasi-carré recuit à différentes pressions : de 200 Torr à 5 Torr (de gauche à droite). Les traitements thermiques sont les mêmes, i.e. 650°C pendant 120 s.*

Enfin, l'influence de la nature du gaz porteur pendant le recuit a été démontré. Le motif quasi-carré a été recuit à 650°C pendant 120 s à 20 Torr sous azote. Sa morphologie a ensuite été comparée à celle obtenue pour un recuit sous hydrogène. Les observations sont similaires aux précédentes dans le sens où sous azote l'arrondissement thermique est plus efficace que sous hydrogène. Ceci s'explique très bien par le fait que les atomes d'azote s'adsorbent très peu à la surface en comparaison aux atomes d'hydrogène. Par conséquent, la diffusion est plus rapide lors d'un recuit sous azote. Cette différence peut être estimée à environ 50°C en termes de température ou à un ratio approximatif de 32 en termes de cinétique. Ceci peut être très avantageux pour les dispositifs pour lesquels le budget thermique se doit d'être limité.

Etude des encapsulations à base de Si

Le comportement morphologique des encapsulations par du Si et du SiGe sur une surface ondulée ou arrondie a été étudié dans cette partie. La sous-couche utilisée est du SiGe 25% d'épaisseur 8 nm recuite à 850°C pendant 60 s sous 20 Torr d'hydrogène. Ce recuit est suffisamment élevé pour avoir des motifs très arrondis et des fortes ondulations dans les TBOX. Les encapsulations étudiées sont recensées dans le **Tab. R.1**.

Tableau R.1 : Caractéristiques des différentes encapsulations déposées sur des épitaxies de SiGe de 8 nm à 25%. Le matériau, l'épaisseur et la cinétique de croissance des encapsulations sont écrits.

Matériau	Epaisseur (nm)	Cinétique (nm/min)
Si	8	2,2
	16	3,4
		4,0
SiGe 25%	8	1,8
	16	
SiGe 31%	8	2,7

Dans un premier temps, l'étude est portée sur les boîtes TBOX. Il est observé que la rugosité mesurée évolue en fonction de la concentration en Ge. En effet, en passant du Si au SiGe la rugosité diminue et de la même manière, en augmentant la concentration en Ge, celle-ci diminue encore. L'épaisseur du cap SiGe affecte également la rugosité qui diminue d'un facteur presque 2 quand le cap est 2 fois plus épais. Les ondulations semblent s'atténuer comme si le SiGe permettrait d'aplanir la surface. Ceci n'est pas le cas des encapsulations Si pour lesquels l'épaisseur ne joue presque pas sur la rugosité. Par contre, la cinétique des encapsulations Si semble influencer la rugosité qui diminue en même temps que la cinétique diminue. En observant plus précisément les ondulations, il est montré que les encapsulations Si présentent une succession de terrasses composées de facettes plus ou moins inclinées. Ces terrasses sont orientées selon la direction <110> (normale à la terrasse) et correspondent donc à des facettes de type {11h}, h étant compris entre 2 et 9 (ou plus). Les marches peuvent aussi être des plans non inclinées (plan {001}). La ***Fig. R.8*** représente des images MET des encapsulations Si et SiGe sur lesquelles les terrasses sont visibles.

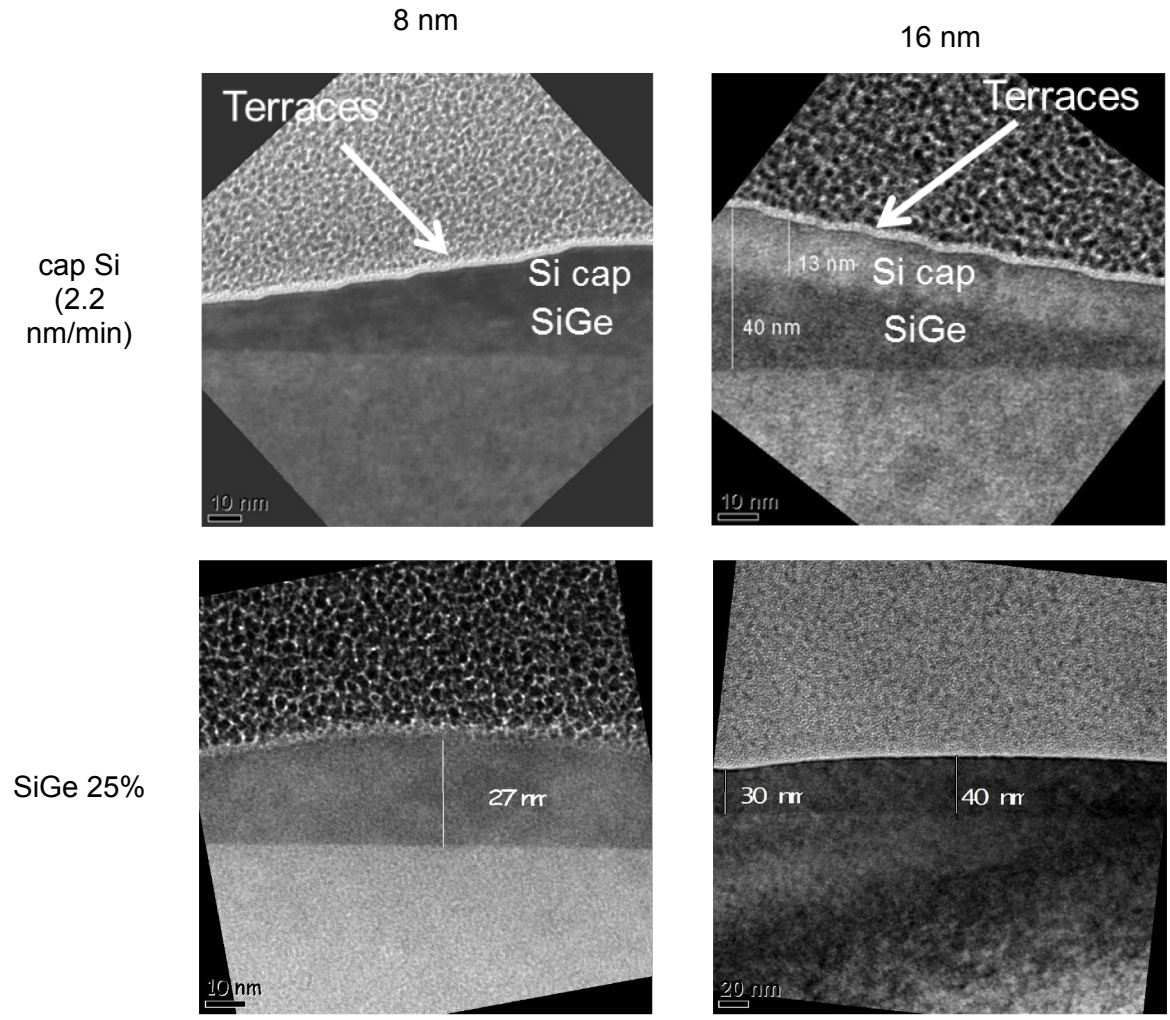

***Fig. R.8**: Images MET des encapsulations (haut) Si et (bas) SiGe sur une surface de SiGe recuite. Les successions de terrasses sont observées uniquement pour les encapsulations Si. Pour les encapsulations SiGe, la surface est juste ondulée.*

Dans un deuxième temps, l'étude s'est portée sur des motifs de plus petites dimensions. Il sera question dans ce résumé des zones actives des circuits SRAM. La ***Fig. R.9*** résume les observations faites. En effet, tout comme il a été vu pour les motifs de grandes dimensions, le SiGe permet de niveler la surface ondulée et même de retrouver la morphologie d'après croissance, et cela d'autant plus que la concentration de Ge est élevée. A contrario, le Si présente toujours des marches et quel que soit l'épaisseur la morphologie reste similaire. Elle semble cependant se modifier en fonction de la cinétique : plus la croissance est lente, plus la morphologie du motif se rapproche de celle d'après croissance.

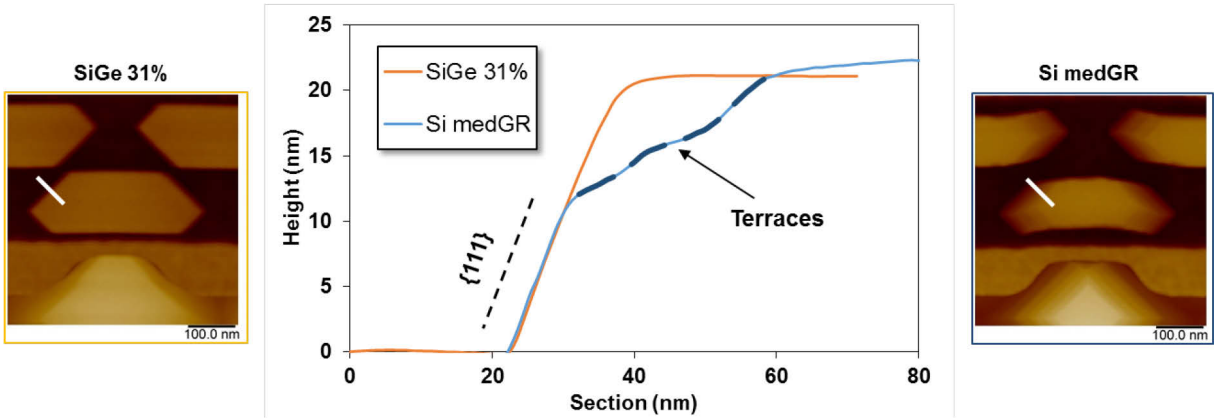

***Fig. R.9** : Images AFM des encapsulations SiGe 31% et Si dans les circuits SRAM. La section dans la direction <110> est représentée dans le graphe. L'encapsulation SiGe présente des facettes {111} sur toute l'épaisseur du motif. L'encapsulation Si présente quant à elle, en plus des facettes {111}, des terrasses.*

Enfin, l'encapsulation Si de 8 nm ayant la plus faible cinétique de croissance a été recuite à 850°C pendant 60 s sous 20 Torr d'hydrogène. Lors de cette expérience, les terrasses successives que ce soit dans les TBOX ou dans les SRAM disparaissent complétement, ce qui va à l'encontre de l'hypothèse de minimisation d'énergie de surface.

Chapitre 5 – Les applications industrielles

Caractéristiques des croissances de SiGe dopées bore

La cinétique de croissance ainsi que l'incorporation des dopants en fonction de la pression partielle du diborane ont été étudiés dans une première partie. Le diborane ou B_2H_6 est le gaz précurseur pour le dopage de bore et est mélangé aux précurseurs du Si et Ge, qui sont respectivement le DCS et le GeH_4. Une petite quantité de HCl est rajoutée pour assurer une parfaite sélectivité. La température des croissances de SiGe :B est 644°C. L'étape de figeage a été évidemment mise à la fin du procédé afin d'obtenir la morphologie d'après croissance. Plusieurs pressions partielles de diborane ont été utilisées : 0,033, 0,065, 0,098, 0,196, 0,293 et 0,389 mT. L'épaisseur des films est 20 nm. Il est tout d'abord montré que la cinétique de croissance du SiGe :B augmente sensiblement linéairement avec l'augmentation du flux de B_2H_6. Ceci est dû à l'effet catalytique du bore qui augmente la désorption des atomes d'hydrogène et par conséquent le nombre de sites libres en surface.

L'incorporation du bore a été mesurée par ToF SIMS pour des pressions de 0,065, 0,196 et 0,293 mT. Les concentrations de bore pour les plus faibles dopages est constante tout le long du film et en moyenne valent 1,23 x 10^{20} at/cm^3 et 6,57 x 10^{20} at/cm^3. Concernant le plus fort dopage, la concentration en bore n'est pas constante dans le film : elle part d'un pic de concentration élevée à l'interface puis diminue et se stabilise à une valeur plus faible en allant vers la surface. Ce pic de concentration fait ainsi varier la concentration de 3,14 x 10^{21} at/cm^3 à 1,08 x 10^{21} at/cm^3 soit une variation de 34%. Le pic de bore à l'interface peut s'expliquer par une saturation de la surface par les atomes de bore et/ou le bore forme des précipités avec le Si ou Ge. Des mesures MBIR ont ensuite été comparées avec les mesures SIMS et il a été observé que la concentration donnée par SIMS est toujours supérieure à celle donnée par

MBIR. Cette variation est d'ailleurs bien plus marquée pour le fort dopage : la mesure SIMS est 8 fois supérieure. Ceci s'explique, en partie, par le fait que tous les atomes ne sont pas dans des sites substitutionnels, certains sont donc en sites interstitiels et de ce fait, non électriquement activés.

La concentration en germanium a aussi été calculée dans un 1er temps par DRX. De cette caractérisation, il en est ressorti plusieurs observations. Premièrement, l'augmentation du dopage de bore entraîne un décalage des pics de diffraction vers les angles plus élevés (plus proche du Si) signifiant une augmentation de la concentration en Ge. Cette concentration est appelée « apparente » puisqu'elle reflète à la fois la dilatation du réseau due au Ge et sa contraction à cause de la petite taille des atomes de B en comparaison aux atomes de Si et de Ge. Cette concentration « apparente » varie de 36% à 27% en augmentant le dopage bore. Ensuite, plus le dopage en bore est élevé plus l'intensité des pics et des satellites diminue. Ceci est attribué à la qualité de l'épitaxie que se voit dégrader avec le dopage. Dans un deuxième temps, des mesures XRF ont été faites afin de remonter à la « vraie » concentration en Ge et ont été comparée avec les mesures SIMS. Par ces deux méthodes, la concentration en Ge varie plus légèrement (de 36% à 31%). Cette légère variation peut s'expliquer par la compétition entre l'incorporation du B et celle du Ge.

La morphologie des couches de SiGe :B

La qualité des épitaxies ainsi que la morphologie des couches de SiGe dopées B ont été caractérisées. La rugosité dans les TBOX a d'abord été mise en évidence par AFM et il est clair que celle-ci augmente fortement pour les forts dopages en bore. En termes de rugosité, l'épitaxie est de bonne qualité avec une rugosité qui oscille autour des 0,12 nm pour les faibles dopages, mais se dégrade fortement pour les forts dopages. En effet, la rugosité peut atteindre une valeur de 0,85 nm et la surface présente de fortes ondulations en surface. Ceci explique donc très bien la baisse d'intensité observée dans les diagrammes DRX. La ***Fig. R.10*** montre des images TEM pour le plus fort dopage dans laquelle des dislocations sont visibles probablement induites par des précipités de bore proche de l'interface avec le Si.

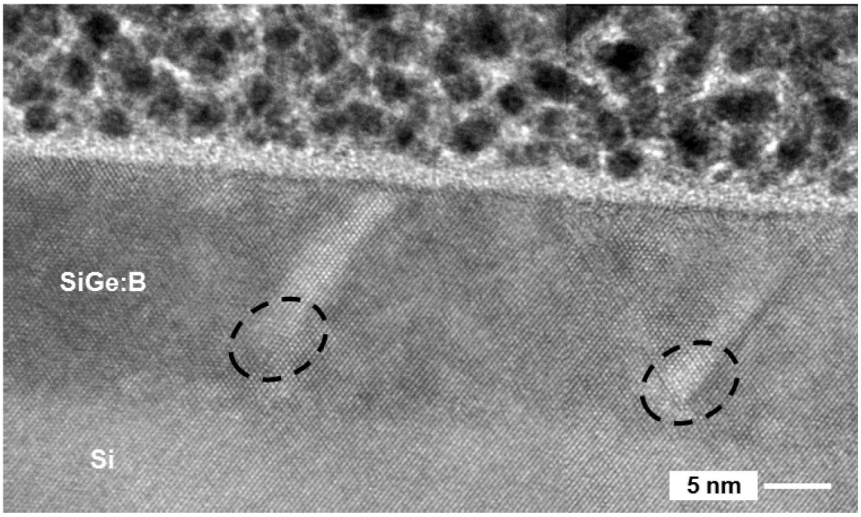

Fig. R.10 *: Image TEM d'une couche de SiGe fortement dopée en B. L'épaisseur est de 20 nm. Les dislocations (marqués par les cercle noirs) sont visibles ce qui explique la dégradation de l'intensité des pics des diagrammes DRX.*

Le phénomène de facettage dans ces mêmes épitaxies a ensuite été étudié en fonction du dopage en B. Concernant les dopages intermédiaires, la morphologie dans les motifs est la même que celle observée pour des couches non dopées, i.e. présence des facettes {111} et {001} avec une surface plane correspondant au plan (001). Pour un dopage plus fort, la morphologie se dégrade grandement : les facettes ne sont pas formées et l'épitaxie présente une croissance non uniforme dans la zone active. Elle est d'ailleurs bien plus dégradée dans les petits motifs que dans les TBOX. En effet, alors que la rugosité était plus ou moins correcte dans les TBOX, dans les circuits SRAM la qualité de l'épitaxie est vraiment mauvaise. Pour un dopage très faible, l'épitaxie est de bonne qualité mais la morphologie change un peu. Effectivement, il apparaît une autre facette en plus des facettes {111} qui se trouve être la facette {112} ayant un angle théorique de 35,3° par rapport au plan (001). C'est ce qui est montré dans la ***Fig. R.11***.

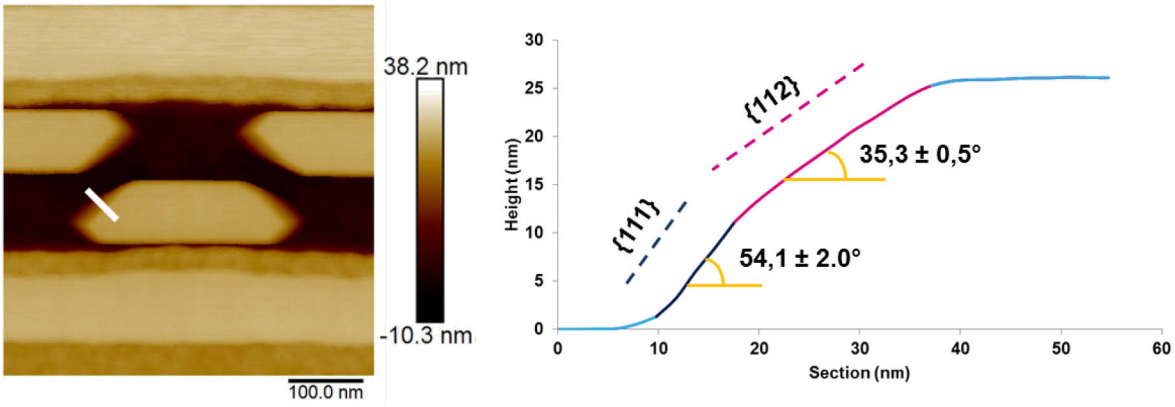

Fig. R.11 *: (A gauche) Image AFM dans les circuits SRAM pour une pression partielle de B_2H_6 de 0,033 mT. (En bas) Section AFM dans le coin du motif (en trait bleu sur l'image). La facette {111} s'efface au détriment de la facette {112}.*

Enfin, l'influence du dopage sur la croissance latérale a été étudiée dans les segments incurvés des circuits SRAM. Pour cela, la largeur du motif a été mesurée et connaissant la largeur de la zone active avant croissance, il est possible de remonter à la croissance latérale. La ***Fig. R.12*** montre l'évolution de la croissance latérale transversale (selon la largeur du motif) en fonction de la pression partielle de diborane. SRAM 1 et 2 sont deux types de circuits ayant des largeurs de zones actives différentes : 36,8 nm et 46 nm, respectivement. Il est visible sur le graphe que la croissance latérale augmente avec la pression partielle de diborane et se stabilise pour une pression de 0,098 mT autour de 19 – 20 nm. Cette valeur correspond à peu près à l'épaisseur déposée, ce qui est identique à ce qui peut être observé pour des couches de SiGe non dopées.

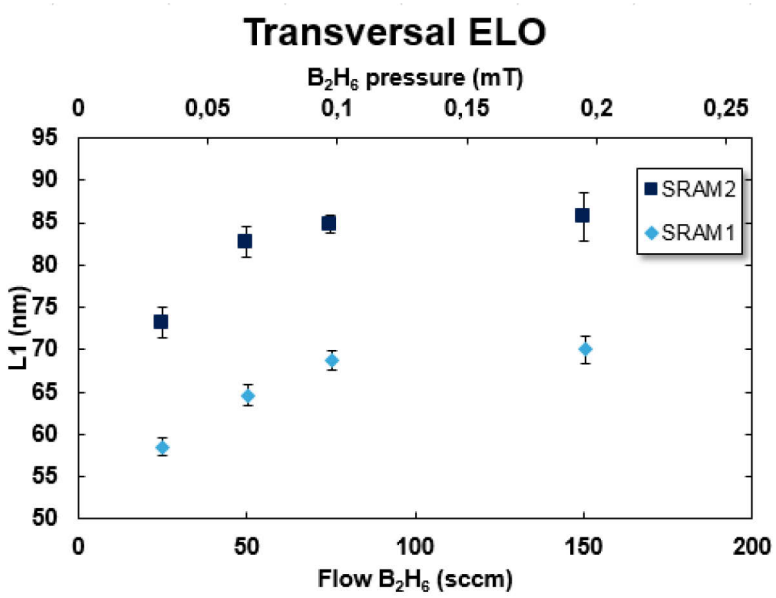

Fig. R.12 *: Evolution de la croissance latérale transversale en fonction de la pression de diborane.*

Ceci est confirmé par la caractérisation TEM exposée dans la ***Fig. R.13*** dans laquelle sont représentés deux dopages différents : 0,196 et 0,065 mT de B_2H_6. Pour le plus faible dopage, la croissance latérale est très faible comparée au dopage intermédiaire. Concernant le dopage plus élevé, la croissance latérale est bien égale à l'épaisseur déposée.

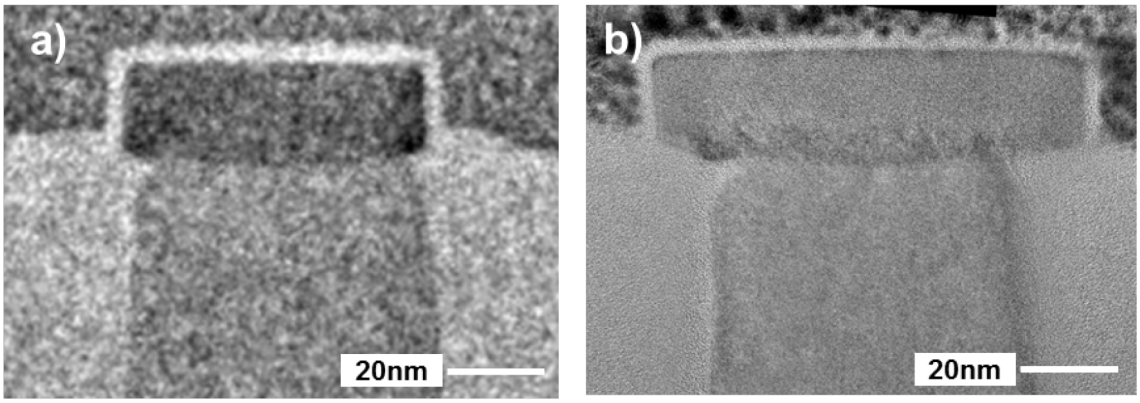

Fig. R.13 *: Images TEM dans les circuits SRAM selon la direction <100>. a) 0.065 mT de diborane. b) 0.196 mT de diborane.*

Morphologie des couches SiGe :B après recuit

L'influence du recuit des couches de SiGe dopées bore a été étudiée. Deux dopages ont été utilisés correspondant à des pressions partielles de 0,196 mT et 0,065 mT de B_2H_6. Les films ont été recuits sous 20 Torr de H_2 à 850°C pendant 60 s. La morphologie est caractérisée par AFM, dans un premier temps, dans les zones TBOX comme montrée dans la ***Fig. R.14***. En comparaison avec les couches SiGe non dopées, il est observé que les ondulations de type SK ayant une orientation bien définie ou des dômes bien réguliers ne sont plus présentes

en présence de bore. En effet, des formes très irrégulières plus ou moins espacées font leur apparition. Ces formes semblent également être entourées de « bulles » en surface qui la rendent particulièrement rugueuse piégeant par la même occasion la propagation des ondulations SK. Comparant les deux dopages, la morphologie est assez différente. Pour une pression de 0,065 mT de B_2H_6, les formes irrégulières sont très nombreuses, moins espacées et également plus larges en moyenne que pour l'autre dopage. Concernant ce dernier, les formes sont moins nombreuses, plus rondes, plus facettées et enfin semblent être plus endiguées dans la surface rugueuse. Ceci peut très bien appuyer l'hypothèse de « piégeage » des ondulations de type SK dû au dopage bore.

Des résultats similaires ont été obtenus pour des recuits dans des motifs de petites tailles. En effet, le retirement de la matière dans la zone active lors de l'arrondissement thermique se fait difficilement. Ceci s'observe notamment par le fait que les coins des motifs restent coupés à 45°, ce qui n'est pas le cas du SiGe non dopé. Egalement, les mêmes bulles que précédemment semblent entourer tout le motif contraignant la diffusion de surface. Enfin les deux dopages présentent des morphologies très différentes renforçant l'idée de « piégeage », cette fois-ci de l'arrondissement thermique. Ceci nous amène à conclure que le B introduit de nombreux mécanismes. Tout d'abord, le B augmente la cinétique de croissance pouvant entraîner une diminution de la couverture de H en surface. Ceci se traduit par une meilleure efficacité de l'arrondissement thermique. D'autre part, le B semble piéger le Si sur le SiO_2 empêchant la matière de se retirer complétement dans la zone active. Ensuite, le B peut faire des précipités avec les atomes de Si ou Ge rendant la qualité de l'épitaxie mauvaise. Enfin, le B diminue la contrainte dans la couche.

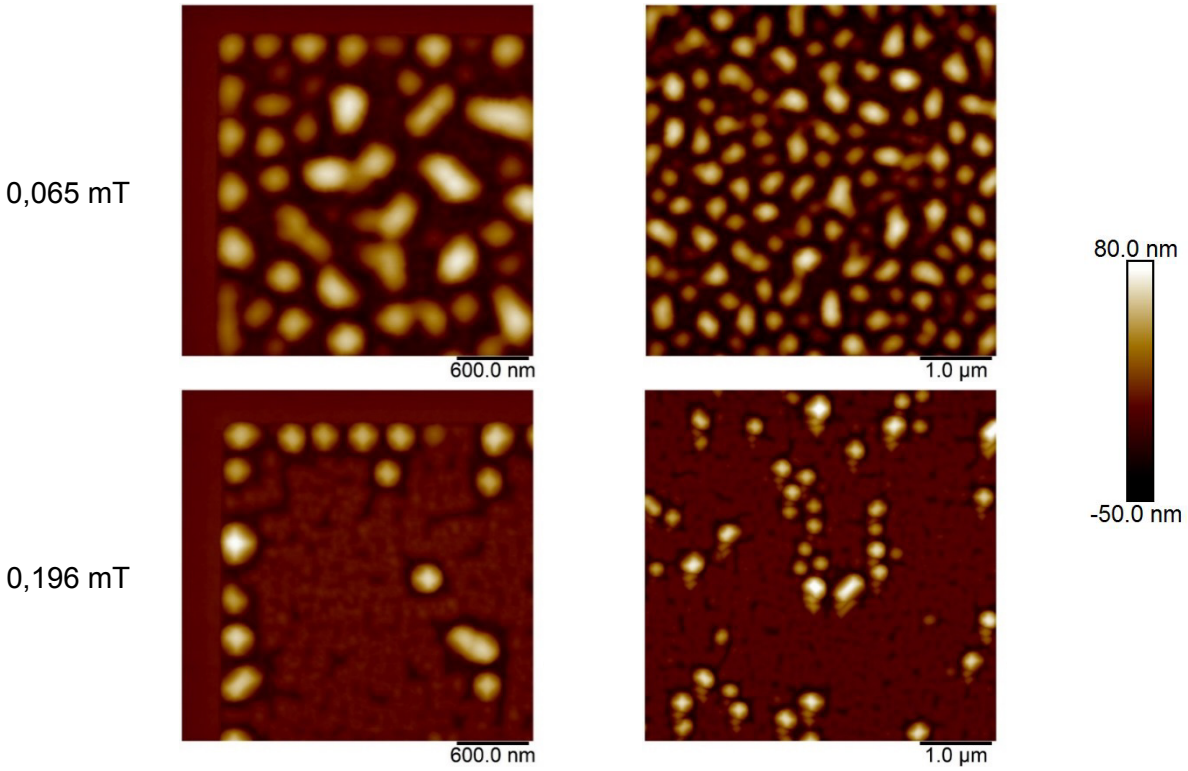

***Fig. R.14**: Images AFM des couches de SiGe:B recuites sous 20 Torr de H_2 à 850°C pendant 60 s dans les TBOX. Des pressions de 0,065 mT (en haut) et 0,196 mT (en bas) de B_2H_6 sont représentées. Le bore semble empêcher la formation des ondulations de type SK en créant des précipités.*

Applications industrielles dans les sources/drains

Cette dernière partie traite de l'intégration des couches de SiGe :B étudiées dans les sources/drains (S/D) de la technologie 14 nm. Les plaques sont orientées selon <110>. Le but était de préparer une épitaxie facettée sans défauts dans les S/D avec une concentration en bore suffisamment élevée (quelques 10^{20} cm^{-3}). En effet, la plupart des épitaxies présentait une morphologie entre les S/D plate non facettée qui pourrait s'apparenter à une morphologie après recuit. Il est d'ailleurs important de noter que dans la plupart des procédés standards, une purge de 10 – 30s est ajoutée en fin de croissance afin de purger les gaz de la chambre. Cependant, il a déjà été vu qu'une purge de 10 s pouvait être suffisante pour avoir un arrondissement thermique conséquent. De ce fait, la morphologie dans les S/D a été comparée pour deux procédés différents : un standard avec une purge de 10 s et un autre dans le lequel la recette de figeage a été intégrée en fin de procédé. C'est ce qui est montré dans la ***Fig. R.15***. Dans cette figure, la couche de SiGe est dopée avec une concentration mesurée par MBIR de 1,4 x 10^{20} at/cm^3. En comparant les deux procédés, il est évident de la purge impacte fortement la morphologie d'après dépôt. En effet, en regardant la morphologie obtenue avec la recette de figeage, des facettes {111} sont présentes tout autour du S/D et semblent disparaître lors de la purge de 10 s. Ainsi, la couche de SiGe :B a été sujet à l'arrondissement thermique pendant la purge ce qui explique l'aplanissement de l'épitaxie. La réalisation de S/D du 14 nm facettés a été accomplie avec succès en utilisant la recette de figeage et nos couches SiGe :B.

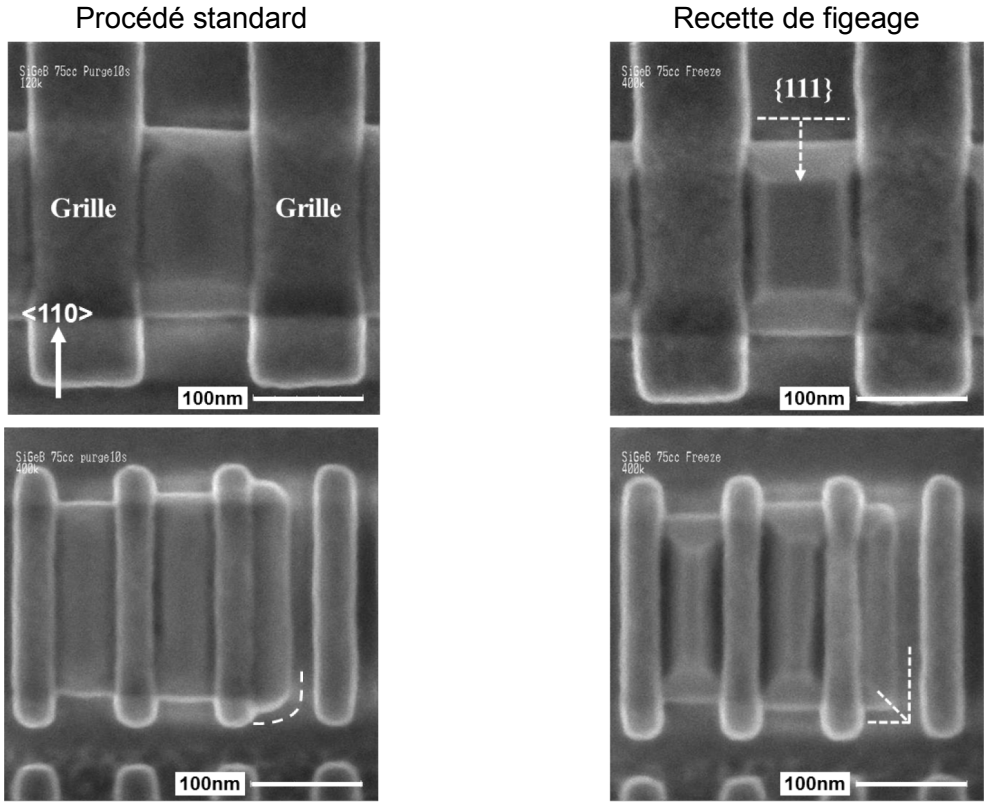

Fig. R.15*: Observation par MEB des couches de SiGe:B dans les structures S/D pour (à gauche) un procédé standard avec une purge de 10 s et (à droite) la recette de figeage. Il est clair que pour un procédé standard la couche de SiGe :B a subi un arrondissement thermique puisque les facettes {111} ont disparu comme montré par les lignes en pointillé.*

Conclusion

L'amélioration continue des procédés d'épitaxie et de leur intégration dans les technologies CMOS ont permis de résoudre de nombreux problèmes engendrés par la constante diminution de la taille des transistors. De nos jours, l'épitaxie est l'une des étapes majeures dans le développement des dispositifs et constitue un facteur clé dans l'amélioration des performances des dispositifs. De plus, le contrôle précis de la morphologie des couches épitaxiées est crucial pour les performances, ce qui est d'autant plus vrai que la dimension des transistors diminue. A cela il faut ajouter qu'avec des dimensions pouvant atteindre la dizaine de nanomètres, les effets thermiques sont très prononcés et ont un impact réel sur la morphologie et par conséquent sur les performances. Les effets qui jadis pouvaient être négligés ne le sont plus et doivent être minutieusement pris en compte. D'autre part, l'augmentation croissante de la complexité des structures rend les croissances d'épitaxie ainsi que leur contrôle morphologique très critique. Par conséquent, ce manuscrit est inscrit dans le cadre de l'étude morphologique et plus précisément l'influence des traitements thermiques sur la morphologie des épitaxies à base de Si (Si, SiGe, SiGe :B).De ce fait, des épitaxies effectuées par RT-CVD dans un environnement industriel, ont été caractérisées dans un premier temps, après croissance et dans un deuxième, après différents recuits.

Le contrôle de la morphologie des épitaxies ne pourrait se faire sans un contrôle précis de la température. C'est pourquoi avant toute expérience, il a été important de prendre des précautions, notamment dans le cas des recuits. Il a été vu que les valeurs des PID, la pression dans la chambre ainsi que les rapports de puissance dans les lampes ont un impact majeur sur le contrôle de la température. Les constantes PID, une fois optimisées, ont permis d'obtenir des rampes en température très répétables, rapides et surtout de minimiser les « overshoots » en fin de rampes. Quant aux rapports de puissance dans les lampes, il a été démontré que, pour une pression donnée, la mesure de la température change. La pression joue également un rôle important du fait qu'elle permet de changer la conductibilité du gaz. Ainsi, lorsque la pression augmente, la température de la plaquette change et se rapproche de la température de consigne. Enfin, il existe un rapport de puissance particulier pour lequel la température de la plaquette est égale à la température du suscepteur et ne dépend plus de la pression.

Des couches ont été étudiées juste après croissance en termes de cinétique. Les taux de croissance du Si et du SiGe ont été obtenus en fonction des pressions partielles de DCS et de GeH_4, respectivement. Par exemple, la présence du Ge joue comme un catalyseur à la désorption de l'H en surface libérant des sites libres. Ceci a pour conséquence une augmentation de la cinétique de croissance. Ensuite, ces mêmes couches ont été caractérisées par AFM. Des motifs différents (grandes boîtes de mesure, lignes, rectangles, carrés, ovales ou des zones actives de circuits SRAM) ont été observés afin d'avoir pour la suite des références morphologiques, notamment sur la rugosité, le facettage et la croissance latérale. Par exemple, il a été observé des rugosités typiquement inférieures à 0,15 nm. Aussi, toutes les épitaxies effectuées dans nos conditions, présentent que deux types facettes qui sont les facettes {001} et {111}. Il a également été confirmé que la surcroissance latérale des facettes {001} est à peu égale à l'épaisseur de croissance tandis que pour les facettes {111} celle-ci est égale à 0,4 fois l'épaisseur.

La passivation par des atomes de Si de couches de SiGe a été examinée. Tout d'abord, la cinétique de passivation par DCS a été quantifiée par XPS pour deux températures : 610°C et 630°C. Il a été montré que la cinétique de croissance n'est pas constante avec le temps : elle

décroit exponentiellement avant d'atteindre une valeur constante. Ceci a été expliqué par la couverture de la surface du SiGe par les atomes de Si et donc à l'extinction de l'effet catalytique du Ge. L'étude s'est ensuite portée sur l'utilité d'une telle passivation dans les procédés d'épitaxie pour conserver et contrôler la morphologie. Cette passivation a été intégrée à différentes étapes et s'est prouvée être d'une importance capitale, spécialement dans le cas de croissances sur SiGe ou encore pendant les purges de post croissance.

Une fois la morphologie d'après croissance bien maîtrisée et bien contrôlée, les études se sont centrées sur l'influence des recuits. Dans un premier temps, l'apparition du phénomène Stranski-Krastanov a été investigué en fonction de la température et du temps de recuit. Les ondulations de type SK mettent un long moment avant d'apparaître mais une fois le mécanisme déclenché, elles se propagent très rapidement faisant augmenter la rugosité de façon exponentielle. Ensuite, les ondulations se transforment en îlots et la rugosité se stabilise. Ce travail a été suivi par l'étude de la couche de mouillage qui tend à se créer entre les dômes. Il a été observé par XPS, qu'elle se forme systématiquement, probablement, par la diffusion des atomes de Si et de Ge. Dans un deuxième temps, l'arrondissement thermique dans les petits motifs a été étudié. Dans les lignes, le comportement des instabilités est différent selon leur orientation, leur épaisseur et leur largeur. L'instabilité augmente entre l'orientation <110> et <100> et avec la diminution de l'épaisseur. En termes de morphologie, les instabilités se caractérisent par l'apparition d'îlots ou de stries ou une combinaison des deux. Le phénomène de formation d'îlots ou de stries parallèles à l'orientation de la ligne, est attribué à la superposition de deux effets : l'arrondissement thermique et les ondulations de type SK. Cette étude nous a menés à la question de stabilisation de lignes présentant des instabilités. Des lignes orientées <100> instables ont ainsi été amincies puis recuites de nouveau. Les mesures AFM ont permis de confirmer que les lignes qui étaient instables ne le sont plus, mettant en évidence le rôle de l'épaisseur et donc du rayon de courbure sur les instabilités de lignes.

L'arrondissement thermique a aussi été étudié dans motifs carrés et rectangulaires. Premièrement, il a été observé que les motifs évoluent tous vers une forme finale d'équilibre globalement plus arrondie et présentant des facettes à faibles angles. Les facettes {105}, {15 3 23}, {715}, {119} et {113} ont été mesurées par AFM. Deuxièmement, la cinétique d'arrondissement a été quantifiée en mesurant le volume de matière déplacé par le recuit. Deux régimes ont été identifiés correspondant aux 2 pentes de l'Arrhenius : 2.9 eV et 7.7 eV. Dans le régime haute température (faible énergie), l'arrondissement est principalement contrôlé par la diffusion de surface. Dans le régime à basse température, la forte énergie d'activation « apparente » provient probablement de la combinaison de cette diffusion de surface avec un autre mécanisme. En effet, à plus faible température, la couverture d'H augmente rendant la diffusion plus difficile et par la même occasion l'arrondissement beaucoup moins rapide. Troisièmement, la pression lors des recuits a été modifiée et son influence mise en évidence. Ainsi, il existe une réelle différence morphologique entre par exemple 5 Torr et 200 Torr : à faible pression l'arrondissement est très avancé (voire même terminé), a contrario plus la pression augmente plus l'arrondissement est lent. Ceci est dû à la couverture d'H qui est plus ou moins importante selon la pression contraignant la diffusion des ad-atomes de Si en surface. Enfin, l'influence du gaz porteur a été étudiée. En passant de H_2 à N_2, l'arrondissement est bien plus efficace, ce qui signifie que les atomes ne collent pas (ou très peu) à la surface. Ceci renforce d'autant plus l'idée de l'impact de l'H sur l'arrondissement.

Le comportement morphologique des encapsulations Si et SiGe crûes sur une surface de SiGe non plane a été analysé. Lors de ce travail, il a été démontré que ces encapsulations Si et de SiGe se comportent différemment. Les encapsulations SiGe permettent d'aplanir la

surface ondulée et de rattraper une morphologie comme crûe bien plus facilement qu'avec les encapsulations Si. Cet effet est d'ailleurs amplifié avec l'augmentation du Ge dans le cap. Concernant les encapsulations Si, la cinétique de croissance semble aussi jouer ce même rôle de nivelage : plus la cinétique est faible, moins la surface est rugueuse. Différents mécanismes ont été proposés pouvant expliquer ces différents phénomènes comme l'interdiffusion, la ségrégation ou encore l'aspect catalyseur du Ge dû à une augmentation du gradient de contrainte entre le sommet des dômes et la couche de mouillage. Enfin, les encapsulations Si présentent des successions de terrasses, ce qui n'est pas le cas pour les encapsulations SiGe. Ces terrasses observées par TEM sont faites des facettes {113} et {119}. Les facettes {112} et {117} (observées par AFM) sont peut-être également présentes. Ces facettes présentes sous forme de terrasses sont attribuées à un aspect cinétique des croissances puisque celles-ci disparaissent complétement après recuit.

Le dernier chapitre de ce manuscrit a été dédié aux couches de SiGe :B. L'aspect cinétique de croissance a été d'abord étudié. Le B permet une meilleure désorption de l'H et donc une meilleure adsorption des atomes de Si ou Ge. Ceci a pour conséquence une augmentation du taux de croissance. L'incorporation du B et du Ge a été examinée en fonction de la pression partielle du B_2H_6, à l'aide de techniques comme le MBIR, l'XRD ou l'XRF. L'XRF nous a permis de remonter au vrai pourcentage de Ge, ce qui n'a pas pu être possible avec l'XRD.

La morphologie des couches comme crûes a été ensuite caractérisée par AFM. Dans les motifs larges, la rugosité augmente fortement pour les forts dopages de B et des dislocations ont été détectées dans la couche. Ces dislocations ont été attribuées à des précipités de B avec le Si et Ge. Dans les petits motifs, la morphologie est d'autant plus atteinte par la présence du B. Cependant, pour des dopages intermédiaires, le facettage est similaire à celui observé pour des couches non dopées : présence des facettes {111} et {001}. Pour les dopages très faibles, le facettage change un peu avec l'apparition de la facette {112} en plus de la facette {111}. Enfin, la croissance latérale semble augmenter avec l'augmentation de la concentration en B.

Ce travail s'est poursuivi par l'étude de l'influence des recuits sur les couches de SiGe :B. il a été vu que l'arrondissement thermique est plus efficace dans le cas de couches dopées B. Ceci peut être dû à la plus forte concentration en Ge de nos croissances et surtout au B. En effet, le B augmente le taux de croissance pouvant se traduire par une diminution de la couverture d'H et par conséquent une amélioration de l'efficacité de l'arrondissement. Cependant, le phénomène est un peu différent pour les couches dopées. Les « bourrelets » créés tout autour du motif ne sont pas lisses et réguliers mais présentent des bosses. De plus, l'intérieur des motifs sont très rugueux notamment à cause de l'apparition de précipités. Une augmentation du traitement thermique a conduit à de nouvelles analyses. Dans les grands motifs, les ondulations très organisées de type SK se sont effacées au détriment de multiples îlots organisés de façon aléatoire en surface et dans les petits motifs, la matière présente des difficultés à se rétracter complétement dans la zone active. Tout ceci peut s'expliquer par les précipités de B formant des composés avec le Si ou le Ge or par le fait que le B modifie la tension de surface du SiO_2 devenant alors plus « collante » pour les atomes de Si ou Ge. Le B induit de ce fait de multiples mécanismes : une plus forte sensibilité aux traitements thermiques, une diminution de la contrainte du film, une modification de l'état de surface du SiO_2 et une apparition de précipités.

La dernière partie du chapitre 5 a été centrée naturellement sur l'application industrielle des épitaxies dopées B dans les S/D de la technologie 14 nm, le but étant de faire des S/D avec une morphologie contrôlée (facetté ou non). L'intégration de nos épitaxies avec la passivation

Si a permis d'obtenir des épitaxies facettées entre les grilles, ce qui n'était pas le cas avec les procédés standard utilisés.

En résumé, les travaux effectués sur l'évolution morphologique des films de SiGe et SiGe :B ont conduit vers une bonne compréhension des mécanismes mis en jeu se produisant lors des recuits. Ceci représente une réelle avancée du fait que cela permet un meilleur contrôle de la morphologie des épitaxies et pour la suite une amélioration certaine des performances des dispositifs. D'autre part, les recherches menées sur la passivation Si ont permis de maintenir une morphologie d'après croissance et d'éviter la formation des instabilités pour les futures technologies qui deviendront toujours plus sensibles. En plus de cela, la passivation a permis de résoudre des problèmes restés jusqu'alors sans réponses, notamment concernant les épitaxies plates dans les S/D du 14 nm. Enfin, la réussite de son intégration dans les différents procédés sera fortement avantageuse pour la plupart des applications demandant des épitaxies, telles que les capteurs utilisés en imagerie ou en photonique, ou les technologies CMOS futures.

Résumé

Dans les technologies avancées, l'épitaxie des matériaux à base de silicium devient de plus en plus critique et les effets morphologiques importants. Les traitements thermiques ainsi que le dopage peuvent altérer la morphologie des épitaxies dégradant de façon considérable les performances des dispositifs. Les travaux de thèse ont pour objectifs de comprendre et résoudre ces problématiques, ils concernent donc l'étude de la morphologie et des forts dopages des épitaxies dans les motifs de petites tailles des technologies CMOS 14 et 10 nm.

Nous avons étudié l'influence des conditions de recuit sous H_2 sur la morphologie des épitaxies. Ceci a conduit à la détermination de la cinétique d'arrondissement thermique dans les petits motifs (100 nm et moins). D'après une analyse de la cinétique, deux énergies ont été identifiées : 2,9 eV et 7,7 eV. L'énergie de 2,9 eV montre qu'aux hautes températures, la diffusion de surface est le principal mécanisme de l'arrondissement thermique. Aux faibles températures, l'augmentation de la couverture d'hydrogène limite encore plus cette diffusion, augmentant fortement l'énergie obtenue. Nous avons observé que la pression du gaz porteur et la nature de celui-ci ont un impact important sur la diffusion de surface et modulent donc la cinétique d'arrondissement thermique.

La caractérisation par microscopie à force atomique de croissances sélectives de couches SiGe dopées bore, montre que le bore modifie grandement la morphologie de croissance, ainsi que l'arrondissement thermique. Pour un même recuit, un motif dopé s'arrondit beaucoup plus rapidement qu'un motif non dopé. Les épitaxies développées au cours de ces travaux ont été intégrées avec succès dans les sources/drains du CMOS 14 nm. Selon le besoin, les épitaxies peuvent soit présenter de larges facettes bien définies soit aucune facette, et cela grâce à un procédé adéquat que ce travail a permis de proposer et développer.

Mots-clés : Hétéro-épitaxie, Si, SiGe, morphologie, facettage, arrondissement thermique, Stranski-Krastanov, dépôt chimique en phase vapeur, encapsulation, dopage.

Abstract

In advanced technologies, the Si-based materials epitaxy becomes more and more challenging and the morphological effects very important. The thermal treatments as well as the doping may degrade the epitaxies' morphology resulting in considerably damaging the devices' performances. The works presented in this thesis, aim at understanding and solving these problematics. Thus, they are focused on the study of the epitaxies' morphology and high doping in the small patterns of the 10 and 14 nm CMOS technologies. The influence of the H_2 annealing conditions on the morphology was studied. This led to determine the thermal rounding kinetics in small patterns. According to a kinetics analysis, two energies were identified: 2.9 eV and 7.7 eV. The 2.9 eV energy shows that at high temperatures, the surface diffusion is the thermal rounding main mechanism. At low temperatures, the hydrogen coverage's increase limits even more this diffusion, greatly increasing the energy obtained. It was observed that the carrier gas pressure and its nature have a strong impact on the surface diffusion and thus modify the thermal rounding kinetics.

The characterization by atomic force microscopy, of boron doped layer selectively grown, shows that the boron greatly modifies the growth's morphology, as well as the thermal rounding. Considering a same annealing, the rounding phenomenon occurs faster in a doped pattern than in an un-doped pattern. The epitaxies developed during this work were successfully integrated to the 14 nm node sources and drains. Depending on the needs, the epitaxies can either present large and well defined facets or no facets, all of this thanks to an adequate process which was proposed and developed through this work.

Keywords: Hetero-epitaxy, Si, SiGe, morphology, faceting, thermal rounding, Stranski-Krastanov, chemical vapor deposition, cap, doping.